



ISSN 1605-2730

MATERIALS PHYSICS AND MECHANICS

Vol. 32, No. 2, 2017

MATERIALS PHYSICS AND MECHANICS

Principal Editors:

Dmitrii Indeitsev
*Institute of Problems of Mechanical Engineering
of the Russian Academy of Science (RAS), Russia*

Andrei Rudskoi
Peter the Great St.Petersburg Polytechnic University, Russia

Founder and Honorary Editor: Ilya Ovid'ko (1961-2017)

*Institute of Problems of Mechanical Engineering
of the Russian Academy of Sciences (RAS), Russia*

Staff Editors:

Anna Kolesnikova
*Institute of Problems of Mechanical Engineering
of the Russian Academy of Sciences (RAS), Russia*

Alexander Nemov
Peter the Great St.Petersburg Polytechnic University, Russia

Editorial Board:

E.C. Aifantis
Aristotle University of Thessaloniki, Greece

K.E. Aifantis
University of Florida, USA

U. Balachandran
Argonne National Laboratory, USA

A. Bellosi
Research Institute for Ceramics Technology, Italy

A.K. Belyaev
Institute of Problems of Mechanical Engineering (RAS), Russia

S.V. Bobylev
Institute of Problems of Mechanical Engineering (RAS), Russia

A.I. Borovkov
Peter the Great St.Petersburg Polytechnic University, Russia

G.-M. Chow
National University of Singapore, Singapore

Yu. Estrin
Monash University, Australia

A.B. Freidin
Institute of Problems of Mechanical Engineering (RAS), Russia

Y. Gogotsi
Drexel University, USA

R.V. Goldshtein
Institute of Problems of Mechanics (RAS), Russia

I.G. Goryacheva
Institute of Problems of Mechanics (RAS), Russia

D. Hui
University of New Orleans, USA

G. Kiriakidis
IESL/FORTH, Greece

D.M. Klimov
Institute of Problems of Mechanics (RAS), Russia

G.E. Kodzhaspirov
Peter the Great St.Petersburg Polytechnic University, Russia

S.A. Kukushkin
Institute of Problems of Mechanical Engineering (RAS), Russia

T.G. Langdon
University of Southampton, U.K.

V.P. Matveenko
Institute of Continuous Media Mechanics (RAS), Russia

A.I. Melker
Peter the Great St.Petersburg Polytechnic University, Russia

Yu.I. Meshcheryakov
Institute of Problems of Mechanical Engineering (RAS), Russia

N.F. Morozov
St.Petersburg State University, Russia

R.R. Mulyukov
Institute for Metals Superplasticity Problems (RAS), Russia

Yu.V. Petrov
St.Petersburg State University, Russia

N.M. Pugno
Politecnico di Torino, Italy

B.B. Rath
Naval Research Laboratory, USA

A.E. Romanov
Ioffe Physico-Technical Institute (RAS), Russia

A.M. Sastry
University of Michigan, Ann Arbor, USA

A.G. Sheinerman
Institute of Problems of Mechanics (RAS), Russia

N.V. Skiba
Institute of Problems of Mechanics (RAS), Russia

A. Thölen
Chalmers University of Technology, Sweden

R.Z. Valiev
Ufa State Aviation Technical University, Russia

K. Zhou
Nanyang Technological University, Singapore

"Materials Physics and Mechanics" Editorial Office:

Phone: +7(812)591 65 28 **E-mail:** mpmjournal@spbstu.ru **Web-site:** <http://www.mpm.spbstu.ru>

International scientific journal "Materials Physics and Mechanics" is published by Peter the Great St.Petersburg Polytechnic University in collaboration with Institute of Problems of Mechanical Engineering of the Russian Academy of Sciences in both hard copy and electronic versions.

The journal provides an international medium for the publication of reviews and original research papers written in English and focused on the following topics:

- Mechanics of nanostructured materials (such as nanocrystalline materials, nanocomposites, nanoporous materials, nanotubes, quantum dots, nanowires, nanostructured films and coatings).
- Physics of strength and plasticity of nanostructured materials, physics of defects in nanostructured materials.
- Mechanics of deformation and fracture processes in conventional materials (solids).
- Physics of strength and plasticity of conventional materials (solids).

Owner organizations: Peter the Great St. Petersburg Polytechnic University; Institute of Problems of Mechanical Engineering RAS.

Materials Physics and Mechanics is indexed in Chemical Abstracts, Cambridge Scientific Abstracts, Web of Science Emerging Sources Citation Index (ESCI) and Elsevier Bibliographic Databases (in particular, SCOPUS).



МЕХАНИКА И ФИЗИКА МАТЕРИАЛОВ

Materials Physics and Mechanics

Том 32, номер 2, 2017 год

Учредители:

ФГАОУ ВО «Санкт-Петербургский политехнический университет Петра Великого»
ФГБУН «Институт проблем машиноведения Российской академии наук»

Редакционная коллегия журнала

Главные редакторы:

д.ф.-м.н., чл.-корр. РАН **Д.А. Индейцев**
Институт проблем машиноведения Российской академии наук (РАН)

д.т.н., академик РАН **А.И. Рудской**
Санкт-Петербургский политехнический университет
Петра Великого

Основатель и почетный редактор: д.ф.-м.н. **И.А. Овидько (1961-2017)**
Институт проблем машиноведения Российской академии наук (РАН)

Ответственные редакторы

д.ф.-м.н. **А.Л. Колесникова**
Институт проблем машиноведения Российской академии наук
(РАН)

к.т.н. **А.С. Немов**
Санкт-Петербургский политехнический университет Петра
Великого

Международная редакционная коллегия:

д.ф.-м.н., проф. **А.К. Беляев**
Институт проблем машиноведения РАН, Россия
д.ф.-м.н. **С.В. Бобылев**
Институт проблем машиноведения РАН, Россия
к.т.н., проф. **А.И. Боровков**
Санкт-Петербургский политехнический у-т Петра Великого, Россия
д.ф.-м.н., проф. **Р.З. Валнев**
Уфимский государственный технический университет, Россия
д.ф.-м.н., чл.-корр. РАН **Р.В. Гольдштейн**
Институт проблем механики РАН, Россия
д.ф.-м.н., академик РАН **И.Г. Горячева**
Институт проблем механики РАН, Россия
д.ф.-м.н., академик РАН **Д.М. Климов**
Институт проблем механики РАН, Россия
д.т.н., проф. **Г.Е. Коджаспиров**
Санкт-Петербургский политехнический у-т Петра Великого, Россия
д.ф.-м.н., проф. **С.А. Кукушкин**
Институт проблем машиноведения РАН, Россия
д.ф.-м.н., академик РАН **В.П. Матвеев**
Институт механики сплошных сред РАН, Россия
д.ф.-м.н., проф. **А.И. Мелькер**
Санкт-Петербургский политехнический у-т Петра Великого, Россия
д.ф.-м.н., проф. **Ю.И. Мещеряков**
Институт проблем машиноведения РАН, Россия
д.ф.-м.н., академик РАН **Н.Ф. Морозов**
Санкт-Петербургский государственный университет, Россия
д.ф.-м.н., чл.-корр. РАН **Р.Р. Мулюков**
Институт проблем сверхпластичности металлов РАН, Россия
д.ф.-м.н., чл.-корр. РАН **Ю.В. Петров**
Санкт-Петербургский государственный университет, Россия
д.ф.-м.н., проф. **А.Е. Романов**
Физико-технический институт им. А.Ф. Иоффе РАН, Россия
д.ф.-м.н. **Н.В. Скиба**
Институт проблем машиноведения РАН, Россия
д.ф.-м.н., проф. **А.Б. Фрейдин**
Институт проблем машиноведения РАН, Россия
д.ф.-м.н. **А.Г. Шейнман**
Институт проблем машиноведения РАН, Россия

Prof., Dr. **E.C. Aifantis**
Aristotle University of Thessaloniki, Greece
Dr. **K.E. Aifantis**
University of Florida, USA
Dr. **U. Balachandran**
Argonne National Laboratory, USA
Dr. **A. Bellosi**
Research Institute for Ceramics Technology, Italy
Prof., Dr. **G.-M. Chow**
National University of Singapore, Singapore
Prof., Dr. **Yu. Estrin**
Monash University, Australia
Prof., Dr. **Y. Gogotsi**
Drexel University, USA
Prof., Dr. **D. Hui**
University of New Orleans, USA
Prof., Dr. **G. Kiriakidis**
IESL/FORTH, Greece
Prof., Dr. **T.G. Langdon**
University of Southampton, UK
Prof., Dr. **N.M. Pugno**
Politecnico di Torino, Italy
Dr. **B.B. Rath**
Naval Research Laboratory, USA
Prof., Dr. **A.M. Sastry**
University of Michigan, Ann Arbor, USA
Prof., Dr. **A. Thölen**
Chalmers University of Technology, Sweden
Prof. Dr. **K. Zhou**
Nanyang Technological University, Singapore

Тел.: +7(812)591 65 28 E-mail: mpmjournal@spbstu.ru Web-site: <http://www.mpm.spbstu.ru>

Тематика журнала

Международный научный журнал "Materials Physics and Mechanics" издается Санкт-Петербургским политехническим университетом Петра Великого в сотрудничестве с Институтом проблем машиноведения Российской академии наук в печатном виде и электронной форме. Журнал публикует обзорные и оригинальные научные статьи на английском языке по следующим тематикам:

- Механика наноструктурных материалов (таких как нанокристаллические материалы, нанокомпозиты, нанопористые материалы, нанотрубки, наноструктурные пленки и покрытия, материалы с квантовыми точками и проволоками).
- Физика прочности и пластичности наноструктурных материалов, физика дефектов в наноструктурных материалах.
- Механика процессов деформирования и разрушения в традиционных материалах (твердых телах).
- Физика прочности и пластичности традиционных материалов (твердых тел).

Редколлегия принимает статьи, которые нигде ранее не опубликованы и не направлены для опубликования в другие научные издания. Все представляемые в редакцию журнала "Механика и физика материалов" статьи рецензируются. Статьи могут отправляться авторам на доработку. Не принятые к опубликованию статьи авторам не возвращаются.

Журнал "Механика и физика материалов" ("Materials Physics and Mechanics") включен в систему цитирования Web of Science Emerging Sources Citation Index (ESCI), SCOPUS и РИНЦ.

© 2017, Санкт-Петербургский политехнический университет Петра Великого
© 2017, Институт проблем машиноведения Российской академии наук

Содержание

The simulation of carbon nanotubes as macromolecular coils: interfacial adhesion.....	103-107
G.V. Kozlov, I.V. Dolbin	
Carbon-based nanostructure created by Ba and Cs atomic layer deposition on the vicinal.....	108-116
3C-SiC(111) surfaces	
G.V. Benemanskaya, P.A. Dementev, S.A. Kukushkin, M.N. Lapushkin, A.V. Osipov, S.N. Timoshnev	
The study of the interaction of hydrogen impurity with point and linear defects in palladium.....	117-122
and nickel	
G.M. Poletaev, I.V. Zorya, E.S. Medvedeva, D.V. Novoselova, M.D. Starostenkov	
Generalized thermoelastic axi-symmetric deformation problem in a thick circular plate with.....	123-132
dual phase lags and two temperatures	
R. Kumar, V.R. Manthena, N.K. Lamba, G.D. Kedar	
An effective method to find Green's functions for layered media.....	133-143
N.S. Markov, A.M. Linkov	
Copper crystals with fragmented structure and developed surface in temperature fields.....	144-151
N.N. Gryzunova, A.A. Vikarchuk, A.M. Gryzunov, A.E. Romanov	
Shock-induced structural instabilities and spall-strength of maraging steels.....	152-164
Yu.I. Mescheryakov, N.I. Zhigacheva, A.K. Divakov, Yu.A. Petrov	
Effect of titanium carbide addition on the workability behavior of powder metallurgy.....	165-177
aluminum preforms during hot deformation	
S. Narayan, A. Rajeshkannan	
Defects in thin epitaxial layers of $(Al_xGa_{1-x})_2O_3$ grown on Al_2O_3 substrates.....	178-185
A.V. Kremleva, D.A. Kirilenko, V.I. Nikolaev, A.I. Pechnikov, S.L. Stepanov, M.A. Odnoblyudov, V.E. Bougrov, A.E. Romanov	
Mathematical model of ultrasound transmission in gradient materials synthesized in.....	186-193
arc surfacing under contact loading	
V.D. Sarychev, A.Y. Granovskiy, S.A. Nevskii, S.V. Konovalov, V.E. Gromov, M.V. Temlyantsev	
Study of antireflection coatings for high speed 1.3 -1.55 μm InGaAs/InP PIN photodetector.....	194-197
E.S. Kolodeznyi, I.I. Novikov, A.G. Gladyshev, S.S. Rochas, K.D. Sharipo, L.Ya. Karachinsky, A.Yu. Egorov, V.E. Bougrov	
Synthesis of silver nanochains with a chemical method.....	198-206
I.M. Sosnin, M.N. Turkov, M.R. Shafeev, E.V. Shulga, I. Kink, A.A. Vikarchuk, A.E. Romanov	
Relaxation in resins with low-frequency mechanical cycling.....	207-212
V.I. Ivlev, A.F. Sigachyov, N.E. Fomin, V.A. Yudin	
On calculation of effective elastic properties of materials with cracks.....	213-221
Ruslan L. Lapin, Vitaly A. Kuzkin	
In-situ measurement and finite element simulation of thermo-mechanical properties.....	222-236
of AA 6063 aluminum alloy for MIG weldment	
S. Baharnejhad, A.P. Golhin	

Contents

The simulation of carbon nanotubes as macromolecular coils: interfacial adhesion.....	103-107
G.V. Kozlov, I.V. Dolbin	
Carbon-based nanostructure created by Ba and Cs atomic layer deposition on the vicinal.....	108-116
3C-SiC(111) surfaces	
G.V. Benemanskaya, P.A. Dementev, S.A. Kukushkin, M.N. Lapushkin, A.V. Osipov, S.N. Timoshnev	
The study of the interaction of hydrogen impurity with point and linear defects in palladium.....	117-122
and nickel	
G.M. Poletaev, I.V. Zorya, E.S. Medvedeva, D.V. Novoselova, M.D. Starostenkov	
Generalized thermoelastic axi-symmetric deformation problem in a thick circular plate with.....	123-132
dual phase lags and two temperatures	
R. Kumar, V.R. Manthena, N.K. Lamba, G.D. Kedar	
An effective method to find Green's functions for layered media.....	133-143
N.S. Markov, A.M. Linkov	
Copper crystals with fragmented structure and developed surface in temperature fields.....	144-151
N.N. Gryzunova, A.A. Vikarchuk, A.M. Gryzunov, A.E. Romanov	
Shock-induced structural instabilities and spall-strength of maraging steels.....	152-164
Yu.I. Mescheryakov, N.I. Zhigacheva, A.K. Divakov, Yu.A. Petrov	
Effect of titanium carbide addition on the workability behavior of powder metallurgy.....	165-177
aluminum preforms during hot deformation	
S. Narayan, A. Rajeshkannan	
Defects in thin epitaxial layers of $(Al_xGa_{1-x})_2O_3$ grown on Al_2O_3 substrates.....	178-185
A.V. Kremleva, D.A. Kirilenko, V.I. Nikolaev, A.I. Pechnikov, S.L. Stepanov, M.A. Odnoblyudov, V.E. Bougrov, A.E. Romanov	
Mathematical model of ultrasound transmission in gradient materials synthesized in.....	186-193
arc surfacing under contact loading	
V.D. Sarychev, A.Y. Granovskiy, S.A. Nevskii, S.V. Konovalov, V.E. Gromov, M.V. Temlyantsev	
Study of antireflection coatings for high speed 1.3 -1.55 μm InGaAs/InP PIN photodetector.....	194-197
E.S. Kolodeznyi, I.I. Novikov, A.G. Gladyshev, S.S. Rochas, K.D. Sharipo, L.Ya. Karachinsky, A.Yu. Egorov, V.E. Bougrov	
Synthesis of silver nanochains with a chemical method.....	198-206
I.M. Sosnin, M.N. Turkov, M.R. Shafeev, E.V. Shulga, I. Kink, A.A. Vikarchuk, A.E. Romanov	
Relaxation in resins with low-frequency mechanical cycling.....	207-212
V.I. Ivlev, A.F. Sigachyov, N.E. Fomin, V.A. Yudin	
On calculation of effective elastic properties of materials with cracks.....	213-221
Ruslan L. Lapin, Vitaly A. Kuzkin	
In-situ measurement and finite element simulation of thermo-mechanical properties.....	222-236
of AA 6063 aluminum alloy for MIG weldment	
S. Baharnezhad, A.P. Golhin	

THE SIMULATION OF CARBON NANOTUBES AS MACROMOLECULAR COILS: INTERFACIAL ADHESION

G.V. Kozlov*, I.V. Dolbin

Kh.M. Berbekov Kabardino-Balkarian State University,
Chernyshevsky st. 173, Nal'chik, 360004, Russian Federation

*e-mail: i_dolbin@mail.ru

Abstract. Simulation of carbon nanotubes ring-like formations as macromolecular coils was performed within the frameworks of fractal physical chemistry of polymer solutions. The dependence of interfacial adhesion level has been shown in nanocomposites polymer/carbon nanotubes on the indicated formations structure, characterized by its fractal dimension. This treatment correctness was confirmed by nanocomposites reinforcement degree description within the framework of reinforcement molecular theory.

Keywords: nanocomposite; epoxy polymer; ring-like formation; interfacial adhesion; fractal dimension.

1. Introduction

As it is well-known [1, 2], carbon nanotubes in polymer nanocomposites form ring-like structure, outwardly resembling macromolecular coils. This circumstance allows to use for the carbon nanotubes indicated structures methods of both classical [3] and fractal [4] physical chemistry of polymer solutions. The authors [2] found interfacial adhesion level reduction in nanocomposites polymer/carbon nanotubes at this specific nanofiller ring-like formations radius, that restricted essentially its possibilities of the indicated nanocomposites properties improvement.

At present a number of extreme experimental dependences of nanocomposites elasticity modulus on carbon nanotubes contents at very small values of the latter (of the order of 0.1 mass % and less) was obtained [5-7], which up to now do not obtain proper explanation. Therefore the present work purpose is intercommunication clarification of ring-like formations structure and interfacial adhesion level in polymer nanocomposites, where the indicated structures are simulated as macromolecular coils, and the explanation of the obtained extreme dependences of elasticity modulus on this basis.

2. Experimental

Epoxy polymers (EP) based on diglycidyl ether of bisphenol A (ED-20) and diglycidyl ether of diphenylolpropane (DED) were used as matrix polymer. The eutectic mixture of μ -phenylenediamine (40 mass %) and 4,4'-diaminodiphenylmethane (60 mass %) at equifunctional ratio was applied as curing agent. The eutectic mixture was prepared in vacuum at heating up to 373 K during 1 hour, cooled and preserved in argon atmosphere. Epoxy polymers were cured by the stepped regime (353 K – 2 hours, 393 K – 2 hours and 443 K – 5 hours) [6].

The single-walled carbon nanotubes (CNT) with diameter of 1.2-1.6 nm and length of ≤ 2 μ m were prepared by voltaic arc method with purification (up to 95 %) by gas-phase oxidation

and washing in hydrochloric acid. After this procedure CNTs are in strongly agglomerated state in the form of bundles with a diameter of ~ 30 nm [6].

The tensile tests are performed in accordance with ASTM D638-96, D882-95a on a tensile tester Zwick at temperature 293 K and deformation rate 1 mm/min [6].

3. Results and Discussion

CNT ring-like structures radius R_{CNT} can be determined within the framework of percolation model [8] with the aid of the following equation:

$$\varphi_n = \frac{\pi L_{CNT} r_{CNT}^2}{(2R_{CNT})^3}, \quad (1)$$

where φ_n is nanofiller volume contents, L_{CNT} and r_{CNT} are length and radius of carbon nanotube, accordingly.

The value φ_n was determined according to the well-known formula [9]:

$$\varphi_n = \frac{W_n}{\rho_n}, \quad (2)$$

where W_n is nanofiller mass contents, ρ_n is its density, which for nanoparticles is determined as follows [9]:

$$\rho_n = 188(D_{CNT})^{1/3}, \text{ kg/m}^3, \quad (3)$$

where D_{CNT} is carbon nanotubes bundle diameter, which is given in nm.

And at last, the fractal dimension D_f^{CNT} of CNT ring-like formations was calculated within the framework of an irreversible aggregation model with the aid of the equation [2]:

$$R_{CNT} = 3.40\varphi_n^{-1/(d-D_f^{CNT})}, \quad (4)$$

where d is dimension of Euclidean space, in which a fractal is considered (it is obvious, that in our case $d = 3$) and R_{CNT} is given in nm.

The interfacial adhesion level in polymer nanocomposites can be characterized with the aid of the dimensionless parameter b_α , which is determined with the equation usage [9]:

$$\frac{E_n}{E_m} = 1 - 11(c\varphi_n b_\alpha)^{1.7}, \quad (5)$$

where E_n and E_m are elasticity moduli of nanocomposite and matrix polymer, respectively (the ratio E_n/E_m is accepted to call nanocomposite reinforcement degree), c is constant coefficient, which is equal to ~ 2.8 for carbon nanotubes [9].

In Figure 1 the dependence $b_\alpha(D_f^{CNT})$ is adduced for the considered nanocomposites, breaks down into two linear parts with a very differing slope. This dependence can be described analytically by the following empirical equations:

$$b_\alpha = 5.5 \times 10^3 - 10^4(D_f^{CNT} - 1) \text{ for } D_f^{CNT} < 1.50, \quad (6)$$

and

$$b_\alpha = 5.5 \times 10^2(2 - D_f^{CNT}) \text{ for } D_f^{CNT} < 1.50 \quad (7)$$

Let us note two specific features of the dependence $b_\alpha(D_f^{CNT})$, adduced in Fig. 1 and described by the equations (6) and (7). As it is known [9], parameter b_α allows not only quantitative, but qualitative gradation of interfacial adhesion level in polymer nanocomposites as well. So, the condition $b_\alpha = 0$ defines interfacial adhesion absence, $b_\alpha = 1.0$ means perfect (by Kerner) adhesion and the condition $b_\alpha > 1.0$ gives criterion of nanoadhesion effect realization in the considered nanomaterials. The data of Fig. 1 demonstrated the possibility of nanoadhesion very high level realization at carbon nanotubes small contents. So, according to the equation (6) the value $b_\alpha = 5500$ for $D_f^{CNT} = 1.0$, i.e. for completely straight-line nanotubes. In case of nanocomposites polymer/carbon nanotubes with large enough nanofiller contents (≥ 1 mass %) the value b_α does not exceed 10.5 (even in case of functionalized CNT) [9].

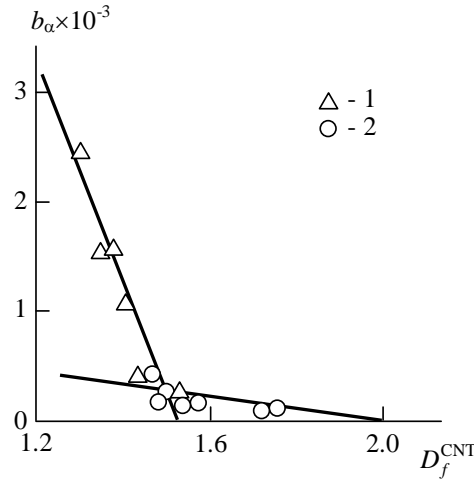


Fig. 1. The dependence of parameter b_α , characterizing interfacial adhesion level, on fractal dimension D_f^{CNT} CNT ring-like formations for nanocomposites EP/CNT based on DED (1) and ED-20 (2).

The value D_f^{CNT} at the transition point, which is equal to 1.50 (Fig. 1), is the second very important feature of the adduced above data. The indicated dimension corresponds to leaking (transparent) macromolecular coil or corresponding CNT ring-like formation. This means, that at $D_f^{CNT} \leq 1.50$ polymer can go freely inside CNT ring-like structure and this, in its turn, assumes, that the greater part of polymer matrix-nanofiller contacts is formed in CNT ring-like formations inner regions. Polymer access (diffusion) restriction inside the indicated structures at $D_f^{CNT} > 1.50$ results in such contacts number sharp decrease and in corresponding interfacial adhesion level reduction, characterized by parameter b_α (Fig. 1).

Let us consider another important structural aspect. The percolation threshold φ_c value for CNT can be determined by several methods and in the present work the method, proposed in paper [1], will be used, where the value φ_c is determined according to the equation:

$$\varphi_c = \frac{0.48}{4\alpha_{ef}^2 N_{cl}^{(3-D_f^{CNT})/D_f^{CNT}}}, \quad (8)$$

where α_{ef} is effective aspect ratio of carbon nanotube, N_{cl} is stiffness sections number per CNT ring-like formation.

The value α_{ef} can be determined with the aid of the following equation [1]:

$$\frac{E_n}{E_m} = 1 + 2\alpha_{ef} C_{or} \varphi_n, \quad (9)$$

where C_{or} is the orientation factor, which is accepted equal to 0.2 for the case of CNT statistically oriented stiffness sections [1].

The parameter N_{cl} was calculated with the following formula usage [1]:

$$R_{CNT} = L_{ef} N_{cl}^{1/D_f^{CNT}}, \quad (10)$$

where L_{ef} is CNT stiffness section effective length, determined as the product $\alpha_{ef} D_{CNT}$.

Calculation according to the indicated methodics, namely, according to the equations (8)-(10), gives the value $\varphi_c = 0.62 \times 10^{-4}$. In its turn, R_{CNT} calculation according to the equation (1) at $\varphi_n = \varphi_c$ gives the value $D_f^{CNT} \approx 1.44$. The adduced estimations show that realization of CNT leaking (transparent) ring-like structures, allowing matrix polymer free diffusion in their inner region, is possible at the condition $\varphi_n < \varphi_c$ only.

The estimated by such method values b_α correctness checking can be performed within the framework of nanocomposites reinforcement molecular conception, the basic equation of which has the look [9]:

$$\frac{E_n}{E_m} = 1 + \frac{0.19W_n l_{st} b_\alpha}{D_{CNT}^{1/2}}, \quad (11)$$

where l_{st} is polymer matrix chain statistical segment length and D_{CNT} value is accepted for a separate carbon nanotube, i.e. equal to ~ 1.5 nm [6].

The value l_{st} was determined as follows [10]:

$$l_{st} = l_0 C_\infty, \quad (12)$$

where l_0 is the main chain skeletal bond length, which is equal to 0.154 nm for the considered EP [10], C_∞ is characteristic ratio, the value of which is connected with structure fractal dimension d_f by the equation [11]:

$$C_\infty = \frac{2d_f}{d(d-1)(d-d_f)} + \frac{4}{3}, \quad (13)$$

where d is, as earlier, the dimension of Euclidean space, in which a fractal is considered (it is obvious, that in our case $d = 3$ again).

For epoxy polymers the value $d_f \approx 2.7$ [12] and then $C_\infty = 4.33$ and $l_{st} = 0.667$ nm.

In Fig. 2 the comparison of calculated according to the equation (11) and the obtained experimentally dependences $E_n/E_m(\varphi_n)$ is adduced for nanocomposites EP/CNT based on DED. As one can see, the proposed model gives a good both qualitative (the dependence extreme character description) and quantitative (the average discrepancy of theory and experiment makes up 2.5 %) correspondence to the experiment. The similar results were obtained for nanocomposites EP/CNT based on ED-20, but with somewhat larger theory and experiment discrepancy (4.5 %).

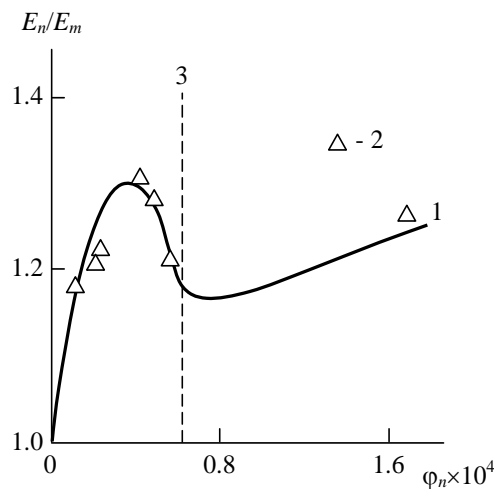


Fig. 2. The comparison of calculated according to the equation (11) (1) and obtained experimentally (2) dependences of reinforcement degree E_n/E_m on nanofiller volume contents φ_n for nanocomposites EP/CNT based on DED. The vertical dashed line 3 indicates percolation threshold φ_c .

4. Conclusions

Hence, the obtained in the present work results have shown that carbon nanotubes ring-like formations in polymer nanocomposites can be simulated successfully as macromolecular coils. The indicated structures fractal dimension reduction results in interfacial adhesion level enhancement and this effect is expressed especially strongly for CNT leaking (transparent) ring-like formations. This supposes that contacts polymer matrix-nanofiller main part is formed in ring-like formations interior part.

References

- [1] D.W. Schaefer, R.S. Justice // *Macromolecules* **40** (2007) 8501.
- [2] Yu.G. Yanovsky, G.V. Kozlov, Y.N. Karnet, Z.M. Zhirikova, V.Z. Aloeov // *Nanoscience and Technology: An International Journal* **3** (2012) 99.
- [3] V.P. Budtov, *Physical Chemistry of Polymer Solutions* (Chemistry, Saint Petersburg, 1992). (In Russian).
- [4] G.V. Kozlov, I.V. Dolbin, G.E. Zaikov, *The Fractal Physical Chemistry of Polymer Solutions and Melts* (Apple Academic Press, Toronto, New Jersey, 2014).
- [5] D. Blond, V. Barron, M. Ruether, K.P. Ryan, V. Nicolosi, W.J. Blau, J.N. Coleman // *Advanced Functional Materials* **16** (2006) 1608.
- [6] B.A. Komarov, E.A. Dzhavadyan, V.I. Irzhak, A.G. Ryabenko, V.A. Lesnichnaya, G.I. Zvereva, A.V. Krestinin // *Polymer Science, Series A* **53(6)** (2011) 502.
- [7] Ya.I. Estrin, E.R. Badamshina, A.A. Grishchuk, G.S. Kulagina, V.A. Lesnichnaya, Yu.A. Ol'khov, A.G. Ryabenko, S.N. Sul'yanov // *Polymer Science, Series A* **54(4)** (2012) 290.
- [8] B. Bridge // *Journal of Materials Science Letters* **8** (1989) 102.
- [9] A.K. Mikitaev, G.V. Kozlov, G.E. Zaikov, *Polymer Nanocomposites: Variety of Structural Forms and Applications* (Nova Science Publishers, Inc., New York, 2008).
- [10] S. Wu // *Journal of Polymer Science Part B: Polymer Physics* **27** (1989) 723.
- [11] G.V. Kozlov, G.E. Zaikov, *Structure of the Polymer Amorphous State* (Brill Academic Publishers, Utrecht, Boston, 2004).
- [12] G.M. Magomedov, G.V. Kozlov, G.E. Zaikov, *Structure and Properties of Cross-Linked Polymers* (A Smithers Group Company, Shawbury, 2011).

CARBON-BASED NANOSTRUCTURE CREATED BY Ba AND Cs ATOMIC LAYER DEPOSITION ON THE VICINAL 3C-SiC(111) SURFACES

G.V. Benemanskaya^{1,2*}, P.A. Dementev¹, S.A. Kukushkin^{2,4}, M.N. Lapushkin¹,
A.V. Osipov^{2,3}, S.N. Timoshnev^{2,5}

¹Ioffe Institute, Politekhnikeskaya 26, St. Petersburg 194021, Russia

²Institute of Problems of Mechanical Engineering, Bolshoj pr. 61, Vas. Ostrov, St. Petersburg, 199178, Russia

³ITMO University, Kronversky pr. 49, St. Petersburg, 197101, Russia

⁴Peter the Great Saint-Petersburg Polytechnic University,
Politekhnikeskaya ul. 29, St. Petersburg, 195251, Russia

⁵Saint Petersburg National Research Academic University, Khlopina 8/3, St. Petersburg, 194021, Russia

*e-mail: Galina.Benemanskaya@mail.ioffe.ru

Abstract. New type of carbon based nanostructure on the vicinal 3C-SiC(111)-4° and 3C-SiC(111)-8° surfaces with adsorbed Ba and Cs nanolayers has been found. The 3C-SiC(111)-4° (8°) samples were grown by low-defect unstressed nanoscaled films epitaxy method on silicon vicinal substrates. Electronic structure of the 3C-SiC(111)-4° (8°) surfaces and the (Ba, Cs)/3C-SiC(111)-4° (8°) interfaces has been detailed studied *in situ* in an ultrahigh vacuum by synchrotron-based photoelectron spectroscopy. The C 1s, Si 2p, Ba 4d core levels and valence band spectra were investigated as a function of Ba or Cs submonolayer coverages. A special fine structure of the C 1s core level spectrum was revealed to appear under Ba and Cs adsorption on the vicinal SiC surface only. Drastic change in the C 1s spectrum was ascertained and shown to be originated from the interacting Si vacancy and adsorbed Ba (Cs) atoms initiating both the electron redistribution and surface reconstruction effects with formation of a new type of the C-enriched graphitic-like nanostructure.

Keywords: silicon carbide on silicon; wide bandgap semiconductors; thin film epitaxy; carbon-based nanostructure; vicinal 3C-SiC(111) surfaces; adsorbed Ba and Cs nanolayers; electronic structure.

1. Introduction

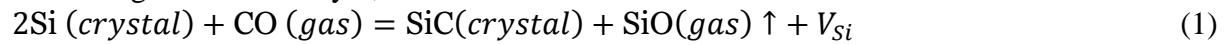
During the last years, the physics and chemistry of silicon carbide (SiC) play an ever increasing role in the nanoelectronic, chemical functionalization and processing of such material, and it has been expanded to various new 2D inorganic materials.

One of the significant problems of micro- and optoelectronics is to grow the high-quality wide-band gap semiconductor films of SiC. Silicon carbide is a very remarkable candidate for electronic devices to be used under extreme conditions such as high temperature, voltage, power and frequency. Furthermore, SiC can be considered as promising material for biophysics applications owing to its low weight, high strength and extreme hardness [1-3].

Most of these applications are oriented toward thin film geometry. The main obstacle to grow the low-defective films on Si is the elastic stresses arising due to mismatch of the lattice

parameters of SiC layer and silicon substrate. To obtain stress-free films of SiC, a original method was developed for the solid-phase synthesis of epitaxial layers when the substrate itself is involved into a chemical reaction and the reaction product is grown inside the substrate layer [4-6]. The epitaxial 3C-SiC layers, synthesized by the original method of chemical atom substitution, were free of the elastic stresses because of their relaxation due to the interaction of point defects arising during the chemical reaction.

To grow the SiC layer, the reaction of Si with carbon monoxide CO was used:



This reaction provides a formation of pair point defects in Si matrix – the silicon vacancies V_{Si} arising due to removed gaseous silicon monoxide, SiO, and the carbon atoms, C, turning out in the interstitial positions in Si crystal after oxygen loss. Then, each pair defect causes dilatation strain, i.e., they become dilatation centers in a cubic silicon crystal.

Formation of the silicon vacancies V_{Si} is accompanied by appearance of the C atoms in the Si lattice because CO molecule transfers one's atomic oxygen to silicon. Therefore such a point dilatation defects are generated by pairs. The strong mutual attraction between pairs caused by interaction with elastic field leads to formation of the relatively stable pair of the defects named by dilatation dipoles [5, 6] by analogy with electric dipoles, providing significant reduction of the total elastic energy. It is eliminated that the most favorable position of the dipoles is the (111) direction in crystals with cubic symmetry. Assembly of dilatation dipoles provides relatively overall relaxation of elastic stress induced by disagreement of Si and SiC lattices.

The integration of new-grown SiC nanolayers into silicon technology requires studies of surface properties, and in particular, the interface formation. Surface electronic properties of SiC grown by traditional method and especially by a new method are still poorly understood and then they cause discussion relative to interface formation, surface state spectra, band-bending, and the effect of 2D phase transition. This is important because of a pivotal role that such properties play in nanostructure research where these surface and interface conditions are crucial. However, the surface and interface electronic structure of silicon carbide is not completely understood.

An effective tool to investigate electronic structure of both the semiconductor bulk and surface is photoelectron spectroscopy (PES). The electronic structure of SiC, grown by traditional method, has been a subject of the number of experimental [7-15] and theoretical [16-21] investigations. The surface related features were obtained by PES and X-ray photoelectron spectroscopy and shown to be correlated to the Si dangling bonds and interaction between the top Si atoms and C atoms [7-9, 13-14]. Calculations based on the density functional theory within the local density approximation have predicted such peculiarities [17, 20, 21]. Moreover, these theoretical studies show that the surface electronic structure corresponding to the occupied states below the Fermi level could be explained by Si-dangling bonds of SiC surface [20, 21].

Adsorbed alkali-metal layers are good candidates for metal-semiconductor interface formation and Schottky barrier composition. Electronic properties of surfaces and interfaces were most thoroughly studied for hexagonal 6H-SiC(0001) surfaces. With respect to Cs/6H-SiC interface the Cs-induced donor states belonging to Cs-Si bonds were obtained together with the semiconducting-like character of interface [22]. The Schottky barrier formation and interfacial chemistry were studied for the Sc/3C-SiC(111) interface [23]. The upward band bending of ~ 0.5 eV and Schottky barrier of ~ 0.7 eV were obtained. Electronic properties were investigated for interfaces consisting of Si(110) face and 3C-SiC (111) face [24]. The coexistence of the floating bonds and the Si dangling bonds with the electron transfer was revealed as the mechanism of the stabilization of the interface.

Recently, formation of the Cs, Ba/3C-SiC(111) interfaces in the case of flat surfaces was investigated as a function of coverage with the use of PES [25, 26]. The plane face 3C-SiC(111)

samples were grown by the method of epitaxy of low-defect unstressed nanoscaled silicon carbide films. Valence band photoemission and both the Si 2*p* and C 1*s* core levels spectra have been investigated as a function of submonolayer coverage. Under Ba and Cs adsorption two surface bands induced by adsorption are found. It is obtained that interfaces can be characterized as metallic-like. Modification of the Si 2*p* and C 1*s* surface-related components was ascertained and shown to be provided by redistribution effect of electron density between adatoms and both the Si surface and C interface atoms.

A number of articles are focused on the effects of metal or nitrogen adsorption on graphene grown on SiC surfaces [27-31]. Adsorption Cs, Rb has been explored in detail on graphene and shown that adatoms deposited on monolayer graphene samples gives rise to *n*-type doping with electron transfer from the metal to the graphene layer [27]. It is obtained that the Na atoms can intercalate into the space between the graphene and the buffer layer [28]. Returning to the study of SiC surfaces, it can be noted that the electronic properties of 3C-SiC(111) surface are less studied in contrast to the well investigated SiC(100) and SiC(0001) ones. Vicinal surfaces of SiC and metal adsorption on those surfaces are also almost completely unexplored. Nevertheless these issues are of great importance from both fundamental and applied points of view. The vicinal surfaces can be useful in facilitating stress relaxation due to significant mismatch of lattice constants at the initial stages of nucleation with the growth of nitrides on the SiC.

In this paper, the electronic structure of the vicinal 3C-SiC(111)-4° and the 3C-SiC(111)-8° surfaces grown by the original method has been first studied by PES. Atomic structure of the samples has been obtained by atomic-force microscopy (AFM). The modification of the electronic structure in the process of Cs and Ba adsorption on the vicinal 3C-SiC(111)-4° and the 3C-SiC(111)-8° surfaces was first studied. It is found drastic change in the C 1*s* core level and valence band spectra for the Ba, Cs/3C-SiC-4° and Ba/3C-SiC-8° interfaces as a function of Ba and Cs coverages.

2. Experimental

Vicinal 3C-SiC(111)-4° and 3C-SiC(111)-8° surface growth. The single-crystal epitaxial 3C-SiC(111)-4° layers have been grown on the vicinal Si(111)-4° and Si(111)-8° surfaces inclined at angles of 4° and 8° to the (111) base orientation. The 3C-SiC(111)-4° and 8° layers were synthesized by the method of chemical atom substitution [4-6]. The temperature in the synthesis zone was 1530 K; the total pressure of the gas mixture (CO + SiH₄) was 79 Pa; the flux rate of the gas mixture was 12 sccm; the silane (SiH₄) percentage in the flux of the mixture corresponded to 45 %. The epitaxial 3C-SiC(111)-4° and 3C-SiC(111)-8° layers were studied by X-ray diffraction (XRD) analysis, AFM, and the electron diffraction technique. The full width at half-maximum (FWHM_{ω - β}) of the XRD peak observed for the samples with CuKα1 radiation was 40 arcmin, which is indicative of the epitaxial orientation of the structures. The layers thickness was ~150 nm.

Figures 1 and 2 present the experimental data that are characterized the morphology of the 3C-SiC(111)-4° sample as a typical case for all samples studied here. Structure of SiC samples was ascertained by scanning electron microscopy (SEM), as can be seen in Fig. 1. Surface morphology of the samples was characterized by AFM, see Fig. 2.

PES experiments. Photoemission studies were carried out at BESSY II, Helmholtz Zentrum, Berlin using the synchrotron radiation with photon energies in the range of 120–450 eV. PES experiments were performed in an ultrahigh vacuum of 5x10⁻¹⁰ Torr at room temperature. The SiC samples were preliminary heated at a temperature of ~ 900 K. The spectra were collected in normal emission. For the 3C-SiC(111)-4° and the 3C-SiC(111)-8° samples the photoemission spectra from the valence band (VB), from the surface states and from the C 1*s*, Ba 4*d*, Cs 5*p* core levels were recorded. The main elements presented in PES overview of

the clean SiC were Si, C and negligible O and no other elements were detected in significant amounts. A total energy resolution of better than 100 meV was used.

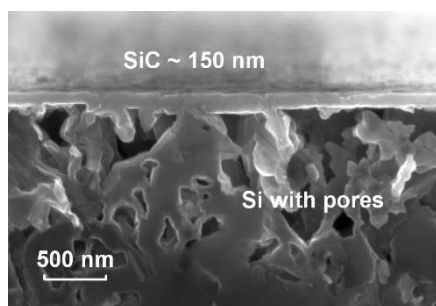


Fig. 1. SEM cross-section of 3C-SiC(111)-4° layer of thickness ~150 nm grown on the vicinal Si(111)-4° substrate.

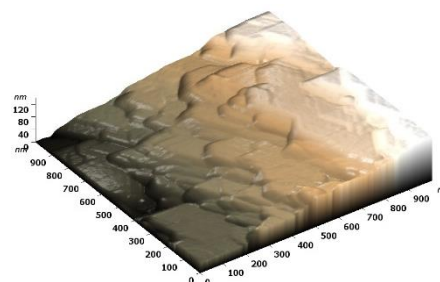


Fig. 2. AFM 3D image of a 1x1 μm region of the vicinal 3C-SiC(111)-4° surface.

Atomically pure cesium or barium were deposited onto the clean samples from a standard sources. Step-by-step deposition of Ba or Cs coverages was performed onto the 3C-SiC(111)-4° and the 3C-SiC(111)-8° samples. It should be noted that the Ba sticking coefficient is equal to one at least up to 1 monolayer (ML). To ascertain the Cs or Ba coverage, the sources were preliminary calibrated to dosage using the original technique [32]. This made possible to determine Ba and Cs coverages deposited onto the samples to better than 20%. Note that 1 ML is defined as one complete layer of Ba (Cs) atoms and equal to $\sim 6 \times 10^{14}$ atoms/cm² [33]. Moreover, the Ba (Cs) overlayer corresponding to 1 ML can be estimated using dependence of the Ba 4*d* and Cs 5*p* core level peak intensities as a function of the Ba (Cs) deposition time [34, 35]. It should be noted that we deal with rough surfaces which are remarkable for steps and buckling. Therefore, it should be indicated as a relative 1 ML coverage.

3. Results and discussion

Figure 3 represents the C 1*s* core level spectra taken from the clean 3C-SiC(111)-4° surface (Fig. 3a) and from the Ba/3C-SiC(111)-4° interface at different Ba coverages (Fig. 3b, c). The exciting photon energy corresponds to $h\nu = 450$ eV. The C 1*s* core level spectrum for the clean SiC surface is found to be composed of two distinct components B and S1 (Fig. 3a). The one at the energy of 283.1 eV (peak B) is originated from the bulk of SiC substrate and the other one S1 at the higher binding energy (285.0 eV) then bulk component B can be assigned to the surface C-C bond. In agreement with the observations [30-31], the component S1 is related to the presence of *s-p*² hybridized C-C bonds. This peak S1 can be considered as a signature of the C-enriched surface.

Drastic change in the C 1*s* core level spectrum was found for the Ba/3C-SiC(111)-4° interface (Fig. 3b, c). The appearance of additional component S2 at the higher binding energy (286.5 eV) was revealed as an effect of Ba adsorption at 0.5 ML and 1.0 ML. Simultaneously with the S2 peak, the additional peak SU on the highest binding energy (291.0 eV) arises. The binding energies of S2 and SU components does not depend on the coverage, only the relative intensities being equally modified throughout the increase of Ba coverage. On the other hand, several components appear at the higher binding energies indicating a stronger degree of interaction between C-C atoms and increase of the C ionicity. The presence of S1 and S2 components is widely identified a corrugation of the vicinal 3C-SiC(111)-4° surface.

An extremely unusual C 1*s* spectrum was found upon one monolayer of Ba adsorption on the 3C-SiC(111)-4° surface (Fig. 3c). Namely, a supplementary peak SU was distinctly found. One should note that both the S2 and SU components synchronously arise and increase in intensities with Ba coverage. This marked peculiarity SU, which differs from the traditional

C 1s core level spectrum, can be identified as a shake-up satellite of the peak S2. The shake-up satellite is a well established characteristic of the photoemission process in graphitic and aromatic systems. The shake-up is a two electron phenomenon; the emitted photoelectrons with energy S2 (286.0 eV) can excite a transition resulting in an additional peak SU (291.0 eV) at the higher binding energy. Graphitic systems show a shake-up peak shifted toward higher binding energy from the main peak by approximately 6.5–7.0 eV [36, 37]. Therefore the modification of surface structure of the vicinal 3C-SiC(111)-4° surface due to Ba adsorption was obtained with the formation of apparently the missing-row reconstruction. It is found that surface phase transition from the 3C-SiC(111)-4° C-enriched surface to graphitic-like one is originated from the Ba adsorption.

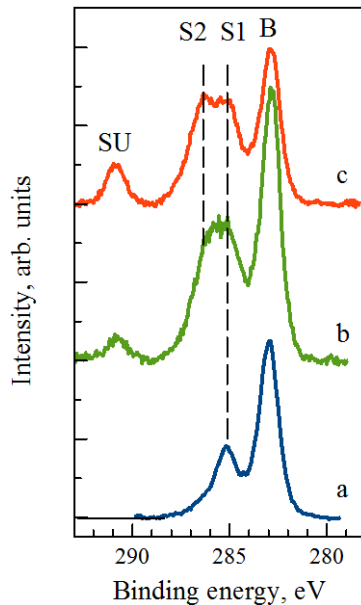


Fig. 3. Photoemission spectra of C 1s core level for Ba/3C-SiC(111)-4° interface at different Ba coverages: (a) clean surface, (b) 0.5 ML, (c) 1.0 ML. Excitation energy $h\nu = 450$ eV.

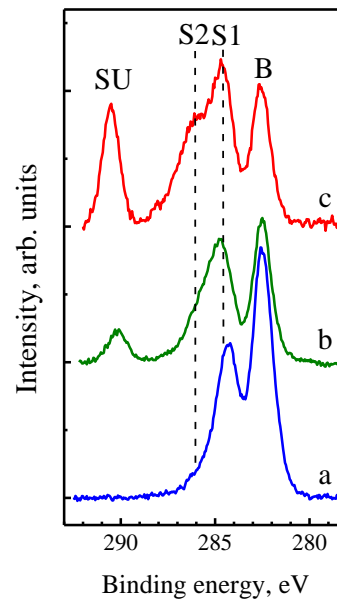


Fig. 4. Photoemission spectra of C 1s core level for Ba/3C-SiC(111)-8° interface at different Ba coverages: (a) clean surface, (b) 0.4 ML, (c) 1.0 ML. Excitation energy $h\nu = 450$ eV.

Figure 4 represents the C 1s core level spectra taken from the clean 3C-SiC(111)-8° surface (Fig. 4a) and from the Ba/3C-SiC(111)-8° interface at different Ba coverages (Fig. 4b, c). The exciting photon energy corresponds to $h\nu = 450$ eV. The C 1s core level spectrum for the clean 3C-SiC(111)-8° surface is found to be composed of two distinct components B and S1 (Fig. 4a). The B peak at the energy of 282.6 eV can be originated from the bulk substrate and the other one S1 at the higher binding energy (284.8 eV) with respect to B peak can be assigned to the surface C-C bond and the C-enriched surface.

An extraordinary C 1s spectrum was found upon Ba adsorption on the 3C-SiC(111)-8° surface (Fig. 4 b, c). As can be seen, the spectra for Ba/3C-SiC(111)-8° interface (Fig. 4) are very similar to the Ba/3C-SiC(111)-4° interface (Fig. 3). Thus, for both cases of vicinal surfaces, the Ba adsorption on the 3C-SiC(111)-4°, (8°) surfaces causes the 2D phase transition from the carbon-enriched surface to the graphitic-like one with the formation of apparently the missing-row reconstruction.

Figure 5 represents drastic change in the C 1s core level spectra initiated by the Cs adsorption on the vicinal 3C-SiC(111)-4° surface. The exciting photon energy corresponds to $h\nu = 450$ eV. It is evident from the comparison of Fig. 5 with Figs. 3 and 4 that both the Cs and

Ba adatoms strongly and in a similar manner interact with the initially C-enriched vicinal surfaces. Therefore, unusual and complex structure of C 1s core level spectra was found upon Ba and Cs adsorption. This effect is originated from the strong interaction of the Ba (Cs) adatoms with C-surface atoms that causes the 2D structural phase transition leading to the formation of the missing-row reconstruction with the graphitic-like surface.

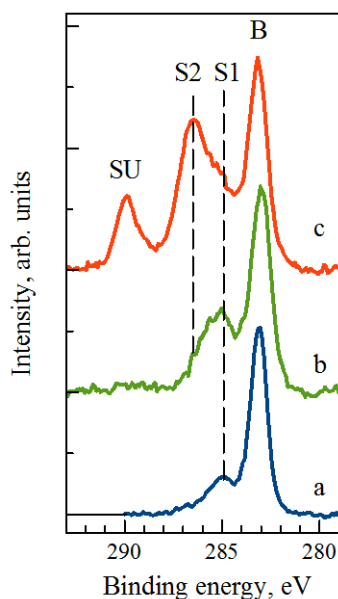


Fig. 5. Photoemission spectra of C 1s core level for Cs/3C-SiC(111)-4° interface at different Cs coverages: (a) clean surface, (b) 0.3 ML, (c) 1.0 ML. Excitation energy $h\nu = 450$ eV.

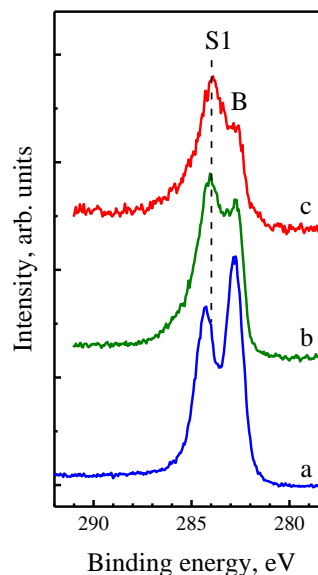


Fig. 6. Photoemission spectra of C 1s core level for Ba/3C-SiC(111) interface at different Ba coverages: (a) clean surface, (b) 0.6 ML, (c) 1.0 ML. Excitation energy $h\nu = 450$ eV.

Figure 6 shows photoemission spectra of the C 1s core level obtained for the flat 3C-SiC(111) surface (Fig. 6a) and for the Ba adsorption at different Ba coverages (Fig. 6 b, c). The C 1s core level for the clean flat SiC surface is found to be composed of two main components: the bulk component B and one shifted component S1 at lower binding energy. In agreement with the observations [30-31], the component S1 is related to the presence of $s-p^2$ hybridized C-C bonds. This peak S1 can be considered as a signature of the C-enriched surface.

Upon Ba adsorption all components B and S1 are decreased in intensity. Comparison of Fig. 6 and Figs. 3 and 4 clearly shows the essential difference in the C 1s core level spectra for the flat and vicinal SiC(111) surfaces. There are no additional components in the C 1s core level spectrum as compared to vicinal SiC surfaces. The C-based new structure can be created by the Ba and Cs adsorption.

Figure 7 presents the Ba 4d and Si 2p core level spectra for the Ba/3C-SiC(111)-4° interface. For the clean surface, dominant peak of the Si 2p is obtained. Upon Ba adsorption it is practically unchanged that indicates about no interaction Si atoms with Ba atoms and absence of Si atoms in top surface layer. Other behavior can be seen for the Ba 4d core level spectra that arise and strongly increase in intensity with growing of the Ba coverage.

The photoemission spectra in the valence band region of Ba/3C-SiC(111)-4° interface are shown in Fig. 8 for the cases of a clean surface (a), and for Ba adsorption: 0.3 ML (b) and 1.0 ML coverage (c). The excitation photon energy is $h\nu = 120$ eV. The spectra are brought to the energy of the VB top at the surface, E_{VBM} . This energy is determined from linear approximation of the low-energy edge of the spectrum.

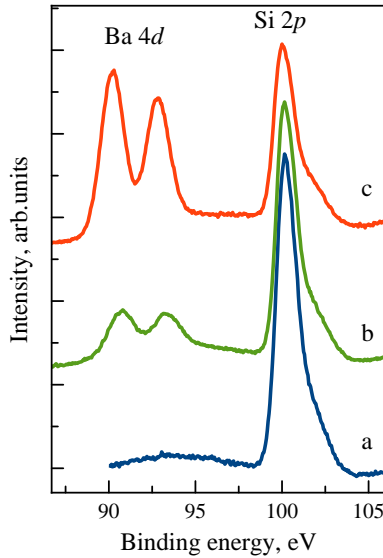


Fig. 7. Photoemission spectra of Ba 4*d* and Si 2*p* core levels for Ba/3C-SiC(111)-4° interface at different Ba coverages: a – clean surface, b – 0.3 ML, c – 1.0 ML. The excitation energy $h\nu = 120$ eV.

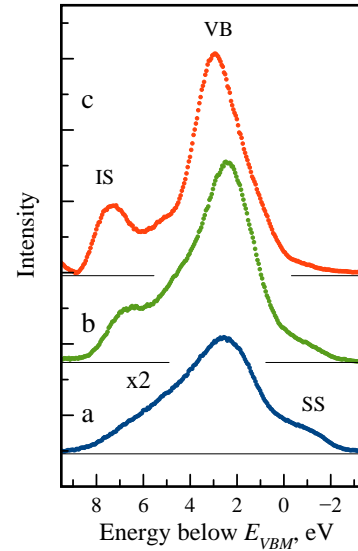


Fig. 8. Normal photoemission spectra in the VB region for Ba/3C-SiC(111)-4° interface at different Ba coverages: a – clean surface, b – 0.3 ML, c – 1.0 ML. The excitation energy $h\nu = 120$ eV.

For the clean 3C-SiC(111)-4° sample, the spectrum presents a slightly structured photoemission band with the width of ~ 8 eV. The maximum at the energy of ~ 2.5 eV corresponds to the photoemission from the VB. This inference is supported by calculations of the density of states (DoS) [15, 21] as well as by experimental data [7, 9, 13]. The additional peak at the binding energy of ~ -1.5 eV above the E_{VBM} can be related to the intrinsic surface states (SS), whose origin is associated with the Si dangling bonds [16, 17].

As the Ba coverage is increased, we observe an appearance and increase in the intensity of photoemission from the induced surface state IS at energy of ~ 7.0 eV, which is indicative of an increase in the electron density (DoS). As can be seen from Fig. 3, the vicinal 3C-SiC(111)-4° surface exhibits C-enriched reconstruction involving C atoms at different spatial positions. Ba adsorption is found to drastic modify initial surface to graphitic-like surface structure. The lack of states in the band-gap is indicative of the semiconductor character of the Ba/3C-SiC(111)-4° interface at coverage of less than 1 ML.

4. Simulation

A model taking into account silicon vacancies is developed for the system of the vicinal 3C-SiC(111)-4° surface interacting with Cs adsorbed atoms to understand formation of a new C-based surface nanostructure. To modeling the Cs atom interaction with the structure of the silicon carbide containing silicon vacancies saturated cluster approach will be used, which allows to use the highly accurate density functional methods [38]. Any Si atom removed from an infinite crystal lattice of atoms of a cubic SiC. Then the cesium atom is positioned on the resulting free place. Thus cluster of atoms that are arranged to the Cs closer than 6.1 \AA obtained, namely, the nearest 7 shells of neighbors of the extracted atom (exactly 42 Si atoms and 42 C atoms) are taken into account. To minimize the cluster boundary influence the dangling bonds are saturated with hydrogen atoms. The geometry optimization of the system was carried out by methods of quantum mechanics, i.e. cluster configuration has been found, which corresponds to the energy minimum. It was assumed that only the Cs atom and nearest 16 atoms can move (see Fig. 9).

The system energy calculations were made with the density functional method, in particular, the hybrid functional B3LYP, which established himself as one of the most high-precision methods for problems of this type. Minimization of the functional was performed in the basis 6-31G++ [38], and appropriate pseudopotential used for cesium [23]. The energy minimization was performed in ORCA (<https://orcaforum.cec.mpg.de/>) and Gamess packages (<http://www.msg.ameslab.gov/GAMESS/index.html>).

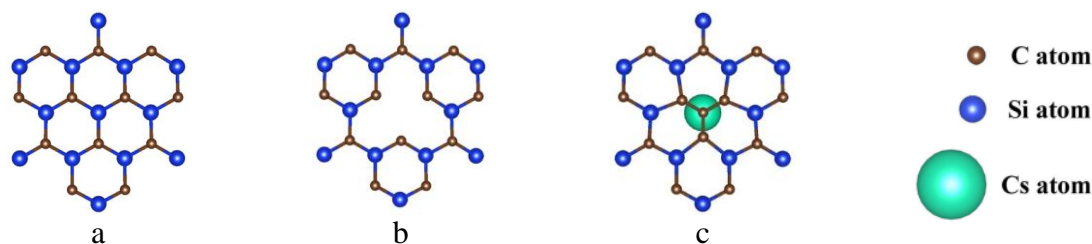


Fig. 9. Scheme of plane and atom arrangements for: (a) 3C-SiC(111) surface, (b, c) 3C-SiC(111) reconstructed surface and Cs atom interacting with Si-vacancy.

The optimization results of the system geometry are as follows. One of the 4 nearest to the Si-vacancy carbon atoms is profitably to take the place of silicon vacancy. The cesium atom is attached to the resulting almost flat cluster of 4 carbon atoms by means of a very short and strong ionic bond ~ 1.1 Å. In this case, cesium atom strongly pushes the remaining nearest 12 neighbors (see Fig. 9). It should be noted that if this structure is removed CsC₄ of 3C-SiC(111) crystal, the bond length between Cs and C atoms will increase by 3 times, namely, this structure can exist within the 3C-SiC(111) crystal only.

5. Conclusions

To summarize, the Ba/3C-SiC(111)-4°, Ba/3C-SiC(111)-8° and Cs/3C-SiC(111)-4° interfaces have been first investigated *in situ* using photoelectron spectroscopy with photon energies in the range of 120–450 eV. The vicinal 3C-SiC(111)-4° and 3C-SiC(111)-8° samples were grown by the original method of epitaxy of low-defect unstressed nanoscaled silicon carbide films. The C 1s, Si 2p, Ba 4d core levels and valence band photoemission spectra were obtained as a function of Ba and Cs submonolayer coverage. A special fine structure of the C 1s core level spectrum was revealed to appear under Ba or Cs adsorption on the vicinal surface exclusively. The drastic change in the C 1s core level spectrum is found to originate from the interacting silicon vacancy and adsorbed Cs or Ba atoms initiating electron redistribution effect which leads to the 2D phase transition from the 3C-SiC(111)-4° (8°) carbon-enriched surface to the graphitic-like one. It is found that Ba and Cs adsorption causes a charge transfer with increasing ionicity of the C surface atoms. In the valence band region, two surface bands induced by Ba adsorption are found to appear.

Acknowledgements. This work was supported by grant # 14-12-01102 of Russian Science Foundation. The authors thank Synchrotron BESSY II and Russian-German Beamline, Synchrotron BESSY II, Helmholtz Zentrum, Berlin for providing the facilities to perform the experiments and for help during experiments.

References

- [1] S.E. Sadow, A.K. Agrawal, *Advances in silicon carbide processing and applications* (Artech House Publishers, London, 2004).
- [2] P.G. Soukiassian, H.B. Enriquez // *Journal of Physics: Condensed Matter* **16** (2004) 1611.
- [3] T. Seyller // *Journal of Physics: Condensed Matter* **16** (2004) 1755.
- [4] S.A. Kukushkin, A.V. Osipov // *Journal of Physics D: Applied Physics* **47** (2014) 313001.
- [5] S.A. Kukushkin, A.V. Osipov, N.A. Feoktistov // *Physics of the Solid State* **56** (2014) 1507.

- [6] S.A. Kukushkin, A.V. Osipov // *Journal of Applied Physics* **113** (2013) 024909.
- [7] L.I. Johansson, F. Owman, P. Mårtensson, C. Persson, U. Lindefelt // *Physical Review B* **53** (1996) 13803.
- [8] V.M. Bermudez, J.P. Long // *Applied Physics Letters* **66** (1995) 475.
- [9] H.W. Yeom, Y.-C. Chao, I. Matsuda, S. Hara, S. Yoshida, R.I.G. Uhrberg // *Physical Review B* **58** (1998) 10540.
- [10] L.I. Johansson, F. Owman, P. Mårtensson // *Physical Review B* **53** (1996) 13793.
- [11] R. Takahashi, H. Handa, S. Abe, K. Imaizumi, H. Fukidome, A. Yoshigoe // *Japanese Journal of Applied Physics* **50** (2011) 070103.
- [12] J. Su, Q. Niu, C. Tang, Y. Zhang, Z. Fu // *Solid State Sciences* **14** (2012) 545.
- [13] P.-A. Glans, T. Balasubramanian, M. Syväjärvi, R. Yakimova, L.I. Johansson // *Surface Science* **470** (2001) 284.
- [14] C. Virojanadara, M. Hetzel, L.I. Johansson, W.J. Choyke, U. Starke // *Surface Science* **602** (2001) 525.
- [15] C.H. Park, B.-H. Cheong, K.-H. Lee, K.J. Chang // *Physical Review B* **49** (1994) 4485.
- [16] C. Persson, U. Lindefelt // *Journal of Applied Physics* **82** (1997) 5496.
- [17] P. Käckell, B. Wenzien, F. Bechstedt // *Physical Review B* **50** (1994) 10761.
- [18] J. Furthmüller, F. Bechstedt, H. Hüsken, B. Schröter, W. Richter // *Physical Review B* **58** (1998): 13712.
- [19] F. Bechstedt, J. Furthmüller // *Journal of Physics: Condensed Matter* **16** (2004) 1721.
- [20] Y. Li, X. Wang, L. Ye // *Journal of Physics: Condensed Matter* **18** (2006) 6953.
- [21] J. Wang, L. Zhang, Q. Zeng, G.L. Vignoles, L. Cheng, A. Guette // *Physical Review B* **79** (2009) 125304.
- [22] V. Elsbergen, T.U. Kampen, W. Mönch // *Journal of Applied Physics* **79** (1996) 316.
- [23] S.W. King, R.J. Nemanich, R.F. Davis // *Physica Status Solidi B* **252** (2015) 391.
- [24] E.K.K. Abavare, J.-I. Iwata, A. Oshiyama // *Physical Review B* **87** (2013) 235321.
- [25] S.A. Kukushkin, G.V. Benemanskaya, P.A. Dementev, S.N. Timoshnev, B.Senkovskiy // *The Journal of Physical Chemistry* **90** (2016) 40.
- [26] G.V. Benemanskaya, P.A. Dementev, S.A. Kukushkin, M.N. Lapushkin, A.V. Osipov // *Semiconductors* **50** (2016) 1327.
- [27] S. Watcharinyanon, C. Virojanadara, L.I. Johansson // *Surface Science* **605** (2011) 1918.
- [28] S. Watcharinyanon, L.I. Johansson, C. Xia, C. Virojanadara // *Journal of Applied Physics* **111** (2012) 083711.
- [29] S.D. Costa, J.E. Weis, O. Frank, M. Kalbac // *Carbon* **93** (2015) 793.
- [30] Z.-H. Sheng, L. Shao, J.-J. Chen, W.-J. Bao, F.-B. Wang, X.-H. Xia // *ACS Nano* **5** (2011) 4350.
- [31] Y. Wang, Y. Shao, D.W. Matson, J. Li, Y. Lin // *ACS Nano* **4** (2010) 1790.
- [32] G.V. Benemanskaya, G.E. Frank-Kamenskaya, N.M. Shmidt, M.S. Dunaevskiy // *Journal of Experimental and Theoretical Physics* **103** (2006) 441.
- [33] C.-P. Cheng, I.-H. Hong, T.-W. Pi // *Physical Review B* **58** (1998) 4066.
- [34] T. Okuda, K.-S. An, A. Harasawa, T. Kinoshita // *Physical Review B* **71** (2005) 085317.
- [35] T.-W. Pi, I.-H. Hong, C.-P. Cheng // *Physical Review B* **58** (1998) 4149.
- [36] L.B. Biedermann, M.L. Bolen, M.A. Capano, D. Zemlyanov, R.G. Reifenberger // *Physical Review B* **79** (2009) 125411.
- [37] D. Briggs, J.T. Grant, *Surface Analysis by Auger and X-ray Photoelectron Spectroscopy* (IM Publications Chichester, UK and SurfaceSpectra, Manchester, UK, 2003).
- [38] S.A. Kukushkin, A.V. Osipov // *Physics of the Solid State* **58** (2016) 747.

THE STUDY OF THE INTERACTION OF HYDROGEN IMPURITY WITH POINT AND LINEAR DEFECTS IN PALLADIUM AND NICKEL

G.M. Poletaev^{1*}, I.V. Zorya², E.S. Medvedeva¹, D.V. Novoselova¹, M.D. Starostenkov¹

¹Altai State Technical University, Lenin Str. 46, 656038 Barnaul, Russia

²Siberian State Industrial University, Kirova Str. 42, 654007 Novokuznetsk, Russia

*e-mail: gmpoletaev@mail.ru

Abstract. The work is devoted to the study of the interaction of hydrogen with point defects (vacancy, bivacancy, trivacancy, stacking fault tetrahedron, intrinsic interstitial atom) and linear (complete and partial edge dislocations, screw dislocation) defects in Pd and Ni by the method of molecular dynamics. The bond energies of the hydrogen impurity with considered defects were obtained. It is shown that the most effective hydrogen traps in Pd and Ni are vacancies and vacancy clusters. The high sorption capacity of vacancies should contribute to significantly effect of their concentration on the overall sorption capacity of the metal, especially for metals such as Ni, for which the energy of absorption by vacancies and vacancy clusters is negative while the absorption energy by a pure crystal is positive. The presence of dislocations and dislocation complexes in Ni, low-angle grain boundaries, according to the obtained data, weakly affects to the sorption ability of the metal in comparison with vacancies and vacancy clusters.

Keywords: molecular dynamics; metal; hydrogen; point defect; bond energy; absorption energy; dislocation; stacking fault tetrahedron.

1. Introduction

Interaction of hydrogen with metals remains a topic of active studies in the last century. On the one hand, this is because of practical importance of metal-hydrogen systems, they find applications as radiation resistant materials, materials for extra-pure hydrogen filters and isotope fractioning, for accumulation and storage of light gases, for hydrogen transportation, etc. On the other hand, hydrogen can have undesirable effects on metallic materials, for instance, hydrogen embrittlement, corrosion, stress corrosion cracking [1].

The traps, which are responsible for capturing hydrogen atoms in technically pure metals, are lattice defects: point defects and their complexes, dislocations, grain boundaries, volume defects. The researchers note that the most effective traps are grain boundaries, dislocations and vacancies [2]. The interaction of hydrogen with these defects is the reason of a number of phenomena associated with changes in the properties of hydrogenated metals, such as embrittlement, change of and mobility of defects caused by this change in the self-diffusion characteristics of the metal. On the other hand, directional introduction of the traps is an effective way of dealing with hydrogen embrittlement [2]. Therefore, the study of processes of hydrogen interaction with the structure imperfections is topical. Nowadays an open question remains on quantifying sorption capacity with respect to hydrogen of different lattice defects.

In addition to the defects mentioned above, there are unique vacancy clusters in fcc crystals are of the interest - stacking fault tetrahedrons (SFT). At present, it is reliably established that small vacancy clusters in fcc metals are mainly stacking fault tetrahedrons

[3, 4]. The faces of the stacking fault tetrahedron (Fig. 1) are oriented along the $\{111\}$ planes and are stacking faults, and the edges are oriented along the $\langle 110 \rangle$ directions and are partial dislocations with the $1/6\langle 110 \rangle$ Burgers vector [3, 5, 6]. SFTs are formed in all fcc metals, but their critical size, at which the vacancy disks become energetically more advantageous, depends to a large extent on the formation energy of the stacking fault in a given metal [6]. In connection with this, the first SFTs were observed in metals with a low energy of stacking fault (Au, Ag, Cu, etc.) [5, 6]. For example, in Au vacancy disks are observed predominantly above a certain size – 230 Å, while the SFT – up to a size of 200 Å [6]. SFTs are formed as a result of radiation damage, rapid cooling from high temperatures, plastic deformation.

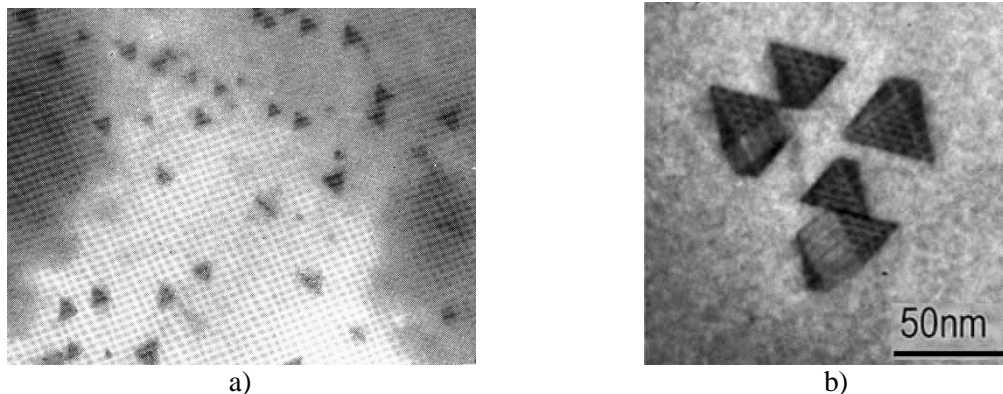


Fig. 1. Stacking fault tetrahedrons in gold observed with the help of an electron microscope: a) the view along the $\langle 111 \rangle$ direction, $\times 10^5$ [5]; b) the group of SFTs [3].

Investigation of the interaction of hydrogen impurities with different structure defects at the atomic level is in its initial stages and is preferably carried out using methods of computer simulation. The present work is devoted to the study of interaction of hydrogen with point defects (vacancy, bivacancy, trivacancy, stacking fault tetrahedron, intrinsic interstitial atom) and linear (complete and partial edge dislocations, screw dislocation) defects in Pd and Ni by the method of molecular dynamics. Selecting of fcc metals Pd and Ni is due to an increased attention to them and a relatively large amount of the available experimental data for these metals. Palladium has an extremely high sorption capacity relative to hydrogen, the absorption energy (the work that must be expended to put one hydrogen atom in the metal taking into account work H-H bond breaking in a diatomic molecule of hydrogen H_2) is negative and amounts to -0.1 eV [7, 8]. Nickel belongs to metals with an average adsorption capacity. The absorption energy is positive for this metal, but a small and amounts to 0.16 eV [2, 9]. Earlier, we conducted studies of the interaction of hydrogen impurity with vacancies and interstitial atoms [10], edge dislocations [11] and low-angle twist boundaries [12]. In the present work these results are combined and supplemented by studies of the interaction of hydrogen with bivacancies, trivacancies, stacking fault tetrahedrons and partial dislocations.

2. Description of the model

The calculation blocks in the computer model included 8400 atoms. The boundary conditions were used periodically. The vacancy was introduced by removing the atom from the calculation block. Bivacancy (two combined vacancies) was created by removing two neighboring atoms located along the close-packed direction and subsequent relaxation. Trivacancy (three combined vacancies) and SFTs were created by introducing "triangular vacancy disks." Additional thermal activation was not required to form a SFT from vacancy disks of triangular shape. The mechanism of the "triangular vacancy disks" rearranging in the $\{111\}$ plane to the SFT consisted of successively displacing (settling) of groups of atoms in the form of an equilateral triangle from the planes parallel to the vacancy disk plane toward it (Fig. 2). Because

of the peculiarities of the fcc lattice, the sizes of the shifting groups of atoms of a triangular shape were successively decreased, as a result of which the free volume of the initial vacancy disk propagated into the tetrahedral region of the crystal and almost uniformly distributed inside the SFT with an insignificant increase in its concentration in the defect boundary region.

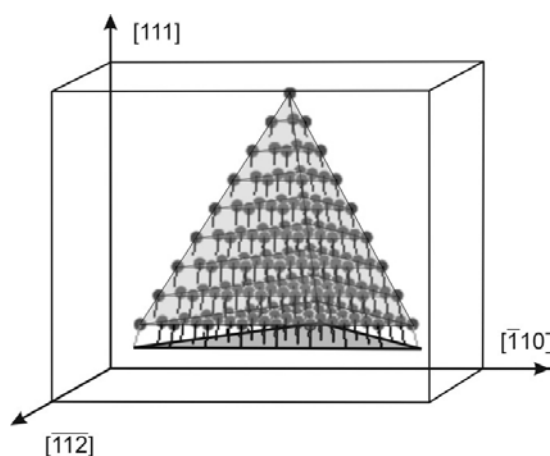


Fig. 2. Formation of the SFT from the "triangular vacancy disk": displacements (shown by segments) of groups of triangular atoms from neighboring planes towards the vacancy disk.

The hydrogen atom was introduced into the computational block at various positions relative to the considered defect. In each case structural relaxation was carried out, at the end of which the calculation block was cooled to 0 K in order to exclude the effect of thermal displacements of atoms in calculating of the energy characteristics of the hydrogen impurity. Structural relaxation was carried out by the method of molecular dynamics. The time step in molecular dynamics experiments was 1 fs. The interactions of metal atoms with each other were described by the many-particle Clery-Rosato potential [13]. The experience of applying of this potential shows that with its help it is possible to describe the various properties of metals [12-17]. The H-H, Pd-H and Ni-H interactions were described using the Morse potentials found in [17] by the absorption energy, the activation energy of hydrogen diffusion (at normal and high temperatures) and the binding energy with the vacancy.

3. Results and discussion

The main energy characteristics describing the interaction of hydrogen with point defects are the binding energy of hydrogen with a defect and the energy of hydrogen absorption by a defect. The binding energy of hydrogen with a point defect E_b was calculated in the present work as the difference in the potential energy of the calculation block containing the considered defect and the hydrogen atom in the octahedral pore (in the fcc lattice, as is known, hydrogen is predominantly located in the octahedral pores [1, 2, 7]) on such a distance from each other which eliminates the interaction of the point defect and the hydrogen atom, and the potential energy of the calculation block containing the hydrogen atom in the defect. Different positions of hydrogen atom in a defect were considered. Wherein the maximal value of all binding energies was chosen, indicating about the most energetically favorable position of hydrogen in the defect.

The energy of hydrogen absorption by a defect is the work that must be spent to put one hydrogen atom from infinity into the defect region taking into account the work of breaking the H-H bond in the diatomic hydrogen molecule H_2 (it is known that hydrogen molecules H_2 in the metal volume dissociate into individual atoms due to significant attenuation covalent bond – in metals, in the crystal lattice and in the region of defects hydrogen is in the atomic state [2]). The energy of hydrogen absorption by a point defect was calculated by formula:

$$E_{ab} = (U_H - U_0) + \frac{1}{2}E_{dis}, \quad (1)$$

where U_0 – potential energy of metal crystal containing considered defect taking into account the relaxation of the atomic structure; U_H – potential energy of the crystal containing a hydrogen atom in the defect region; E_{dis} – dissociation energy of hydrogen molecule H_2 ($E_{dis} = 4.485$ eV [2]).

Fig. 3 shows the positions of the hydrogen atom in the trivacancy and the SFT for which the binding and absorption energies were calculated. All obtained values of E_b and E_{ab} for point and linear defects in Pd and Ni are given in Table 1. The data from other works are indicated in parentheses in the table.

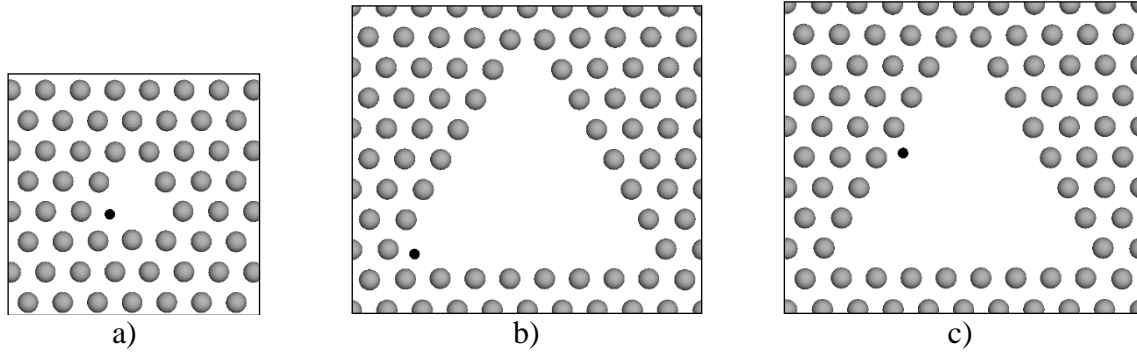


Fig. 3. The positions of the hydrogen atom shown in the section in which the SFT or the trivacancy face lies: a) in the trivacancy; b) at the top of the SFT; c) on the edge of the SFT.

Table 1. The binding energy of hydrogen with a defect E_b and the energy of hydrogen absorption by a defect E_{ab} in Pd and Ni.

	Pd		Ni	
	E_b , eV	E_{ab} , eV	E_b , eV	E_{ab} , eV
vacancy [10]	0.262 (0.25-0.27 [18, 19])	-0.362	0.401 (0.32-0.54 [9,20])	-0.241
bivacancy	0.172	-0.272	0.310	-0.150
trivacancy	0.105	-0.205	0.229	-0.069
SFT top	0.106	-0.206	0.197	-0.037
SFT edge ($1/6\langle 110 \rangle$ partial dislocation)	0.003	-0.103	0.105	0.055
interstitial atom [10]	0.041	-0.141	0.095	0.065
$1/2\langle 110 \rangle$ edge dislocation [11]	0.21 (0.19 – 0.22 [21])	-0.31	0.16 (0.09 – 0.15 [22])	0
kink on $1/2\langle 110 \rangle$ edge dislocation [11]	0.23	-0.33	0.23	-0.07
$1/2\langle 110 \rangle$ screw dislocation [12]	0.01	-0.11	0.01	0.15

When one hydrogen atom was introduced into vacancy there were obtained the binding energies E_b : 0.262 eV for Pd and 0.401 eV for Ni. Since this quantity was one of the parameters by which the potentials of the interaction of metal atoms with a hydrogen atom were selected in [17], the obtained values are in complete agreement with the known experimental data: 0.25-0.27 eV for Pd [18, 19] and 0.32-0.54 eV for Ni [9, 20].

Good agreement with the data of other authors is also observed for the binding energy of hydrogen with edge dislocation. We obtained the following values: 0.21 eV for Pd and 0.16 eV

for Ni. Very close values are given in [21, 22]: 0.19-0.22 eV [21] for Pd and 0.09-0.15 eV [22] for Ni. The binding energy of the hydrogen atom with the kink (step or threshold) on the edge dislocation is higher than with an uncorrelated dislocation core: 0.23 eV for Pd and Ni.

With $1/6\langle 110 \rangle$ partial dislocation, which is also an edge of the SFT, the binding energy is lower than with the nucleus of a complete dislocation. It is energetically more advantageous for the hydrogen atom to be located in the top of the SFT than in any other place in the SFT. At the same time, as can be seen from the table, the binding energy with the SFT top is almost the same as with the trivacancy, which indicates about a similar arrangement of atoms near the top of the SFT and the complex of three vacancies.

The sorption capacity of bivalencies relative to hydrogen, according to the obtained data, is between the sorption capacity of vacancies and trivacancies. In general, the most effective trap for hydrogen among the considered defects is a vacancy. The binding energy of hydrogen with dislocations turned out to be lower than for vacancies, especially for Ni. The high sorption capacity of vacancies should contribute significantly to the effect of their concentration on the overall sorption ability of the metal. For example, for a pure Ni crystal, the absorption energy is positive (0.16 eV [2, 9]), i.e. placing hydrogen in a Ni crystal is energetically disadvantageous and in a state of thermodynamic equilibrium the hydrogen concentration in Ni is low, usually a tenth of a percent [2]. However, the energy of absorption by vacancies and vacancy clusters, according to the obtained data, is negative. This means that the sorption capacity of such metals as Ni should strongly depend on the concentration of vacancies. For Pd, for which the absorption energy by a pure crystal is negative enough (-0.1 eV [7, 8]), the effect of vacancies should apparently be less significant.

4. Conclusion

With the help of the molecular dynamics method, there were obtained the binding and absorption energies of hydrogen by point (vacancy, bivacancy, trivacancy, stacking fault tetrahedron, intrinsic interstitial atom) and linear (complete and partial edge dislocations, screw dislocation) defects in Pd and Ni. It is shown that the most effective hydrogen traps in Pd and Ni are vacancies and vacancy clusters. The high sorption capacity of vacancies should contribute to significantly effect of their concentration on the overall sorption capacity of the metal, especially for metals such as Ni, for which the energy of absorption by vacancies and vacancy clusters is negative while the absorption energy by a pure crystal is positive. The presence of dislocations and dislocation complexes in Ni, low-angle grain boundaries, according to the obtained data, weakly affects to the sorption ability of the metal in comparison with vacancies and vacancy clusters.

Acknowledgment

The reported study was partially supported by Ministry of Education and Science of the Russian Federation within the framework of the state task (project No. 3.4820.2017/8.9) and RFBR (project No. 16-48-190182-r_a).

References

- [1] Yu.K. Tovbin, E.V. Votyakov // *Physics of the Solid State* **42** (2000) 1192.
- [2] *The interaction of hydrogen with metals*, ed. by A.P. Zakharov (Nauka, Moscow, 1987).
- [3] Y. Matsukawa, S.J. Zinkle // *Journal of Nuclear Materials* **329-333** (2004) 919.
- [4] D. Rodney, G. Martin, Y. Brechet // *Materials Science and Engineering* **309-310** (2001) 198.
- [5] M. Thompson, *Defects and radiation damage in crystals* (Mir, Moscow, 1971). (In Russian).
- [6] J. Hirth, J. Lothe, *Theory of Dislocations* (Atomizdat, Moscow, 1972). (In Russian).

- [7] *Hydrogen in Metals*, ed. by G. Alefeld, J. Volkl (Mir, Moscow, 1981). (In Russian).
- [8] F.A. Lewis // *Platinum Metals Review* **26** (1982) 20.
- [9] M.S. Daw, M.I. Baskes // *Physical Review B* **29** (1984) 6443.
- [10] N.A. Kulabukhova, G.M. Poletaev // *Khimicheskaya fizika i mezoskopiya* **15** (2013) 231.
- [11] N.A. Kulabukhova, G.M. Poletaev, M.D. Starostenkov // *Fundamental'nye problemy sovremennogo materialovedeniya* **11** (2014) 99. (In Russian).
- [12] G.M. Poletaev, E.S. Medvedeva, I.V. Zorya, D.V. Novoselova, M.D. Starostenkov // *Materials Physics and Mechanics* **29** (2016) 133.
- [13] F. Cleri, V. Rosato // *Physical Review B* **48** (1993) 22.
- [14] N.A. Kulabukhova, G.M. Poletaev, M.D. Starostenkov, V.V. Kulagina, A.I. Potekaev // *Russian Physics Journal* **54** (2012) 1394.
- [15] R.Yu. Rakitin, G.M. Poletaev, M.S. Aksenov, M.D. Starostenkov // *Technical Physics Letters* **31** (2005) 650.
- [16] G.M. Poletaev, M.D. Starostenkov // *Technical Physics Letters* **35** (2009) 1.
- [17] G.M. Poletaev, M.D. Starostenkov, S.V. Dmitriev // *Materials Physics and Mechanics* **27** (2016) 53.
- [18] S.M. Myers, S.T. Picraux, R.E. Stoltz // *Journal of Applied Physics* **50** (1979) 5710.
- [19] T.B. Flanagan, R. Balasubramaniam, R. Kirchheim // *Platinum Metals Review* **45** (2001) 114.
- [20] F. Besenbacher, J. Bottiger, S.M. Myers // *Journal of Applied Physics* **53** (1982) 3536.
- [21] G. Sicking, M. Glugla, B. Huber // *Physical Chemistry Chemical Physics* **87** (1983) 418.
- [22] G.J. Thomas, In: *Hydrogen effects in metals*, ed. by I.M. Bernstein, A.W. Thompson (Met. Soc. AIME, N.Y., 1981), p. 77.

GENERALIZED THERMOELASTIC AXI-SYMMETRIC DEFORMATION PROBLEM IN A THICK CIRCULAR PLATE WITH DUAL PHASE LAGS AND TWO TEMPERATURES

Rajneesh Kumar¹, V. R. Manthana^{2*}, N. K. Lamba³, G. D. Kedar²

¹ Department of Mathematics, Kurukshetra University, Kurukshetra, India.

² Department of Mathematics, RTM Nagpur University, Nagpur, India.

³ Department of Mathematics, Shri Lemdeo Patil Mahavidyalaya, Nagpur, India.

*e-mail: vkmanthana@gmail.com

Abstract. In the present work, a thick circular plate with axisymmetric heat supply has been considered. It is assumed that lower and upper surfaces of the plate are traction free. The plate is subjected to an axisymmetric heat supply depending on the radial and axial directions of the cylindrical polar co-ordinate system with symmetry about z -axis. The initial temperature in the thick plate is given by a constant temperature T_0 and the heat flux is prescribed on the upper and lower boundary surfaces. Integral transform technique and its inversion is applied to determine displacement components, stresses, conductive temperature and temperature change. The results have been computed numerically and are illustrated graphically.

Keywords: thermoelastic problem; two-temperatures; dual phase lags; thermal stresses; thick circular plate; integral transform.

1. Introduction

The generalized theory of thermoelasticity is one of the modified versions of classical uncoupled and coupled theory of thermoelasticity and has been developed in order to remove the paradox of physical impossible phenomena of infinite velocity of thermal signals in the classical coupled thermoelasticity. Hetnarski and Ignaczak [1] examined five generalizations of the coupled theory of thermoelasticity.

Lord and Shulman [2] formulated the generalized thermoelasticity theory involving one thermal relaxation time. Green and Lindsay [3] developed a temperature rate-dependent thermoelasticity that includes two thermal relaxation times.

The third generalization of the coupled theory of thermoelasticity is developed by Hetnarski and Ignaczak [4] and is known as low temperature thermoelasticity. The fourth generalization to the coupled theory of thermoelasticity introduced by Green and Nagdhi [5]. The fifth generalization to the coupled theory of thermoelasticity is developed by Tzou [6] and Chandrasekhariah [7] and is referred to dual phase lag thermoelasticity.

Tzou [6] introduced two phase lags to both the heat flux vector and the temperature gradient and considered constitutive equations to describe the lagging behavior in the heat conduction in solids. Roychoudhuri [8] has recently introduced the three phase lag heat conduction equation in which the Fourier law of heat conduction is replaced by an approximation to a modification of the Fourier law with the introduction of three different phase lags for the heat flux vector, the temperature gradient and the thermal displacement gradient.

Chen and Gurtin [9], Chen et al. [10] and Chen et al. [11] have formulated a theory of heat conduction in deformable bodies which depends upon two distinct temperatures, the conductive temperature φ and the thermodynamical temperature T . For time independent situations, the difference between these two temperatures is proportional to the heat supply, and in absence of heat supply, the two temperatures are identical. For time dependent problems, the two temperatures are different, regardless of the presence of heat supply. The two temperatures T , φ and the strain are found to have representations in the form of a travelling wave plus a response, which occurs instantaneously throughout the body (Boley and Tolins [12]). Various investigators have studied different problems of thermoelastic dual and three phase lag models with two temperatures e.g. [13, 14, 15, 16, 17, 18, 19, 20]. Recently, Tripathi et al. [21] discussed generalized thermoelastic diffusion problem in a thick circular plate with axisymmetric heat supply.

Recently Kumar et. al [22] studied the effects of two temperatures and thermal phase lags in a thick circular plate. In this paper, we have extended the work of Kumar et. al. [22] and studied the axisymmetric deformation due to thermomechanical sources for dual phase lags in a thick circular plate with two temperatures.

Basic Equations. The constitutive relations, equations of motion, heat conduction in a homogeneous isotropic thermoelastic solid with dual phase lags and two temperatures in the absence of body forces, heat sources are:

$$\sigma_{ij} = 2\mu e_{ij} + \delta_{ij}(\lambda e_{kk} - \beta_1 T) \quad (1)$$

$$(\lambda + \mu)\nabla(\nabla \cdot u) + \mu\nabla^2 u - \beta_1 \nabla = \rho \ddot{u} \quad (2)$$

$$\left(1 + \tau_t \frac{\partial}{\partial t}\right) KT, \quad ij = \left(1 + \tau_q \frac{\partial}{\partial t} + \tau_q^2 \frac{\partial^2}{\partial t^2}\right) [\rho C_E \dot{T} + \beta_1 T_0 \dot{e}_{kk}] \quad (3)$$

$$T = (1 - a\nabla^2)\varphi, \quad (4)$$

where λ, μ are Lamé's constants, ρ is the density assumed to be independent of time, u_i are components of displacement vector u , K is the coefficient of thermal conductivity, C_E is the specific heat at constant strain, T is the absolute temperature of the medium, σ_{ij} and e_{ij} are the components of stress and strain respectively, e_{kk} is dilatation, S is the entropy per unit mass, $\beta_1 = (3\lambda + 2\mu)\alpha_t$, α_t is the coefficient of thermal linear expansion. τ_t, τ_q are respectively phase lag of temperature gradient, the phase lag of heat flux, 'a' is the two temperatures parameter. In the above equations, a comma followed by suffix denotes spatial derivative and a superposed dot denotes derivative with respect to time.

2. Formulation and Solution of the Problem

Consider a thick circular plate of thickness $2b$ occupying the space D defined by $0 \leq r \leq \infty, -b \leq z \leq b$. Let the plate be subjected to an axisymmetric heat supply depending on the radial and axial directions of the cylindrical polar co-ordinate system (r, θ, z) with symmetry about z -axis. The initial temperature in the thick plate is given by a constant temperature T_0 and the heat flux $g_0 F(r, z)$ is prescribed on the upper and lower boundary surfaces. With these restrictions, thermomechanical quantities are required to be determined. As the considered problem is two dimensional axisymmetric problem, therefore we have

$$u = (u_r, 0, u_z) \quad (5)$$

Equations (2)-(3) with the aid of (5) takes the form

$$(\lambda + \mu) \frac{\partial e}{\partial r} + \mu \left(\nabla^2 - \frac{1}{r^2}\right) u_r - \beta_1 \frac{\partial T}{\partial r} = \rho \frac{\partial^2 u_r}{\partial t^2} \quad (6)$$

$$(\lambda + \mu) \frac{\partial e}{\partial z} + \mu \nabla^2 u_z - \beta_1 \frac{\partial T}{\partial z} = \rho \frac{\partial^2 u_z}{\partial t^2} \quad (7)$$

$$\left(1 + \tau_t \frac{\partial}{\partial t}\right) K \nabla^2 T = \left(1 + \tau_q \frac{\partial}{\partial t} + \frac{\tau_q^2}{2} \frac{\partial^2}{\partial t^2}\right) \left[\rho C_E \frac{\partial}{\partial t} (1 - a\nabla^2)\varphi + \beta_1 T_0 \frac{\partial}{\partial t} \text{div } u\right], \quad (8)$$

where

$$e = \frac{\partial u_r}{\partial r} + \frac{u_r}{r} + \frac{\partial u_z}{\partial z}, e_{rr} = \frac{\partial u_r}{\partial r}, e_{\theta\theta} = \frac{u_r}{r} + \frac{\partial u_\theta}{\partial \theta}, e_{zz} = \frac{\partial u_z}{\partial z}, e_{rz} = \frac{1}{2} \left(\frac{\partial u_r}{\partial z} + \frac{\partial u_z}{\partial r} \right) \quad (9)$$

To facilitate the solution, the following dimensionless quantities are introduced:

$$r' = \frac{\omega_1^*}{c_1} r, z' = \frac{\omega_1^*}{c_1} z, (u'_r, u'_z) = \frac{\omega_1^*}{c_1} (u_r, u_z), t' = \omega_1^* t, (T', \varphi') = \frac{\beta_1}{\rho c_1^2} (T, \varphi) \quad (10)$$

$$(\tau'_q, \tau'_t) = \omega_1^* (\tau_q, \tau_t), (\sigma'_{rr}, \sigma'_{\theta\theta}, \sigma'_{zz}, \sigma'_{rz}) = \frac{1}{\beta_1 T_0} (\sigma_{rr}, \sigma_{\theta\theta}, \sigma_{zz}, \sigma_{rz}),$$

$$\text{where } \omega_1^* = \frac{\rho C_E c_1^2}{K} \text{ and } c_1^2 = \frac{\lambda + 2\mu}{\rho}$$

In equations (6)-(8) and after that suppressing the primes and then applying the Laplace and Hankel transforms defined by:

$$\hat{f}(r, z, s) = \int_0^\infty f(r, z, t) e^{-st} dt \quad (11)$$

$$\bar{f}(\xi, z, s) = \int_0^\infty \hat{f}(r, z, s) r J_n(r\xi) dr \quad (12)$$

On the resulting quantities and simplifying we obtain:

$$(D^2 - \xi^2 - k_i^2) (\bar{\varphi}_i^*, \bar{e}_i^*) = 0 \quad (13)$$

The solution of (13) has the form:

$$\bar{e}^* = \sum_{i=1}^2 A_i(\xi, s) \cosh(q_i z) \quad (14)$$

$$\bar{\varphi}^* = \sum_{i=1}^2 d_i A_i(\xi, s) \cosh(q_i z), \quad (15)$$

where

$$q_i = \sqrt{\xi^2 + k_i^2}, d_i = \frac{\tau_q^0 \xi_2}{\tau_q^0 \xi_1 - \zeta_3 q_i^2}, \zeta_3 = \tau_2^0 \delta_1 - \tau_t^0 k, \tau_q^0 = 1 + s\tau_q + \frac{s^2 \tau_q^2}{2}, \tau_t^0 = 1 + s\tau_t$$

$$\zeta_1 = \frac{\rho C_E c_1^2}{\omega_1^*}, \zeta_2 = \frac{\beta_1^2 T_0}{\rho \omega_1^*} s, \delta_1 = \frac{a \omega_1^{*2}}{c_1^2}$$

The inverse Hankel transform is given by the relation:

$$\bar{f}(r, z, s) = H^{-1} \hat{f}(\xi, z, s) = \int_0^\infty \hat{f}(\xi, z, s) \xi J_0(r\xi) d\xi$$

Applying inversion of Hankel transform on (14), and (15), we obtain:

$$\bar{e} = \int_0^\infty [\sum_{i=1}^2 A_i(\xi, s) \cosh(q_i z)] \xi J_0(\xi r) d\xi \quad (16)$$

$$\bar{\varphi} = \int_0^\infty [\sum_{i=1}^2 d_i A_i(\xi, s) \cosh(q_i z)] \xi J_0(\xi r) d\xi \quad (17)$$

Boundary Conditions. We consider a thermal source and normal force of unit magnitude along with vanishing of shear stress components at the stress free surface $z = \pm b$. Mathematically, these can be written as:

$$\frac{\partial \varphi}{\partial z} = \pm F(r, z) \quad (18)$$

$$\sigma_{zz} = H(t) f(r) \quad (19)$$

$$\sigma_{rz} = 0, \quad (20)$$

$$\text{where } \sigma_{zz} = 2\mu e_{zz} + \lambda e - \beta_1 (1 - a\nabla^2) \varphi, \sigma_{rz} = \mu e_{rz} \quad (21)$$

and $H(t)$ is the Heaviside unit step function.

Applying Laplace transform and Hankel transforms defined by (11)-(12) on the boundary conditions (18)-(20), we obtain:

$$\frac{d\bar{\varphi}}{dz} = \pm \bar{F}(\xi, z) \quad (22)$$

$$\bar{\sigma}_{zz} = \frac{1}{s} \bar{f}(\xi) \quad (23)$$

$$\bar{\sigma}_{rz} = 0 \quad (24)$$

Substituting the values of \bar{e} and $\bar{\varphi}$ from equations (16) and (17) in the boundary conditions (22)-(24), and using equations (6)-(10), we obtain the displacement components, stress components, conductive temperature and temperature change as:

$$\bar{u}_r(r, z, s) = \int_0^\infty \frac{1}{\Delta} \left[\Delta_3 \cosh(qz) \xi J_0(\xi r) + \sum_{i=1}^2 \Delta_i \left\{ \left((-\eta_i + \mu_i) q_i^2 \xi^2 \cosh(q_i z) \right) J_1(\xi r) + \left\{ \delta_1 \mu_i \cosh(q_i z) \left(\frac{\xi^3}{r} J_2 - J_1 \left(\xi^4 - \frac{\xi^2}{r^2} + \xi^2 q_i^2 \right) + \frac{\xi^3}{r} J_0 \right) \right\} \right\} \right] d\xi \quad (25)$$

$$\bar{u}_z(r, z, s) = \int_0^\infty \frac{1}{\Delta} \left[\Delta_3 \sinh(qz) \xi^3 J_0(\xi r) + \sum_{i=1}^2 \Delta_i \left\{ (-\eta_i + \mu_i) \sinh(q_i z) \xi J_0(\xi r) - \delta_1 \mu_i \sinh(q_i z) \left(\frac{\xi^2}{r} J_2 - J_1 \left(\xi^3 - \frac{\xi}{r} + \xi q_i^2 J_0 \right) \right) \right\} \right] d\xi \quad (26)$$

$$\bar{\sigma}_{zz} = \frac{2\mu}{\Delta \beta_1 T_0} \int_0^\infty \left[\xi J_0(\xi r) \left\{ \xi^2 \Delta_3 \cosh(qz) + \left(\sum_{i=1}^2 (-\eta_i + \mu_i) q_i^2 - \zeta d_i + \lambda' \right) \Delta_i \cosh(q_i z) \right\} - \sum_{i=1}^2 \left\{ \delta_1 (\mu_i q_i - \zeta d_i) \Delta_i \cosh(q_i z) \left(\xi^3 J_0(\xi r) - J_1(\xi r) \left(\frac{\xi^{-1}}{r} \right) + \xi q_i^2 J_0(\xi r) \right) \right\} \right] d\xi \quad (27)$$

$$\bar{\sigma}_{rz} = \frac{\mu}{2\Delta \beta_1 T_0} \int_0^\infty \left[\xi^2 J_1(\xi r) \left\{ \left(\frac{q^2 - \xi^2}{q} \right) \Delta_3 q \sinh(qz) + 2 \sum_{i=1}^2 (\eta_i - \mu_i) q_i \Delta_i \sinh(q_i z) \right\} + \sum_{i=1}^2 \delta_1 \mu_i \Delta_i \sinh(q_i z) \left\{ \left(q_i \left(\frac{\xi^3}{r} J_2(\xi r) \right) - J_1(\xi r) \left(\xi^4 + q_i^2 \xi^2 + \frac{4}{\xi^2 r^2} + q_i^2 \xi \right) + \left(\frac{2}{\xi r} - \xi^4 - \frac{\xi^2(\xi-1)}{r} + q_i^2 \xi^2 \right) J_0(\xi r) \right) \right\} \right] d\xi \quad (28)$$

$$\bar{\varphi} = \int_0^\infty \frac{1}{\Delta} \left\{ \sum_{i=1}^2 d_i \Delta_i(\xi, s) \cosh(q_j z) \right\} \xi J_0(\xi r) d\xi \quad (29)$$

$$\bar{T} = \int_0^\infty \frac{1}{\Delta} \left\{ \sum_{i=1}^2 \left(d_i \Delta_i(\xi, s) \cosh(q_i z) \left[\xi J_0(\xi r) \left(1 + \delta_1 q_i^2 - \delta_1 \xi \right) + J_1(\xi r) \delta_1 \xi \left(1 - \frac{1}{r} \right) \right] \right) \right\} d\xi, \quad (30)$$

where

$$\begin{aligned} \Delta &= -\frac{2\mu}{\beta_1 T_0} \cosh(qb) (\Delta_{11} \Delta_{32} - \Delta_{12} \Delta_{31}) + \sinh(qb) (\Delta_{11} \Delta_{22} - \Delta_{12} \Delta_{21}) \\ \Delta_1 &= g_0 \bar{F}(\xi, z) (\Delta_{21} \Delta_{32} - \Delta_{22} \Delta_{31}) - \bar{f}(\xi) (\Delta_{11} \Delta_{32} - \Delta_{12} \Delta_{31}) \\ \Delta_2 &= -g_0 \bar{F}(\xi, z) \left(\frac{2\mu}{\beta_1 T_0} \cosh(qb) \Delta_{32} - \Delta_{22} \sinh(qb) \right) + \frac{1}{s} \bar{f}(\xi) (-\Delta_{12} \sinh(qb)) \\ \Delta_3 &= g_0 \bar{F}(\xi, z) \left(\frac{2\mu}{\beta_1 T_0} \cosh(qb) \Delta_{31} - \Delta_{21} \sinh(qb) \right) + \frac{1}{s} \bar{f}(\xi) (\Delta_{11} \sinh(qb)) z \end{aligned} \quad (31)$$

and

$$\begin{aligned} \Delta_{1i} &= d_i q_i \sinh(q_i b), \quad \Delta_{2i} = \left((\mu_i - \eta_i) q_i^2 - \delta_1 \mu_i q_i - \zeta d_i (1 + \delta_1) + \lambda^0 \right) \cosh(q_i b) \\ \Delta_{3i} &= (2(\eta_i - \mu_i) q_i + \delta_1 \mu_i) \sinh(q_i b), \quad i = 1, 2 \end{aligned} \quad (32)$$

Applications. As an application of the problem, we take the source functions as:
 $F(r, z) = z^2 e^{-\omega r}$ and $f(r) = H(a - r)$ (33)

Applying Laplace and Hankel Transforms defined by (11)-(12) on (33), we obtain:

$$\bar{F}(\xi, z) = \frac{z^2 \omega}{(\xi^2 + \omega^2)^{3/2}} \quad (34)$$

$$\bar{f}(\xi) = \frac{a J_1(\xi a)}{\xi} \quad (35)$$

Making use of the values of $\bar{F}(\xi, z)$ and $\bar{f}(\xi)$ from (34) and (35) in (25)-(30), one can obtain the displacement components, stress components, conductive temperature and temperature change for thermomechanical sources.

Particular Cases. (1) In the limiting case $a \rightarrow 0$ in equation (25)-(30), yields the expressions for displacements and stresses, conductive temperature and temperature change for dual-phase-lag thermoelastic solid without two temperatures. These results are similar if we solve the problem directly.

(2) If $\tau_q = \tau_t = 0$ we obtain the corresponding expressions for thermoelasticity with two temperatures model .

(3) If $\tau_q = 0$ then the corresponding expressions for dual phase lag thermal model (DPLT) model reduce to single-phase-lag thermal model (SPLT) with two temperatures.

Numerical Inversion of Transforms. To obtain the solution of the problem in physical domain, we must invert the transforms in (25)-(30) for all the theories. Here the displacement components, normal and tangential stresses, temperature change, chemical potential and mass concentration are functions of z . We first invert the Hankel transform, which gives the Laplace transform expression $\bar{f}(r, z, s)$ of the function $f(r, z, t)$ as:

$$\bar{f}(r, z, s) = \int_0^\infty \eta \hat{f}(\eta, z, s) J_n(\eta r) d\eta \tag{36}$$

Now for fixed values of η, r and z the function $\bar{f}(r, z, s)$ in (36) can be considered as the Laplace transform $\bar{g}(s)$ of the same function $g(t)$. Following Honig and Hirdes [23], the Laplace transform function $\bar{g}(s)$ can be inverted as given below:

$$g(t) = \frac{1}{2\pi i} \int_{C-i\infty}^{C+i\infty} e^{st} \bar{g}(s) ds, \tag{37}$$

where C is an arbitrary real number greater than all the real parts of the singularities of $\bar{g}(s)$. Taking $s = C + iy$, we get:

$$g(t) = \frac{e^{Ct}}{2\pi} \int_{-\infty}^\infty e^{ity} \bar{g}(C + iy) dy, \tag{38}$$

Now, taking $e^{-Ct}g(t)$ as $h(t)$ and expanding it as Fourier series in $[0, 2L]$ we obtain approximately the formula Honig and Hirdes [23]:

$$g(t) = g_\infty(t) + E_D \tag{39}$$

$$g_\infty(t) = (C_0/2) + \sum_{k=1}^\infty C_k, \text{ for } 0 \leq t \leq 2L \tag{40}$$

and

$$C_k = (e^{Ct}/L) \text{Re} [e^{ik\pi t/L} \bar{g}(C + (ik\pi/L))] \tag{41}$$

E_D is the discretization error that can be made arbitrarily small by choosing a large enough C . The values of C and L are chosen according to the criteria outlined by Honig and Hirdes [23].

Since the infinite series in (40) can be summed up only to a finite number of N terms, the approximate value of $g(t)$ becomes:

$$g_N(t) = (C_0/2) + \sum_{k=1}^N C_k, \text{ for } 0 \leq t \leq 2L \tag{42}$$

We now introduce a truncation error E_T that must be added to the discretization error to produce the total approximate error in evaluating $g(t)$ using the above formula. Two methods are used to reduce the total error. The discretization error is reduced by using the ‘Korrektur’ method Honig and Hirdes [23] and then the ‘ ε -algorithm’ is used to reduce the truncation error and hence to accelerate the convergence. The Korrektur method formula, to evaluate the function $g(t)$ is:

$$g(t) = g_\infty(t) - e^{-2CL} g_\infty(2L + t) + E'_D, \tag{43}$$

where $|E'_D| \ll |E_D|$ Honig and Hirdes [23].

Thus the approximate value of $g(t)$ becomes:

$$g_{N_k}(t) = g_N(t) - e^{-2CL} g_{N'}(2L + t), \tag{43}$$

where N' is an integer such that $N' < N$.

We shall now describe the ε -algorithm, which is used to accelerate the convergence of the series in (42). Let N be an odd natural number and $s_m = \sum_{k=1}^m C_k$ be the sequence of partial sums of (42). We define the ε -sequence by:

$$\varepsilon_{0,m} = 0, \varepsilon_{1,m} = s_m, \varepsilon_{n+1,m} \varepsilon_{n-1,m+1} + \frac{1}{\varepsilon_{n,m+1} - \varepsilon_{n,m}}; n, m = 1, 2, 3 \tag{44}$$

It can be shown that Honig and Hirdes [23], the sequence $\varepsilon_{1,1}, \varepsilon_{3,1}, \dots, \varepsilon_{N,1}$ converges to $g(t) + E_D - (C_0/2)$ faster than the sequence of partial sums $s_m, m = 1, 2, 3$. The actual procedure to invert the Laplace transform consists of (43) together with the ε -algorithm.

The last step is to calculate the integral in equation (36). The method for calculating this integral is described by Press et al. [24]. It involves the use of Romberg's integration with adaptive step size. This also uses the results from successive refinements of the extended trapezoidal rule followed by extrapolation of the results to the limit when the step size tends to zero.

3. Numerical Results and Discussion

The mathematical model is prepared with copper material for the purpose of numerical computation. The material constants for the problem are taken from Dhaliwal and Singh [25]

$$\lambda = 7.76 \times 10^{10} Nm^{-2}, \mu = 3.86 \times 10^{10} Nm^{-2}, K = 386 JK^{-1} m^{-1} s^{-1}$$

$$\beta_1 = 5.518 \times 10^6 Nm^{-2} deg^{-1}, \rho = 8954 Kgm^{-3}, a = 1.2 \times 10^4 m^2 s^{-2} k^{-1}$$

$$b = 0.9 \times 10^6 \frac{m^5}{kgs^2}, D = 0.88 \times 10^{-8} kgs/m^3, \beta_2 = 61.38 \times 10^6 Nm^{-2} deg^{-1}$$

$$T_0 = 293K, C_E = 383.1 Jkg^{-1} k^{-1}$$

The graphical representation has been given to study the effect of phase lags and two temperatures on the various quantities for the range $0 \leq r \leq 10$.

In all the figures, solid line with ($a = 0.08, t = 0.2$) and without centre symbols ($a = 0, t = 0.2$) corresponds to the dual-phase-lags thermoelastic with and without two temperatures. Small dash line with ($a = 0.08, t = 0.4$) and without centre symbols ($a = 0, t = 0.4$) corresponds to the dual-phase-lags thermoelastic with and without two temperatures.

Figure 1 exhibits variations of radial displacement u_r with distance r . Near the loading surface, there is a sharp decrease for the range $0 \leq r \leq 2$ and behaviour is oscillatory for the rest corresponding to all the cases with amplitudes of oscillations decreasing as r increases. Amplitude of oscillation is more with two temperatures than without two temperatures. For $a = 0$, small variations near zero are observed for $t = 0.2$ and $t = 0.4$.

Figure 2 shows variations of axial displacement u_z with distance r . Here behaviour is oscillatory for the whole range except for $0 \leq r \leq 1.5$, as for this range, there is a sharp decrease. Maximum variations are observed corresponding to $a = 0, t = 0.2$ for the range $0 \leq r \leq 4$. As r diverges from point of application of source, variations start decreasing.

Figure 3 shows variation of vertical stress σ_{zz} with distance r . We find that there is a sharp increase for the range $0 \leq r \leq 3$ for all the cases and similar oscillatory trend is observed afterwards. Small variations near zero are noticed for the range $5 \leq r \leq 10$. Figure 4 gives variations of shear stress σ_{rz} with distance r . It is evident from this figure that the behaviour is descending oscillatory with a sharp decrease for the range $0 \leq r \leq 2$. For $a = 0$, more variations are noticed.

Figure 5 gives variations of conductive temperature φ with distance r . Here, we notice that either there are sudden increases and decreases or there are small variations. Here descents are observed at the points $r = 0.5$ and $r = 2.5$ and hikes are observed at the points $r = 6.5$ and $r = 9$ for all the cases. Figure 6 exhibits variations of temperature change T with displacement r . Here there is a descent at the point $r = 0.5$ and hikes at the points $r = 2.5, r = 4.5, r = 6.5$ and a small descent is observed at $r = 9$ and small variations are noticed for the remaining range except the small neighbourhoods of these points.

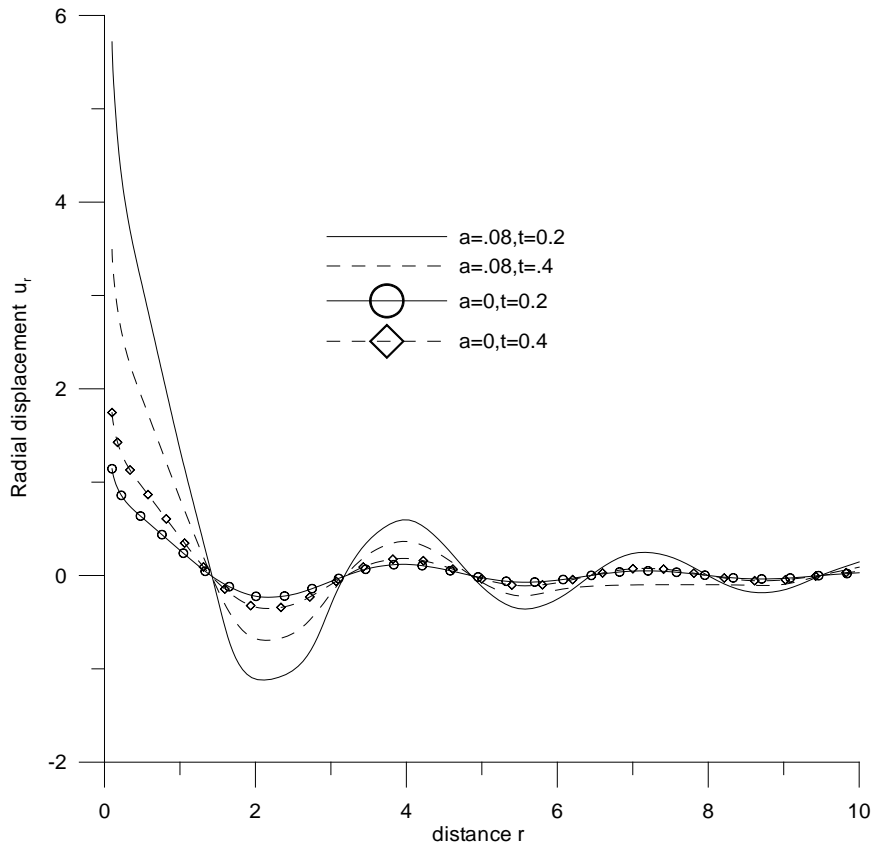


Fig. 1. Variations of radial displacement u_r with distance r .

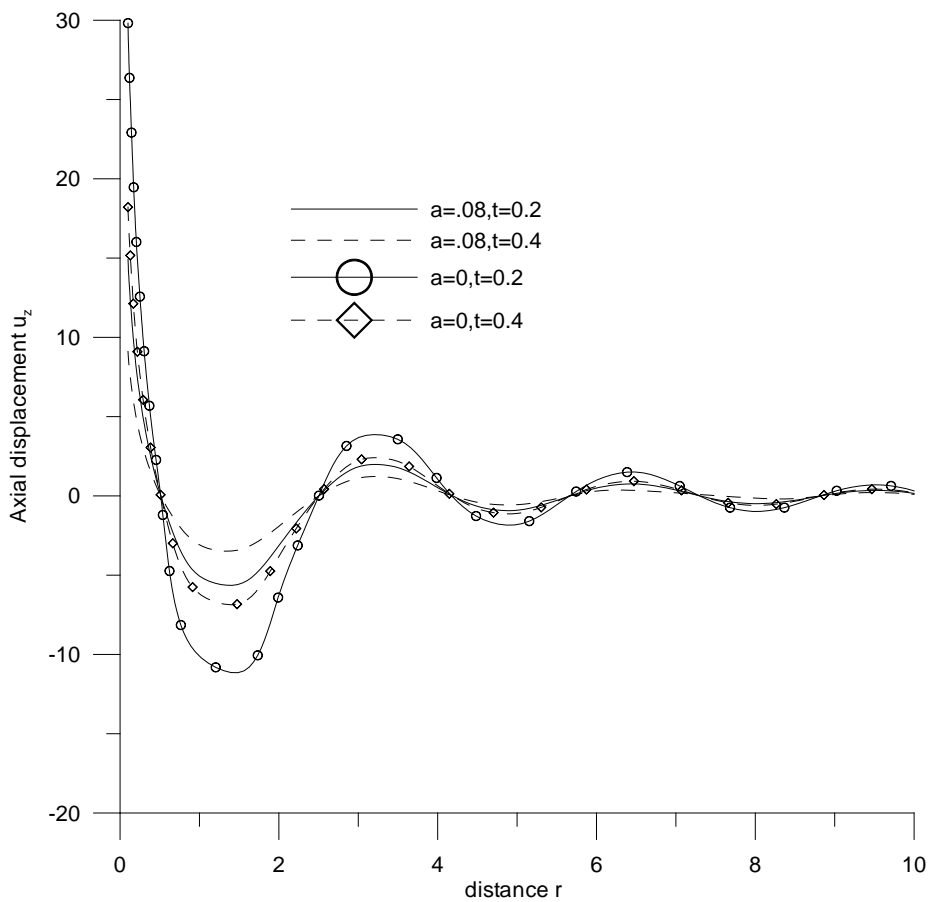


Fig. 2. Variations of axial displacement u_z with distance r .

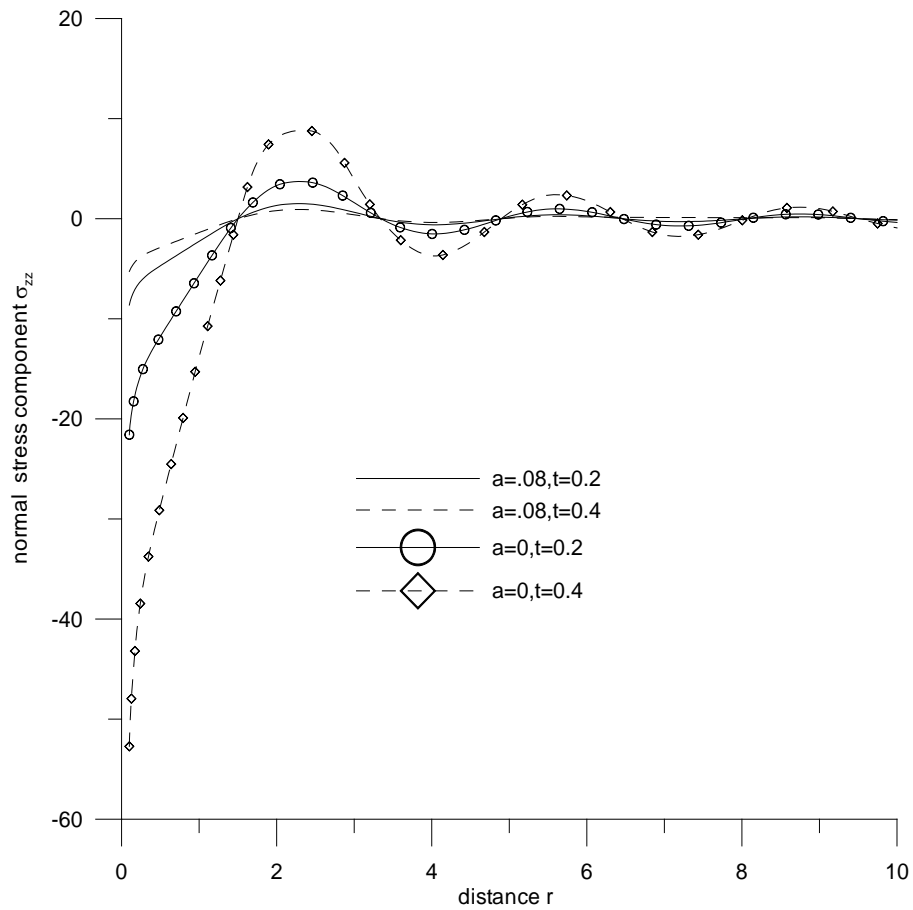


Fig. 3. Variation of normal stress component σ_{zz} with distance r .

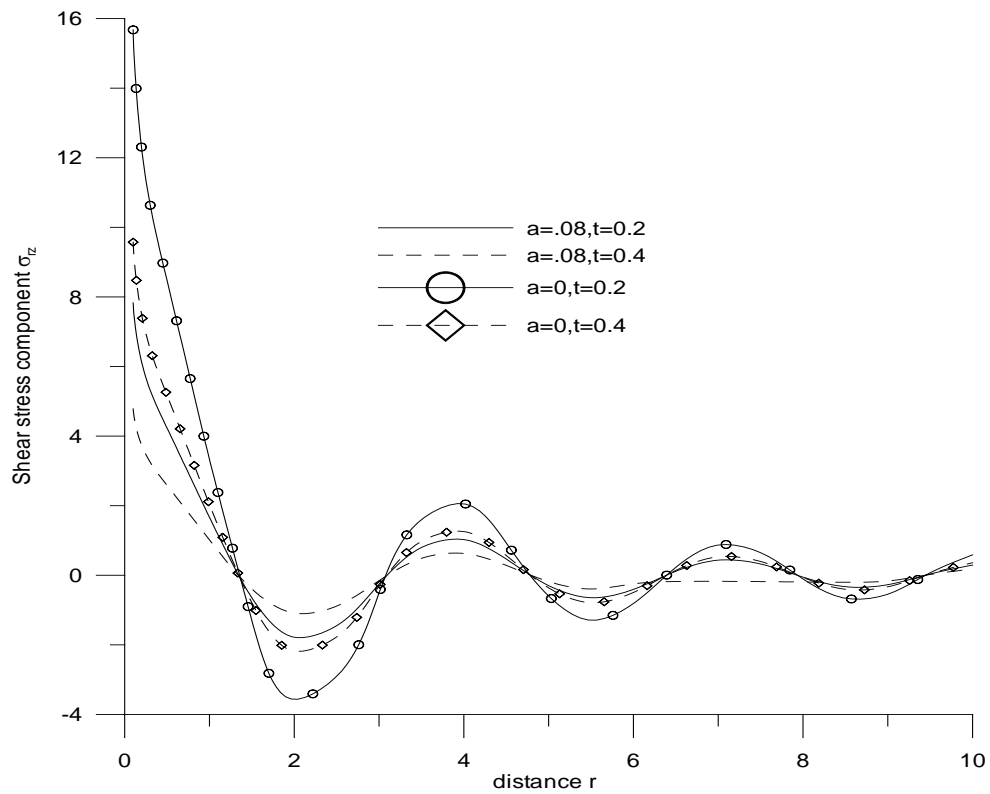


Fig. 4. Variations of shear stress component σ_{rz} with distance r .

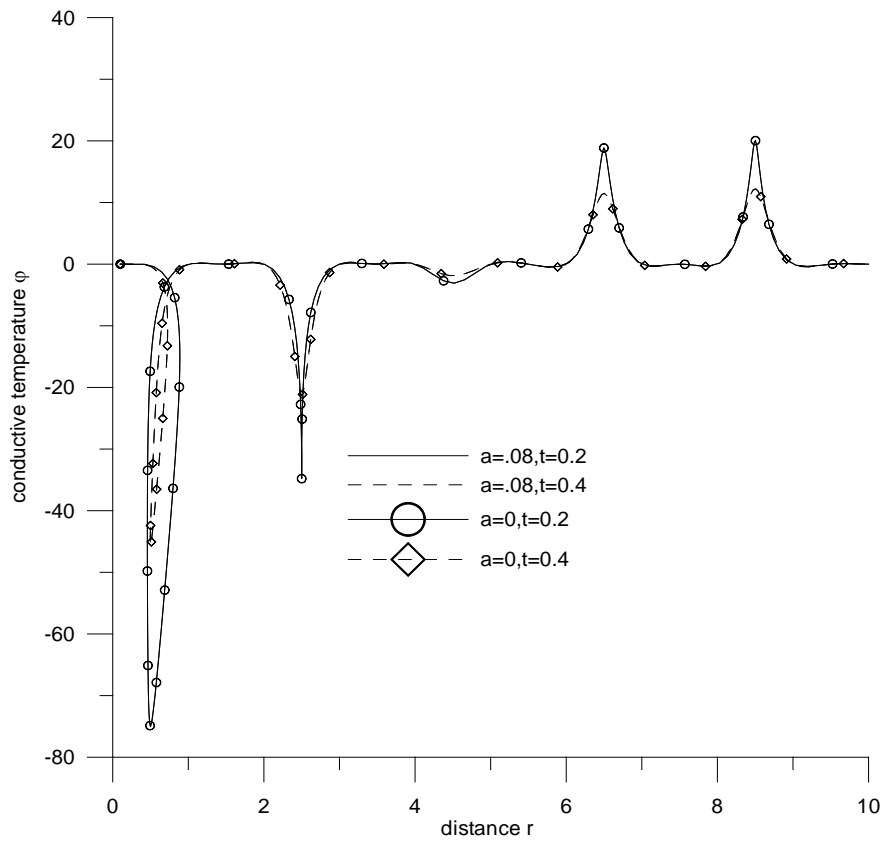


Fig. 5. Variation of conductive temperature φ with distance r .

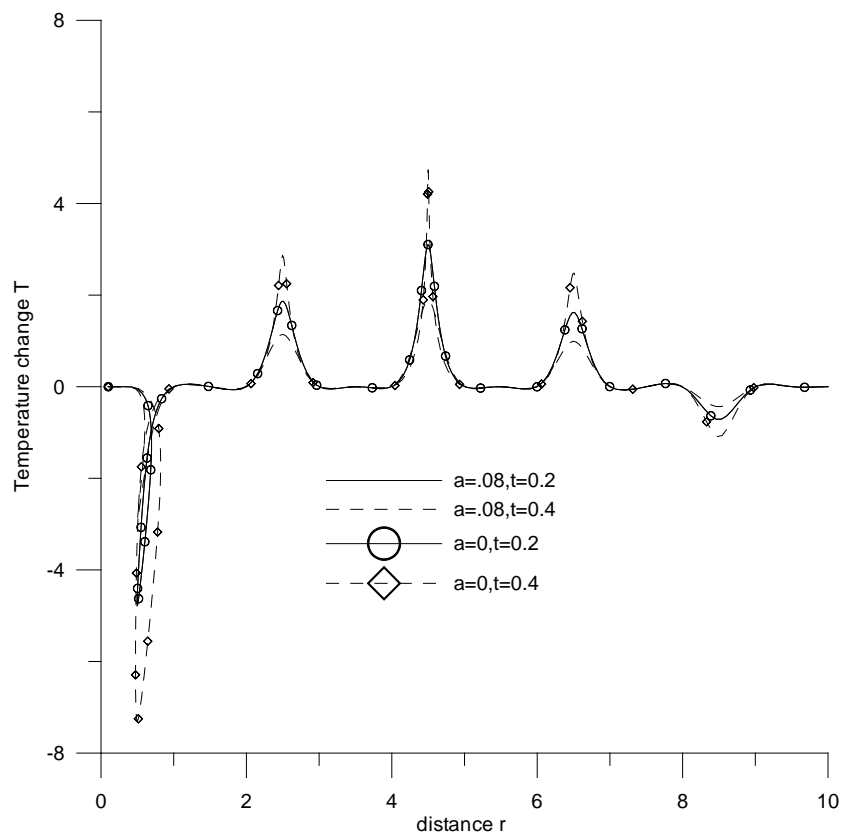


Fig. 6. Variations of temperature change T with distance r .

4. Conclusion

From the graphs, it is evident that there is a significant impact on behaviour of deformation of various components of stresses, components of displacement, conductive temperature and temperature change in the thick circular plate due to time variation with dual phase lags and two temperatures. Due to two temperatures and dual phase lags, instant hikes and descents are observed in temperature change, conductive temperature and radial stress σ_{rr} . Oscillatory trends are observed in components of displacement, shear stress and normal stress σ_{zz} . As r diverges from point of application of source, variations start decreasing and small variations near zero are observed. As disturbance travels through the constituents of the medium, it suffers sudden changes resulting in an inconsistent / non uniform pattern of graphs in case of conductive temperature, temperature change. The use of thermal phase-lags in the heat conduction equation gives a more realistic model of thermoelastic media as it allows a delayed response to the relative heat flux vector. The result of the problem is useful in the two dimensional problem of dynamic response due to various thermal and mechanical sources which has various geophysical and industrial applications.

References

- [1] R. B. Hetnarski, J. Ignaczak // *J. Therm. Stress* **22** (1999) 451.
- [2] H.W. Lord, Y. Shulman // *J. Mech.Phys. Solid* **15** (1967) 299.
- [3] A.E. Green, K.A. Lindsay // *J. Elasticity* **2** (1972) 1.
- [4] R. B. Hetnarski, J. Ignaczak // *Int. J. Eng. Sci.* **34** (1996) 1767.
- [5] A.E. Green, P.M. Nagdhi // *J. Elasticity* **31** (1992) 189.
- [6] D.Y. Tzou // *ASME J. Heat Transf* **117** (1995) 8.
- [7] D.S. Chandrasekharaiah // *Appl. Mech. Rev.* **51** (1998) 705.
- [8] S.K. Roychoudhuri // *Journal of Thermal Stresses* **30** (2007) 231.
- [9] P.J. Chen, M.E. Gurtin // *Zeitschrift für angewandte Mathematik und Physik (ZAMP)* **19** (1968) 614.
- [10] P.J. Chen, M.E. Gurtin, W.O. Williams // *Journal of Applied Mathematics and Physics (ZAMP)* **19** (1968) 969.
- [11] P.J. Chen, M.E. Gurtin, W.O. Williams // *Journal of Applied Mathematics and Physics (ZAMP)* **20** (1969) 107.
- [12] B. Boley, I.S. Tolins // *Journal of Applied Mechanics* **29** (1962) 637.
- [13] R. Kumar, V. Chawla, I.A. Abbas // *Theoret. Appl. Mech.* **39(4)** (2012) 313.
- [14] X.H. Ying, J.X. Yun // *Chin. Phys. B* **24(3)** (2015) 034401.
- [15] H.M. Youssef // *Journal of Thermal Stresses* **34** (2011) 138.
- [16] I.A. Abbas, R. Kumar, L.S. Reen // *Canadian Journal of Physics* **92(11)** (2014) 1305.
- [17] H.M. Youssef // *IMA Journal of Applied Mathematics* **71(3)** (2006) 383.
- [18] R. Kumar, K.D. Sharma, S.K. Garg // *Advances in Acoustics and Vibrations* **2014** (2014) ID 846721, 11 pages. doi:10.1155/2014/846721
- [19] M.A. Ezzat, E.S. Award // *Journal of Thermal Stresses* **33(3)** (2010) 225.
- [20] K. Sharma, M. Martin // *U. P. B. Sci. Bull Series* **75(2)** (2013) 121.
- [21] J.J. Tripathi, G.D. Kedar, K.C. Deshmukh // *Acta Mechanica* **226(7)** (2015) 2121.
- [22] R. Kumar, N. Sharma, L. Parveen // *Cogent Mathematics* **3(1)** (2016) 1129811.
- [23] G. Honig, U. Hirdes // *Journal of Computational and Applied Mathematics* **10** (1984) 113.
- [24] W.H. Press, B.P. Flannery, S.A. Teukolsky, W.A. Vetterling, *Numerical recipes, The art of scientific computing* (Cambridge University Press, Cambridge, 1986).
- [25] R.S. Dhaliwal, A. Singh, *Dynamic coupled thermoelasticity* (Hindustan Publisher Corporation, New Delhi, India, 1980).

AN EFFECTIVE METHOD TO FIND GREEN'S FUNCTIONS FOR LAYERED MEDIA

N. S. Markov^{1*}, A. M. Linkov^{1,2,3}

¹Peter the Great St. Petersburg Polytechnic University, Russia

²Rzeszow University of Technology, Poland

³Institute for Problems in Mechanical Engineering of the Russian Academy of Sciences, Russia

*e-mail: markovnicholas@gmail.com

Abstract. Layered structure of rocks strongly influences propagation of hydraulic fractures widely used in practice to increase oil and gas production. The paper aims to facilitate modeling of hydraulic fractures. We develop a method to overcome the main difficulty, which arises when modeling fractures in layered systems: the need in building Green's functions for systems of layers. The method employs highly efficient fast Fourier transform (FFT) in frames of the difference equations method. Its key computational parameters are established by studying bench-mark problems. Green's functions with log-type singularity are included into the theory and the algorithm developed. The accuracy of the method and its application are illustrated with numerical examples.

Keywords: layered structures; Green's function; hydraulic fractures; Fourier transform; boundary element method.

1. Introduction

Solving problems for systems of layers, containing internal cracks, cavities, pores, inclusions and/or interacting grains, is important for various applications of continuum mechanics, including hydraulic fractures, mining, geomechanics, nano-technology, etc. To account for the internal structure of a layer, the boundary element methods (BEM) is a good choice when fundamental solutions entering appropriate boundary integral equations (BIE) are known or calculated in advance. However, except for the simplest cases of homogeneous infinite space or bonded half-spaces, finding the fundamental solutions (Green's functions) is quite involved and time expensive. It may be notably simplified if the geometry of a problem suggests using methods *ad hoc*. Specifically, simplifications become possible when the layers have parallel plane or spherical (circular in 2D) boundaries. These cases, being of practical significance, we focus on building Green's functions for them. For certainty, the case of layers with plane parallel boundaries is considered. In particular, it is of prime interest for modeling hydraulic fractures.

The specific geometry of layers suggests using the Fourier expansions/transforms. Starting from early sixties of the last century [4,5,22,23], this approach to solving problems for multi-layered media has been employed in numerous papers (e.g. [1,2,6,10–21,26–29]). However, to the date the advantage of using the fast Fourier transform (FFT) has not been employed except for a few papers concerning with particular problems [1,13,14]. The case of Green's functions with log-type singularity, which tend to infinity with growing distance from a source point, has even stayed out of the general scheme sketched in [11].

The *objective* of the present paper is to make a step in developing universal algorithms employing the fast Fourier transform (FFT) for the problems for layered structures. The log-type singular solutions are to be included into the general scheme. For the beginning, we develop such an algorithm and extend the theory to log-type singularities for *plane harmonic problems*. The efficiency of the method suggested is illustrated by examples.

2. Problem formulation

For certainty, we discuss the problem formulation in terms used in the elasticity theory. Consider a package of n elastic layers with plane parallel boundaries (Fig. 1).

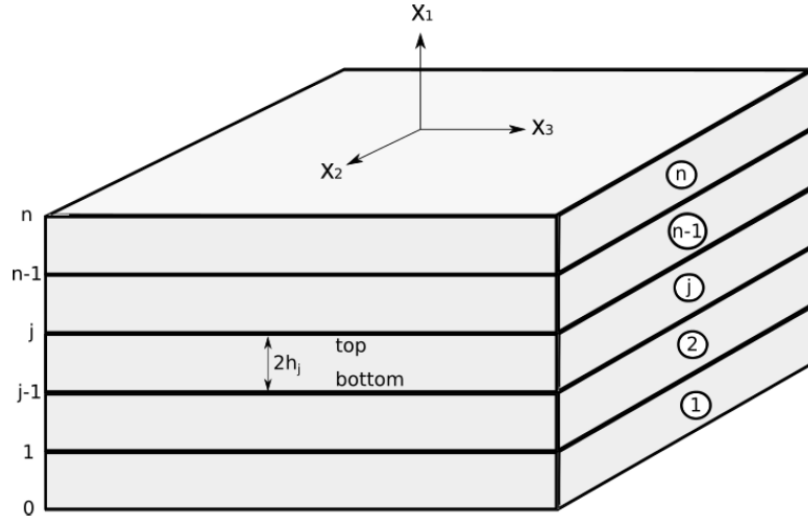


Fig. 1. Scheme of a layered structure.

The layers may contain cracks, cavities, pores, inclusions, interacting grains, etc. We numerate the layers from 1 to n and boundaries from 0 to n . The superscript “ i ” will denote that a quantity refers to the i -th layer or to the i -th contact. The axes x_2 and x_3 are directed along the boundaries in the horizontal plane. The unit normal to layer boundaries is directed along the axis x_1 . Values, corresponding to the top and bottom boundaries of the i -th layer, are marked with a subscript “ t ” and “ b ”, respectively. Then the displacement discontinuity vector is $\Delta u^i = u_t^i - u_b^{i+1}$.

For a system of n layers, the partial differential equations (PDF) are:

$$L^i u = 0 \quad (i = 1, \dots, n), \quad (1)$$

where L^i is a differential operator with physical constants of the i -th layer. Specifically, for elasticity problems, it is the Lamé operator; for harmonic problems, it is the Laplace operator.

The contact conditions at interfaces may include continuity of tractions q

$$q_t^i = q_b^{i+1} = q^i \quad (i = 1, \dots, n - 1) \quad (2)$$

and linear dependence of the displacement discontinuity Δu on the traction

$$-\Delta u^i = A_c^i q^i, \quad (3)$$

where A_c^i is a square matrix of contact interaction on the boundary between layers i and $i + 1$. If a contact is ideal, then $A_c^i = 0$ and $\Delta u^i = 0$.

On the boundaries of cracks and cavities, the boundary conditions are assigned as

$$-\Delta u = B_c q + \Delta u^0, \quad (4)$$

where B_c is a symmetric matrix and Δu^0 is a prescribed displacement discontinuity. The inversion of (4) $q = -B_c^{-1} \Delta u + q^0$ with $q^0 = -B_c^{-1} \Delta u^0$ includes the case when a traction q^0 is assigned. The particular case of assigned tractions corresponds to $B_c^{-1} = 0$; then

$$q = q^0 \quad (5)$$

The problem consists of finding the solution to (1) under the contact conditions (2) and (3) and the boundary conditions (4) or (5).

3. Green's function

By using the theory of potential, the problem is reduced to a boundary integral equation (e.g. [3, 7, 8]). It includes the Green's functions. For a layered system, the latter are unknown and to be found by solving the equation:

$$L^i U(x, y) = -\delta(x - y)I \tag{6}$$

for homogeneous (without cracks, cavities, etc.) layers under the contact conditions (2), (3). In (6), I is the unit matrix; $\delta(x)$ is the Dirac delta function. The Green's function may be found by following the line of the paper [11]. It is as follows.

Let the singular point x on the right hand side of (6) is a point x^k of the k -th layer in the layered system (Fig. 2a). Consider an infinite homogeneous media with elastic properties of the considered layer. The Green's function for such a medium is the known fundamental solution $U^0(x, y)$, say Kelvin's solution of the elasticity theory. The l -th column of U^0 provides the displacements u_t^k and tractions q^k on the top boundary of the k -th layer, and the displacements u_b^k and tractions q^{k-1} on its bottom boundary.

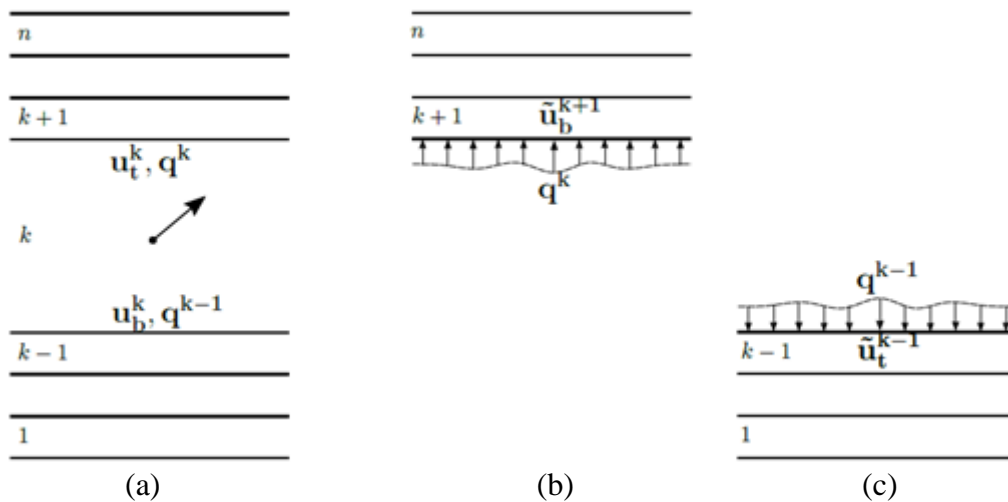


Fig. 2. Schemes to find the Green's matrix.

The needed Green's function $U(x, y)$ is represented as the sum:

$$U = U^0 + U^a, \tag{7}$$

where $U^a(x, y)$ is an additional matrix serving to meet the contact conditions (2), (3). This matrix is non-singular in all the layers including the layer k . It is found by considering separately the upper package of layers (Fig. 2b) and lower package of layers (Fig. 2c) under the loads q^k and q^{k-1} , respectively. Hence, the condition (2) of continuity of the tractions is met.

After solving the elasticity problems for these packages, we obtain the displacements u^* in the upper and lower packages. In particular, the displacements u_b^{*k+1} on the bottom boundary of the layer $k + 1$ and u_t^{*k-1} on the top boundary of the layer $k - 1$ are known. However, in general, the differences $u_t^k - u_b^{*k+1}$ and $u_t^{*k-1} - u_b^k$ do not satisfy the contact conditions (3) on the top and bottom boundaries of the k -th layer. There appear known discrepancies in the conditions (3), which are to be removed. It is done by solving the problem for the whole system (Fig. 2a) with the prescribed discontinuities (equal to the assigned discrepancies taken with the minus sign) on the top and bottom boundaries of the k -th layer and with contact conditions (3) on remaining contacts. The correcting solution \tilde{u} is easily found by the sweep method. Finally, the additional matrix is

$$U^a = U^* + \tilde{U} \quad (8)$$

Then the whole Green's matrix U becomes the sum of three matrices

$$U = U^0 + U^* + \tilde{U}, \quad (9)$$

of which $U^0 = 0$ outside the k -th layer and $U^* = 0$ inside this layer. In general, the matrix \tilde{U} is non-zero in all the layers. Thus, to find the Green's matrix we have to solve three similar standard problems. It can be efficiently done by using the Fourier transform and the sweep-method [11].

4. Plane harmonic problem with using FFT

For a plane harmonic problem, the potential u in each layer satisfies the Laplace equation:

$$\Delta u = \frac{\partial^2 u}{\partial x_1^2} + \frac{\partial^2 u}{\partial x_2^2} = 0 \quad (10)$$

The corresponding vector of the flux q is

$$q = k \nabla u \quad (11)$$

Herein, k is the conductivity, taken with the minus sign, in problems of heat (current, fluid) flow; $k = E/[2(1 + \nu)]$ in anti-plane elasticity problems with E being the Young's modulus, ν the Poisson's ratio.

Instead of the Fourier transform on an infinite interval, we consider a finite interval $[-A, A]$. Its length $2A$ should be sufficiently large to replace an infinite layer with a periodical system having the period $2A$. Clearly, the period $2A$ should notably exceed the thickness of a layer, containing the source point, and also the characteristic size of the structural elements, say cavities, within the layer. Below we shall establish quantitative estimations of $2A$, which may be used when building the Green's functions.

It is of essence to perform direct and inverse transforms as efficient as possible. This suggests using the *fast Fourier transform* (FFT) [13,14]. Then the number N of sampling points is a degree of 2: $N = 2^m$ where m is non-zero positive integer. The sampling points x_j are uniformly distributed on the interval $[-A, A]$. For a function $f(x)$ with values $f_j = f(x_j)$ at the sampling points x_j ($j = -N/2, \dots, N/2 - 1$), the direct transform, marked with wave, gives its image $\tilde{f}_k = \tilde{f}(s_k)$ at N points s_k uniformly distributed on the interval $[-A, A]$ of the axis s . For certainty, the direct FFT is defined as

$$\tilde{f}_k = \frac{1}{N} \sum_{j=-N/2}^{j=N/2-1} f_j \exp(-2\pi i k j / N) \quad (12)$$

Then the transform inverse to (12) is:

$$f_j = \sum_{k=-N/2}^{k=N/2-1} \tilde{f}_k \exp\left(\frac{2\pi i k j}{N}\right), \quad (13)$$

where $i = \sqrt{-1}$. From now on, to keep track with results for layered systems, commonly presented in terms of the Fourier transform on the infinite interval or in terms of Fourier series, we shall employ the usual notation of original functions and their images. We shall write a discrete function f_j as $f(x)$ and its discrete image \tilde{f}_k as $\tilde{f}(s)$.

With these agreements, application of the FFT (12) to (10) along the x_2 -axis yields:

$$\Delta \tilde{u} = \frac{\partial^2 \tilde{u}}{\partial x_1^2} - s^2 \tilde{u} = 0 \quad (14)$$

The image \tilde{q}^i of the component q_1 of the flux q in the i -th layer is:

$$\tilde{q}^i = \kappa_i \frac{\partial \tilde{u}}{\partial x_1} \quad (i = 1, \dots, n) \quad (15)$$

By using (14), the contact conditions (2)-(4) are re-written in terms of images. Finally, a harmonic problem for n homogeneous layers is reduced to the algebraic system of difference equations in fluxes \tilde{q}^i on the boundaries of layers (see, e.g. [10, 11]):

$$A^i \tilde{q}^{i-1} - C^i \tilde{q}^i + B^i \tilde{q}^{i+1} + F^i = 0, \quad (16)$$

where $A^i = -R_{tb}^i$; $C^i = -A_c + R_{tt}^i - R_{bb}^{i+1}$; $B^i = R_{bt}^{i+1}$; $F^i = -\Delta \tilde{u}_0^i$ are the images of assigned discontinuities of the potential. For the harmonic problems considered, the coefficients are scalar; the explicit formulae for them are:

$$\begin{aligned} R_{tt} &= \frac{1}{2}(R_s + R_a) \\ R_{tb} &= -\frac{1}{2}(R_s - R_a) \quad R_s = \frac{2}{\kappa s} \coth(sx_1) \\ R_{bt} &= \frac{1}{2}(R_s - R_a) \quad R_a = \frac{2}{\kappa s} \tanh(sx_1) \\ R_{bb} &= -\frac{1}{2}(R_s + R_a) \end{aligned} \tag{17}$$

The images of the potential on boundaries of layers are obtained by employing the dependences used when deriving (16):

$$\begin{aligned} \tilde{u}_t &= R_{tt}\tilde{q}_t + R_{tb}\tilde{q}_b \\ \tilde{u}_b &= R_{bt}\tilde{q}_t + R_{bb}\tilde{q}_b \end{aligned} \tag{18}$$

The solution to the system (16) under assigned boundary conditions on external boundaries of a package, is promptly found by the highly efficient sweep method for any fixed frequency (wave number) s (see, e.g. [9,25]). Then the images of the solutions to the three standard problems, presented in the previous section, become known. Consequently, the image of the Green's function becomes known, as well. Its inversion through (13) provides the needed Green's function in the physical space.

Alternatively, a system analogous to (16) may be written in terms of the images of the potential on upper boundaries of layers by employing the dependences (18).

5. Choice of the period for building log-type Green's function by FFT

In contrast with 3D problems, the starting fundamental solution for 2D elliptic problems has log-type singularity. In particular, in 2D harmonic problems, the Green's function for a homogeneous plane is:

$$U^0 = -\frac{1}{2\pi} \ln(r), \tag{19}$$

where r is the distance to the point source. It is clear that U^0 tends to infinity with growing r . However, when applying the Fourier method at a finite interval of a length $2A$, a function is assumed periodic with the period $2A$. The fundamental solution for the periodic harmonic potential is:

$$U_{per}^0 = -Re \frac{1}{2\pi} \ln \left(\sin \left(\frac{\pi}{2A} z \right) \right), \tag{20}$$

where $z = x_2 + ix_1$ is the complex coordinate in the system with the origin at the source point.

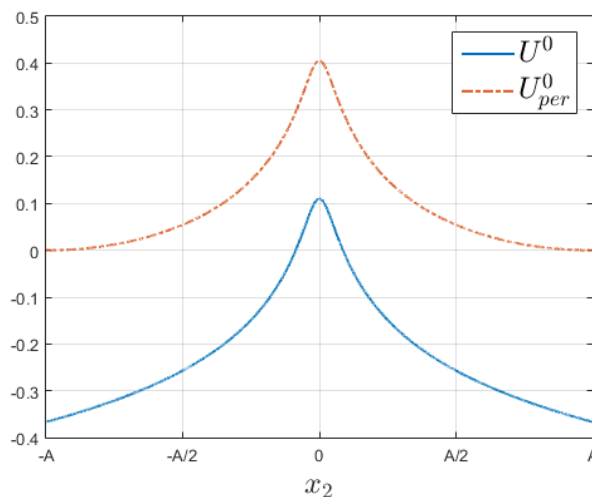


Fig. 3. Graphs of the Green's functions along the x_2 -axis for $\eta = 20, x_1 = d$.

The question arises: which period $2A$ suffices using the Green's function (19) for an infinite plane instead of the Green's function (20) for a periodic (with the period $2A$) problem? Clearly the answer depends on the characteristic size $2d$ of an area where the Green's function is of interest for a problem considered. Introduce the parameter:

$$\eta = \frac{A}{d} \quad (21)$$

Take into account that the potentials are actually defined to arbitrary constants. This can be seen in Fig. 3, presenting the functions U^0 and U_{per}^0 along the x_2 -axis for $\eta = 20$, $x_1 = d$. To exclude the constants, when comparing U^0 with U_{per}^0 , we use the measure ζ , defined as the ratio

$$\zeta = \frac{\max_D |C(x_1, x_2)| - \min_D |C(x_1, x_2)|}{\max_D |C(x_1, x_2)|} \cdot 100\%, \quad (22)$$

where $C(x_1, x_2) = U^0 - U_{per}^0$; D is a square region with the center at the source point and the side $2d$. If $C(x_1, x_2) = const$ in some region, then $\zeta = 0$ in this region. The dependence of ζ on the ratio $\eta = A/d$ is presented in Fig. 4.

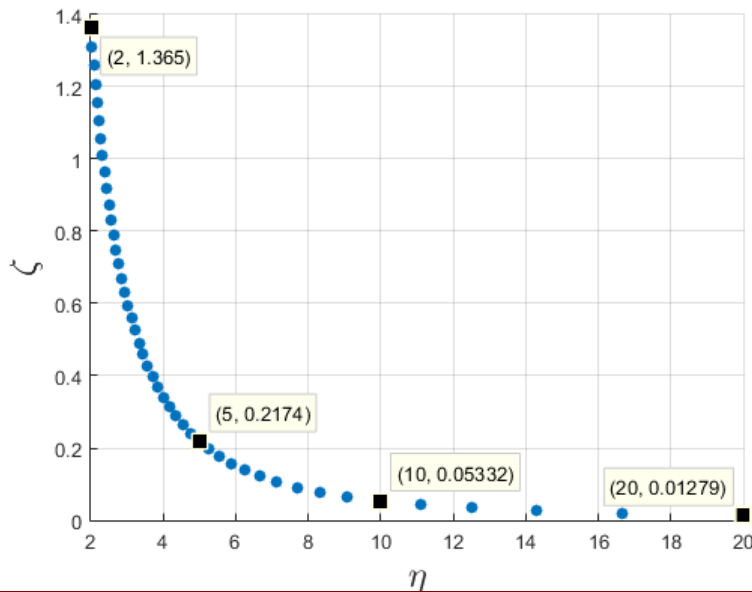


Fig. 4. Dependence of the ratio ζ on the relative period η .

It can be seen that ζ tends to zero when η grows. This confirms that with growing interval of periodicity, its ends exert rapidly decreasing influence on a region with sizes of order d under consideration. To the accuracy of 0.053 percent, the value of η may be set 10 when using the function U^0 instead of U_{per}^0 .

6. Choice of the number of sampling points

There are three plane harmonic problems, for which the Green's functions of log-type have simple analytical forms. They serve us as benchmarks to properly choose the number of sampling points when employing the FFT to find Green's functions for a layered medium. The first problem is that for a *homogeneous* medium with the Green's function given by (19). The second is the problem for a half-plane with *zero flux* at its boundary. It serves to estimate influence of low-permeable (highly compliant in elasticity problems) layers above or/and below a layer with much greater permeability (rigidity). The third problem is for a half-plane with *zero potential* at its boundary. It corresponds to the opposite limiting case and serves to estimate influence of highly-permeable (highly rigid in elasticity problems) layers above or/and below a layer with much less permeability (rigidity).

The two limiting problems provide the thresholds of the accuracy of numerical finding the Green's functions in a region of size $2d$ for various numbers N of sampling points located on various intervals $2A$ of periodicity. The first problem, being intermediate, gives typical accuracy, when neighbors of a layer, containing the source point, have conductivity (rigidity), which does not drastically differs from that of the layer. The tests 1, 2 and 3 below refer, respectively, to the first, second and third problems.

Test 1. Consider two homogeneous half-planes with a package of n homogeneous layers between them. The point source acts in the i -th layer. All layers have the same conductivity and ideal contacts at interfaces. Such a structure is actually a homogeneous isotropic plane. The Green's function for it is given by (19).

As above, distinguish the region of interest as a square D with the center at the source point and the sides $2d$. The accuracy is estimated by the maximum relative error in this region:

$$\xi = \max_D \left[\frac{q_i^a}{q_i^0} \right] \cdot 100\%, \tag{23}$$

where q_i^a is the flux on the i -th boundary, corresponding to the additional function $U^a(x, y)$ in (7); q_i^0 is the flux defined by the exact fundamental solution (19). The errors, found for various numbers N of the sampling points, are summarized in Table 1 when the relative period $\eta = A/d$ increases from 8 to 64. The results, presented in Table 1, are obtained for a particular structure consisting of five layers ($n = 5$); they stay the same for any other number of layers.

Table 1. The relative error (in %) in the region D as a function of N and η for a homogeneous medium

	$N = 128$	$N = 256$	$N = 512$	$N = 1024$
$\eta = 8$	0.605	0.588	0.58	0.576
$\eta = 16$	0.402	0.388	0.382	0.379
$\eta = 32$	0.143	0.134	0.131	0.129
$\eta = 64$	0.104	0.04	0.038	0.037

From Table 1 it can be seen that the influence of the period on the accuracy is notably greater than the influence of the number of sampling points. Better accuracy for large values of η is due to the fact that with growing period $2A$, the influence of its boundaries on the region of interest D rapidly decreases.

Test 2. Consider two half-planes, lower of which has the unit conductivity, while the upper has the conductivity tending to zero. The source point is located in the lower half-plane. We represent each of the half-planes by packages of layers of the same thickness and conductivity and find the additional solution U^a in (7) by solving the problem for the layered system.

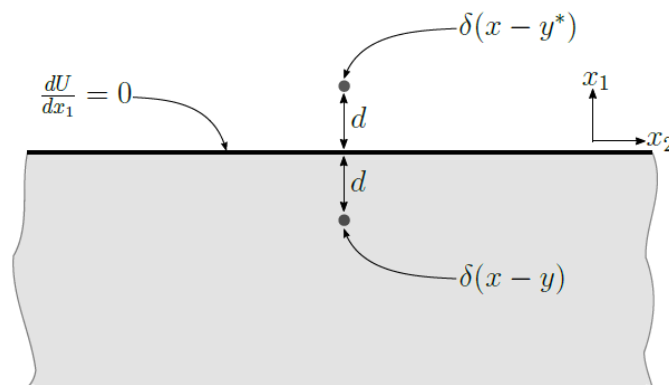


Fig. 5. A point source in a half-space.

For impermeable upper half-plane (Fig. 5), the exact Green's function is the sum of the Green's function (19) for homogenous infinite plane and that of the reflected source, located symmetrically with respect to the boundary and having the same (unit) intensity:

$$U = -\frac{1}{2\pi} \ln(r) - \frac{1}{2\pi} \ln(r^*), \quad (24)$$

where r^* is the distance from the reflected source.

The Green's function, found as a result of numerical calculations, must have the additional term U^a close to the term corresponding to the reflected source. As an error, we consider the maximal relative error in the region D :

$$\xi = \max_D \left[\frac{q_i^a - q_i^*}{q_i^*} \right] \cdot 100\%, \quad (25)$$

where q_i^a is the calculated additional flux on the i -th boundary; q_i^* is the flux corresponding to the reflected source in (24). The values of ξ are summarized in Table 2.

Table 2. The relative error (in %) ($\times 10^{-4}$) in the region D as a function of N and η for a half-space with impermeable boundary.

	$N = 128$	$N = 256$	$N = 512$	$N = 1024$
$\eta = 8$	2.5755	2.575	2.5748	2.5747
$\eta = 16$	2.5703	2.57	2.5698	2.5697
$\eta = 32$	2.5637	2.5635	2.5633	2.5632
$\eta = 64$	2.562	2.561	2.561	2.5609

The data presented in Table 2 show that the error is practically the same for all the considered pairs N and η . It remains on the level of $2.57 \cdot 10^{-4}\%$. Therefore, the case of low-conductive boundary is quite favorable for the accuracy of the method developed.

Test 3. Consider again two half-planes, lower of which has the unit conductivity, while now the upper has the conductivity tending to infinity. In this case, the exact Green's function is obtained by taking the reflected source with opposite sign:

$$U = U^0 + U^* = -\frac{1}{2\pi} \ln(r) + \frac{1}{2\pi} \ln(r^*) \quad (26)$$

We again use equation (25) to estimate errors. The relative errors are summarized in Table 3.

Table 3. The relative error (in%) in the region D as a function of N and η for a half-space with a highly conductive boundary.

	$N = 128$	$N = 256$	$N = 512$	$N = 1024$
$\eta = 8$	1.212	1.177	1.16	1.152
$\eta = 16$	0.804	0.777	0.764	0.758
$\eta = 32$	0.286	0.269	0.261	0.257
$\eta = 64$	0.21	0.08	0.076	0.074

From the table it follows that for highly permeable boundary, the error is merely two-fold greater than that for the first problem. In the both cases, to improve the accuracy, it looks preferable to increase the interval of periodicity rather than the number of sampling points.

The comparison of the results in Tables 1, 2 and 3 for the cases 1, 2, and 3, respectively, shows that, as could be expected, the case 1 is intermediate between the two limiting. Still, the results for the case 1 are closer to those for the case 3.

7. Application of the method to a harmonic boundary value problem

Consider an example of building and using the harmonic Green's function for a plane layered system. The j -th layer contains a cavity with the contour L_s (Fig. 6). The region of interest D includes the parts by D_s and D^* , which are respectively inside and outside the cavity. The contour L_s is travelled in the direction which leaves the area D^* to the left; the normal n is directed to the right to this direction. The superscript plus (minus) refers to the limit from the side with respect to which the normal is outward (inward). The flux q_n^0 is assigned on the counter L_s . The problem consists of finding the potential u in the region D^* .

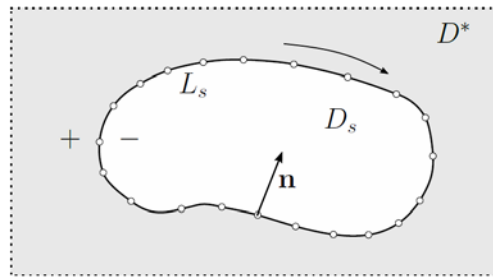


Fig. 6. The geometric scheme for a cavity in layered structure.

To find the solution, we need to build the Green's functions U_* and Q_* entering the complex boundary integral equations (C-BIE) for plane harmonic problems [8]:

$$Re \left\{ -\frac{1}{2\pi} \int_{L_s} [q_n^+(\tau)U(\tau - z)ds + u^+(\tau)Q(\tau - z)d\tau] \right\} = \begin{cases} ku(z), & z \in D^* \\ \frac{1}{2}\kappa^+u^+, & z \in L_s, \\ 0, & z \notin D^* + L_s \end{cases} \quad (27)$$

where τ, z are coordinates in the complex plane; $q_n^+ = q_n^0$ is the assigned flux. When having U and Q the solution to the BIE, given in the second line of (27), is found by the BEM. Having it, the first line of (27) provides the flux within the region D^* .

We built the Green's functions U and Q by the method described in Sec. 3 and 4. Specifically, they are represented as the sums of known Green's functions and additional functions $U^a(\tau, z)$ and $Q^a(\tau, z)$:

$$U = \ln(\tau - z) + U^a(\tau, z); \quad Q = i \frac{\kappa^+}{\tau - z} + Q^a(\tau, z) \quad (28)$$

The parameters of the FFT transform are chosen in accordance with estimates of Sec. 4 and 5. Standard translations along the x_2 -axis are used to adjust the images, obtained for point sources in the local system with the origin at a source point, to the global system used in the BIE (27).

8. Example of circular cavity in a layered structure

Assume that there is a circular cavity of the radius $R \leq h_d$ within the second layer of a three-layered structure. The flux q_n^0 is constant on the boundary of the cavity. The geometrical and physical parameters used for calculations are:

- Half-heights of the layers: $h_1 = h_3 = 2h_2$
- Conductivities of the layers: $\kappa_1 = 25\kappa_2, \kappa_3 = 2\kappa_2$
- The period $2A$ of the interval assumed in FFT: $2A = 40h_2$
- The number of sampling points of the FFT: $N = 1024$
- The number of boundary elements on the cavity contour: $N_s = 90$
- The total intensity of the assigned flux $\int_{L_s} q_n^0 ds = -1$

The results of calculations of the potential in the layered system with cavities of different radii are presented in Fig.7-10.

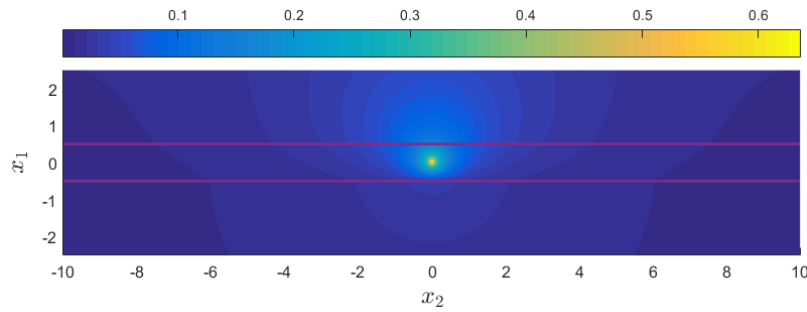


Fig. 7. The field of the potential for a circular cavity of radius $R = 10^{-4}h_2$.

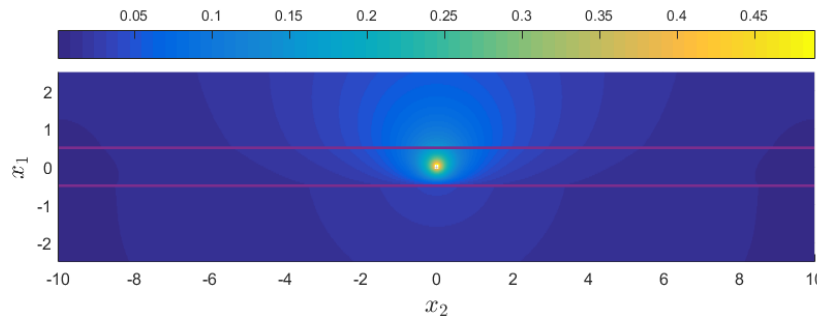


Fig. 8. The field of the potential for a circular cavity of radius $R = 0.1h_2$.

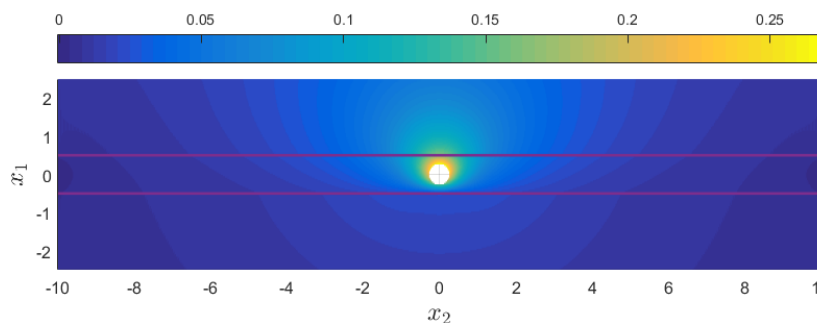


Fig. 9. The field of the potential for a circular cavity of radius $R = 0.5h_2$.

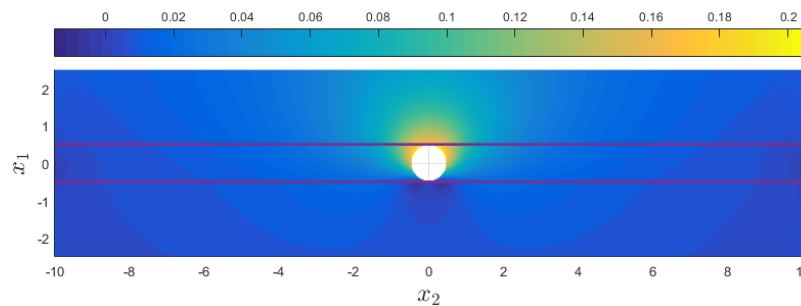


Fig. 10. The field of the potential for a circular cavity of radius $R = 0.9h_2$.

The results demonstrate that the method developed may serve for efficient solving harmonic and elasticity problems for layers with quite different thicknesses and physical properties.

Acknowledgement. This research was financed by Ministry of Education and Science of the Russian Federation within the framework of the Federal Program "Research and development in priority areas for the development of the scientific and technological complex of Russia for 2014-2020", Activity 1.2., Agreement on Grant No. 14.575.21.0146 of 26 September, 2017, unique identifier: RFMEFI57517X0146.

References

- [1] M. Al Heib, A. M. Linkov, V. V. Zoubkov, In: *International Symposium of the International Society for Rock Mechanics (EUROCK 2001)*, ed. by Sarkka & Floranta (Swets&Zeitinger Lisse, Espoo, 2001), 795.
- [2] F. G. Benitez, L. Lu, A. J. Rosakis // *Int. J. for Numerical Methods in Engineering*, **36** (1993) 3097.
- [3] C.A. Brebbia, J.C.F. Telles, L.C. Wrobel // *Journal of Applied Mathematics and Mechanics*, **65** (1984) 259.
- [4] H. Buffler // *Ingenieur-archiv*, **30** (1961) 417.
- [5] H. Buffler // *Ingenieur-archiv*, **31** (1962) 229.
- [6] H. Buffler // *Journal of Elasticity*, **1** (1971) 125.
- [7] S.L. Crouch, A.M. Starfield, *Boundary Element Method in Solid Mechanics* (Cambridge University Press, Cambridge, 1983).
- [8] A.A. Dobroskok, A.M. Linkov // *Journal of Applied Mathematics and Mechanics*, **73** (2009) 313.
- [9] S.K. Godunov, V.S. Ryabenkii, *Difference Schemes* (North Holland, 1987).
- [10] A.M. Linkov, N.A. Filippov // *Meccanica*, **26** (1991) 195.
- [11] A.M. Linkov, A.A. Linkova, A.A. Savitski // *International Journal of Damage Mechanics*, **3** (1994) 338.
- [12] A.M. Linkov, N.A. Filippov, L.A. Milova, V.V. Zoubkov, In: *Advances in Rock Mechanics*, ed. by Yunmei Lin (USA-World Scientific Publications Co, New York, 1998), 135.
- [13] A.M. Linkov, V.V. Zoubkov, M. Sylla, M. al Heib, *Spectral BEM for multi-layered media with cracks or/and openings*. (IABEM 2000 Symposium, Brescia, Italy) 141.
- [14] A.M. Linkov, V.V. Zoubkov, In: *Proceedings of the XIX International Conference BEM & FEM-2001*, ed. by V.A. Postnov (St. Petersburg, 2001), 236 (in Russian).
- [15] G. Maier, G. Novati, In: *Proceedings of the 7th Intrnat. Conf. on Boundary Elements in Engineering* (Como, 1985), 1.
- [16] G. Maier, G. Novati // *Engineering Analysis*, **3** (1986) 208.
- [17] G. Maier, G. Novati // *International Journal for Numerical and Analytical Methods in Geomechanics*, **11** (1987) 435.
- [18] V.S. Nikishin, G.S. Shapiro, *Problems of Elasticity Theory for Multi-layered Media* (Nauka, Moscow, 1973) (in Russian).
- [19] E.I. Obolashvili, *Fourier Transform and its Application in the Theory of Elasticity* (Tbilici, Metcierba, 1979) (in Russian).
- [20] A.P. Peirce, E. Siebrits // *Comput. Methods Appl. Mech. Engrg.* **190** (2001) 5935.
- [21] A.P. Peirce, E. Siebrits // *International Journal of Fracture*, **110** (2001) 205.
- [22] R.M. Ruppoport // Proc. Hydrotechnical Institute, Leningrad (1963) 3 (in Russian).
- [23] R.M. Ruppoport // Proc. Hydrotechnical Institute, Leningrad (1966) 149 (in Russian).
- [24] A.A. Samarskii, E.S. Nikolaev, *Numerical Methods for Grid Equations* (Nauka, Moscow, 1978).
- [25] A.A. Samarskii, A.V. Gulin, *Numerical Methods* (Nauka, Moscow, 1989).
- [26] U.A. Shevliakov, *Matrix Algorithms in the Theory of Elasticity for Inhomogeneous Media* (Visha Shcola, Kiev-Odessa, 1977) (in Russian).
- [27]. E. Siebrits, A.P. Peirce // *Int. J. Numer. Meth. Engng.* **53** (2002) 691.
- [28] I.E. Vigdorovich, V.D. Lamziuk, A.K. Privarnikov // *Reports of Ukrainian Acad. Sci.*, A (6) (1979) 434 (in Russian).
- [29] L.J. Wardle, *Stress Analysis of Multilayered Anisotropic Elastic Systems Subject to Rectangular Loads* (CSIRO Institute of Earth Resources, Melbourne, 1980).

COPPER CRYSTALS WITH FRAGMENTED STRUCTURE AND DEVELOPED SURFACE IN TEMPERATURE FIELDS

N.N. Gryzunova^{1*}, A.A. Vikarchuk¹, A.M. Gryzunov¹, A.E. Romanov^{1,2}

¹Togliatti State University, Belorusskaya str. 14, Togliatti, 445020, Russian Federation

²ITMO University, Kronverkskiy pr. 49, St. Petersburg, 197101, Russian Federation

*e-mail: gryzunova-natalja@yandex.ru

Abstract. The effect of electrodeposition regimes of copper polycrystalline foils and coatings on their structure, morphology and behavior during subsequent heat treatment is studied. Electrodeposition is carried out with simultaneous mechanical activation of the surface of foils and coatings, which leads both to the materials internal structural changes and to the appearance of features of the surface morphology: the specific faceting of growth terrains, the formation of polyatomic growth steps, and the appearance of crystals (grains) with pentagonal symmetry. The results of changes in the morphology, structure and phase composition of the polycrystalline copper obtained during the heat treatment in oxidizing or inert atmospheres are presented.

Keywords: electrodeposition; copper polycrystalline foils; structure; morphology.

1. Introduction

Materials based on metals with a developed surface are widely used as catalysts in the gas processing, petrochemical and chemical industries, as well as in solving various problems in the field of ecology [1-3]. The main goal of creating such materials is to obtain particles, microcrystals, granules, layers, foils and coatings with the maximum possible specific surface; it is believed that the catalytic activity of metallic materials is mainly determined by chemical reactions on their surfaces [1, 4-6]. There is another conception [7, 8], based on the fact that the catalytic activity of metallic materials is determined not only by their specific surface, but also strongly depends on the internal structure of the material and the features of the morphology of its surface.

The latter concept has not yet been realized, firstly, because of the difficulties in manufacturing catalysts with preferential development of certain morphological features of the surface, i.e. faces, edges and vertices with given crystallography and growth steps with specific geometry; secondly, because of the thermal instability of these morphological features of the surface in the course of catalytic processes. Still, the development of this direction for creating new catalysts is very promising. To do this, metal materials with a specific surface structure should be used to carry out catalytic reactions at relatively low temperatures, in which the processes of surface morphology reconstruction proceed very slowly, so that the non-equilibrium surface structures remain relatively stable.

In this paper, we investigate the effect of the regimes for producing polycrystalline copper foils on their structure, morphology, and behavior in temperature fields. The interrelation between defects of disclination type of growth origin in crystals with features of their morphology, such as the presence of pentagonal symmetry, specific faceting and the formation of terraces and polyatomic steps of growth, is shown. The results of studies of the evolution of

the morphology, structure and phase composition of copper foils subjected to the heat treatment in oxidizing and inert atmospheres are presented. The dependence of the stored elastic energy and the temperature of its relaxation on the presence of high-energy disclination defects is discussed.

2. Methods of materials preparation and characterization

The foils under investigation were fabricated by electrodeposition of copper exploring the author's method [9-10]. Electrodeposition was carried out on stainless steel plates using mechanical activation of the growing crystals with abrasive microparticles suspended in the electrolyte [9-10]. Activation was applied either at the initial stage of electrocrystallization or periodically, in particular, three minutes with stirring of the electrolyte and three minutes without stirring. The purpose of surface activation was to create high-energy defects in the crystalline structure, to form so-called fragmented structures, and, as a result, to produce copper polycrystalline foils with developed surface and specific morphological features, such as the pentagonal symmetry of individual grains, the specific crystallography of faceting, and with of polyatomic growth terraces.

For a comparative analysis of the samples, copper foils were grown by electrodeposition with and without mechanical activation of the cathode.

Changes in the surface morphology and crystal structure before and after heat treatment were observed using electron microscopes Carl Zeiss Sigma and JEOL JCM 6000.

Calorimetric experiments were performed on the differential scanning calorimeter HITACHI EXTARX-DSC 7000. The investigations were carried out in the temperature range from 25 to 700 °C with a heating rate of 10 deg / min and a gas flow rate of 50 ml / min.

To study the evolution of the morphology of the surface of crystals with defects in temperature fields, disks with a mass of 5.7-6.7 mg were cut out from electrodeposited copper foils. The temperature studies were carried out both in the oxidizing (oxygen) and in the inert (nitrogen) atmospheres.

3. Results of experiments and discussion

Microscopic studies of the surface of copper obtained with mechanical activation of the cathode (Fig. 1) showed the appearance of the following features: pentagonal pyramids (PPs) (Fig. 1a), cone-shaped crystals (CCs) with high (polyatomic) growth steps (Fig. 1b), as well as crystals containing defects of the disclination type – defective crystals (DCs) (Fig. 1c).

Pentagonal pyramids (PPs) and CCs (Figs. 1a,b) were found in samples subjected to mechanical activation at the initial stage of electrodeposition, and coatings with the DCs (Fig. 1c) were obtained by periodically stirring the electrolyte with the particles during electrocrystallization. In our opinion, the mechanical activation of crystals growing in the process of electrodeposition promotes the formation of disclination defects [11-12], which in turn determine the features of the morphology of foils (Fig. 1). To confirm this idea, structural studies of PPs (Fig. 1a) and CCs with a stepped structure (Fig. 1b), and DCs with a developed surface (Fig. 1c) were carried out.

Electron microscopic studies of PPs formed during electrodeposition under cathode activation conditions (Fig. 1a) showed that they grow in the direction of $\langle 110 \rangle$ -type and have a fragmented/twin structure, possess fifth-order symmetry axes (Figs. 1a and 2a). In addition, PPs' interior were separated by twin boundaries into five main parts (sectors) containing a high concentration of twin lamella of $\{111\} \langle 112 \rangle$ -type, parallel to the boundaries of the parts (Fig. 2a).

The conical crystals (CCs) (Fig. 1b) also grow in the direction of $\langle 110 \rangle$ -type. They are separated by the high-angle grain boundaries of growth origin into fragments, contain a high concentration of twin lamella (Fig. 2b), but do not have fifth-order symmetry axes and the common twinning center. The main structural elements of such crystals are twins whose height

and width correlate with the growth steps on the surface of the crystal. The presence of the twin boundaries separating the fragments in the PPs and CCs and the high concentration of twin lamella testifies the manifestation of the relaxation processes even during electrodeposition. The fragmented/twin initial structure of these crystals, the presence of twin lamella, and disclination-type defects (Figs. 2a,c) are the reason for the formation of the developed surface in the form of polyatomic growth steps (Figs. 1a,b) with certain crystallographic planes, mainly of $\{111\}$ - and $\{110\}$ -type. The shape of the crystals is related to the features of the electrodeposition process.

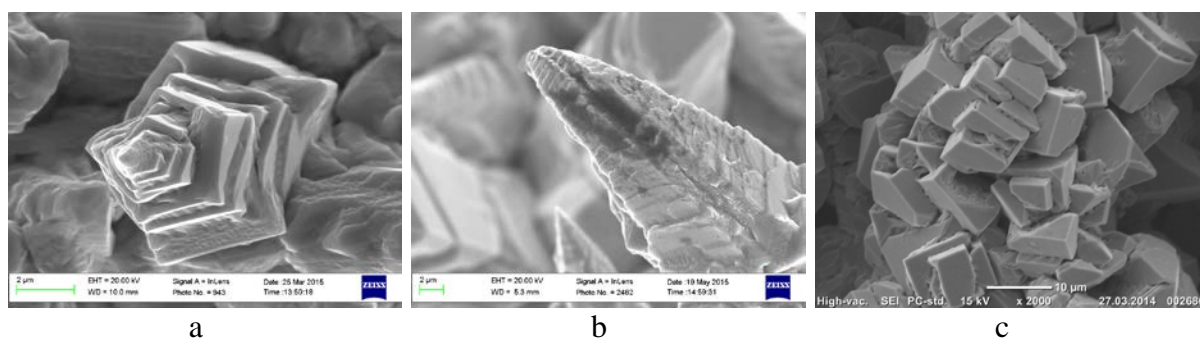


Fig. 1. Morphology of crystals and coatings obtained by electrodeposition using mechanical activation: a) pentagonal pyramids (PPs); b) cone-shaped crystals (CCs), which have polyatomic growth stages; c) coatings with a developed surface of defective crystals (DCs).

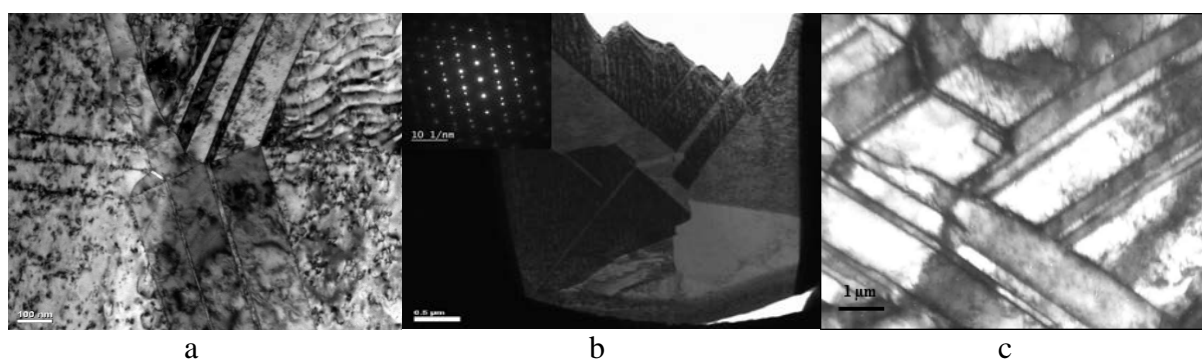


Fig. 2. Electron microscopic images of copper crystals grown by electrodeposition using mechanical activation: a) pentagonal pyramids (PPs); b) conical crystals (CCs) with twinned structure; c) defective crystals (DCs) with a fragmented structure.

In case mechanical activation of the deposited foils with abrasive microparticles was carried out periodically, the materials with a developed surface in the form of terraces and polyatomic growth steps (Fig. 1c), consisting of relatively large but defective crystals (DCs) (Fig. 2c) can form. Electron microscopic studies of DCs showed that they have nonequilibrium dislocation-disclination structure, contain twins, dislocation and high-angle grain boundaries, including broken ones. They demonstrate characteristic mesoscale (0.1-1.0 μm) of structural elements, i.e. misorientation bands, twin lamella and fragments (Fig. 2c). Usually, such fragmented structures can be formed at the large plastic deformations [13]. In our case, they appear in electrodeposited metal subjected to *in situ* mechanical activation (Fig. 2c). All defects of the dislocation-disclination type are, as it can be seen from the extinction contours (Fig. 2c), powerful sources of long-range internal stress fields.

Electron microscope studies of foils and coatings grown without the mechanical activation showed that such samples have a relatively smooth surfaces, consist of crystals with a block sub-structure (Fig. 3), and do not have the above-mentioned morphological features

(Fig. 3a,b). The most commonly observed defects are multilayered dislocation boundaries (Fig. 3b) and deformation twins of $\{111\}\langle 112 \rangle$ -type. The dislocation boundaries separating grains into blocks (Fig. 3b) are non-equilibrium and create long-range stress fields [14]. This is because their formation during electrodeposition occurred at room temperatures, i.e. in conditions, when dislocation climb is limited.

The results of the experiments allows one to say, that the mechanical activation of crystals growing in the process of electrodeposition causes the formation of fragmented structures with high-energy disclination defects. The exit of twin lamella, fragments and misorientation bands on the crystal surface led to the formation to a specific microrelief. The height of microrelief correlates with the size of the structural elements. Using mechanical activation of growing crystals we have created favorable conditions for the formation of disclination-type defects, controlled the appearance of high-energy fragmented structures and, as a result, provided developed surface (Fig. 1).

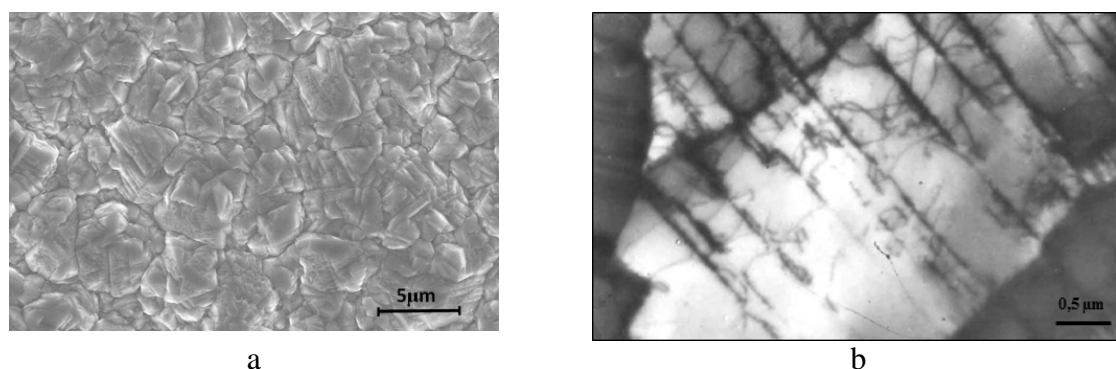


Fig. 3. Surface morphology (a) and electron microscopic image (b) of copper electrodeposited without mechanoactivation.

In our opinion, foils consisting mainly of defective crystals with fragmented structures and showing polyatomic growth steps (Fig. 1 and 2) have large stored elastic energy that should relax in temperature fields. A crystal growing in the process of electrodeposition is an open thermodynamic system, as it exchanges energy and matter with the surrounding medium. In the final state, its volume does not change, external stresses are absent, and internal stresses due to structural defects are the driving force for the system to return to an equilibrium. In the temperature field (T_{ann}), the relaxation processes are realized, in such way that the energy leaving the open system (crystal) $\Delta Q = T\Delta S_{str}$ should be maximum, where ΔS_{str} is the structural entropy. Structural entropy is a measure of the disequilibrium of open systems, including the presence of internal stresses due to defects of crystalline structure [15]. The structural entropy can be related to the energy released when annealing the defective crystals.

To confirm this idea, we applied the heat treatment in a differential scanning calorimeter (DSC) to copper foils of two types: (i) electrodeposited without mechanical activation (Fig. 3a) and (ii) electrodeposited applying mechanical activation (Figs. 1, 2). Earlier, we used a similar method to study structural changes in electrodeposited nickel coatings subjected to the heat treatment [16].

Calorimetric studies in oxygen showed that on thermograms of foils grown without mechanical activation (Fig. 3a), two discretely located exothermic peaks can be observed (Fig. 4a). The first clear peak appeared at temperatures 350-413 °C, the second weak peak – at 500-580 °C. For the foils grown with mechanical activation (Fig. 1), a diffuse exothermic peak was also observed at 220 °C. It decreases at approximately 360 °C (Fig. 4b). More significant peak was found at approximately the same temperatures (500-580 °C) as for the foils without mechanical activation. We associate the exothermic peaks on thermograms not only with the

phase transformations that occur during the oxidation of copper in oxygen (Fig. 5), but also with the simultaneous occurrence of other processes in the investigated temperature range.

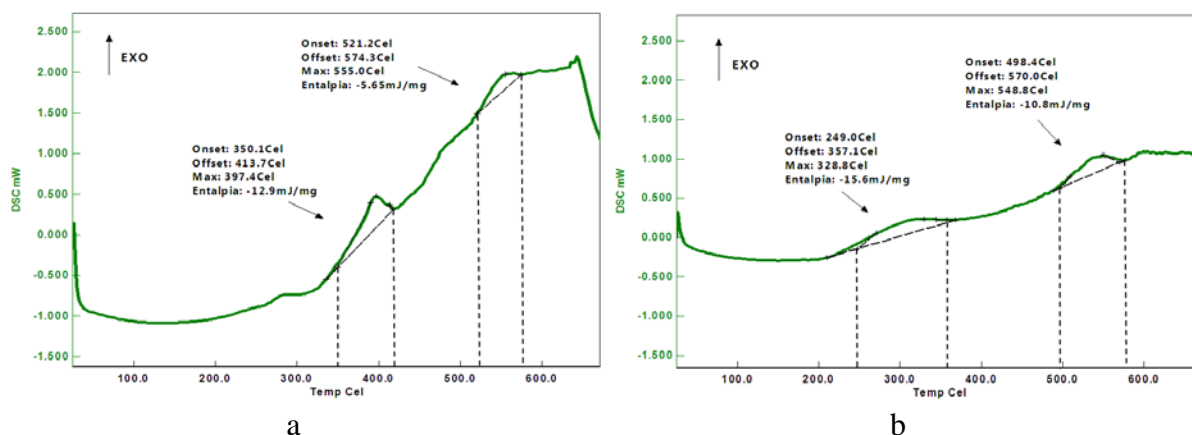


Fig. 4. Thermograms after heating of copper films in oxygen: a) foil electrodeposited without mechanical activation; b) foil grown with mechanical activation.

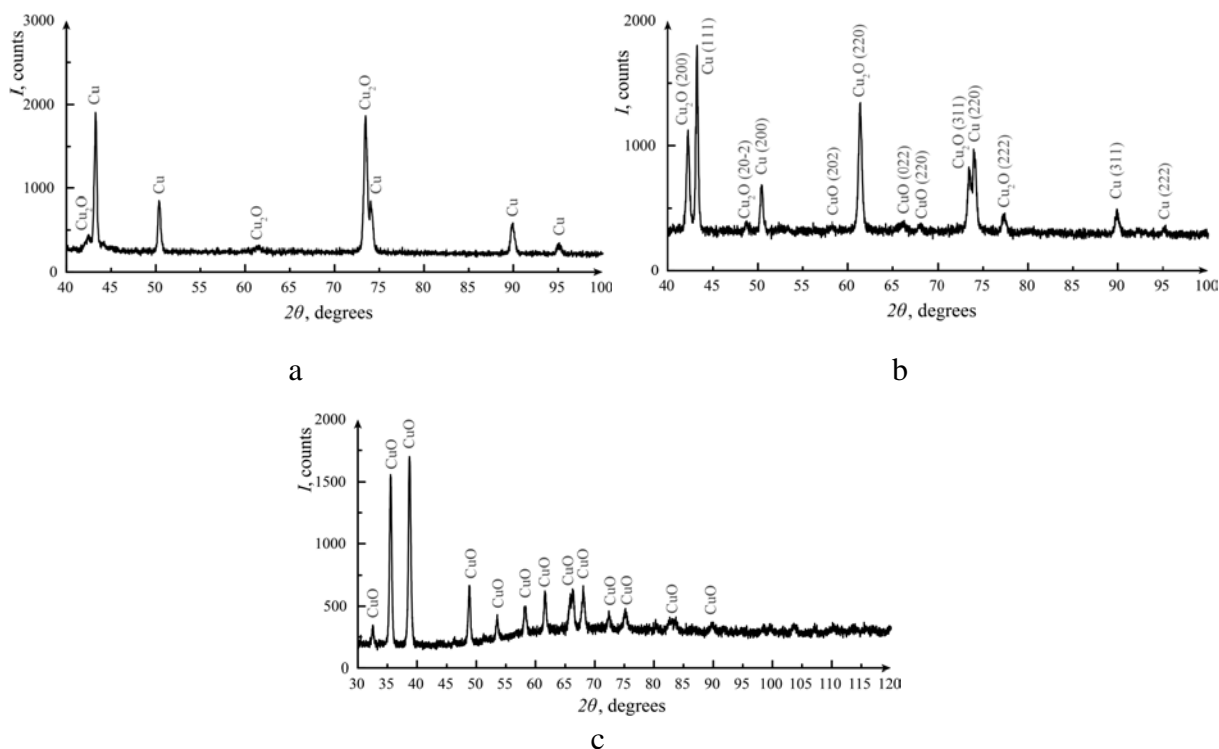


Fig. 5. X-ray patterns for copper foils heated in DSC in oxygen to a temperature of 300 °C (a), to a temperature of 400 °C (b), and to a temperature of 600 °C (c).

X-ray phase studies (Fig. 5) and thermograms of the samples indicated that the surface layers of copper undergoes two successive phase transformations during oxidation: first, copper is oxidized to copper oxide Cu₂O (I), then copper oxide (I) transforms into copper oxide CuO (II). Copper oxidation processes occur unevenly, their rates increase in some temperature intervals, and they are accompanied by the heat release (Fig. 4).

The change in the enthalpy (ΔH) determined from the DSC curves (Fig. 4), for foils of two types turned out to be different. For foils grown without the mechanical activation, these changes at temperatures 350-413 °C and 500-580 °C are 12.9 kJ / kg and 5.65 kJ / kg, respectively. For foils grown using mechanical activation, the change in enthalpy ΔH at

temperatures of 220-360 °C is 15.6 kJ / kg, and at temperatures of 500-580 °C it is 10.8 kJ / kg. At temperatures about 0.5 T_{melt} of copper, in foils consisting of microcrystals with pentagonal symmetry (PPs), CCs with high growth steps, and DCs the enthalpy change is larger.

The difference in the enthalpy change and the shift in the peaks (Fig. 4) indicate that in the addition to intense oxidation during the heating of copper foils, relaxation processes are also realized, probably due to the presence in the material of a high concentration of crystalline defects of growth origin (Figs. 2, 3b).

To test this hypothesis, we analyzed in details the change in the morphology of the surface of copper foils grown with mechanical activation before and after calorimetric studies, see Fig. 6. Microscopic investigation of the surface of foils and crystals in them showed that during the oxidation of copper at temperatures about 600 °C, whiskers and a significant concentration of surface pores can be observed (Fig. 6b). An analysis of changes in the morphology of the surfaces of PPs and CCs, which have high growth steps, made it possible to detect partial smoothing of the lateral faces of the pyramids and cones (Fig. 6b). Smoothing was more noticeable for steps of lower depth and height.

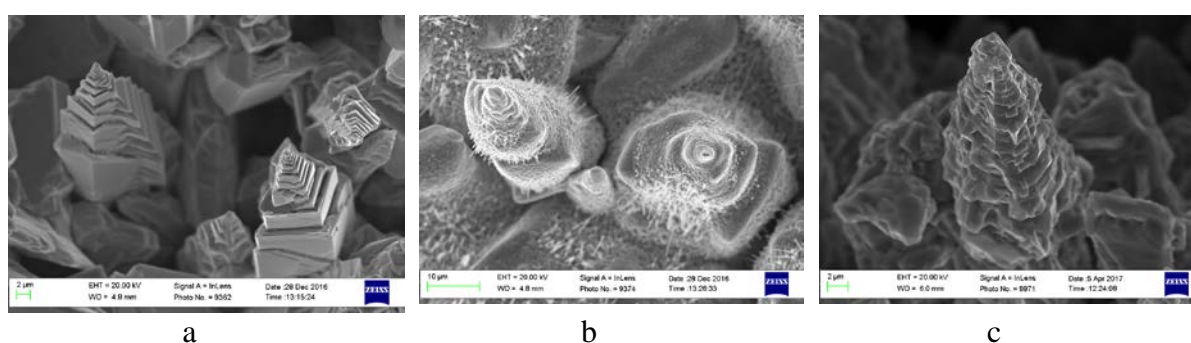


Fig. 6. SEM photomicrographs of copper electrodeposited in a mode with mechanical activation. Surface morphology: a) initial; b) after heating to 600 °C in oxygen; c) after heating to 600 °C in nitrogen.

Exoeffects fixed by DSC thermograms (Fig. 4 and Fig. 7) indicate the operation of several processes simultaneously occurring in temperature range 250-600 °C. Processes that cannot occur in a vacuum or an inert atmosphere realized in temperature fields and an oxygen-containing medium. The heat release in copper samples during annealing in the oxygen-containing atmosphere is associated with phase and structural transformations. In particular, such transformations include the formation of copper oxides Cu_2O and CuO , surface nanopores, and growth of CuO nanowhiskers [17-19]; the fusion of growth steps, the formation of internal cavities, degradation of defects in the crystalline structure, evolution of the initial dislocation and disclination-fragmented structures formed during electrocrystallization (Fig. 2 and Fig. 3b).

Calorimetric studies carried out in an inert medium (nitrogen) allowed us to confirm this assumption (Fig. 7). In contrast to studies of foils annealed in oxygen, for foils without mechanical activation, one insignificant peak was observed on thermograms at temperatures of 300-400 °C (Fig. 7a), and for foils with mechanical activation two different exothermic peaks significantly spaced from each other on the temperature scale, were observed (Fig. 7b). Both peaks were accompanied by a significant change in the enthalpy $\sim 10\text{-}15$ kJ/kg (Fig. 7b), which is not associated with the oxidative processes in copper. In our opinion, during the heating process, the annealing of low-energy defects of growth origin in the sample occurred (Fig. 3b) and this causes the appearance of the first of the exothermic peaks on the heating curves (Fig. 7). The temperature of the peak depends on the concentration and types of defects. In samples of copper foils grown with mechanical activation (Fig. 1) and without activation (Fig. 3) low-energy defects of growth origin and nonequilibrium dislocation substructures are formed (Figs. 2 and 3), which are easily annealed (the first peak) in the temperature interval 250 °C -

450 °C (Figs. 4 and 7). In the same temperature range, the growth steps are "smoothed" on crystals with a developed surface, when annealing occurs both in oxygen and in nitrogen (Figs. 4, 6, and 7). This can be caused not only by an increase in the mobility of surface atoms in temperature fields, but also by high internal stresses concentrated in the vertices and edges of the crystals. At the same temperatures, the disruption of nonequilibrium dislocation substructures begins in copper [10, 12, 13], the number of structural defects, formed during electrocrystallization, decreases, the grain size changes and the surface of the foils is transformed.

The presence of a second exothermic peak on the thermogram, shown in Fig. 7b, in the case of annealing of crystals with a fragmented structure, is probably associated with the relaxation of long-range internal stresses due to disclination defects, the stabilization of nonequilibrium high-energy structures, and the change in the shape of the crystals. An estimate of the internal stresses with the help of the heat released during the relaxation process using the technique proposed in [15] gives a value of the order of 30 MPa, which is close to the yield point of copper. Estimation of internal stresses with the help of lattice distortions also gives the value of the same order.

Summarizing the calorimetric data obtained in the study of copper polycrystalline foils heat-treated in different media, X-ray phase analysis and microscopy data (Fig. 6c), it can be said that high-energy defects are formed in copper materials obtained by electrodeposition with mechanical activation. These defects are disclination-type defects, which generate long-range elastic fields and, as a result, are the cause of the considerable elastic energy stored in the bulk of crystals. The relaxation of elastic fields is carried out both in an inert medium and in oxygen, but the relaxation mechanisms, which determines the final structure and affects the morphology of the foil surface after annealing, can be different.

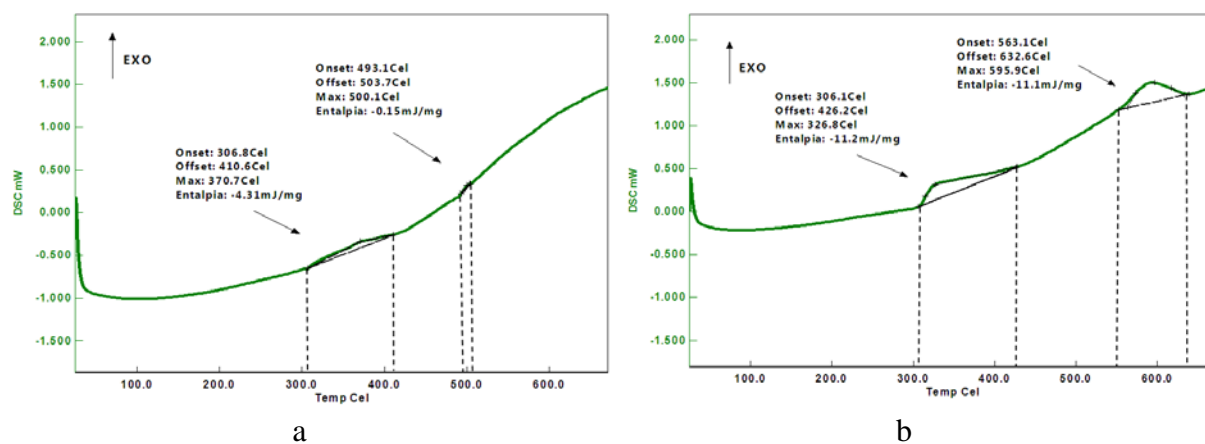


Fig. 7. Thermograms of electrodeposited copper foils annealed in nitrogen at temperatures up to 700 °C: a) without mechanical activation; b) with mechanical activation.

4. Conclusion

We have demonstrated that mechanical activation of the cathode by abrasive particles causes the formation in electrodeposited copper polycrystalline foils and coatings the high-energy disclination-type defects, crystals possessing the fifth order symmetry axes, and developed surface with polyatomic growth steps.

It has been shown that the presence of defects creating long-range elastic fields and therefore providing a large stored elastic energy, contributes and intensifies various relaxation processes in studied copper crystals. Analysis of thermograms of copper foils, X-ray diffraction and microscopic studies showed that exothermic peaks in 250-600 °C range are associated with phase and structural transformations, i.e. with copper oxidation, with formation of

nanowhiskers and nanopores on the surface of crystals, surface restructuring, annealing of low-energy defects and transformation of high-energy defects, stabilization of nonequilibrium dislocation-disclination structures that formed in the process of electrodeposition.

Acknowledgment. The work was supported by the Ministry of Education and Science of Russian Federation, state task No. 16.2314.2017/4.6.

References

- [1] G.K. Boreskov, *Heterogeneous catalysis* (“Science”, Moscow, 1988). (In Russian).
- [2] I.V. Mishakov, V.A. Likholobov, *Introduction to catalysis. Textbook for students of Universities* (NGU,Novosibirsk, 2015). (In Russian).
- [3] A.G. Balandina, R.N. Jangildin, V.A. Martynov // *Bashkir Chemical Journal* **22(3)** (2015) 31 (In Russian).
- [4] D.G. Yakhvarov, E.A. Trofimova, I.H. Rizvanov, O.S. Fomin, O.G. Sinyashin // *Electrochemistry* **10** (2011) 1180. (In Russian).
- [5] L.P. Didenko, A.M. Kolesnikov, M.S. Voronetsky, V.I. Savchenko, I.A. Domashnev, L.A. Sementsov // *Catalysis in the chemical and petrochemical industries* **2011(2)** (2011) 7. (In Russian).
- [6] V.V. Boldyrev // *Soros Educational Journal* **5** (1996) 49. (In Russian).
- [7] K.A. Dadayan, G.K. Boreskov, V.I. Savchenko, N.N. Bulgakov, M.D. Smolikov // *Proceedings of the USSR Academy of Sciences* **239**(1978) 356. (In Russian).
- [8] G.A. Somorjai, *The Physical Basis for Heterogeneous Catalysis* (Plenum-Press, N.Y., 1975).
- [9] N.N. Gryzunova, A.A. Vikarchuk, V.V. Bekin, A.E. Romanov // *Bulletin of the Russian Academy of Sciences: Physics* **79(9)** (2015) 1093. (In Russian).
- [10] N.N. Gryzunova, A.A. Vikarchuk, M.N. Tyur'kov // *Russian Metallurgy (Metally)* **2016(10)** (2016) 924. (In Russian).
- [11] V.I. Vladimirov, A.E. Romanov *Disclinations in crystals* (“Science”, Leningrad, 1986). (In Russian).
- [12] V.G. Gryaznov, J. Heidenreich, A.M. Kaprelov, S.A. Nepijko, A.E. Romanov, J. Urban // *Crystal Research and Technology* **34** (1999) 1091.
- [13] V.V. Rybin, *Large plastic deformation and fracture of metals* (“Metallurgy”, Moscow, 1986). (In Russian).
- [14] I.S. Yasnikov, A.A. Vikarchuk // *Metal Science and Heat Treatment* **49(3-4)** (2007) 97.
- [15] N.G. Kolbasnikov, S.Y. Kondrat'ev *Structure. Entropy. Phase transformations and properties of metals* (“Science”, Saint Petersburg, 2006). (In Russian).
- [16] N.N. Gryzunova, A.A. Vikarchuk, M.R. Shafeev, A.E. Romanov // *Materials Physics and Mechanics* **21(2)** (2014) 119. (In Russian).
- [17] A.A. Vikarchuk, M.V. Dorogov // *JETP Letters* **97** (2013) 594. (In Russian).
- [18] A.N. Abramova, M.V. Dorogov, S. Vlassov, I. Kink, L.M. Dorogin, R. Löhmus, A.E. Романов, A.A. Vikarchuk // *Materials Physics and Mechanics* **19(1)** (2014) 88. (In Russian).
- [19] N.N. Gryzunova, A.G. Denisova, I.S. Yasnikov, A.A. Vikarchuk // *Russian Journal of Electrochemistry* **51(12)** (2015) 1176. (In Russian).

SHOCK-INDUCED STRUCTURAL INSTABILITIES AND SPALL-STRENGTH OF MARAGING STEELS

Yu.I. Mescheryakov*, N.I. Zhigacheva, A.K. Divakov, Yu.A. Petrov

Institute of Problems of Mechanical Engineering, Bolshoi 61, V.O., Saint Petersburg, 199178, Russia

*e-mail: ym38@mail.ru

Abstract. The shock-induced structural instability for three kinds of maraging steel is studied with two experimental techniques: Taylor technique and uniaxial strain conditions. Spall strength of steels is shown to be determined by the structural instability threshold under compression at the front of compressive pulse. Microstructure investigation of post-shocked specimens show that structural instability of maraging steel results from two factors: (i) disintegration of strengthen phase created in the process of aging of steel and (ii) shock-induced nucleation of localized austenite inclusions responsible for decrease of yield stress and fragmentation. Dynamic fracture of maraging steels is found to occur along the boundaries between shock-induced austenite laths and rest of the matrix.

Keywords: shock loading; structural instability; austenite; intermetallide; spallation.

1. Introduction

Spall fracture of material is known to be a result of interference of release waves propagating from rear surfaces of impactor and target. A common thread is that spall-strength is a characteristic of tensile strength of material at the microsecond region of dynamic loading. In reality, however, the spall strength sensitively depends on the processes flowing at the front and plateau of compressive pulse. Preliminary compression of material at the front and plateau of compressive pulse can change the structural state of material compared to its initial state. If the strain rate achieves a critical value, the irreversible structural changes of solid occur which affect the dynamic strength of material. The structural instability can be considered as a strain-rate dependent structural transition by means of which the shock self-consistently establishes the scale features of deformed medium.

The objective of paper is to establish the coupling between structural instability threshold and dynamic strength of maraging steels.

2. Experimental technique and materials

Shock tests of materials were performed with two experimental techniques. The first technique implies the plane shock loading under uniaxial strain conditions. Experimental setup for plane shock tests is shown in Fig. 1. It includes a one-stage light gas gun facility, and two-channel velocity interferometer [1]. In the majority of experiments, the thickness of target and impactor were adjusted to provide spallation. The main quantitative characteristic of material response in this technique is a time-resolved free surface velocity profile $u_{fS}(t)$.

As example, in Fig. 2 the free surface velocity profile registered during the plane shock loading of 5 mm 38KHN3MFA steel target is presented. The velocity profile consists of several pieces, which are identified in all the experiments. Piece OA' is the elastic precursor, AA' plastic front, AB - transient zone, BC is the smooth piece of loading plastic front, CD is the plateau of

compressive pulse where the particle velocity is invariable, and DF is the unloading front. To infer the instability threshold in this technique, a series of tests at different impact velocities must be conducted. For each impact, the free surface velocity profile similar that presented in Fig. 2 is registered. Structural instability threshold is identified as impact velocity at which dependence of the free surface velocity on the impact velocity suffers a beak.

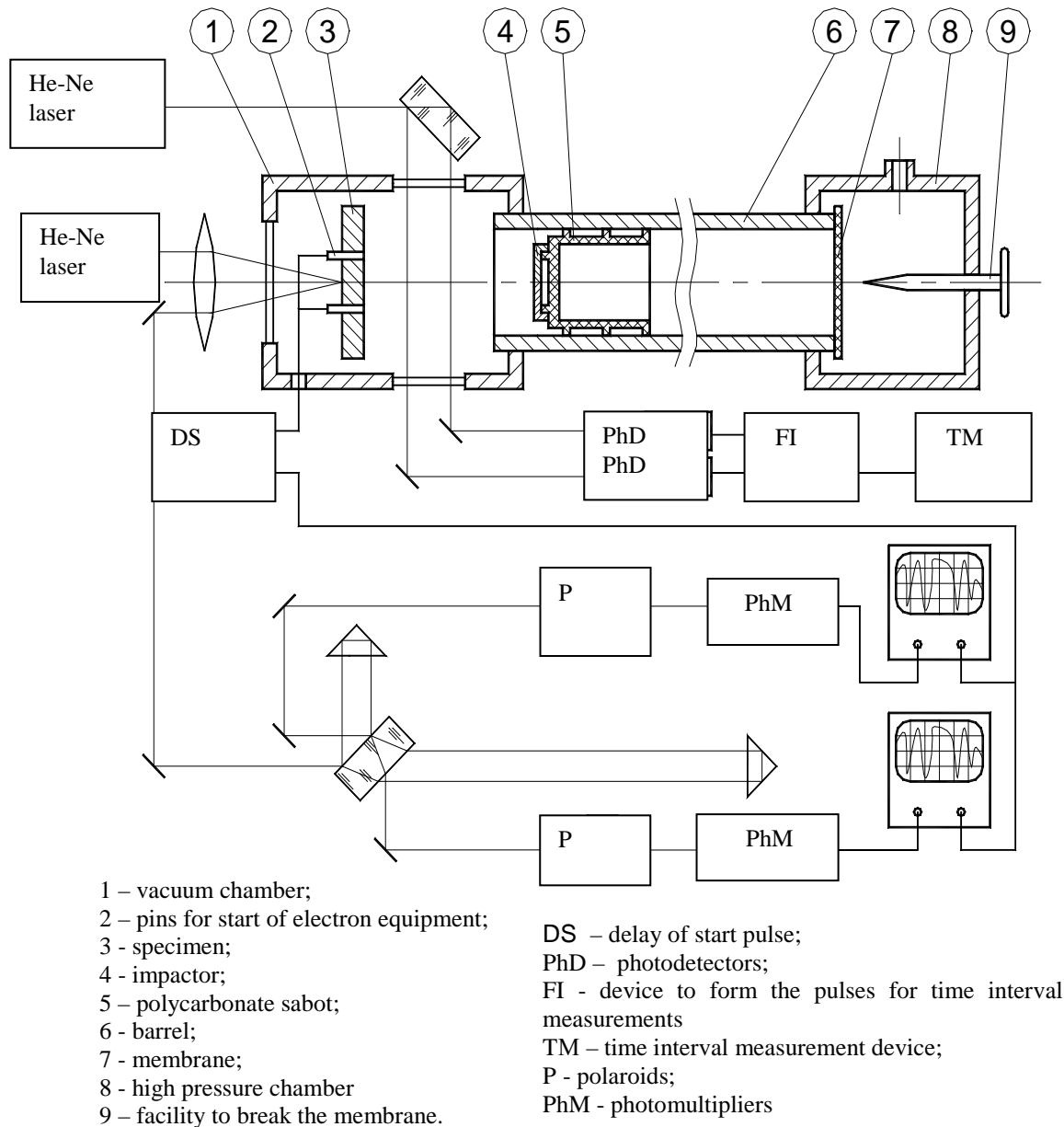


Fig. 1. Functional scheme of experimental setup for plane shock tests.

The second experimental technique is grounded on the high-velocity collision of rod and rigid anvil. This technique has been developed by Taylor [2]. The shape of rod head reflects a response of material to dynamic load and sensitively depends on the type of dynamic stress-strain diagram [3]. In Fig. 3 two possible types of rod deformation are shown. The upper shape of rod demonstrates a gradual increase of the rod head diameter while the bottom figure shows the so-called mushroom shape of rod head.

In Fig. 4 two types of stress-strain diagram are qualitative shown. Bi-linear diagram (1) corresponds to gradual increase of rod diameter as shown in Fig.3, whereas the mushroom shape of rod head corresponds to diagram (2).

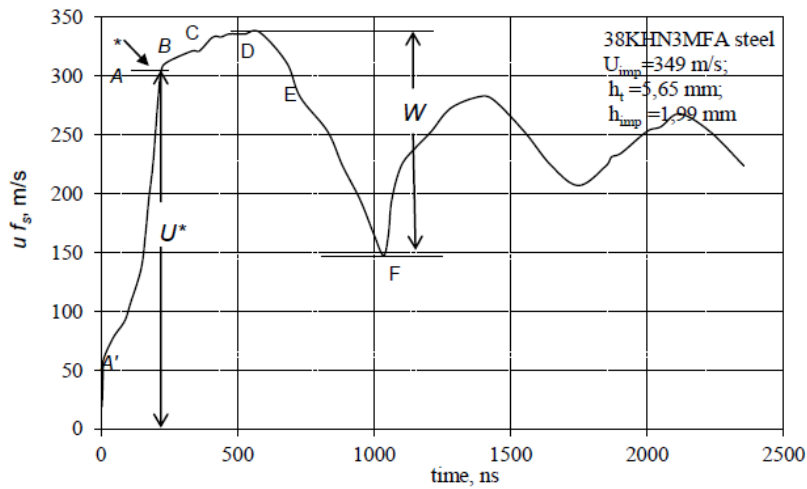


Fig. 2. Free surface velocity profile u_{fs} for 5 mm 38KHN3MFA steel target loaded at the impact velocity of 349 m/s. The break point at the plastic front is indicated by symbol*).

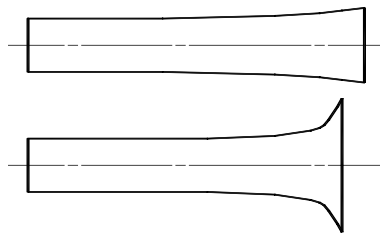


Fig. 3. Two possible types of rod deformation in Taylor tests.

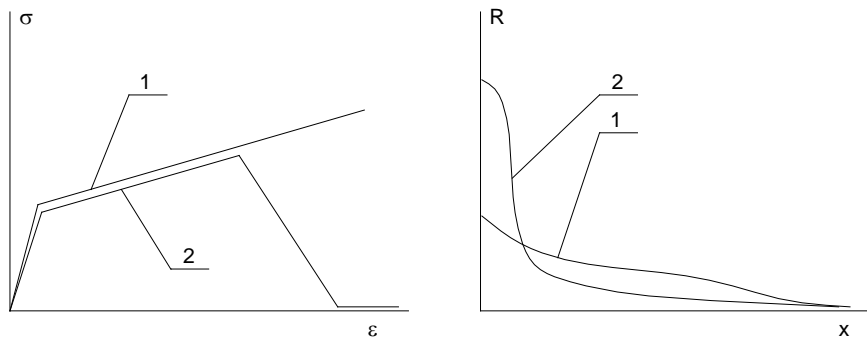


Fig. 4. Two types of stress-strain diagrams for Taylor tests.

Functional scheme of experimental setup for Taylor tests is presented in Fig. 5. The facility for Taylor tests uses the same light gas gun as that for shock tests under uniaxial strain conditions. In this setup, the hard anvil (2) manufactured from high-strength KHVG steel (hardness RCV 64) is sited inside the vacuum chamber (1). The impactor is the rod (5) which is produced from the material under investigation. The only what can be measured in this experiment is the velocity of impactor. The impact velocity when rod begins to fracture is accepted as a criterion for structural instability of material, (Table 3).

The main goal of study is to investigate the strength characteristics and structural mechanisms of fracture for maraging steels which behavior under dynamic load is unknown

and is expected to be much complex. Additional task to be solved in present study is to check whether the shock-induced structural instability threshold obtained in Taylor tests correlates with that obtained in plane shock tests. To solve this task, both Taylor tests and plane shock tests were conducted at identical strain rates with the material of well-known dynamic properties. As a test-material, 38KHN3MFA constructional steel was taken.

3. Instability threshold under compression and spall strength of materials

Determination of the strain rate at which transition to structure-unstable state of material occurs is performed by using both above experimental techniques.

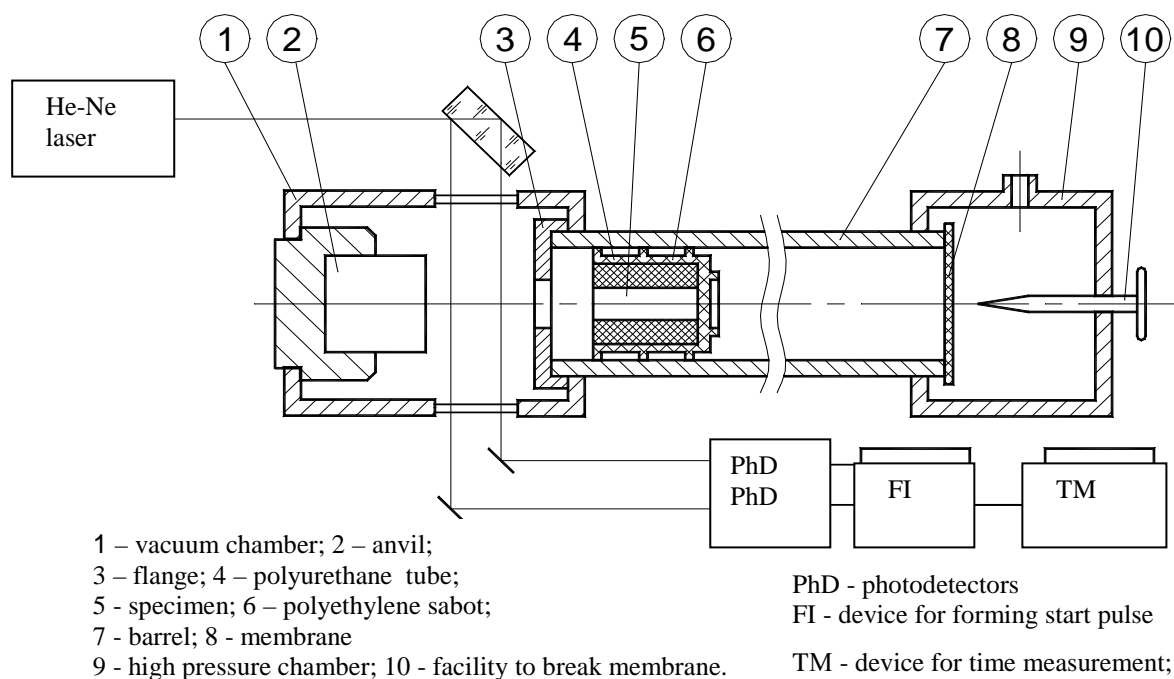


Fig. 5. Experimental setup for Taylor tests.

Chemical composition and quasistatic strength-characteristics of steels are provided in Tables 1 and 2, respectively.

Table 1. Chemical composition of materials (element: weight %).

38KHN3MFA	C: 0.36 Mn: 0.34 P: 0.022 S: 0.009 Cr: 1.29 Ni: 3.19 Mo: 0.42 Si: 0.29 V: 0.15 Cu: 0.08 Fe: basic
02KH18K9M5-VI	C: <0.03 Mn: 0.5 S: 0.02 Ni: 18.5 Mo: 4.0 Si: 0.4 Co: 10.2 Ti: 0.2 Fe: basic
02KH16K9M5T1	C: <0.015 Mn: <0.1 P: <0.01 S: <0.01 Ni: 16.2 Cr: <0.1 Co: 9 Mo: 5.2 Ti: 0.9 Fe: basic
05KH12N5K14M5TB	C: <0.02 Mn: 0.11 P: <0.01 S: <0.005 Ni: 5.0 Cr: 11.61 Co: 14.5 Mo: 4.67 Si: 0.005 W: 0.17 Ti: 0.44 Fe: basic

Table 2. Quasistatic strength-characteristics materials.

	$\sigma_{0.2}$, MPa	σ_b , MPa	δ , %	ψ , %	a_n
38KHN3MFA	1100	1200	12	50	80
02N18K9M5-VI	2000.3	2054	63	43.55	35-55
02KH18K9M5T1	2075-2125	2145-2185	7.4-7.6	45-47.6	45-80
05KH12N5K14M5TV	1590	1710	12.8	45.7	5-49

38KHN3MFA steel. a). *Shock tests under uniaxial strain conditions.* Results of plane shock tests under uniaxial strain conditions are provided in Table 3.

Thicknesses of target and impactor are given in the second and third columns of table, respectively. Fourth column is the impactor velocity. Maximum free surface velocity at the plateau of compressive pulse is given in the fifth column. The sixth column indicates the free surface velocity U^* at which plastic front suffers a break and transits into plateau of compressive pulse. Lastly, seventh column provides a value of pull-back velocity W which is the measure of strength of material under dynamic tensile (spall-strength). In Fig. 6 the dependencies $U^* = f(U_{imp})$ and $W = f(U_{imp})$ for 38KHN3MFA steel are provided. The impact velocity at which above dependencies suffer a break we consider as the point of structural instability in shock loadings under uniaxial strain conditions.

Table 3. Results of plane shock tests for 38KHN3MFA steel.

No. shots	h_t , mm	h_{imp} , mm	U_{imp} , m/s	U_{max} , m/s	U^* , m/s	W , m/s
1	5.68	2.06	200.9	181.3	172	-
2	5.68	2.04	239.3	221.2	207.5	169.4
3	5.68	2.10	263.1	247.8	232.7	180.7
4	5.68	2.10	306.4	282.5	247.3	160.4
5	5.68	2.09	346.7	321.2	295.0	187.1
6	5.65	1.99	349.0	337.0	311.0	189.8
7	5.62	2.02	373.5	363.9	323.3	193.3
8	5.68	2.09	404.3	390.5	335.0	203.3

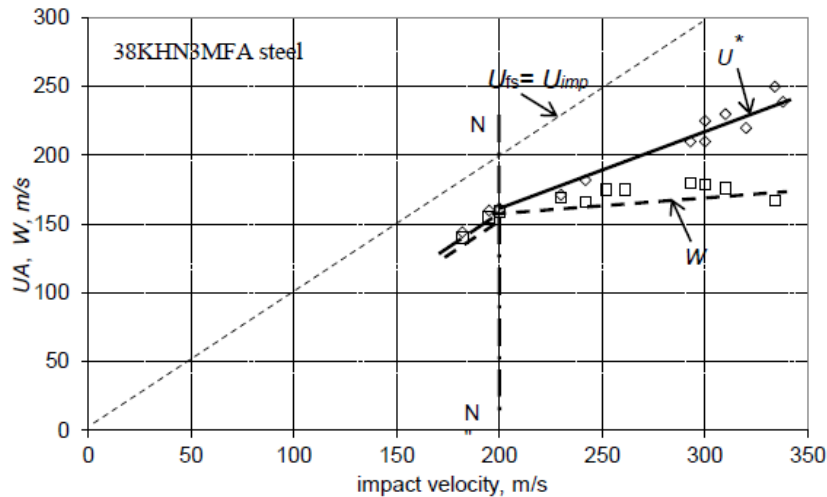


Fig. 6. Dependencies of the free surface velocity at the break point, U^* , and pull-back velocity, W , versus impact velocity for 38KHN3MFA steel.

Curve $U_{imp} = U_{fs}$, corresponds to symmetrical collision of impactor and target when acoustic impedances of impactor and target equal each other ($\rho_{imp} C_{imp} = \rho_{tg} C_{tg}$). One can see that break of dependence $U^* = f(U_{imp})$ for 38KHN3MFA steel occurs at the impact velocity of 200 m/s after what a slope of the dependence decreases. The impact velocity at which dependence $U^* = f(U_{imp})$ suffers a break, corresponds to instability threshold of material under dynamic compression, which can be considered as a shock-induced structural transition.

In Fig. 6a dependence of pull-back velocity $W = f(U_{imp})$ is also plotted. Spallation begins just at the impact velocity at which the break on the dependence $U^* = f(U_{imp})$ happens (line NN')

in Fig. 6). Irreversible structural changes in material occur at the impactor velocity of 200 m/s, which results in change of resistance to spallation.

b). Taylor tests. Results of Taylor tests for the 38KHN3MFA steel are provided in Table 4. Taylor tests were performed within impact velocity range from 90 m/s to 450 m/s. Within that range, there exist three stages of the rod head deformation and fracture:

1. Uniform deformation with gradual increase of the rod head;
2. Deformation and splitting of rod head by two pieces at 45°.
3. Fracture by numerous fragments.

Table 4. Result of Taylor tests for the 38KHN3MFA steel.

No. shots	U_{imp} , mm	Y_{02} , GPa	Type of deformation (fracture)
1	89.4	1.37	uniform deformation
2	126.5	1.213	uniform deformation
3	136.6	1.65	uniform deformation
4	190.6	1.64	uniform deformation
5	206.2	1.17	uniform deformation
6	234.3	-	split under 45°
7	382.3	-	damaged
8	451.7	-	damaged

In determination, the instability threshold with Taylor tests one can use only those experimental data, which correspond to boundary impact velocity between uniform straining of rod head and beginning of fracture (shots 1-5 in Table 4). For 38KHN3MFA steel, the upper impact velocity where straining of rod head is still uniform equals 206.2 m/s. This value can be considered as critical impact velocity corresponding to structural instability threshold for the material under uniaxial stress conditions.

Thus, in Taylor tests the transition to structural instability for 38KHN3MFA steel happens approximately at the same impact velocity as in plane shock tests.

02KH18K9M5-VI maraging steel. Results of Taylor tests and plane shock tests for 02KH18K9M5-VI maraging steel are presented in Table 5 and Table 6.

a). Taylor tests. Depending on the character of rod deformation, the overall region of impact velocity for Taylor tests can be subdivided by three sub-regions.

1. Homogeneous dynamic straining of the rod head occurring at the impact velocities below 126.3 m/s.
2. The rod head splits by two parts in a plane inclined under 45° relatively rod axis. This occurs within velocity range from 126.3 m/s through 170 m/s.
3. Full fragmentation of the rod head which occurs from 198.4 m/s to 473.3 m/s.

Again, since the determination of yield stress and structural instability threshold in Taylor tests is correct only for the undamaged specimens, the critical impact velocity in Taylor tests for this steel is accepted to be 126.3 m/s.

b). Uniaxial strain tests. The instability threshold for the 02H18K9M5-BИ maraging steel under dynamic compression and spallation is determined by using the $U^* = f(U_{imp})$ and $W = f(U_{imp})$ dependencies shown in Fig. 7. Both dependencies suffer a break at the impact velocity of 383 m/s (line NN' in Fig. 7) where the structural instability under dynamic compression is thought to occurs. As distinct from the 38KHN3MFA steel, the critical impact velocity for structural instability under uniaxial strain conditions for the 02H18K9M5-BИ maraging steel turns out to be much higher than that for Taylor tests.

Table 5. Results of plane shock tests for 02KH18K9M5-VI maraging steel.

№№ shots	h_t , mm	h_{imp} , mm	U_{imp} , m/s	U_{max} , m/s	U^* , m/s	W , m/s
1	6.47	1.77	156.9	169.5	-	-
2	6.47	1.77	243.0	234.4	215.0	227.5
3	6.49	1.78	263.1	290.0	265.0	239.3
4	6.47	1.77	324.6	318.8	300.0	271.5
5	6.48	1.78	386.0	392.0	365.0	295.6
6	6.49	1.75	461.5	461.7	410.0	281.2

Table 6. Results of Taylor tests for 02KH18K9M5-VI maraging steel.

№№ shots	U_{imp} , m/s	$Y_{0.2}^{stress}$, GPa	Type of deformation (fracture)
1	51.1	3.37	uniform deformation
2	69.5	3.52	uniform deformation
3	87.4	3.42	uniform deformation
4	93.9	2.41	uniform deformation
5	126.3	3.51	uniform deformation
6	127.8	-	split under 45°
7	170.0	-	split under 45°
8	198.4	-	damaged
9	200.7	-	damaged
10	250.3	-	damaged
11	256.1	-	damaged
12	273.5	-	damaged
13	320.6	-	damaged
14	321.6	-	damaged
15	409.9	-	damaged
16	412.2	-	damaged
17	473.3	-	damaged

02N16K9M5T1 maraging steel. Results of plane shock tests and Taylor tests are presented in Table 7 and Table 8, respectively. Taylor tests can be subdivided by two sets depending on the character of deformation and fracture of the rod head.

1. Uniform straining of rod head within impact velocity range from 92.6 m/s to 153.6 m/s.
2. Fracture of rod head.

Table 7. Results of plane shock tests for 02N16K9M5T1 maraging steel.

№№ shots	h_t , mm	h_{imp} , mm	U_{imp} , m/s	U_{max} , m/s	Y , GPa	U^* , m/s	W , m/s
1	6.47	1.78	226.8	219.7	3.44	210	-
2	6.47	1.78	311.5	304.1	3.49	290	227.5
3	6.49	1.77	358.0	354.0	3.68	340	239.3
4	6.47	1.78	416.2	416.2	3.61	365	271.5

Table 8. Results of Taylor tests for 02N16K9M5T1 maraging steel.

№№ shots	U_{imp} , m/s	$Y_{0.2}^{stress}$, GPa	Type of deformation (fracture)
1	92.6	4.92	uniform deformation
2	94.2	3.75	uniform deformation
3	130.1	3.75	uniform deformation
4	153.6	2.123	uniform deformation
5	172.2	-	damaged
6	174	-	damaged
7	174.3	4.0	uniform deformation
8	175	-	damaged
9	204.8	3.72	uniform deformation
10	305.7	-	damaged
11	341	-	damaged
12	363.1	-	damaged
13	557.8	2.82	uniform deformation

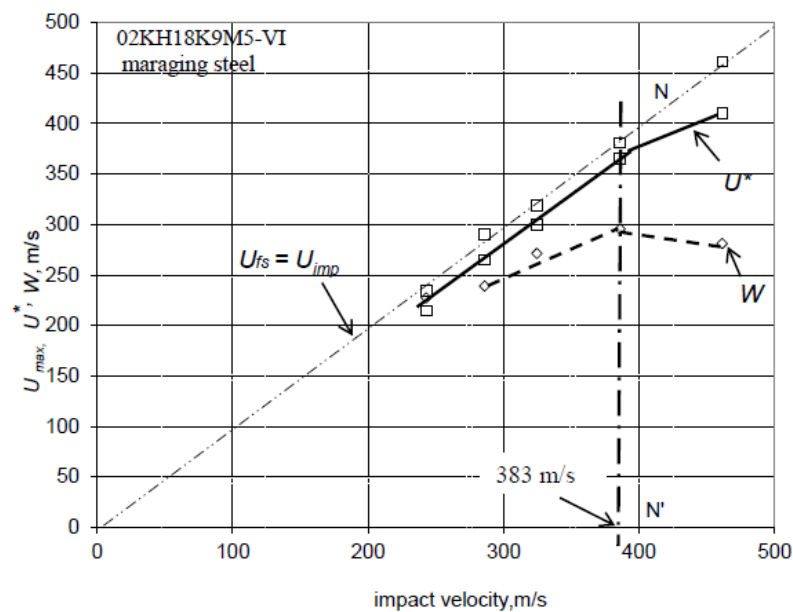


Fig. 7. Dependencies of the free surface velocity at the break-point, U^* , and pull-back velocity, W , versus impact velocity for 02KH18K9M5-VI steel.

The analogous value for uniaxial strain conditions resulted from the dependencies $U^* = f(U_{imp})$ and $W = f(U_{imp})$ is presented in Fig. 8.

In Taylor tests, impact velocity of 153.6 m/s can be considered as a critical velocity for initiating the structural instability of 02KH16K9M5T1 maraging steel. The critical impact velocity for structural instability in plane tests is 371 m/s, which is much higher than that for uniaxial stress conditions.

05KH12N5K14M5TV maraging steel. The third kind of maraging steel under investigation is the so-called chromium maraging steel commonly used for producing the high-pressure vessels. This steel shows the high quasistatic strength properties both at room and low temperatures. Results of plane shock tests and Taylor tests are presented in Table 9 and 10,

respectively. Structural instability threshold under uniaxial strain conditions determined from the dependencies $U^* = f(U_{imp})$ and $W = f(U_{imp})$ is indicated in Fig. 9.

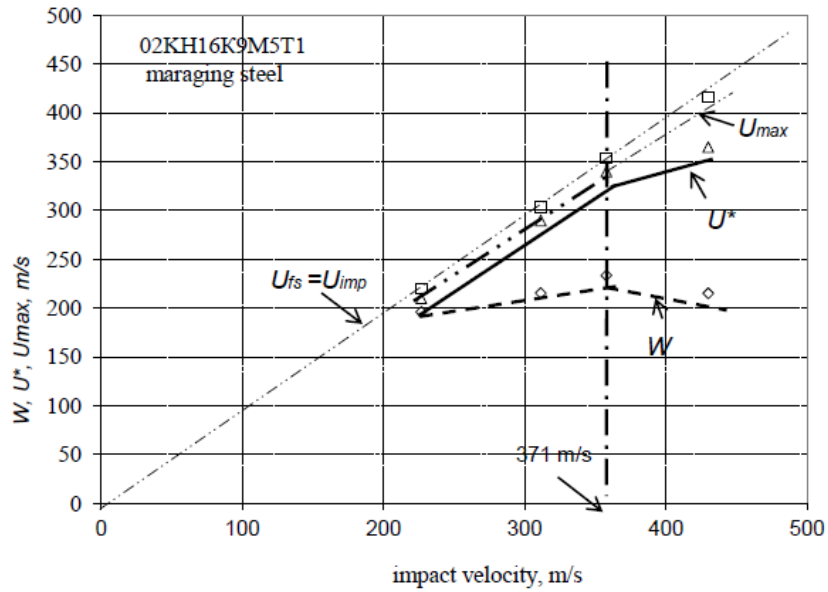


Fig. 8. Dependencies of maximum free surface velocity U_{max} , break velocity U^* and pull-back velocity W for 02KH16K9M5T1 maraging steel versus impact velocity.

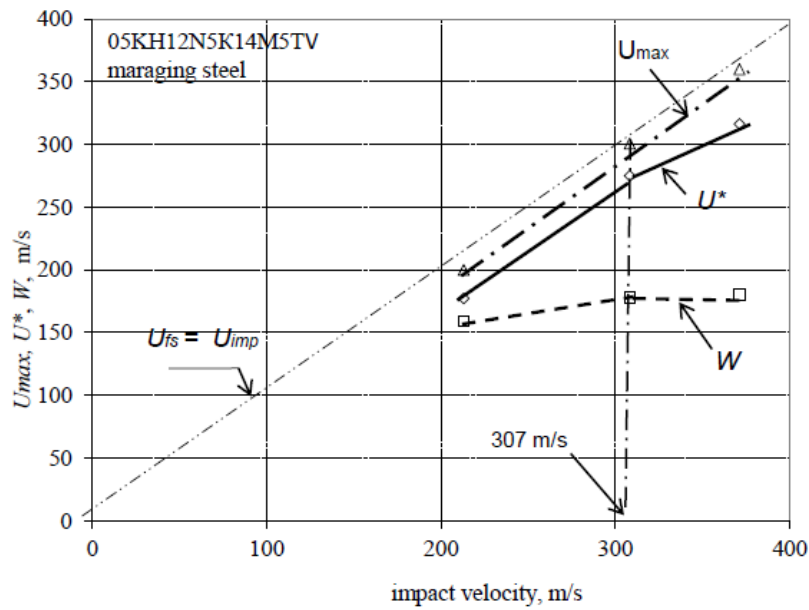


Fig. 9. Maximum free surface velocity U_{max} , break velocity U^* and pull-back velocity W versus impact velocity for 02KH12N5K14M5TV maraging steel.

Table 9. Results of plane shock tests for 05KH12N5K14M5TV maraging steel.

№ №	h_i , mm	h_t , mm	U_{imp} , m/s	U_{fs}^{max} , m/s	Y , GPa	U^* , m/s	W , m/s
1	5.03	1.78	213.1	201.1	2.8	177.2	159
2	5.04	1.80	308.4	300.8	2.94	275	178
3	5.05	1.79	371.3	360.0	3.29	316.4	180.4

Table 10. Results of Taylor tests for 05KH12N5K14M5TV maraging steel.

No shots	U_{imp} , m/s	$Y_{0.2}^{stress}$, GPa	Type of deformation (fracture)
1	93.9	1.816	uniform deformation
2	122.4	1.835	uniform deformation
3	161.9	1.925	uniform deformation
4	200.1	1.90	uniform deformation
5	237.3	2.02	uniform deformation
6	245.1	1.89	uniform deformation
7	296.3	2.11	uniform deformation
8	322.3	-	damaged
9	326	-	damaged
10	368.7	-	damaged
11	396.2	-	damaged

The critical impact velocity for structural instability of 02KH12N5K14M5TV maraging steel equals 307 m/s. It is close to that for Taylor tests (296.3 m/s). Thus, for chromium maraging steel, similar to 38KH12N5K14M5TV steel, the critical velocities for structural instability under uniaxial strain conditions and Taylor tests practically coincide.

Microstructure investigations. Microstructure investigation of 02KH18K9M5-VI, 02KH16K9M5T1 and 05KH12N5H5K14M5TV maraging steels were conducted with microscope NEOPHOT-32. The measurement of microhardness were performed with PMT-3 device under load of 50 g. Etching of specimens were conducted in mixture of three acids: hydrochloric acid, nitric acid and sulphuric acid.

Structure of the first and second kinds of maraging steels is the mixture of the martensitic matrix and uniformly distributed particles of intermetallide phase. The 02N18K9M5-VI and 02KH16K9M5T1 maraging steels contain about 2 % of austenite. The third kind of steel is the stainless chromium 05KH12N5K14M5TV maraging steel which contains about 25 % austenite.

02KH18K9M5-VI maraging steel. The initial state of microstructure for this steel is presented in Fig. 10a. In spite of the high degree of scattering in grain size (grain size ranges from 5 μm through 50 μm), the difference in microhardness between neighbor regions of matrix equals 150 MPa whereas the mean microhardness of matrix equals 4700 MPa. Shock loading with Taylor technique leads to increase the difference in microhardness which achieves a maximum value at the impact velocity corresponding to beginning of rod head damage. So, at the impact velocity of 256 m/s the difference in microhardness equals 1650 MPa (see Fig. 10b).

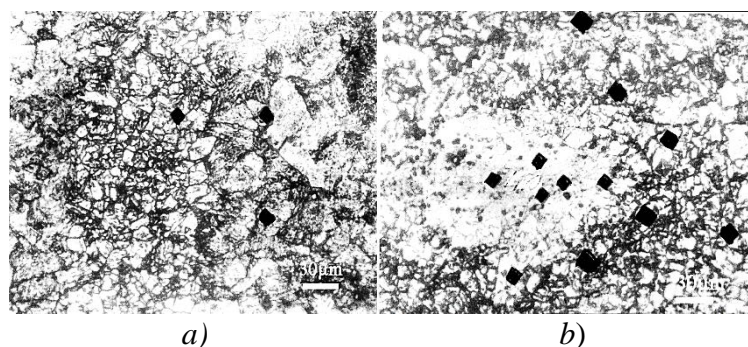


Fig. 10. Structure of 02KH18K9M5-VI maraging steel in Initial state (a). Structure of the steel after shock loading at the impact velocity of 256 m/s (b). Microhardness measurements are seen in the form of black points of different size.

In Fig. 11 the microstructure of the steel after shock loading under uniaxial strain conditions at the impact velocity of 324 m/s is presented. Microhardness of matrix equals 4760 MPa whereas in damaged zone it equals 2660 MPa. Since the austenite inclusions were not found in initial state of the steel, it may be concluded that austenite inclusions are nucleated in the process of shock loading. Fracture occurs along the austenite-matrix boundaries as the most stressed regions of material (see Fig. 11). Difference in microhardness between neighbor regions of target herein is 2100 MPa.

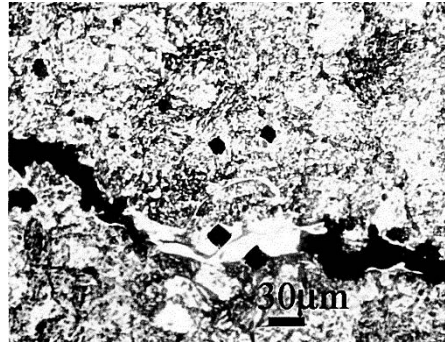


Fig. 11. Structure of the steel after shock loading at the impact velocity of 324 m/s.

02KH16K9M5T1 maraging steel. The microstructure of 02KH16K9M5T1 maraging steel is provided in Fig. 12. Mean microhardness of matrix in this steel equals 4100 MPa. Similar to previous kind of steel, the growth of difference in microhardness between neighbor regions of specimen leads to fracture of rod head. In Taylor tests, this difference ranges from 300 MPa in initial state through 1500 MPa at the impact velocity of 256 m/s.

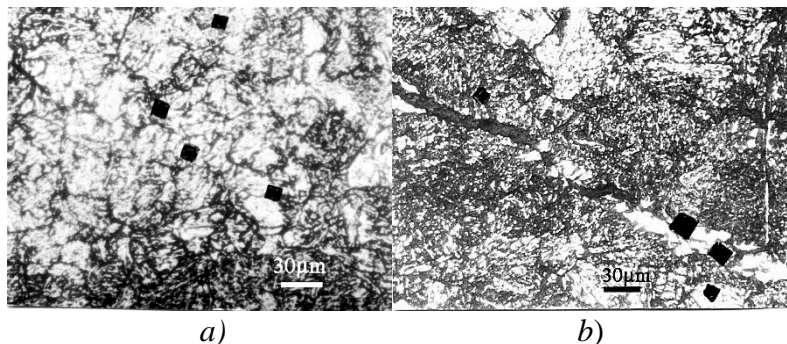


Fig. 12. Initial structure of steel (a), structure of steel with microhardness measurements after shock loading at the impact velocity of 226 m/s (b).

With the increase of impact velocity up to 557 m/s, the difference in microhardness between neighbor regions begins to drop. So, the microstructure of steel at the impact velocity of 557 m/s is identical to that at the impact velocity of 130 m/s. The difference in microhardness between neighbor regions equals 450 MPa whereas dynamic deformation of rod head is uniform.

Microstructural investigations of this steel after plane shock loading at the impact velocity of 226 m/s shows that damage of specimens flows mainly along the matrix-austenite boundaries appeared in the process shocking (Fig. 12b). Microhardness of austenite inclusions equals 2700 MPa. Microhardness data and common character of fracture of 02KH18K9M5-VI and 02KH16K9M5T1 maraging steels evidence the presence of resonance interaction between strain rate and rate of direct and reverse alpha-gamma transformations. This interaction is thought to result in disintegration of strengthen phase created in the process of technological aging of steel.

05X12H5K14M5TB maraging steel. As distinct from the previous kinds of maraging steel, this steel has a much higher contents of Cr, which results in a large percentage of austenite in the initial state of the steel (~ 25 % instead of 2-3 % for the 02KH18K9M5-VI and 02KH16K9M5T1 maraging steels).

Microhardness of matrix equals 4530 MPa whereas the microhardness of the austenite equals 2800 MPa. Dynamic deformation of specimen in Taylor tests flows uniformly up to impact velocities of $296 \div 320$ m/s. The head of rod in Taylor tests has a mushroom shape (see Fig. 3). The strength behavior of the steel in the velocity range is much stable although the value of yield stress is smaller than that for the previous kinds of maraging steel.

The same can be said about microstructure behavior. There is no change of microstructure state within overall range of the impact velocity of interest. Micrograph for the steel at the impact velocity of 237 m/s is identical that for the material in initial state (Fig. 13a). In planar tests, the behavior of this steel turns out to be much brittle (see Fig. 13b).

Thus, the presence of large percentage of austenite in initial state of 05KH12N5K145TV maraging steel provides the stable behavior under dynamic loading though the yield stress and critical strength threshold values decrease.

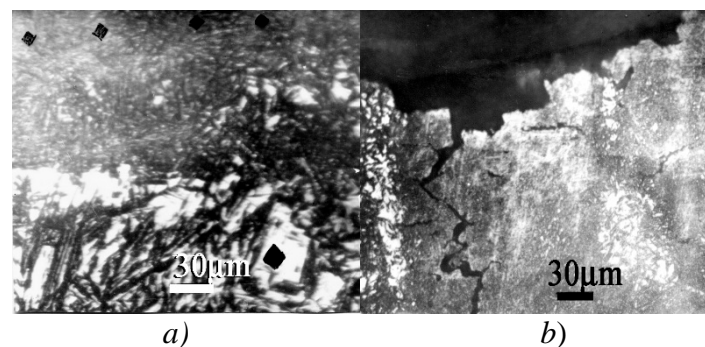


Fig. 13. Initial structure of steel (a), structure of steel with microhardness measurements after shock loading at the impact velocity of 308 m/s (b).

4. Discussion

In the case of quasistatic strain rates, possibility for existence of structural transitions has been theoretically analyzed in [4]. Micro-deformation model based on solution to sine-Gordon equation predicts a non-stable behavior of crystalline lattice subjected to shear deformation in non-linear elastic region of loading. This instability leads to nucleation of large-scale structures such as meso-rotations, shear bands and their combinations. The large-scale structures appear long before the transition to macroscopic plasticity occurs. If, however, the *stress gradients* do not exceed critical value, the large-scale structures may disappear, i.e. at that stage, the structural transition turns out to be reversible. At higher strain gradients, a bifurcation transition takes place, which results in irreversible nucleation of large-scale structures.

As distinct from quasistatic condition of straining, in the case of dynamic deformation under uniaxial strain conditions, the criterion for transition of material into structure-unstable state is determined by the *strain rate*. The microstructural mechanisms responsible for structural transition were found to be the particle velocity pulsations at the mesoscale [5, 6]. In turn, amplitude of particle velocity pulsations is determined by the strain rate. Transition to structure-unstable state happens when rate of change of the particle velocity pulsations becomes higher than rate of change of mean particle velocity, which occurs just at the critical strain rate [7].

In the case of 38KHN3MFA steel and 05KH12N5K145TV maraging steel the critical impact velocities for dynamic fracture in Taylor tests and in planar tests practically coincide, which means that mechanisms for transition to structure-unstable state are identical. As for the 02KH18K9M5-VI and 02KH16K9M5T1 maraging steels, the critical impact velocity for

structural instability in Taylor tests is much lower than that for the tests under uniaxial stress conditions. In this situation, it may be supposed that an additional mechanism for transition into structure-unstable state is incorporated. For all the materials tested, the initial stage for dynamic fracture of rod head occurs along the planes of maximum tangent stress (under 45° relatively direction of shock loading). Taylor tests turn out to be more sensitive to structural instability of material than planar tests. The reason lies in different stress state for above situations. Dynamic deformation under uniaxial strain conditions flows under high value of hydrostatic pressure whereas the shear stress constitutes only 0.05 of total normal stress [8]. The shear stress under uniaxial strain conditions is known to be equalled $\tau = \frac{1}{2}(\sigma_x - \sigma_y)$ whereas the same value under uniaxial stress conditions is $\tau = \frac{1}{2}\sigma_x$, that is much higher, since under uniaxial strain conditions σ_x and σ_y are sufficiently close. This is thought to be the reason for weak resistance of rod to splitting under dynamic compression. Another reason lies in structural specifics of 02KH18K9M5-VI and 02KH16K9M5T1 maraging steels. The above results show that 02H18K9M5-BII and 02H16K9M5T1 maraging steels lose their shear resistance under shock loading in Taylor tests much easily than in planar tests. Microstructure studying of specimens shows that spallation of these steels happens mainly along the boundaries of austenite inclusions nucleated during dynamic straining. As for the 38KH12N5K145TV maraging steel, their phase state after shock loading does not change. Thus, it may be concluded that structural instability of 02KH18K9M5-VI and 02KH16K9M5T1 maraging steels results from shock-induced localized phase transformation.

5. Conclusions

As a result, it can be concluded:

1. Shock tests of 02KH18K9M5-VI and 02KH16K9M5T1 maraging steels under uniaxial strain conditions and Taylor technique show that possible reason for losing the aging properties of these kinds of maraging steel at high strain rates is the shock-induced localized phase transformation
2. Where observed, the fracture mainly occurs along the shock-induced austenite laths
3. Microhardness data and common character of fracture of 02KH18K9M5-VI and 02KH16K9M5T1 maraging steels indicate a presence of resonance interaction between strain rate and rate of direct and reverse alpha-gamma transformations. This interaction is thought to result in disintegration of strengthen phase created in the process of technological aging of steels. As for the 02KH12N5K14M5TV maraging steel, the austenite phase is present in initial state of the material so the shock loading does not affect the phase state of steel.

Acknowledgments. The work was performed in the frame of RNF Project 17-11-01053.

References

- [1] Yu.I. Mescheryakov, A.K. Divakov // *Dymat Journal* **1** (1994) 271.
- [2] G.I. Taylor // *Proceedings of the Royal Society A* **194** (1948) 2899.
- [3] V.N. Kukudjanov // *Bulletin of the Russian Academy of Sciences* **45** (1998) 388.
- [4] E.L. Aero, A.N. Bulygin // *Mechanics of Solid* **5** (2007) 190.
- [5] Yu.I. Meshcheryakov // *International Journal of Shock Waves* **26** (2016) 2.
- [6] D.A. Indeitsev, Yu.I. Meshcheryakov, A.Yu. Kuchmin, D.S. Vavilov // *Acta Mechanica* **226** (2014) 917.
- [7] Yu.I. Meshcheryakov, A.K. Divakov, N.I. Zhigacheva, B.K. Barakhtin // *International Journal of Impact Engineering* **57** (2013) 99.
- [8] D.E. Grady, M.E. Kipp // *Journal of the Mechanics and Physics of Solids* **35** (1987) 95.

EFFECT OF TITANIUM CARBIDE ADDITION ON THE WORKABILITY BEHAVIOR OF POWDER METALLURGY ALUMINUM PREFORMS DURING HOT DEFORMATION

S. Narayan *, A. Rajeshkannan

School of Engineering and Physics, Faculty of Science, Technology & Environment, The University of the
South Pacific, Laucala Campus, PO Box 1168, Suva, FIJI.

*e-mail: narayan_su@usp.ac.fj

Abstract. Experimental investigation has been carried out to evaluate the effect of titanium carbide (TiC) addition on the composite aluminium preforms. The hot upsetting of the composite aluminium preforms with varying TiC contents, namely, 1%, 2%, 3% and 4%, and different aspect ratios, namely, 0.2, 0.4 and 0.6, was carried out and the workability behavior of the same was determined. The influence of TiC addition, in the aluminium composite, on the relative density (R), stress ratio parameters, $\sigma_{\theta}/\sigma_{eff}$, σ_m/σ_{eff} and σ_z/σ_{eff} and formability stress index was studied. The effects of initial preform geometry and initial theoretical density on the workability behavior have been studied.

Keywords: workability; stress ratio parameter; formability stress index; relative density; triaxial stress.

1. Introduction

Today, many researchers are working on producing frontier materials in this research field that will benefit our society in one way or another. Technological advancement and improved materials in terms of cost, manufacturability and strength are not the only concern today unlike in the traditional days. One of the most important issues today is global warming, climate change issues, ecological, etc. and for any developments in technology and materials there is need to capture these important issues. One of the manufacturing routes so called powder metallurgy manufacturing route is considered to be green materials processing route [1] in comparison to traditional or conventional casting materials processing route. Some of the merits of powder metallurgy manufacturing route over traditional casting process is that energy consumption is reduced by 50%, very little fumes & chemicals emitted in the atmosphere, use of re-cycled metals, the emerging consumer preferences for green products, and increasing disposal costs due to scarcity of land fields [1-2]. Every manufacturing process has its own merits and demerits and one of the main concerns with powder metallurgy processing route is that it produces parts with residual porosity. Hence, high strength applications of powder metallurgy parts are limited in the practical world. Secondary operations such as pressing or repressing, powder extrusion, powder rolling and infiltration etc., can be employed to increase the strength of the powder metallurgy materials by eliminating the residual porosity [3]. Aluminium metal matrix composites are highly used in high strength industrial application due to low specific density, high strength, good wear resistance, low thermal expansion coefficient, etc [4, 5]. Sahin [5] studied the preparations of metal matrix composites by developing the method and some properties (hardness, tool wear in turning, density and porosity) of SiC

particles reinforced aluminium alloy composites. It is shown that metal matrix composites of 10 and 20 wt.% SiC particles can be produced successfully using molten metal mixing method. Titanium carbide based composites are currently used in high strength application where wear and corrosion are the main mode of failure. Titanium carbide particulates are extremely hard and the improvement in wear resistance and reduced corrosion rate is expected [6]. Narayanasamy et al. [6] studied the effect of TiC addition of the densification behaviour on the composite steel preforms. The two composites prepared via P/M route and analyzed were Al-3%TiC and Al-4%TiC. Titanium and its alloy are developed because of its low cost and good performance. Liu et al. [7] has shown that low cost P/M Ti alloys and their composites with their attractive properties can be produced through a single primary P/M processing route, although secondary treatments are required for high strength applications. Titanium carbide based composites with nickel alloys and iron alloys are currently used in high performance applications [6, 8].

Workability is an important parameter that needs to be studied while powder metallurgy preforms are subject to secondary deformation. During secondary deformation powder metallurgy preforms has substantial material flow in the lateral direction due to induced height strain. During lateral flow of material or deformation, apart from pore closing mechanism, the pores also elongate in the lateral direction. Workability is a measure of the extent of deformation that a material can withstand the induced internal stresses of forming prior to failure. Workability characteristics are not only dependent on the material but also by several forming parameters such as stress and strain rate, porosity, friction, temperature, etc [9-11]. To investigate the workability criteria of the material, ductile fracture criterion for ductile fracture must be established as workability of any material depends mainly on the amount of ductile fracture present in the material. There are many theories developed and verified with experimental results in study the workability behavior of powder metallurgy materials. Shima and Oyane [12], Gurson [13] and Doraivelu et al. [14] proposed a plasticity theory for porous materials, continuum theory of ductile rupture considering yield criteria for porous material and a new yield criterion for porous material validating it using experiments and simulations, respectively. Narayansamy et al. investigated the working behavior of Al-Al₂O₃ composites under various stress state conditions, namely uniaxial, plane and triaxial stress states. The effects of different curve fitting techniques, aspect ratio, and initial preform density on the workability criteria were presented [15]. They used a generalized yield criterion considering an-isotropic parameters for powder metallurgy metals which was earlier proposed by Narayansamy et al. [16] with a new flow rule with an-isotropic parameters for porous metals. Rahman and El-Sheikh [10] proposed the stress formability criteria (β) for describing the effect of mean stress and the effective stress by employing theories proposed by Kuhn-Downey [17] and Whang-Kobayashi [18]. Gouveia et al. [19] conducted experiments on P/M compacts of several geometries and reported that the initiation of the ductile fracture can be predicted. The attention on the hoop stress, hydrostatic stress and axial stress behaviour of any P/M materials is much required for any forging processes and Narayanamurti et al. [20] presented some of the important criteria generally used for the prediction of ductile fracture. Crack appearance on the powder metallurgy preform can be avoided by careful selection of process parameters and deformation process. Thus, the present investigation is aimed to establish the workability limit under triaxial stress state condition of powder metallurgy preforms of Al-1%TiC, Al-2%TiC, Al-3%TiC, and Al-4%TiC experimentally and to establish the technical relationship that exists between the characteristics of axial stress, hoop stress, hydrostatic stress, effective stress and formability stress index with respect to true height strain and densification.

2. Experimental details

Aluminium powder of less than or equal to 150 μm and titanium carbide powder of less than or equal to 50 μm were mixed to obtain the alloy of Al-1%TiC, Al-2%TiC, Al-3%TiC, and Al-4%TiC via ball milling. The ball mill was operated for 2 hours at 200 rpm to get a homogenized mixture. The sieve analysis of pure aluminium powder and powder characterization of aluminium powder and its respective blends are given in Tables 1 and 2, respectively.

Table 1. Sieve size analysis of aluminium powder.

Sieve size (μm)	250	+200	+150	+100	+75	+45	-45
Wt % Ret.	0.2	0.3	16.3	55.3	9.5	7.9	10.5

Table 2. Characterization of aluminium powder and its blends.

Si. No.	Property	Al	Al-1%TiC	Al-2%TiC	Al-3%TiC	Al-4%TiC
1.	Apparent Density (g/cc)	1.091	1.133	1.186	1.247	1.280
2.	Flow rate, (s/50g) by Hall Flow Meter	87.306	86.801	85.202	83.086	81.478
3.	Compressibility (g/cc) at pressure of 130 \pm 10MPa	2.356	2.342	2.325	2.302	2.280

The powders with different aspect ratios and different initial theoretical density were then compacted using 100 tons capacity hydraulic press. The compaction pressure was controlled so as to obtain an initial theoretical density of 0.82 ± 0.01 and 0.86 ± 0.01 . The compacts were coated on all surfaces with ceramic coating. This coating was allowed to dry for a period 12 hours at normal atmospheric conditions. Recoating was employed to the preforms in the direction 90° to that of the earlier coating. Again the compacts were allowed to dry for a period of 12 hours. The coating was applied to avoid oxidation of compacts.

The ceramic coated compacts were sintered in an electric muffle furnace at a temperature of 220°C for 30 minutes and then the temperature was increased to 594°C . At this temperature the compacts were sintered for a further period of 60 minutes. After the sintering operation, the preforms were upset forged at a temperature of 594°C to the different levels of height strain. The forging operation was carried out with no lubricant. The density of forged preforms was determined using Archimedes principle. After the above mentioned forging schedule, the dimensions, namely, the height of forged specimen (h_f), the contact diameter (D_{c1} and D_{c2}) of top and bottom surfaces and the bulged diameter (D_b), were measured. Initial dimensions of the specimen (initial height h_o , initial diameter D_o) and the initial preform density were measured for each preform before conducting the experiment.

3. Theoretical analysis

Using the mathematical expressions, the various upsetting parameters of upsetting were determined under uniaxial stress state condition, plane stress state condition and triaxial stress state condition.

3.1. Uniaxial stress state condition. According to Abdel-Rahman and El-Sheikh [10], the expression for true axial stress and mean stress for powder metallurgy materials are as follows:

$$\sigma_z = \frac{\text{load}}{\text{contact surface area}} = -\sigma_{eff}, \sigma_r = \sigma_\theta = 0 \quad (1)$$

$$\sigma_m = \left(\frac{\sigma_z}{3}\right) = -(\sigma_{eff}/3) \quad (2)$$

and the expression for the axial strain can be written as follows:

$$\varepsilon_z = -\varepsilon_{eff} = \ln\left(\frac{h_f}{h_o}\right) \quad (3)$$

and true hoop strain is

$$\varepsilon_\theta = \varepsilon_r = \ln\left(\frac{D_f}{D_o}\right), \quad (4)$$

where h_o is the initial height of the preform; h_f the forged height of the preform; D_f the contact diameter after deformation of the preform; D_o the initial diameter of the preform.

3.2. Plane stress state condition. According to Narayansamy et al. [9, 15], the hoop strain which includes the forged bulged diameter (D_b) and forged contact diameter (D_c) can be expressed as follows

$$\varepsilon_\theta = \ln\left[\frac{2D_b^2 + D_c^2}{3D_o^2}\right] \quad (5)$$

and state of stress can be written as

$$\sigma_{eff} = (0.5 + \alpha)[3(1 + \alpha + \alpha^2)]^{0.5} \sigma_z, \quad (6)$$

where α is the Poisson's ratio = $(\varepsilon_\theta/2\varepsilon_z)$

The hoop stress can be written as ($\sigma_r = 0$ at the free surface in plane stress state condition)

$$\sigma_\theta = \left[\frac{1+2\alpha}{2+\alpha}\right] \sigma_z \quad (7)$$

and the hydrostatic stress is

$$\sigma_m = \frac{\sigma_\theta + \sigma_z}{3} \quad (8)$$

The various stress ratio parameters can be written as follows from Equations 6-8:

$$\frac{\sigma_{eff}}{\sigma_z} = (0.5 + \alpha)[3(1 + \alpha + \alpha^2)]^{0.5} \quad (9)$$

$$\frac{\sigma_\theta}{\sigma_z} = \left[\frac{1+2\alpha}{2+\alpha}\right] \quad (10)$$

$$\frac{\sigma_m}{\sigma_z} = \frac{1}{3} \left(1 + \frac{\sigma_\theta}{\sigma_z}\right) \quad (11)$$

The formability stress index proposed by Vujovic and Shabaik [21] stating the importance of the spherical component of stress state on fracture can be expressed as

$$\beta = 3 \left[\frac{(\sigma_m/\sigma_z)}{(\sigma_{eff}/\sigma_z)} \right] \quad (12)$$

3.2. Triaxial stress state condition. According to Narayansamy et al. [6], the state of stress in a triaxial stress condition is given by

$$\alpha = \frac{d\varepsilon_\theta}{d\varepsilon_z} = \frac{(2+R^2)\sigma_\theta - R^2(\sigma_z + 2\sigma_\theta)}{(2+R^2)\sigma_\theta - R^2(\sigma_z + 2\sigma_\theta)} \quad (13)$$

Using Eq. (13) for the values of Poisson's ratio (α), relative density (R) and axial stress (σ_z) the hoop stress (σ_θ) under triaxial stress state condition can be determined as given below:

$$\sigma_\theta = \left[\frac{2\alpha + R^2}{2 - R^2 + 2R^2\alpha} \right] \sigma_z, \quad (14)$$

where $\alpha = \frac{d\varepsilon_\theta}{d\varepsilon_z}$

and relative density (R) is important in finding the hoop stress.

Further, rearranging Equation 14

$$\frac{\sigma_\theta}{\sigma_z} = \left[\frac{2\alpha + R^2}{2 - R^2 + 2R^2\alpha} \right] \quad (15)$$

Under triaxial stress state cylindrical coordinates, the hydrostatic stress can be written as follows assuming $\sigma_\theta = \sigma_r$:

$$\sigma_m = \frac{\sigma_r + \sigma_\theta + \sigma_z}{3} = \frac{2\sigma_\theta + \sigma_z}{3} \quad (16)$$

Further, rearranging Equation 16

$$\frac{\sigma_m}{\sigma_z} = \frac{1}{3} \left(1 + \frac{2\sigma_\theta}{\sigma_z} \right) \quad (17)$$

The effective stress can be written as explained elsewhere [22]

$$\frac{\sigma_{eff}}{\sigma_z} = \left[\frac{1 + 2(\sigma_\theta/\sigma_z)^2 - R^2(2(\sigma_\theta/\sigma_z) + (\sigma_\theta/\sigma_z)^2)}{2R^2 - 1} \right]^{0.5} \quad (18)$$

The stress formability factor under triaxial stress state condition is given as

$$\beta = 3 \left[\frac{(\sigma_m/\sigma_z)}{(\sigma_{eff}/\sigma_z)} \right] \quad (19)$$

The stress formability factor as expressed in Eq. (19) is used to describe the effect of mean stress and the effective stress on the forming limit of P/M compacts in upsetting.

Different stress ratio parameters, namely, $(\sigma_\theta/\sigma_{eff})$, (σ_m/σ_{eff}) and (σ_z/σ_{eff}) are expressed as follows:

$$\frac{\sigma_\theta}{\sigma_{eff}} = \left(\frac{\sigma_\theta/\sigma_z}{\sigma_{eff}/\sigma_z} \right) \quad (20)$$

$$\frac{\sigma_m}{\sigma_{eff}} = \left(\frac{\sigma_m/\sigma_z}{\sigma_{eff}/\sigma_z} \right) \quad (21)$$

$$\frac{\sigma_z}{\sigma_{eff}} = \left(\frac{1}{\sigma_{eff}/\sigma_z} \right) \quad (22)$$

4. Results and discussion

A plot has been presented as shown in Fig. 1 between true height strain and percentage fractional theoretical density for Al-2TiC preforms for two different initial aspect ratios, namely, 0.20 and 0.60, these plots being drawn for two different initial theoretical densities of 82% and 86%. From Fig. 1 it can be seen that there are two stages of deformation. During the initial stages of deformation the densification increases rapidly and thereafter the densification remains constant. Most of the pores are closed effectively during the first stage of deformation and thereafter the pores are elongated due to increasing material flow in the lateral direction before effective closure. For a given true height strain, the density attained by a lower aspect ratio preforms is higher in comparison to higher aspect ratio preforms. Further, the same is true for higher initial density preforms in comparison to lower initial density preforms. Lower aspect ratio preforms has lower pore bed height compared to higher aspect ratio preforms, hence, the density attained for any given height strain is higher for lower aspect ratio preform. It is impossible to achieve 100 percent density for powder metallurgy materials and during the initial stages of the deformation most of the pores are closed effectively, hence, lower aspect ratio and higher initial density preforms has high attained density for any given true height strain. A plot has been presented as shown in Fig. 2 between true height strain and percentage fractional theoretical density for various sintered aluminium composites with aspect ratio of 0.40 and initial theoretical density of 86%. From Fig. 2 it can be seen that for any given true height strain, the density attained by the preforms decreases as the percentage of titanium carbide particles (TiC) increases in the preforms, however, the fracture strain is increased as the TiC content in the aluminium composite increases. With increasing hard carbide particles in the preforms, the increasing lateral flow of the material is evident in Fig. 3 signaling the increasing strength of the preforms. Hence, more applied load is required for further deformation. Further, with the increasing smaller carbide particles in the preforms increases the number of smaller pores further delaying the densification rate with increasing carbide particles.

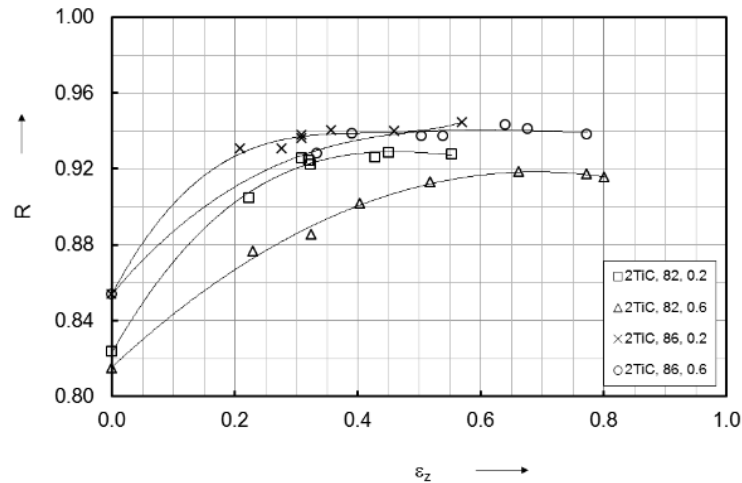


Fig. 1. Influence of aspect ratios and initial theoretical density on the relationship between percent theoretical density and true height strain of Al-2TiC.

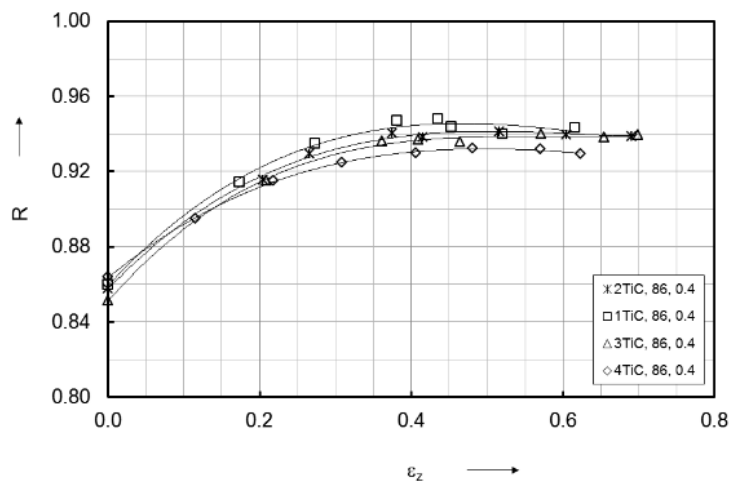


Fig. 2. Relationship between percent theoretical density and true height strain for various sintered aluminium composites.

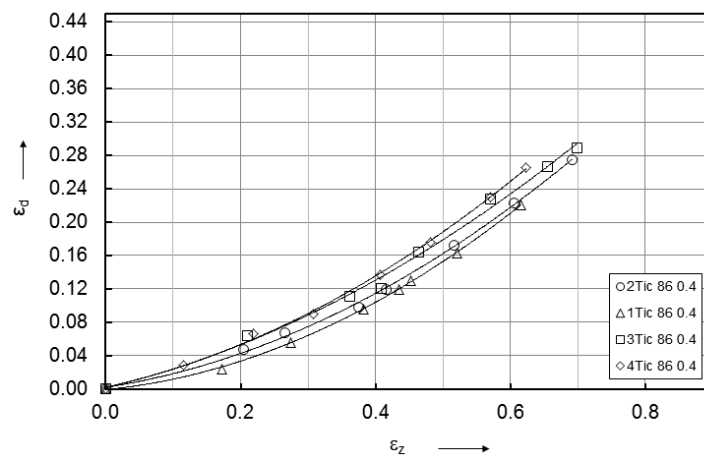


Fig. 3. Relationship between diametral strain and true height strain for various sintered aluminium composites.

A plot has been presented as shown in Fig. 4 between true height strain and stress ratio parameter, $\sigma_\theta/\sigma_{eff}$, for Al-2TiC preforms for two different initial aspect ratios, namely, 0.20 and 0.60, these plots being drawn for two different initial theoretical densities of 82% and 86%. Further, a plot has been presented as shown in Fig. 5 between true height strain and stress ratio parameter, $\sigma_\theta/\sigma_{eff}$, for various sintered aluminium composites with aspect ratio of 0.40 and initial theoretical density of 86%. It can be seen from Figs. 4 & 5 that the hoop stress on the cylindrical preforms during hot deformation increases sharply to almost a maximum value with the increase in strain followed by attainment of steady state stress. The curves plotted in Figs. 4 & 5 clearly portrays the effect of initial relative density, geometry and percentage of TiC in the preforms on the maximum stress achieved for any given true height strain and the final steady state stress. As expected, the stress ratio parameter, $\sigma_\theta/\sigma_{eff}$, increases with increasing levels of strain and increasing initial theoretical density and decreasing aspect ratio. It is found that the stress ratio parameter, $\sigma_\theta/\sigma_{eff}$, decreases for any given true height strain as the TiC content in the aluminium composite is increased. To achieve same hoop stress in the aluminium composites with varying TiC contents, the higher TiC containing composite needs to be deformed more than the lower TiC containing composite. This suggests that the aluminium composite strength increases with the increasing TiC content in the composites. The same is true for stress ratio parameters σ_m/σ_{eff} and σ_z/σ_{eff} as seen in Figs. 6 & 7 as the difference between hydrostatic stress, hoop stress, and axial stress is literally nil against true height strain.

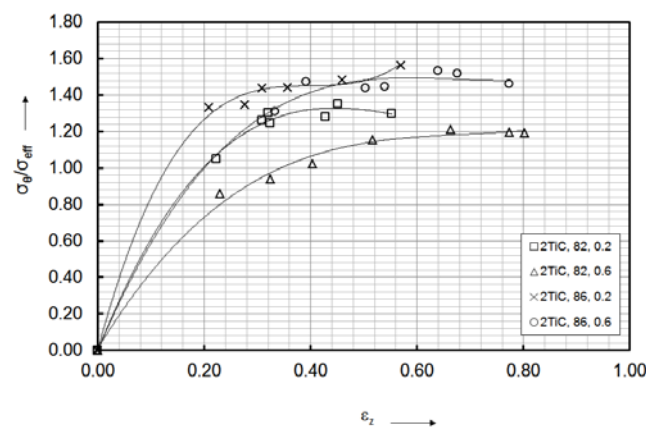


Fig. 4. Influence of aspect ratios and initial theoretical density on the relationship between stress ratio parameter, $\sigma_\theta/\sigma_{eff}$, and true height strain of Al-2TiC.

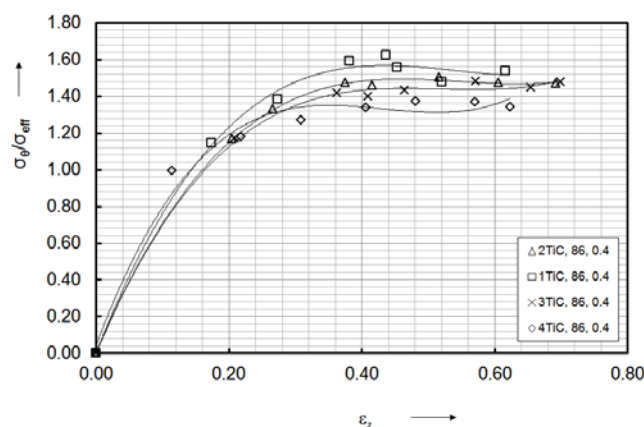


Fig. 5. Relationship between stress ratio parameter, $\sigma_\theta/\sigma_{eff}$, and true height strain for various sintered aluminium composites.

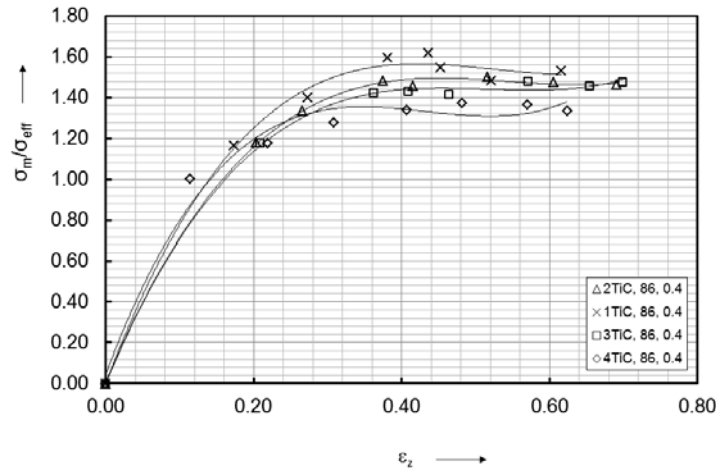


Fig. 6. Relationship between stress ratio parameter, σ_m/σ_{eff} , and true height strain for various sintered aluminium composites.

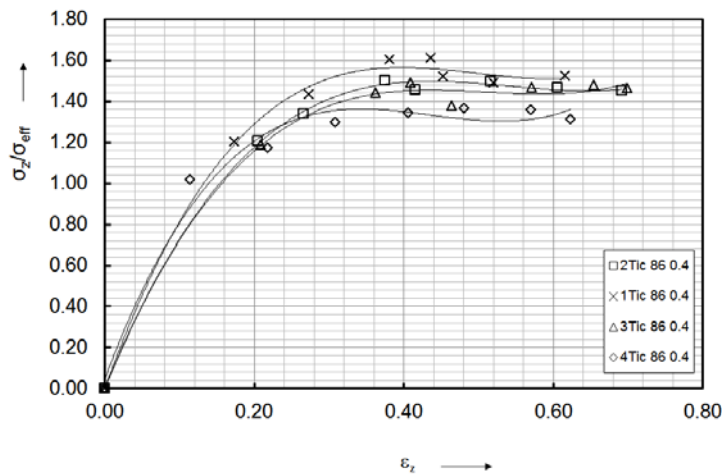


Fig. 7. Relationship between stress ratio parameter, σ_z/σ_{eff} , and true height strain for various sintered aluminium composites.

Figures 8 to 10 is drawn for hoop ($\sigma_\theta/\sigma_{eff}$), mean (σ_m/σ_{eff}), and axial (σ_z/σ_{eff}) stress ratios to that of relative density (R) respectively for various sintered aluminium composite with aspect ratio of 0.40 and initial theoretical density of 86% under hot upsetting of triaxial stress state condition. The stress ratio behavior of the composite plotted in Figs. 8 to 10 was found to be identical. It is noted that the effect of TiC content in the aluminium composite made zero impact on the stress ratio behavior. However, the highest stress ratio value obtained for the smallest percentage of TiC containing composite, which is true for all the stress ratio conditions. As the TiC percentage decreases in the aluminium composite, the maximum stress ratio parameters, ($\sigma_\theta/\sigma_{eff}$), (σ_m/σ_{eff}), and (σ_z/σ_{eff}) also decreases. Hence, Al-4TiC composite can be deformed further provided it is free of defects. Increasing the TiC particles in the preforms, increases chances of further deformation, promoting densification and strength in the composite. It is also noted that there is enhancement in the rate at which the stress ratio parameters increase as the densification progresses.

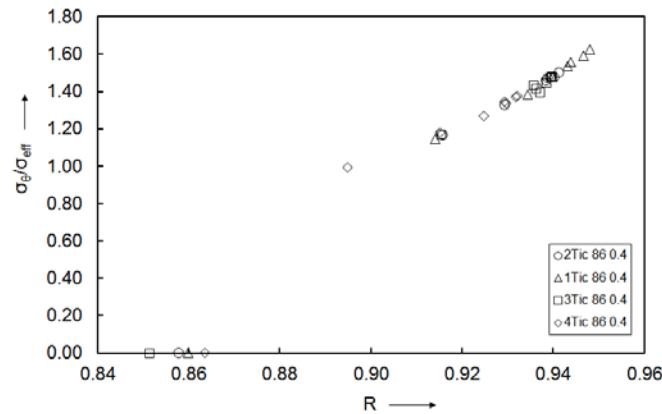


Fig. 8. Relationship between stress ratio parameter, $\sigma_{\theta}/\sigma_{eff}$, and relative density for various sintered aluminium composites.

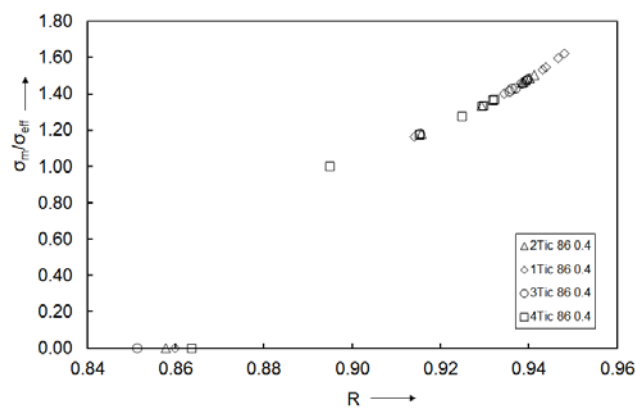


Fig. 9. Relationship between stress ratio parameter, σ_m/σ_{eff} , and relative density for various sintered aluminium composites.

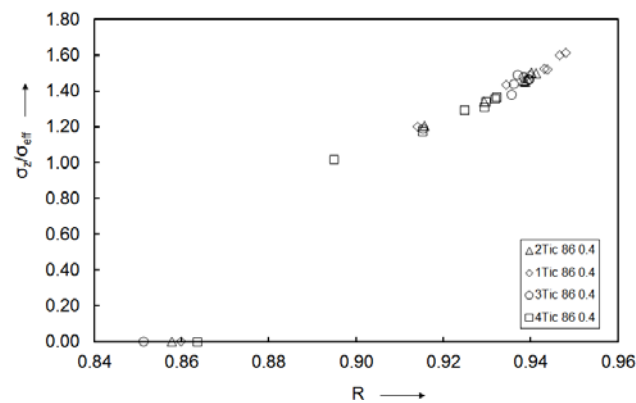


Fig. 10. Relationship between stress ratio parameter, σ_z/σ_{eff} , and relative density for various sintered aluminium composites.

A plot has been presented as shown in Fig. 11 between true height strain and formability stress index for Al-2TiC preforms for two different initial aspect ratios, namely, 0.20 and 0.60, these plots being drawn for two different initial theoretical densities of 82% and 86%. Further, a plot has been presented as shown in Fig. 12 between true height strain and formability stress index for various sintered aluminium composites with aspect ratio of 0.40 and initial theoretical density of 86%. It is observed that formability stress index varies with initial theoretical density, aspect ratio and percentage of TiC content in the preforms. The formability stress index increases with the increasing true height strain. Further, as the initial theoretical density

increases and aspect ratio decreases, the formability stress index also increases for any given true height strain. Also as the percentage of TiC increases in the preforms, the formability stress index decreases for any given true height strain. Formability stress index determines the fracture limit of the deforming material and it can be seen with the increasing percentage of TiC in the preforms, increasing pore bed height and decreasing initial theoretical density decreases the workability of the materials. With increasing smaller TiC hard carbide particles taking up space between Al particles in the preform increases the number of smaller pores giving rise to more lateral deformation (Fig. 3) which in turn reduces the formability of the material.

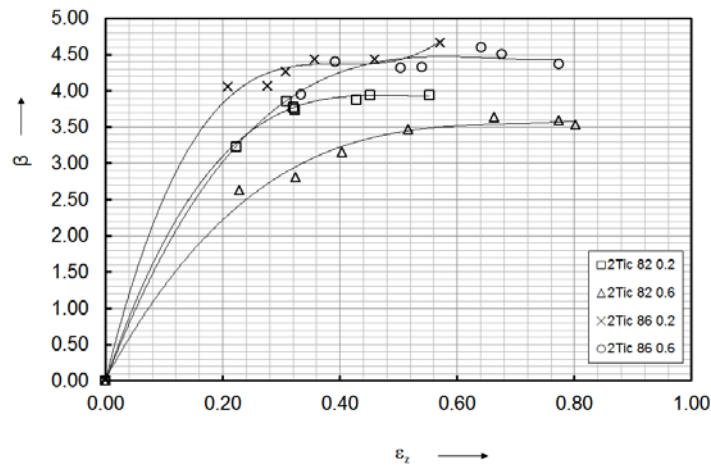


Fig. 11. Influence of aspect ratios and initial theoretical density on the relationship between the formability stress index and true height strain of Al-2TiC.

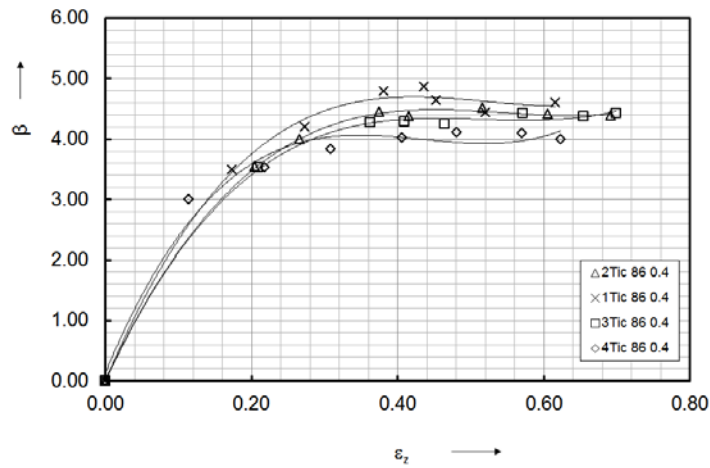


Fig. 12. Relationship between formability stress index and true height strain for various sintered aluminium composites.

Experimental data obtained during the hot deformation of TiC containing aluminium composite has been utilized to plot fracture strain (ϵ_z^f) and formability stress index at fracture (β^f) as shown in Fig. 13. It can be observed that the height strain at fracture increases with the increasing percentage of TiC content in the composites, however, the formability of the material is reduced. This plot can be utilized in the design of preform geometry and die constraints at the free surface of the deforming preform.

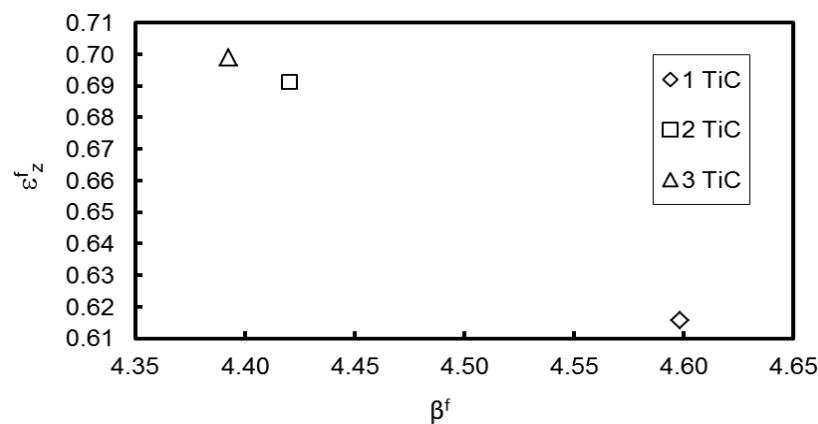


Fig. 13. Relationship between true height strain at fracture and formability stress index at fracture for various sintered aluminium composites.

Figure 14 show the optical micrographs of hot forged aluminium composites containing 1%, 2%, 3% and 4% TiC particles along the upsetting direction. Upon increasing the TiC content in the composite, the interparticle spacing between the powders decreases and the matrix grains change from elongated to equi-axed form. With the increasing TiC particles in the aluminium composite preforms, the particles have axis of approximately same length, thus more planes on which to slip promoting strength in the preform. Further, the elongated particles are frequently observed 45 degrees along the upsetting direction as the material undergoes lateral deformation along with axial (upsetting) deformation. Figure 15 show the microstructure of material consisting of 3% TiC at 100X magnification. The presence of porosity at the centre was little in comparison to extreme diametric end. Further, the pores present at the centre have round shape whilst the pores at extreme diametric side are elongated in the direction of metal flow. It can be said that effective closure of pores of a cylindrical preform at the centre is much higher in comparison to extreme diametric side.

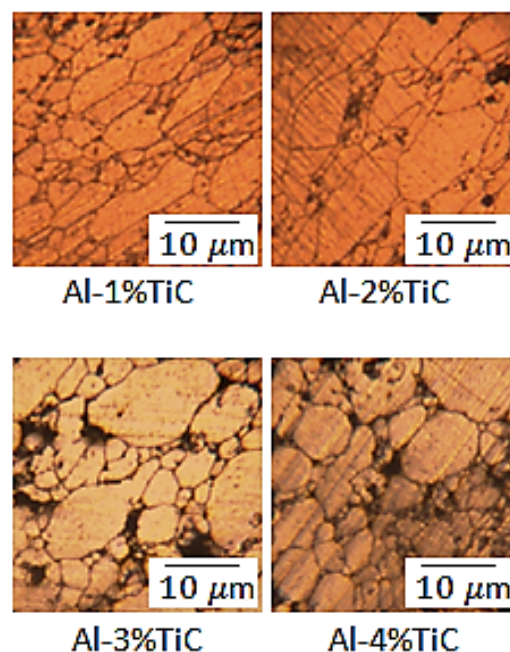


Fig. 14. Optical micrographs of various sintered aluminium composites.

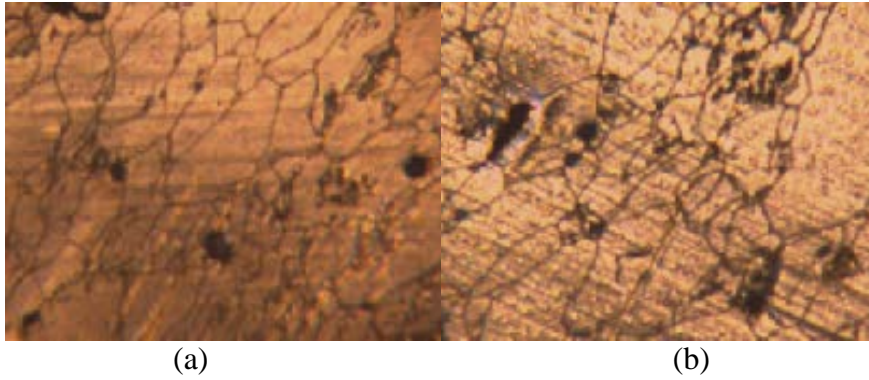


Fig. 15. (a) and (b): Optical micrographs at centre and diametric extreme of the preform, respectively.

5. Conclusions

The design of preform shape and die are very important such that the final part produced is free from defects (fracture) since there is little possibility that the cracks can be arrested during the repressing stage of the deformation. Accordingly, the major conclusions have been drawn that are as follows.

The increase in the addition of TiC content decreases the densification thereby the stress formability index of the preform.

Decreasing the aspect ratio and increasing the initial theoretical density facilitates uniform deformation resulting in improved densification and formability behavior of the preform, however, limits the height strain to fracture.

The variation of aspect ratio, initial theoretical density and TiC content in the preform made nil impact in the stress ratio behavior against densification, however, against true axial strain induced is prominent.

The increase in the addition of TiC content decreases the interparticle spacing and the matrix grains change from elongated to equi-axed form.

Acknowledgements. *The authors would like to acknowledge the help rendered by Mr. Sanjay Singh, Mr. Shiu Prasad and Mr. Navneel Prasad, Metal Workshop Technicians at the University of the South Pacific, during the experimental phase of this project.*

Notation

ε_{θ}	True hoop strain
ε_z	True axial strain
ε_z^f	True axial strain to fracture
ε_{eff}	Effective strain
σ_z	Axial stress
σ_{θ}	Hoop stress
σ_r	Radial stress
σ_m	Hydrostatic stress
σ_{eff}	Effective stress
β	Stress formability factor
β^f	Stress formability factor at fracture
R	Relative density
α	Poisson's ratio
$d\varepsilon_{\theta}$	Plastic hoop strain increment
$d\varepsilon_z$	Plastic axial strain increment

References

- [1] J. Mascarenhas // *Materials Science Forum* **455** (2004) 857.
- [2] Powder metallurgy – Intrinsically Sustainable (Metal Powder Industries Federation, 105 College Road East, Princeton, New Jersey).
- [3] R.M. German Powder Metallurgy Science (MPIF, Princeton, New Jersey, USA, 1994).
- [4] R.H. Derakhshandeh, A.J. Jahromi // *Materials & Design* **32** (2011) 3377.
- [5] Y. Sahin // *Materials & Design* **24** (2003) 671.
- [6] R. Narayanasamy, V. Senthilkumar, K.S. Pandey // *Materials Science and Engineering: A* **456** (2007) 180.
- [7] Y. Liu, L.F. Chen, H.P. Tang, C.T. Liu, B. Liu, B.Y. Huang // *Materials Science and Engineering: A* **418** (2006) 25.
- [8] M.C. Butuc, J.J. Gracio, B.A. Rocha // *International Journal of Mechanical Sciences* **48** (2006) 414.
- [9] R. Narayanasamy, T. Ramesh, K.S. Pandey // *Materials Science and Engineering: A* **391** (2005) 418.
- [10] M.A. Rahman, M.N. El-Sheikh // *Journal of Materials Processing Technology* **54** (1995) 97.
- [11] R. Narayanasamy, V. Anandakrishnan, K.S. Pandey // *Materials & Design* **29** (2008) 1582.
- [12] S. Shima, M. Oyane // *International Journal of Mechanical Sciences* **18** (1976) 285.
- [13] A.L. Gurson // *Journal of Engineering Materials and Technology* **99** (1977) 2.
- [14] S.M. Doraivelu, H.L. Gegel, J.S. Gunasekara, J.C. Malas, J.T. Morgan // *International Journal of Mechanical Sciences* **26** (1984) 527.
- [15] R. Narayanasamy, T. Ramesh, K.S. Pandey // *Materials & Design* **27** (2006) 566.
- [16] R. Narayanasamy, R. Ponalagusamy, K.R. Subramanian // *Journal of Materials Processing Technology* **110** (2001) 182.
- [17] H.A. Kuhn, C.L. Downey // *The International journal of powder metallurgy & powder technology* **10** (1974) 59.
- [18] B.B. Hwang, S. Kobayashi // *International Journal of Machine Tools and Manufacture* **30** (1990) 309.
- [19] B.P.P.A. Gouveia, J.M.C. Rodrigues, P.A.F. Martins // *Journal of Materials Processing Technology* **101** (2000) 52.
- [20] S.V.S. Narayanamurti, B.R. Nageswara, B.P. Kashyap // *Journal of Materials Processing Technology* **147** (2004) 94.
- [21] V. Vujovic, A.H. Shabaik // *Journal of Engineering Materials and Technology* **108** (1986) 245.
- [22] A. Rajeshkannan // *Materials Research* **13** (2010) 457.

DEFECTS IN THIN EPITAXIAL LAYERS OF $(\text{Al}_x\text{Ga}_{1-x})_2\text{O}_3$ GROWN ON Al_2O_3 SUBSTRATES

**A.V. Kremleva^{1,2*}, D.A. Kirilenko^{1,2}, V.I. Nikolaev^{1,2,4}, A.I. Pechnikov^{1,4},
S.L. Stepanov^{1,4}, M.A. Odnoblyudov³, V.E. Bougrov¹, A.E. Romanov^{1,2}**

¹Saint Petersburg National Research University of Information Technologies, Mechanics and Optics,
Kronverskii avenue 49, St. Petersburg, 197101, Russia

²Ioffe Institute of the Russian Academy of Sciences, Polytechnicheskaya str. 26, St. Petersburg, 194021, Russia

³Peter the Great St. Petersburg Polytechnic University, Polytechnicheskaya str.29, St. Petersburg, 195251, Russia

⁴LLC Perfect Crystals, Polytechnicheskaya str. 26 A, St. Petersburg, 194064, Russia

*e-mail: avkremleva@corp.ifmo.ru

Abstract. Gallium oxide is considered as a perspective functional material for a wide range of applications. This includes light emitting devices, high power electronics, gas sensors and catalysts. Investigation of its structural features, particularly, defect structure of the gallium oxide epitaxial layers is crucial for the high quality devices production technology development. This work is focused on the investigation of the defect structure of thin epitaxial layers of $(\text{Al}_x\text{Ga}_{1-x})_2\text{O}_3$ possessing monoclinic structure grown by hydride vapor phase epitaxy on Al_2O_3 substrates. Some of the observed plane defects, twins and stacking faults, are shown for the first time.

Keywords: gallium oxide; twins; stacking faults; dislocations; hydride vapor phase epitaxy; tilted domains; transmission electro microscopy.

1. Introduction

Development of the semiconductor technology is approaching the point where the potential of conventional materials is depleted. In order to overcome the possible stagnation significant efforts have been focused on elaboration of new semiconducting material concepts. In this sphere, the so-called transparent oxide semiconductors (TOS) are considered as a very perspective class of materials, which presents certain advantages over conventional bases of semiconductor technology like Si, SiC, GaAs, sapphire etc. Transparency is the crucial advantage for a variety of light-emitting devices leading to higher standards of efficiency in energy-saving applications. Transparent oxides are highly chemically inert and yet chemically sensitive which enables their diverse application in chemical sensors for harsh environments. Descent electrical conductivity of these materials makes them a preeminent substitute for insulating substrates, and, thus, allows to produce electronic devices with vertical chip design. Transparent semiconductors, being a wide-gap material, are well suited for high power applications. A prominent representative from this class is gallium oxide – it can be employed in most of the above-mentioned fields.

This material, especially the monoclinic phase $\beta\text{-Ga}_2\text{O}_3$, which is the most stable form at ambient conditions has been studied from a view point of possible applications [1]. Gallium oxide can be implemented as a rare-earth phosphor host for electroluminescent devices and displays because tri-valent rare earth species are isovalent to Ga(III) cations in the gallium oxide

structure. This property combined with high transparency and chemical stability allows to produce efficient phosphors of wide spectral range [2-4]. Transparent and conductive gallium oxide substrates can be employed in light emitting devices based on III-nitride technology. High brightness InGaN diodes grown on β -Ga₂O₃ substrates have been demonstrated [5]. Schottky diodes with outstanding characteristics have been produced using various metal contacts [6-8]. Gallium oxide nanowires have shown high performance of field emission [9]. β -Ga₂O₃ can be used for sensing hydrogen [10], oxygen [11] and various organic vapors [12]. Gallium oxide possesses high catalytic activity in dehydrogenation and oxidation of hydrocarbons [13,14] and photoelectrolysis of water [15] due to unique structural characteristics of coordinatively unsaturated surface Ga³⁺ cations. Additionally, β -Ga₂O₃ has a significantly higher critical electric field value and Baliga's figure of merit (FOM) [16] compared to those for SiC or sapphire, which is beneficial for applications in high-power devices [17].

The interest provoked by possible technological applications of gallium oxide has stimulated fundamental studies of electronic, structural and other basic properties of the material. Significant progress has been made to date; however, many uncertainties and unexplained phenomena remain to be explored as it can be seen in literature sources (e.g. in the reviews [18-21]). Structural properties of monoclinic gallium oxide phase (β -Ga₂O₃) are also non-trivial due to complexity of the structure itself and can exhibit unpredicted behavior, especially, in the case of gallium oxide nanostructures. For this reason, we present a study of plane defects found in epitaxial layers of (Al_xGa_{1-x})₂O₃ grown on sapphire substrates. Besides the defects, described in the literature (e.g. [22-30]), we observed certain defects, which might be specific for the gallium oxide grown on sapphire. The focus of the study lies on the possible orientational relationships between various gallium oxide grains and between the grains and the substrate. The observed twins and stacking faults may point to some new ways in epitaxial structures engineering and provide a better understanding of the structural and mechanical properties of the material.

2. Experimental

Epitaxial layers (Al_xGa_{1-x})₂O₃ were grown on *c*-plane sapphire substrates in a home-made hot wall atmospheric pressure HVPE reactor. The reactor consisted of a 75 mm quartz tube placed in a multi zone horizontal furnace. GaCl and dry air were used as precursors. The air was produced by liquefaction and evaporation of atmospheric air and therefore consisted mainly of 21 % of oxygen, 78 % of nitrogen, 1 % of argon and other noble gases. Impurities such as moisture, carbon dioxide, hydrocarbons, etc. were present only in trace amounts (ppm range). The GaCl vapor was synthesized *in-situ* upstream in the reactor by the reaction of metallic gallium (99.9999%) and gaseous hydrogen chloride (99.999 %) at 600 °C. The yield of GaCl formation was estimated to be over 80 %. Similarly to that AlCl₃ vapor was synthesized by reaction of HCl stream with Al. Then the precursor vapors were transported to the deposition zone of the reactor held at 1050 °C where it was mixed with air to produce (Al_xGa_{1-x})₂O₃. The HCl flow through the source was varied from 100 sccm to 400 sccm. The maximal HCl flow was limited by the range of the mass flow controller used, so higher flows were not investigated. The air flow was kept constant at 4 slm. Argon was used as a carrier gas and the total gas flow through the reactor was 10 slm. The input VI/III ratio was in the range from 2 to 8. Under these conditions the deposition rate was in the range from 70 to 250 nm/h. The deposition time was adjusted accordingly to obtain (Al_xGa_{1-x})₂O₃ layers with the thickness in the range of 0.5–1 mm. After the growth the substrate was cooled down to room temperature under argon flow.

The structure of (Al_xGa_{1-x})₂O₃ layers was analysed by means of transmission electron microscopy (TEM). For this purpose cross-sectional TEM specimens were prepared by a conventional procedure comprising face-to-face gluing of the wafer pieces, mechanical grinding and polishing down to the thickness of about 10-20 μm and subsequent ion milling

using Ar^+ beam at 4 keV. Areas of the specimen, which were sufficiently transparent for high-energy electrons (i.e. less than about 100 nm in thickness), were studied and the defect structure of the epitaxial layers was analysed using Jeol JEM-2100F transmission electron microscope (accelerating voltage 200 kV, point-to-point resolution 0.19 nm). Conventional selected area electron diffraction (SAED) technique was used for analysis of the crystal structure and orientational relationships. Conventional dark-field (DF) imaging was used for the visualization of crystal grains, grain boundaries and for the analysis of plane defects in gallium oxide.

3. Results and Discussion

3.1 Twinning on the plane (100). This type of twinning in gallium oxide grown on c -plane oriented sapphire is often observed because (100) plane is a cleavage plane in this structure and stacking fault formation energy is quite low on this plane. For this reason, twin boundaries usually coincide with the twinning plane; an example of such structure with multiple (100) twins is presented in Fig. 1. It is well seen in these images that twin boundaries are mostly parallel to (100) planes. However, some of the boundaries are obviously inclined to this system of planes and are almost parallel either to (001) or (001)* planes (here and further the asterisk sign denotes crystallographic objects of the twinned part of the crystal) which actually coincide with $(\bar{2}02)^*$ or $(\bar{2}02)$ respectively.

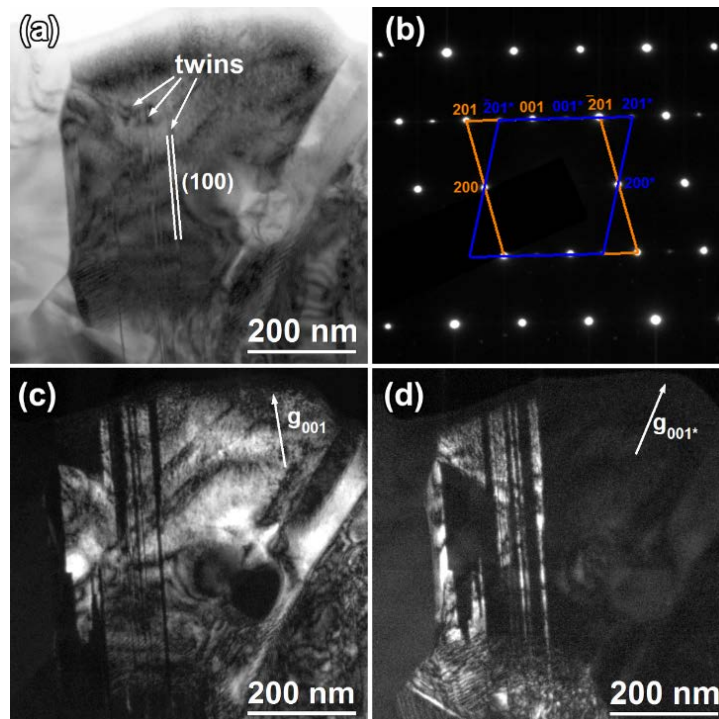


Fig. 1. (100) twins in epitaxial $(\text{Al}_x\text{Ga}_{1-x})_2\text{O}_3$ layer grown on sapphire substrate (0001). (a) Bright-field image showing a grain with multiple (100) twins. (b) Electron diffraction pattern with two subsets of diffraction spots related to the original and twinned crystal lattices. (c) Dark-field image obtained using (001) spot of original lattice. (d) Dark-field image obtained using (001)* spot of the twinned structure so that only twins are visible.

TEM images for m -plane $(\text{Al}_x\text{Ga}_{1-x})_2\text{O}_3$ epitaxial layer grown on c -plane oriented sapphire present another evidence for the presence of twin boundaries non-parallel to the (100) twinning plane. Fig. 2 shows an example of such structure with multiple twinning on the (100) plane similar to the described above. However, in this case the diffraction pattern (Fig. 2a) shows a set of forbidden diffraction spots which arise due to double-diffraction. This, in turn, is possible if twin and parent crystals are both in the way of the electron beam, which is perpendicular to

the TEM image plane. Therefore the twin boundary is inclined to the electron beam which is parallel to the [010] direction in the presented images. Thus the twin boundary cannot be (100) plane or any other plane from the [010] zone axis. Also, dark-field images (Fig. 2b and Fig. 2c) showing twinned and original crystal parts show that some areas introduce bright contrast in both images. Additionally, the presence of the crystal and its twin above each other in such projection produces Moiré patterns (Fig. 2d), which usually arise because of superposition of two lattice images.

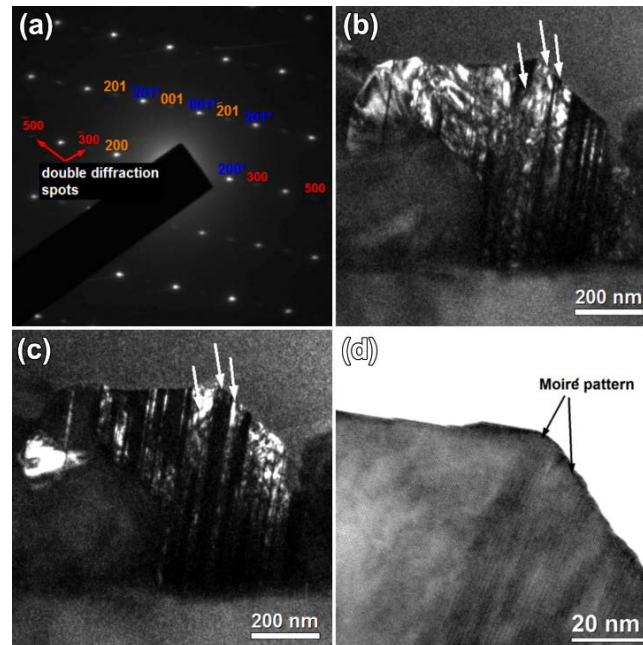


Fig. 2. Example of multiple (100) twins in epitaxial $(\text{Al}_x\text{Ga}_{1-x})_2\text{O}_3$ layer grown on sapphire substrate (0001). (a) Electron diffraction pattern with two subsets of diffraction spots, the systematic row $\{1+2n\ 0\ 0\}$ related to double diffraction is visible. (b) and (c) Dark-field images of the structure. Arrows indicate areas of bright contrast in both images where twin boundary is inclined to the image plane. (d) High-resolution TEM image of the $(\text{Al}_x\text{Ga}_{1-x})_2\text{O}_3$ lattice showing Moiré pattern produced by superposition of diffraction patterns from twin domains.

The (100) plane is a cleavage plane of monoclinic gallium oxide, and thus energy of plane defect formation along this plane is relatively low. Such defects can be generated during the cooling of the structure after growth due to mechanical stress caused by the difference of the thermal expansion coefficients of the layer and the substrate. However, we also observed twin boundaries which were inclined to the (100) twinning plane. It is very unlikely that these anomalous twin boundaries resulted from thermal mechanical stresses because this scenario is energetically unfavorable. Alternatively, twinning can occur during the very process of epitaxial growth and the observed anomalous twin boundaries are formed by crystal grains growing over each other. This kind of defects can be potentially eliminated by careful optimization of the growth parameters, especially for the initial stage of growth.

3.2 Stacking faults in (111) plane. Another type of defects which we found in these structures are stacking faults on (111) plane (Fig. 3). Stacking faults provide specific contrast in a dark-field image (e.g., Fig. 3b) if the scalar product of their fault vector \mathbf{R} with the diffraction vector \mathbf{g} used for this image is non-zero or non-integer. For this reason the stacking faults are almost invisible for certain diffraction vectors used (Fig. 3c and Fig. 3d).

The presented dependence of the stacking fault visibility on diffraction vector allows us to suppose that the fault vector \mathbf{R} lays in the stacking fault plane thus the stacking faults can result from mechanical stress. In order to determine the stacking fault plane more precisely we tilted the specimen to another zone axis and found that the stacking faults visible as narrow lines when $[010]$ direction is parallel to the electron beam. That is their plane is perpendicular to the image plane in this case.

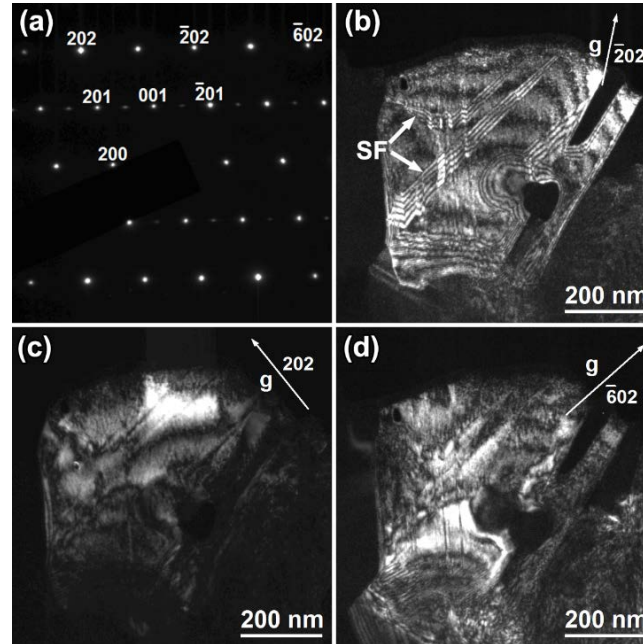


Fig. 3. Stacking fault in $(\text{Al}_x\text{Ga}_{1-x})_2\text{O}_3$ layer grown on sapphire substrate (0001). (a) Electron diffraction pattern where the used diffraction spots are marked. (b) Dark-field image obtained using $\bar{2}02$ spot. The stacking faults (SF) are clearly visible. The zigzag shape of the stacking fault is caused by its propagation through a set of twins on (100) plane, so that the direction of the stacking fault plane changes inside twinned part of the crystal lattice. (c) and (d) Dark-field images obtained using $\bar{6}02$ and 202 spots, which are almost perpendicular to each other. The stacking fault in these cases is practically invisible.

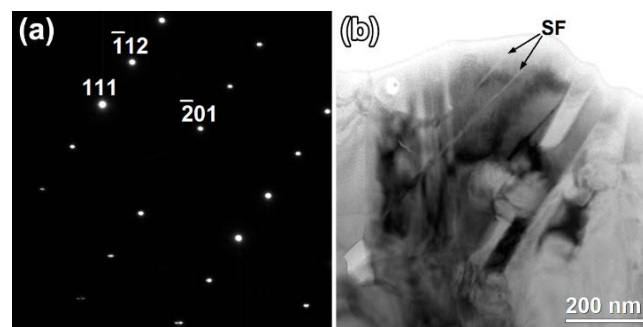


Fig. 4. The observed stacking faults at crystal orientation by $[1\bar{3}2]$ zone axis in $(\text{Al}_x\text{Ga}_{1-x})_2\text{O}_3$ on c -plane sapphire. (a) Electron diffraction pattern. (b) Image of the stacking faults which are visible as narrow lines because their plane is almost parallel to the electron beam.

According to the relation between stacking fault image and diffraction spots in the diffraction pattern (Fig. 4) we deduced that the observed stacking faults are on (111) plane. It is remarkable, that the stacking fault continuously extends through the (100) twins in the grain and its zig-zag shape (Fig. 3b) corresponds to the different orientation of (111) planes in the twins.

3.3. Growth plane change due to the twinning on $(\bar{1}12)$ plane. Another type of plane defects has been revealed. Fig. 5 presents TEM images of a $(\text{Al}_x\text{Ga}_{1-x})_2\text{O}_3$ layer grown on a c -plane oriented sapphire substrate. Some of the $(\text{Al}_x\text{Ga}_{1-x})_2\text{O}_3$ grains has typical orientation so that $(\bar{2}01)$ plane is parallel to the substrate surface, while their $[010]$ or $[132]$ direction oriented along $[1\bar{1}00]$ axis of sapphire [31]. However, some of the grains have another orientation as can be seen in the electron diffraction pattern presented in Fig. 3a. Analysis of the diffraction spots location shows that it corresponds to the presence of a twin on $(\bar{1}12)$ plane. So, the planes $(\bar{1}12)$ in the twinned and untwinned lattices coincide. The twin boundary parallel to this plane in the presented case.

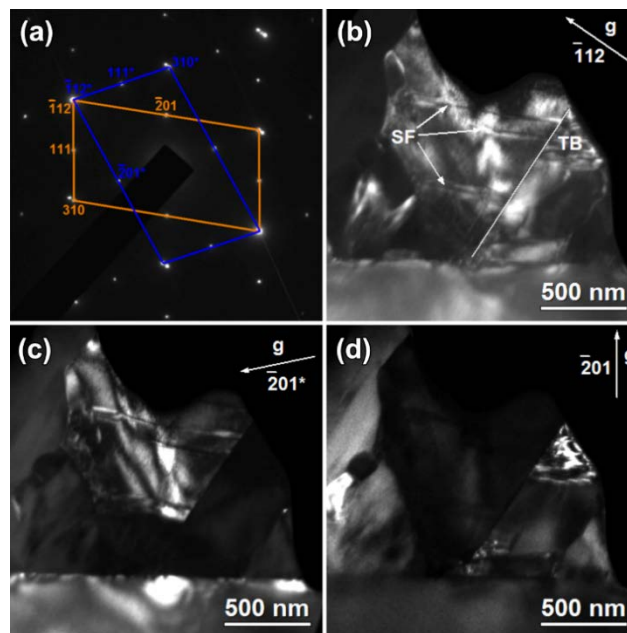


Fig. 5. Twin on the $(\bar{1}12)$ plane in epitaxial $(\text{Al}_x\text{Ga}_{1-x})_2\text{O}_3$ layer grown on sapphire substrate (0001). (a) Electron diffraction pattern with the two subsets of diffraction spots. (b) Dark-field image obtained using $\bar{1}12$ spot that corresponds to the twinning plane. The grains are separated by the twin boundary (TB) parallel to $(\bar{1}12)$ plane are visible. (c) and (d) Dark-field images obtained using dedicated $\bar{2}01$ spots of the twin and basic grain. Note, that stacking faults (SF) in (310) plane are visible in the twin.

3.4. Tilted domains. Domains which differ from the rest of the layer by their crystal lattice tilt of about $2\text{-}3^\circ$ have been discovered in the studied samples. The presence of the tilt and its magnitude are determined using electron diffraction patterns (Fig. 6a). In the case of tilt, the shape of diffraction spots changes to elongated streaks. The dark-field images obtained using left and right parts of a streak (Fig. 6b and Fig. 6c) show the shape of the domain tilted respectively to the main part of the layer.

The domains has characteristic size of about several micrometers and consist of various crystalline grains similar to the whole epitaxial film grown on the sapphire substrate. That is the grains in the tilted domain possess the same orientation relationships as described before. However, all the grains, thus, tilted by small angle with respect to the layer and the substrate. The observed domains were overgrown by the main layer structure and, thus, did not affect the orientation of the layer surface. It is worth noting, that the tilted domains were found only in $(\text{Al}_x\text{Ga}_{1-x})_2\text{O}_3$ layers thicker than $1\ \mu\text{m}$.

4. Conclusions

We present a set of plane defects emerging in $(\text{Al}_x\text{Ga}_{1-x})_2\text{O}_3$ grown on sapphire substrates. The observed features of the defect structure provide a new insight into the material structural

properties. The fact of twinning on the plane $(\bar{1}12)$, which transforms the growth plane into (310) , may be useful for better control of the growth modes and epitaxial design development.

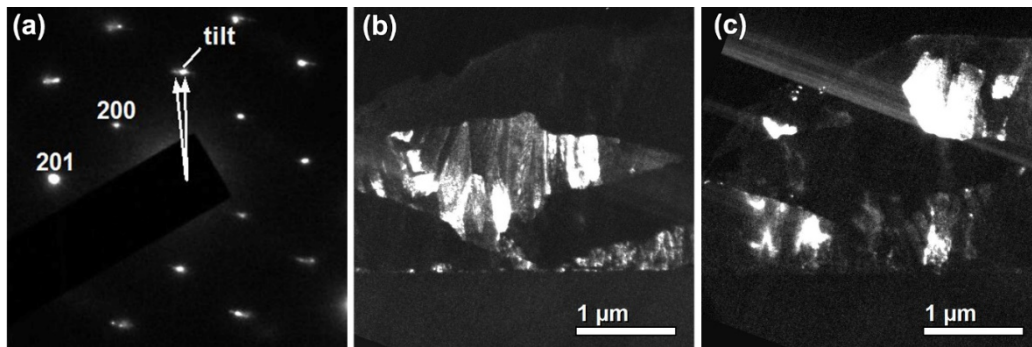


Fig. 6. A domain tilted by small angle. (a) Electron diffraction pattern showing presence of a tilt in the structure. (b) Dark-field image obtained in a part of a diffraction streak showing the tilted domain in the layer. (c) Dark-field image showing the rest of the layer.

The new type of plane defect – stacking fault in (111) plane – is interesting from the point of view of $(\text{Al}_x\text{Ga}_{1-x})_2\text{O}_3$ structural properties. Additionally, peculiarities of the twin boundaries in the case of (100) twins are important for understanding of the structural and mechanical properties of gallium oxide layers grown on sapphire substrates. These findings point that the initial stages of the growth are crucial for the obtaining of the layers with predefined crystalline quality and the corresponding studies are essential for the technology development of gallium oxide based semiconductor devices.

Acknowledgements. V.I. Nikolaev, A.I. Pechnikov, V.E. Bougrov, A.E. Romanov acknowledge support from the Russian Science Foundation (Grant no. 14-29-00086) of the research of gallium oxide crystallization. The work has been carried out with the use of equipment of the Federal Joint Research Centre «Material science and characterization in advanced technology» (Ioffe Institute, St.-Petersburg, Russia).

References

- [1] J. Ahman, G. Svensson, J. Albertsson // *Acta Crystallographica Section C* **52** (1996) 1336.
- [2] J.H. Kim, K.H. Yoon // *Journal of the Korean Physical Society* **53** (2008) 818.
- [3] T. Miyata, T. Nakatani, T. Minami // *Journal of Luminescence* **87** (2000) 1183.
- [4] Y. Tokida, S. Adachi // *ECS Journal of Solid State Science and Technology* **3** (2014) R100.
- [5] D. Inomata, K. Aoki // *Proceedings of SPIE* **8987** (2014) 89871U.
- [6] K. Sasaki, M. Higashiwaki, A. Kuramata, T. Masui, S. Yamakoshi // *IEEE Electron Device Letters* **34** (2013) 493.
- [7] T. Oishi, Y. Koga, K. Harada, M. Kasu // *Applied Physics Express* **8** (2015) 031101.
- [8] M.A. Rozhkov, E.S. Kolodeznyi, A.M. Smirnov, V.E. Bougrov, A.E. Romanov // *Materials Physics and Mechanics* **24** (2015) 194.
- [9] I. Lopez, E. Nogales, P. Hidalgo, B. Mendez, J. Piqueras // *Physica Status Solidi A* **209** (2012) 113.
- [10] S. Nakagomi, K. Yokoyama, Y. Kokubun // *Journal of Sensors and Sensor Systems* **3** (2014) 231.
- [11] M. Fleischer, L. Hollbauer, E. Born, H. Meixner // *Journal of the American Ceramic Society* **80(8)** (1997) 2121.
- [12] S.P. Arnold, S.M. Prokes, F.K. Perkins, M.E. Zaghoul // *Applied Physics Letters* **95** (2009) 103102.
- [13] B. Zheng, W. Hua, Y. Yue, Z. Gao // *Journal of Catalysis* **232** (2005) 143.

- [14] Y. Hou, L. Wu, X. Wang, Z. Ding, Z. Li, X. Fu // *Journal of Catalysis* **250** (2007) 12.
- [15] N.K. Shrestha, K. Lee, R. Kirchgeorg, R. Hahn, P. Schmuki // *Electrochemistry Communications* **35** (2013) 112.
- [16] B.J. Baliga // *Journal of Applied Physics* **53** (1982) 1759.
- [17] M. Higashiwaki, K. Sasaki, A. Kuramata, T. Masui, S. Yamakoshi // *Physica Status Solidi A* **1** (2014) 21.
- [18] S.I. Stepanov, V.I. Nikolaev, V.E. Bougrov, A.E. Romanov // *Reviews of Advanced Materials Science* **44** (2016) 63.
- [19] S. Kumar, R. Singh // *Physica Status Solidi RRL* **7** (2013) 781.
- [20] H. Frenzel, A. Lajn, M. Grundmann // *Physica Status Solidi RRL* **7** (2013) 605.
- [21] H. Peelaers, C.G. Van de Walle // *Physica Status Solidi B* **252** (2015) 828.
- [22] S.Y. Lee, H.C. Kang // *Journal of Crystal Growth* **412** (2015) 25.
- [23] M. Mitome, S. Kohiki, K. Hori, M. Fukuta, Y. Bando // *Journal of Crystal Growth* **286** (2006) 240.
- [24] S.-C. Zhu, S.-H. Guan, Z.-P. Liu // *Physical Chemistry Chemical Physics* **18** (2016) 18563.
- [25] M. Baldini, M. Albrecht, D. Gogova, R. Schewski, G. Wagner // *Semiconductor Science and Technology* **30** (2015) 024013.
- [26] H.W. Kim, S.H. Shim // *Thin Solid Films* **515** (2007) 5158.
- [27] G. Wagner, M. Baldini, D. Gogova, M. Schmidbauer, R. Shewski, M. Albrecht, Z. Galazka, D. Klimm, R. Fornari // *Physica Status Solidi A* **211** (2014) 27-33.
- [28] K. Nakai, T. Nagai, K. Noami, T. Futagi // *Japanese Journal of Applied Physics* **54** (2015) 051103.
- [29] H.-S. Chung, S.C. Kim, D.H. Kim, J.W. Kim, O-J. Kwon, C. Park, H.H. Oh // *Journal of the Korean Physical Society* **55** (2009) 68.
- [30] V.I. Nikolaev, A.I. Pechnikov, S.I. Stepanov, I.P. Nikitina, A.N. Smirnov, A.V. Chikiryaka, S.S. Sharofidinov, V.E. Bougrov, A.E. Romanov // *Materials Science in Semiconductor Processing* **47** (2016) 16.
- [31] V.I. Nikolaev, A.I. Pechnikov, S.I. Stepanov, S.S. Sharofidinov, A.A. Golovatenko, I.P. Nikitina, A.N. Smirnov, V.E. Bugrov, A.E. Romanov, P.N. Brunkov, D.A. Kirilenko // *Semiconductors* **50** (2016) 980.

MATHEMATICAL MODEL OF ULTRASOUND TRANSMISSION IN GRADIENT MATERIALS SYNTHESIZED IN ARC SURFACING UNDER CONTACT LOADING

V.D. Sarychev¹, A.Y. Granovskiy¹, S.A. Nevskii^{1*}, S.V. Konovalov^{1,2}, V.E. Gromov¹,
M.V. Temlyantsev¹

¹Siberian State Industrial University, Novokuznetsk, 654007, Russia

²Samara National Research University, Samara, 443086, Russia

*e-mail: nevskiy.sergei@yandex.ru

Abstract. The paper deals with a two-dimensional problem of time-dependent elasticity theory, examining waves generated on the top layer interface by the source of normal stresses applied to the top layer interface. Here the lower layer interface is free of stresses. The use is made of integral transformations to relate displacement transforms with stresses on the top layer interface. Exponent power series expansion is obtained for the transform of vertical displacements. Analytical approach to each member of the series ensures a precise solution of the problem. Displacement field vs. time dependence on the layer interface has been calculated. The findings are referred to in the process of ultrasound controlling the layer by finite size sensors.

Keywords: stress; deformation; strengthened layer; surfacing; ultrasound waves.

1. Introduction

Arc surfacing is a procedure applied for wear protection of large-sized products [1, 2]. The point of it is coating of the product surface with a wear-resistant overlay via welding electrode melting. As a result, product structure and properties become depth gradient. On the interface “surfaced layer/substrate”, there are mechanical stresses, arising due to the difference and resulting in overlay splitting off. On the other hand, calculated stress-strain state of the overlay in static contact loading [3] indicates compressive stresses on these boundaries, making it possible to conclude that harder overlays further not varying propagation of stresses on the interface of contacting layers. However, the overlays are subject to time-dependent contact loading in the process of operation, as a consequence, temporal variation of stress-strain state is possible. As known, elastic waves appear in a material under such loading and might cause both failure and healing of diverse defects [4]. Therefore, studies on specifics of wave propagation in multilayered materials have been gaining particular importance. The papers are focused on wave propagation in these materials [4 – 8]. The authors [4] investigate Rayleigh wave propagation on the interface “solid/fluid”. As found out, it is relevant for Rayleigh wave velocity whether there is fluid, and it also depends on the wave trajectory curvature, as well on the curvature in the direction perpendicular to the trajectory. The scientists [5, 6] offered a general theory of seismic wave field propagation in multilayered materials and applied it to wave interference in these materials. Pham Chi Vinh et al. [7] explored transmission of elastic waves in the system “functionally gradient material layer/elastic layer”. As a result, reflection and transmission coefficients were obtained

explicitly; they were in line with findings of numerical methods. The paper [8] studies Love wave propagation using Wentzel–Kramers–Brillouin method. The dispersion equation for surface Love waves is in ordinary mathematical form. As revealed, coefficients of gradient members influence significantly dispersion curves and phase velocities of Love waves.

Volumetric wave (Lamb wave) transmission in heterogeneous materials is explored in papers [9, 10]. A.V. Avershieva et al [9] used numerical and analytical methods to examine Lamb wave propagation in elastic isotropic and orthotropic layers. They offered a procedure of surface Lamb wave generation with the help of finite elements method and carried out a comparative analysis of a fundamental symmetric mode of Lamb waves around the second critical velocity, determined numerically and analytically. It has been revealed that the growing Poisson’s ratio is associated with the monotonous decline of the relative second critical velocity. The layer thickness is of significant importance for dispersion curves corresponding with the fundamental symmetric mode. The review of research procedures to explore Lamb wave transmission in anisotropic materials is provided in [10]. This paper is concerned with six-dimensional Cauchy formalism. It helped to form dispersion curves of these waves and carry out a comparative study on the results of numerical methods. It is in a reasonably good agreement with numerical calculations.

The main drawback of investigations into elastic wave transmission, as stated in papers [4 – 10], is insufficient information about peculiarities of wave transmission in a particular layer. A great number of works pay attention to time-dependent load; some of them are of significant importance [11 – 12]. The authors [11] applied the method of integral transformations to solve two-dimensional problem analytically and identify influence of time-dependent load on the elastic layer surface in conditions of mixed boundary value problem on each interface. As a result, normal stress propagation has been obtained in different instants of time and at different distances from the source. Their analysis has pointed out clear stress steps on the symmetry axis; and a forward and the first reflected widening wave have a form of a single jog. Under further reflection the behavior of stress propagation through the layer depth differs from the stepped one due to the distortion wave influence and gradual spreading of wave energy in the cross-sectional direction. When moving away from the source there is smooth stress propagation. The authors [12] investigated the effect on time-dependent load moving on the surface of a homogenous isotropic elastic semi-space. For uniform motion quadrature solutions were obtained and normal motion propagation of the semi-space surface was analyzed in diverse ranges of load motion speed.

Therefore, this work aims at obtaining solutions of dynamic elasticity theory equations, which are appropriate for ultrasound control of the layer by finite size sensors.

2. Problem statement

We consider the motion problem of waves emitted by the source with a finite action radius r (Fig. 1). Wave receiver is in the point M at the finite length L . We use non-dimensional variables to write the equations:

$$(\bar{x}, \bar{z}) = (x, z)/h, \bar{t} = c_1 t/h, (\bar{u}, \bar{w}) = (u, w)/h, (\bar{\sigma}_z, \bar{\sigma}_x, \bar{\tau}) = (\sigma_z, \sigma_x, \tau)/(c_1^2 \rho) \quad (1)$$

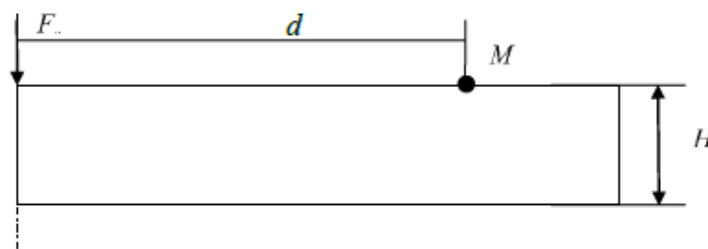


Fig. 1. Statement of the wave propagation problem in the finite thickness layer.

For variables (1) generalized Hooke's law and motion equation are written in the form:

$$\begin{aligned} \sigma_x &= \frac{\partial u}{\partial x} + (1 - 2c^2) \frac{\partial w}{\partial z}, \sigma_z = (1 - 2c^2) \frac{\partial u}{\partial x} + \frac{\partial w}{\partial z}, \tau = c^2 \left(\frac{\partial u}{\partial z} + \frac{\partial w}{\partial x} \right); \\ \frac{\partial^2 u}{\partial x^2} + (1 - c^2) \frac{\partial^2 w}{\partial x \partial z} + c^2 \frac{\partial^2 u}{\partial z^2} - \frac{\partial^2 u}{\partial t^2} &= 0, \\ c^2 \frac{\partial^2 w}{\partial x^2} + (1 - c^2) \frac{\partial^2 u}{\partial x \partial z} + \frac{\partial^2 w}{\partial z^2} - \frac{\partial^2 w}{\partial t^2} &= 0, \end{aligned} \quad (2)$$

where $c^2 = \frac{c_2^2}{c_1^2}$, $c_1^2 = \frac{2\mu + \lambda}{\rho}$, $c_2^2 = \frac{\mu}{\rho}$, λ and μ – Lamé parameters, ρ – material density. The conditions on the layer interface are in the form:

$$\begin{aligned} z = 1: \sigma_z &= -\frac{1}{\pi} \frac{\delta}{\delta^2 + x^2} (\theta(t) - \theta(t - T_0)), \sigma_{xz} = 0; \\ z = -1: \sigma_z &= \sigma_{xz} = 0, \end{aligned} \quad (3)$$

where θ – Heaviside function, T_0 – signal response time.

3. Results of calculations

We use the method of finite elements to solve the boundary problem (2), (3). Problem parameters are given in Table 1.

Table 1. Problem parameters.

Symbol	Description	Value
d	Source to receiver distance	20 mm
H	Plate thickness	50,15, 10, 3 mm
F_y	Source force amplitude	100 H
t_0	Pulse duration	$2 \cdot 10^{-6}$ s
E	Young modulus	70 GPa
ν	Poisson's ratio	0.33
Δx	Width of load pulse	1 mm

A fit for vertical loading (3) was made using Fourier method to ease the calculations. Longitudinal (a) and time (b) propagation of load from the source is given in Fig. 2.

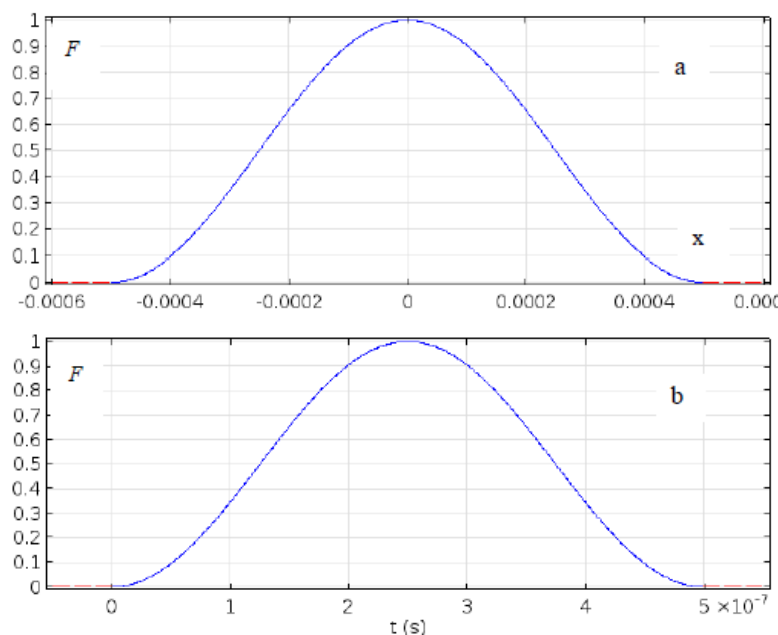


Fig. 2. Load propagation from the source.

The calculation data of cross-sectional displacement velocity fields in the point M at a plate thickness of 50 mm is given in Fig. 3. Their analysis demonstrates the similarity of these plates to Raleigh wave propagation. The situation gets more complicated when layer thinning (Fig. 4).

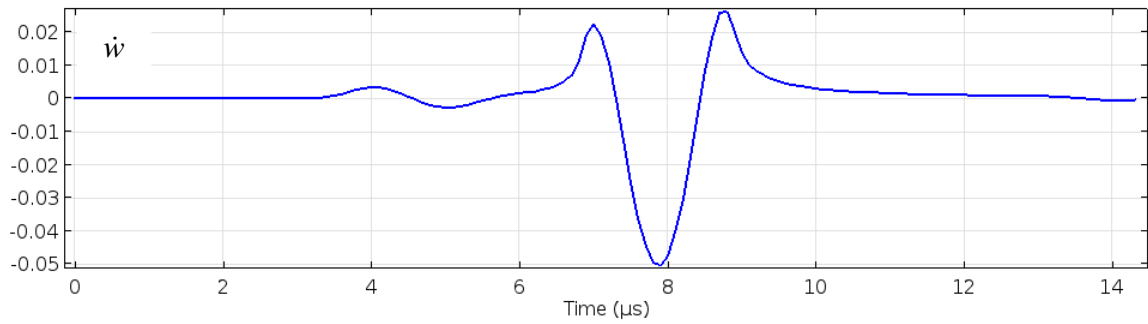


Fig 3. Calculation data of velocity fields for a 50 mm thick plate.

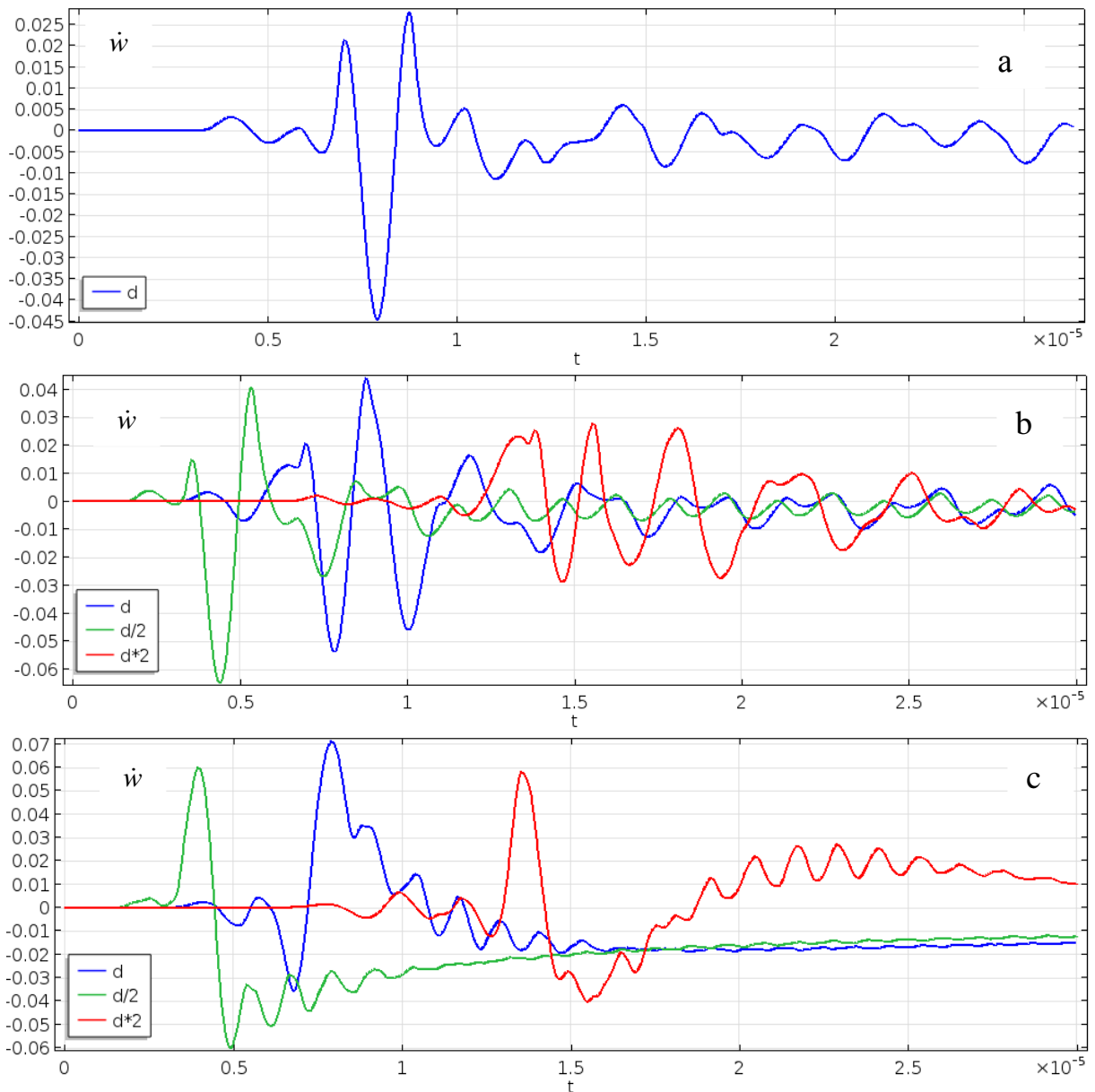


Fig. 4. Calculation data of velocity fields for 15 mm (a), 10 mm (b), 3 mm (c) plates.

The observed wave pattern is a result of travelling pulse overlapping and multi-reflected waves from the lower boundary. It is noteworthy, that after pulse termination in a 3 mm thick plate (Fig. 4c) the displacement velocity gets stabilized in the range of negative values around the value of -0.015 , whereas at the distance of $2d$ from the source there is strengthening observed in the range of positive values in the interval $1.5 < t < 2 \mu\text{s}$, and declining to 0.01 at $t > 2.5 \mu\text{s}$. This fact indicates volumetric Lamb waves in the material alongside with the surface waves.

4. Results of analytical estimations

We transform (2) and (3) using integral Laplace transform for time and Fourier method for the coordinate. Then (3) is written in the form:

$$\Sigma_1 = -\frac{\exp(-\delta|q|)(1-\exp(-pT))}{p}, T_1 = T_{-1} = \Sigma_{-1} = 0, \quad (4)$$

and the system of equations (2)

$$W'''' - (n_1^2 + n_2^2)W'' + n_1^2 n_2^2 W = 0, U = -\frac{i}{(1-b^2)qn_1^2} (W'''' - (n_2^2 + n_1^2(1-b^2))W'),$$

$$n_1^2 = q^2 + p^2, n_2^2 = q^2 + p^2 b^2, b^2 = 1/c^2, \quad (5)$$

$$\Sigma(z) = W'(z) - i(2c^2 - 1)qU(z),$$

$$T(z) = c^2(U'(z) + iqW(z)).$$

We express stresses on the interfaces with the help of displacement value W on the interfaces and its derivatives

$$\Sigma = -\frac{1}{b^2(b^2-1)n_1^2} ((b^2-1)W'''' - (2(b^2-1)n_1^2 + (b^2-1)n_2^2)W'),$$

$$T = \frac{i}{b^2(b^2-1)qn_1^2} (b^2W'' - (2n_2^2 + n_1^2 b^2)W). \quad (6)$$

For displacement transform W we obtain a boundary problem:

$$W'''' - (n_1^2 + n_2^2)W'' + n_1^2 n_2^2 W = 0,$$

$$(2-b^2)W''''(1) - (2(1-b^2)n_1^2 + (2-b^2)n_2^2)W'(1) = -b^2(1-b^2)n_1^2 \Sigma_1,$$

$$(2-b^2)W''''(-1) - (2(1-b^2)n_1^2 + (2-b^2)n_2^2)W'(-1) = 0,$$

$$b^2W''(1) - (2n_2^2 - n_1^2 b^2)W(1) = 0,$$

$$b^2W''(-1) - (2n_2^2 - n_1^2 b^2)W(-1) = 0. \quad (7)$$

The solution of the boundary problem (11) is in the form:

$$W(z) = S_1 \sinh(n_1 z) + S_2 \sinh(n_2 z) + C_1 \cosh(n_1 z) + C_2 \cosh(n_2 z). \quad (8)$$

Substituting (8) into (7) results in two systems of algebraic equations:

$$\begin{cases} s_{11}S_1 + s_{12}S_2 = f, \\ s_{21}S_1 + s_{22}S_2 = 0; \end{cases} \begin{cases} c_{11}C_1 + c_{12}C_2 = f, \\ c_{21}C_1 + c_{22}C_2 = 0; \end{cases}$$

$$s_{11} = (n_2^2 + q^2) \cosh(n_1), s_{12} = 2n_1 n_2 \cosh(n_2),$$

$$s_{21} = 2q^2 \sinh(n_1), s_{22} = (n_2^2 + q^2) \sinh(n_2), \quad (9)$$

$$c_{11} = (n_2^2 + q^2) \sinh(n_1), c_{12} = 2n_1 n_2 \sinh(n_2),$$

$$c_{21} = 2q^2 \cosh(n_1), c_{22} = (n_2^2 + q^2) \cosh(n_2), f = -b^2 n_1 \Sigma_1 / 2.$$

Solution (9):

$$S_1 = \frac{b^2 n_1 (n_2^2 + q^2) \sinh(n_2)}{2\Delta_s} \Sigma_1, S_2 = -\frac{b^2 n_1 q^2 \sinh(n_1)}{\Delta_s} \Sigma_1,$$

$$C_1 = \frac{b^2 n_1 (n_2^2 + q^2) \cosh(n_2)}{2\Delta_c} \Sigma_1, C_2 = -\frac{b^2 n_1 q^2 \cosh(n_1)}{\Delta_c} \Sigma_1, \quad (10)$$

$$\Delta_s = (n_2^2 + q^2)^2 \cosh(n_1) \sinh(n_2) - 4n_1 n_2 q^2 \cosh(n_2) \sinh(n_1),$$

$$\Delta_c = (n_2^2 + q^2)^2 \cosh(n_2) \sinh(n_1) - 4n_1 n_2 q^2 \cosh(n_1) \sinh(n_2).$$

Using (10) and (8) we write the expression for $W(1)$, which relates stress transforms to those of displacement on the top layer interface:

$$W = \frac{b^2 n_1 (n_2^2 - q^2)}{2} \left(\frac{\cosh n_1 \cosh n_2}{\Delta_c} + \frac{\sinh n_1 \sinh n_2}{\Delta_s} \right) \Sigma_1. \quad (11)$$

Taking into account (3) the formula (11) is given in the form:

$$W = -\frac{b^4 p n_1 \exp(-\delta|q|)(1-\exp(-pT))}{2} L, \quad (12)$$

$$L = \left(\frac{\cosh n_1 \cosh n_2}{\Delta_c} + \frac{\sinh n_1 \sinh n_2}{\Delta_s} \right).$$

To compare with the numerical results a time-correlation of cross-sectional displacements on the upper interface is required at distances $x = l: w(l, h, t) = \Psi(t)$. For this purpose, we transform denominators (11) as follows:

$$\Delta_s = \frac{R_1}{4} \exp(n_1 + n_2) (1 - q_1), \Delta_c = \frac{R_1}{4} \exp(n_1 + n_2) (1 - q_2), \quad (13)$$

$$R_1 = (n_2^2 + q^2)^2 - 4q^2 n_1 n_2, R_2 = (n_2^2 + q^2)^2 + 4q^2 n_1 n_2,$$

$$q_1 = A + \gamma B, q_2 = A - \gamma B,$$

$$A = \exp(-2(n_1 + n_2)), B = \exp(-2n_2) - \exp(-2n_1), \gamma = R_2/R_1.$$

We obtain for L:

$$L = \frac{2}{R_1} (1 + F_1 + F_2 + \dots), \quad (14)$$

$$F_1 = \gamma(\gamma - 1) \exp(-4n_1) + \gamma(\gamma + 1) \exp(-4n_2) - 2(\gamma^2 - 1) \exp(-2n_1 - 2n_2),$$

$$F_2 = -\gamma^3 \exp(-8n_1) + \gamma^3 \exp(-8n_2) - 2(4\gamma^2 - 1) \exp(-4n_1 - 4n_2) +$$

$$2\gamma(\gamma^2 + 2\gamma - 1) \exp(-6n_1 - 2n_2) - 2\gamma(\gamma^2 - 2\gamma - 1) \exp(-2n_1 - 6n_2).$$

We substitute obtained expressions into W_1 . It is proper to consider velocities instead of displacements. For velocity transform $\dot{W} = pW$ we have:

$$\dot{W} = -\frac{b^4 p^2 n_1 \exp(-\delta|q|)(1-\exp(-pT))}{R_1} (1 + F_1 + F_2). \quad (15)$$

Finally, we obtain a sum total, where the first summand is the time, when waves propagating along the surface arrive at the observation point, the second one (F_2) is the time, when single-reflected waves from the back surface arrive at the observation point; the third summand (F_3) is the time of double-reflected waves arrival. The general view of a summand in (15) can be given in the form:

$$W^{LF}(q, p) = \frac{1}{p} \Phi(p, q) \exp(-\delta|q| - \alpha n_1 - \beta n_2 - \tau p) = \sigma_0^{LF}(p, q) \exp(-\delta|q|). \quad (16)$$

Here $n_{1,2}$ are homogenous first-order functions, Φ is of the zero-order, τ can have a zero or T value. Transforms like (16) are found in more simple dynamic problems, when one of the coefficients α or β is equal to zero. When both of them are not equal to zero, these cases are considered more complicated. The required correlation $\dot{w}(t)$ is written as a sum total of original functions, each of them is obtained using a double inverse transform of expressions like (16). For inverse transform we apply the procedure proposed in [13]. We determine function (L – image of the required function), as in [14]:

$$\sigma^L(p, s) = \frac{1}{\pi} Re \int_0^\infty \sigma_0^{LF}(p, q) \exp(-sq) dq; s = \delta + ix. \quad (17)$$

In (17) we replace $q = \xi p$.

$$\sigma^L(p, s) = \frac{1}{\pi} Re \int_0^\infty \Phi(\xi) \exp(-p(\alpha m_1 + \beta m_2 + s\xi + \tau)) d\xi, \quad (18)$$

$$m_1 = \sqrt{1 + \xi^2}, m_2 = \sqrt{b^2 + \xi^2}, \text{ at } Re\xi > 0, Im\xi = 0.$$

We introduce a new variable t according to the formula:

$$t = \alpha m_1 + \beta m_2 + s\xi - \alpha - \beta b. \quad (19)$$

Function $t(\xi)$ increases monotonically, since the derivative is positive

$$t' = (\xi')^{-1} = \alpha m_1' + \beta m_2' + s > 0 (\xi > 0). \quad (20)$$

Therefore, the equation (19) is assumed as a single-valued function $\xi(t, s)$. Using in (18) the variable t we obtain:

$$\sigma^L(p, s) = \frac{1}{\pi} Re \left(\exp(-p(\tau + \alpha + \beta b)) \int_0^\infty \frac{\Phi(\xi(t, s))}{\alpha m_1' + \beta m_2' + s} \exp(-pt) d\xi \right), \quad (21)$$

$$m_1 = \sqrt{1 + \xi^2}, m_2 = \sqrt{b^2 + \xi^2}; m_{1,2} > 0 \text{ at } Re\xi > 0, Im\xi = 0$$

Using the displacement theorem of original we get Laplace transform of the function in the right part (21):

$$\sigma(t, s) = \frac{1}{\pi} \operatorname{Re} \left(\frac{\Phi(\xi(t - (\tau + \alpha + b\beta), s))}{am'_1 + \beta m'_2 + s} \right), s = \delta + ix, x > 0. \quad (22)$$

The formula (22) provides an expression for the reversal double Fourier – Laplace transform and is a required function of t, x . We consider the first summand in (19) in the form:

$$\dot{W}_0 = -\frac{b^4 p^2 n_1 \exp(-\delta|q|)(1 - \exp(-pT))}{R_1}. \quad (23)$$

To compare (23) with (16) we have $\alpha = \beta = 0$, and for Φ_0

$$\Phi_0(\xi) = -\frac{b^4 m_1(\xi)}{R_1(\xi)}; R_1(\xi) = (m_2^2 + \xi^2)^2 - 4\xi^2 m_1 m_2; \xi = t/s. \quad (24)$$

Consequently,

$$\dot{w}_0(t, s) = \frac{1}{\pi} \operatorname{Re} \frac{1}{s} \left(\Phi(\xi(t, s)) - \Phi(\xi(t - \tau), s) \right). \quad (25)$$

Using the formula (25), time correlation of the transverse velocity ($\dot{w}_0(t, s)$) is plotted (Fig. 5). The dependence above is similar to that given in Fig. 3 for a 50 mm thick plate, making it possible to conclude that travelling waves will be registered in thick plates at the distances of approximately 20 mm.

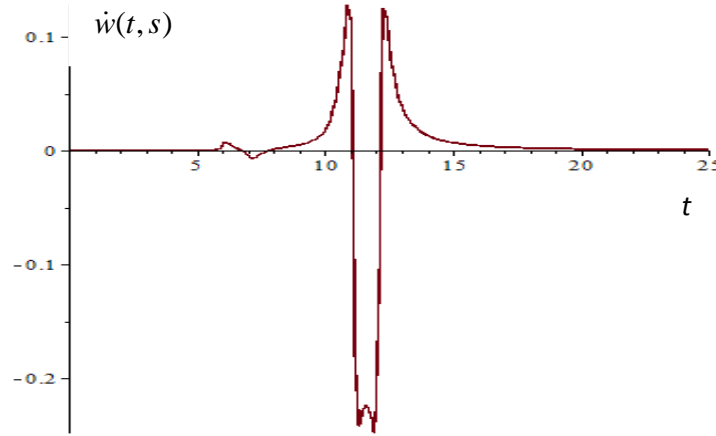


Fig. 5. Transverse velocity ($\dot{w}_0(t, s)$) vs. time dependence at $x = 6$; $b = 1.7$; $\tau = 1$; $\delta = 0.1$.

To take into account reflected waves the second summand in (15) is written in the form

$$\begin{aligned} \dot{W}_1^{LF} &= \dot{W}_0^{LF} L_1 \text{ it can be presented as three summands provided that } T \rightarrow \infty \\ \dot{W}_{11}^{LF} &= -\frac{b^4 p^2 n_1 \gamma(\gamma-1) \exp(-\delta|q| - 4n_1)}{R_1}, \\ \dot{W}_{12}^{LF} &= -\frac{b^4 p^2 n_1 \gamma(\gamma+1) \exp(-\delta|q| - 4n_2)}{R_1}, \\ \dot{W}_{13}^{LF} &= \frac{2b^4 p^2 n_1 (\gamma^2 - 1) \exp(-\delta|q| - 2n_1 - 2n_2)}{R_1}. \end{aligned} \quad (26)$$

Therefore, for functions Φ we will have with regard to (14) and replacement $q = \xi p$

$$\begin{aligned} \Phi_{11}^{LF} &= -\frac{8b^4 \xi^2 m_1^2 m_2 R_2(\xi)}{R_1^3(\xi)}, \Phi_{12}^{LF} = -\frac{2b^4 m_1 (m_2^2 + \xi^2)^2 R_2(\xi)}{R_1^3(\xi)}, \\ \Phi_{13}^{LF} &= \frac{32b^4 \xi^2 m_1^2 m_2 (m_2^2 + \xi^2)^2}{R_1^3(\xi)}, \end{aligned} \quad (27)$$

$$R_1(\xi) = (m_2^2 + \xi^2)^2 - 4\xi^2 m_1 m_2, R_2(\xi) = (m_2^2 + \xi^2)^2 + 4\xi^2 m_1 m_2.$$

For each function Φ_{1k} ($k = 1, 2, 3$) its own dependence is to be found out $\xi_k(t, s)$, and for them an equation like (15) is to be obtained. This equation in the general case can be

reduced to a biquadratic algebraic equation with complex coefficients, this equation is solved numerically. In the general case of four solutions we select those, which agree with (15), and in the rest – those, which can satisfy with the correlation $Re(\xi(t)) > 0, Im(\xi(t)) < 0$. Using (22) and (26) at $\tau = 0$ we write formulae for single-reflected waves

$$\begin{aligned}\Psi_{11}(t) &= \frac{1}{\pi} Re \left(\frac{\Phi_{11}(\xi)m_1(\xi)}{2 + sm_1(\xi)} \right), \xi = \xi_1(t - 4), \\ \Psi_{12}(t) &= \frac{1}{\pi} Re \left(\frac{\Phi_{12}(\xi)m_2(\xi)}{2 + sm_2(\xi)} \right), \xi = \xi_2(t - 4b), \\ \Psi_{13}(t) &= \frac{1}{\pi} Re \left(\frac{\Phi_{13}(\xi)m_1(\xi)m_2(\xi)}{2(m_1(\xi) + m_2(\xi)) + sm_1(\xi)m_2(\xi)} \right), \xi = \xi_3(t - 2 - 2b).\end{aligned}\quad (28)$$

For the resultant signal we obtain $\Psi_1(t) = \Psi_{11}(t) + \Psi_{12}(t) + \Psi_{13}(t)$. As long as $\tau \neq 0$, we have

$$\dot{w}_1(t, x, \delta, \tau) = \Psi_1(t) - \Psi_1(t - \tau). \quad (29)$$

Therefore, analytical solutions have been obtained and can be used to analyze wave propagation in the system “source-receiver” of the finite sizes. For travelling waves they were compared with the numerical results, principal agreement of calculations with analytical solutions was identified for thick plates.

Acknowledgment. The study is carried out under the financial support of Russian Scientific Foundation (project number 15-19-00065).

References

- [1] I.A. Ryabtsev, I.K. Senchenkov, *Theory and practice of surfacing* (Eco-technology, Kiev, 2013). (In Russian).
- [2] E.V. Kapralov, E.A. Budovskikh, V.E. Gromov, S.V. Raykov, Yu.F. Ivanov, *Structure and properties of composite wear-resistant overlays on steel* (Publishing of Siberian State Industrial University, Novokuznetsk, 2014). (In Russian).
- [3] V.D. Sarychev, S.A. Nevsky, V.E. Gromov // *Materials Physics and Mechanics* **27** (2016) 171.
- [4] L.A. Molotkov // *Journal of Mathematical Sciences* **175** (2011) 672.
- [5] G.I. Petrashen // *Journal of Mathematical Sciences* **116** (2003) 3077.
- [6] G.I. Petrashen // *Journal of Mathematical Sciences* **117** (2003) 3805.
- [7] Pham Chi Vinh, Tran Thanh Tuan, Marcos A. Capistran // *Wave Motion* **54** (2015) 134.
- [8] Zheng-Hua Qian, Feng Jin, Tianjian Lu, Kikuo Kishimoto // *Acta Mechanica* **207** (2009) 183.
- [9] A.V. Avershieva, R.V. Goldstein, S.V. Kuznetsov // *Mechanics of Solids* **51** (2016) 571.
- [10] S.V. Kuznetsov // *Mechanics of Solids* **50** (2015) 81.
- [11] V.D. Kubenko // *Reports of National Academy of Science of Ukraine* **7** (2015) 47.
- [12] A.S. Okonechnikov, D.V. Tarlakovsky, G.V. Fedotenkov // *Trudy MAI* **82** (2015).
- [13] L.I. Slepyan, *Time-dependent elastic waves* (Shipbuilding, Leningrad, 1972). (In Russian).
- [14] V.A. Saraykin // *Applied Mechanics and Technical Physics* **4** (1973) 148.

STUDY OF ANTIREFLECTION COATINGS FOR HIGH-SPEED 1.3 -1.55 μm InGaAs/InP PIN PHOTODETECTOR

E.S. Kolodeznyi^{1*}, I.I. Novikov^{1,2}, A.G. Gladyshev^{1,2}, S.S. Rochas¹, K.D. Sharipo¹,
L.Ya. Karachinsky^{1,2}, A.Yu. Egorov¹, V.E. Bougrov¹

¹ITMO University, Kronverkskiy 49, Saint Petersburg, 197101, Russia.

²Connector Optics LLC, Domostroitel'naya 16, Saint Petersburg, 194292, Russia.

*e-mail: e.kolodeznyy@gmail.com

Abstract. Single layer antireflection coatings have been studied for optimization InGaAs/InP photodetector with normal incident light over the 1300-1550-nm wavelength range. Silicon nitride coatings with various thicknesses were fabricated using plasma enhanced chemical vapor deposition and inductively coupled plasma chemical vapor deposition. The antireflection coating with thickness of 200 nm demonstrated reflection below 10 % at 1550 nm wavelength.

Keywords: single layer antireflection coating; silicon nitride coating; InGaAs/InP photodetector.

1. Introduction

Infrared photodetectors (PD) have a big number of applications in telecommunications, sensing and gas monitoring. One of the most rapidly developing area is microwave photonics where high-speed PDs with 1.3–1.55 μm spectral range corresponds to II and III transmission windows are demanded [1]. In photonic links, PDs convert modulated light signal into ultrahigh-frequency electrical current [2]. One of the important performance criteria for these devices is the quantum efficiency, thus it is important to minimize the power of reflected light from a PD surface. Decrease of the quantity of light reflected from a PD surface leads to increase in the sensitivity of a PD and expands the dynamic range of wavelengths where a PD operates. An antireflection (AR) coating may be used to decrease the quantity of reflected light from a PD surface [3-4].

In this paper we reported on studies of single layer AR coatings fabricated by plasma-enhanced chemical vapor deposition (PECVD) and inductively coupled plasma chemical vapor deposition (ICP CVD) for InGaAs/InP PD for normal incident light. The parameters of the deposited AR coatings and measurements results are described below.

2. Experiment

Heterostructure for high-speed PIN type PD for $\lambda=1300\text{-}1550$ nm was grown by molecular beam epitaxy on semi-insulating InP substrate. The absorption layer is represented by $\text{In}_{0.53}\text{Ga}_{0.47}\text{As}$ layer of 0.8 μm thickness that provides small tunneling time of generated charge carriers resulting in high-speed operation. At the same time, the high absorption coefficient of $\text{In}_{0.53}\text{Ga}_{0.47}\text{As}$ provides sufficient photosensitivity. Several gradient layers are designed between contact layer, window layer $\text{In}_{0.52}\text{Al}_{0.48}\text{As}$ and absorption layer to decrease the serial resistance of the heterostructure.

The PD chips were fabricated by dry etching double mesa processing. Ti/Au layer was deposited successively on top p-type contact InGaAs layer and patterned by a lift-off process to form an enclosed circular mesa-structure instituted as a p+ ohmic contact with an inner diameter of 20 μm . Standard photolithography was used for dry etching first and second mesas by BCl_3/Ar . Then AuGe/Ni/Au layer is deposited successively on n-type contact capping layer InGaAs and patterned by a lift-off process. Both ohmic contacts then were rapid thermal annealed at 360 $^\circ\text{C}$. The next step was deposition and patterning PECVD Si_3N_4 . Ti–Au interconnect metal was evaporated forming the coplanar waveguide transmission lines by a lift-off process. The AR coating deposition was the last technological operation. Afterward, the wafer was lapped and polished down 120 μm and then dicing on the single PD chips.

To study and optimize the AR coatings for the frontside illuminated PDs a special test structure was grown. The structure consisted of rather thick $\text{In}_{0.53}\text{Ga}_{0.47}\text{As}$ layer emulated the p-contact layer of the PDs. Fig. 1(a) illustrates the cross section of the test structure that was used to study the reflectivity of the high-speed InGaAs/InP PD.

For calculation of a reflectivity of the test structure, we use the transfer-matrix method where each layer of a multilayer structure is described by a characteristic matrix which includes an index of refraction, a layer thickness, a wave number and a wave impedance of a layer. The multilayer structure is described by serial multiplication of the matrixes of all containing layers [5]. Thicknesses of the AR coating were chosen with taking into account the index of refraction of silicon nitride in the range of 1400-1600 nm and the high p-doped contact $\text{In}_{0.53}\text{Ga}_{0.47}\text{As}$ layer [6]. Results of the calculations are shown on the Fig. 1(b).

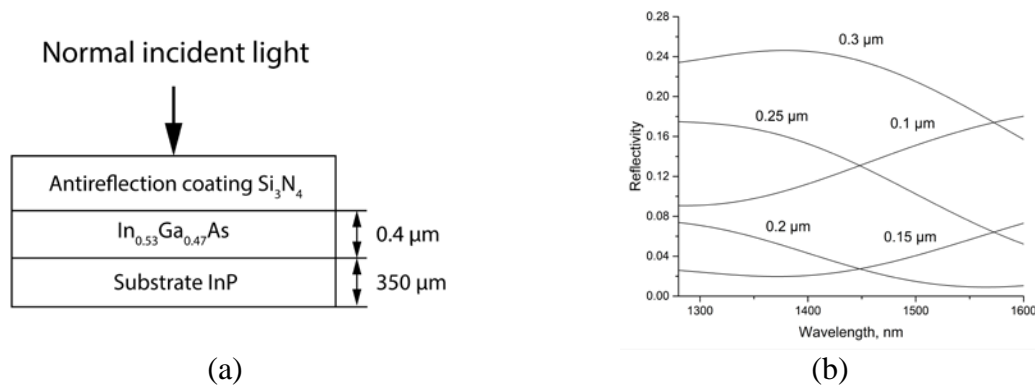


Fig. 1. Cross section of the test structure simulating the PD with AR coating (a) and calculated reflectivity of the test structures with different thicknesses of the AR coating.

The AR coating on the surface of test structure (dielectric coating Si_3N_4 with refractive index of 2.0) was deposited by two different methods i.e. PECVD with high temperature deposition and IPC CVD with a low temperature. Detailed characteristics of the deposited AR coatings can be found in the Table 1.

Table 1. Characteristics of the deposited AR coatings.

No.	Processing technique	Temperature, $^\circ\text{C}$	Thickness, μm
1	PECVD	250 $^\circ\text{C}$	0.1 μm
2	PECVD	250 $^\circ\text{C}$	0.15 μm
3	PECVD	280 $^\circ\text{C}$	0.15 μm
4	PECVD	280 $^\circ\text{C}$	0.3 μm
5	ICP	70 $^\circ\text{C}$	0.1 μm
6	ICP	70 $^\circ\text{C}$	0.2 μm
7	ICP	70 $^\circ\text{C}$	0.3 μm
8	Test sample	–	–

For comparison with the PD without AR coating, we use the test sample (No. 8 in the Table 1), which was chemically cleaned with dimethylformamide.

3. Experimental results and discussion

The RPSigma system by Nanometrics was used for measurements of a PD reflectivity. Reflection spectra for samples No.1-No.4 with PECVD silica nitride are represented on the Fig. 2. Samples No.2 and No.3 had demonstrated minimum reflectivity among the PECVD samples i.e. about 10 % and 13 % of incident light power at the wavelength 1550 nm reflected from the PD. Samples No.1 and No.4 with thicknesses 0.1 nm and 0.3 nm correspondingly had demonstrated reflectivity about 23 %, what demonstrates high interference between the AR coating and top p- $\text{In}_{0.53}\text{Ga}_{0.47}\text{As}$ layer.

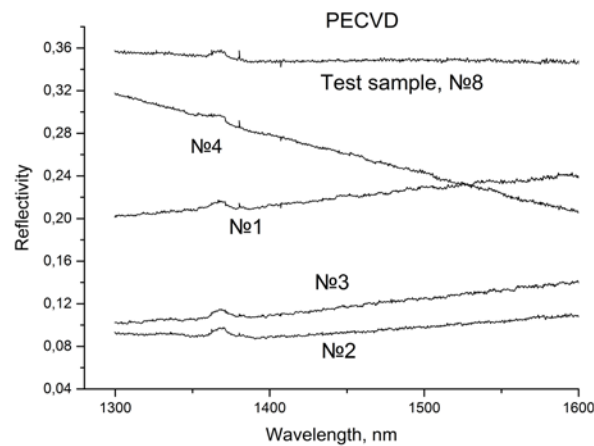


Fig. 2. Reflectivity of the samples with AR coating deposited by PECVD.

Reflection spectra for samples No.5-No.7 with IPC CVD silica nitride are represented on the Fig. 3. Samples No.7 with thickness 0.3 μm deposited at low temperature had demonstrated high reflectivity about 30% at the wavelength 1550 nm close to the test sample No.8 without AR coating, at the same time sample No. 6 had demonstrated the lowest reflectivity 9% at the wavelength 1550 nm about among the all samples.

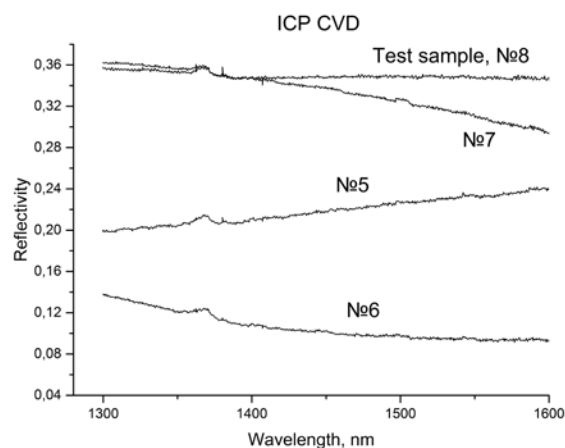


Fig. 3. Reflectivity of the samples with AR coating deposited by IPC CVD.

4. Conclusions

The single layer AR coating has been developed for use with the high-speed InGaAs/InP frontside illuminated PD. The silicon nitride (Si_3N_4) coatings with thicknesses 0.1, 0.15, 0.2 and 0.3 μm were fabricated using PECVD and ICP CVD techniques. Among the samples

fabricated by PECVD the sample No. 2 (250 °C temperature deposition and 0.15 μm thickness) had shown < 10 % reflected power at 1550 nm wavelength. Among the samples fabricated by IPC CVD sample No. 6 (70 °C temperature deposition and 0.2 μm thickness) had shown < 9 % reflectivity. The obtained results can be used for optimization of high-speed InGaAs/InP photodiodes operating at 1550 nm.

Acknowledgment

This work was supported by the Ministry of Education and Science of the Russian Federation in the framework of the Federal Target Program "Research and development on priority directions of scientific-technological complex of Russia for 2014-2020", the code 2015-14-582-0038, agreement № 14.581.21.0013 of August 4, 2015, unique ID RFMEF158115X0013.

References

- [1] V.J. Urick, J.D. McKinney, K. J. Williams, *Fundamentals of microwave photonics* (John Wiley & Sons, New Jersey, 2015).
- [2] N. Dagli, *High-Speed Photonic Devices* (CRC Press, New York, 2007).
- [3] D.M. Braun // *Applied Optics* **27** (1988) 2006.
- [4] J. Yuan, B. Chen, A. L. Holmes // *Electronics Letters* **48** (2012) 1230.
- [5] M. Born, E. Wolf, *Principles of optics: electromagnetic theory of propagation, interference and diffraction of light* (Cambridge University Press, New York, 1999).
- [6] H.W. Dinges, H. Burkhard, R. Lösch, H. Nickel, W. Schlapp // *Applied Surface Science* **54** (1992) 477.

SYNTHESIS OF SILVER NANOCHAINS WITH A CHEMICAL METHOD

I.M. Sosnin^{1*}, M.N. Turkov¹, M.R. Shafeev¹, E.V. Shulga², I. Kink², A.A. Vikarchuk¹,
A.E. Romanov^{1,3}

¹Togliatti State University, Belorusskaya str. 14, Togliatti, 445020, Russia

²University of Tartu, Ülikooli str. 18, Tartu, 50090, Estonia

³University ITMO, Kronverksky pr. 49, St. Petersburg, 197101, Russia

*e-mail: sim.nanosci@gmail.com

Abstract. We describe the method of synthesis of chain-like silver nanowires (nanochains) and find the favorable conditions to fabricate them. The nanochains are processed in the hot ethylene glycol solution with constant stirring in the presence of nickel nanoparticles and polyvinylpyrrolidone 360000 molecules. Silver nanochains consist of straight-linear segments connected end-to-end. The length of straight-linear segments is from 100 to 500 nm, the diameter is about 80 nm; the angle between segments varies from 30 to 90°. The total nanochain length reaches 100 microns. The mechanism of silver nanochain formation is discussed.

Keywords: chain-like silver nanowires; silver nanowires; chemical synthesis of nanostructures; metal nanoparticles.

1. Introduction

Silver nanowires (AgNWs) belong to the class of one dimensional nanomaterials (1D), together with carbon nanotubes, semiconductor nanorods and other [1]. The most promising application of AgNWs are in flexible electronics, optoelectronics, photovoltaics and sensorics [2-5]. Properties of AgNWs depend on their morphology and size that can be influenced by changing of synthesis conditions or coating with additional shells on the surface of nanowires [6].

In general, methods to fabricate metal nanowires can be subdivided into physical and chemical ones [7]. While physical methods allow to get nanowires without chemical reactions, chemical methods imply production of metal nanowires by chemical transformation starting from metal precursor and ending with atom agglomeration into nanoobjects. Among physical methods one can mention physical vapor deposition, electrodeposition through a porous membrane or synthesis by control of electrical charging, polarization and electrochemical potential [8-10]. Chemical reduction of silver ions is the most well-known method, which is often used to fabricate AgNWs [11]. Variation of conditions of AgNW synthesis, such as temperature, molar fraction of surfactants and duration of synthesis process influence the morphology of resulting nanoobjects.

In many cases, the reduction takes place in liquid solutions that act as the media for the chemical process. Ethylene glycol (EG) is usually used as such a liquid, but there are other substances, which serve the same purpose, e.g. water, N,N-dimethylformamide (DMF) and other [12, 13]. EG can be both a reduction agent and a capping agent, whereas water normally is only the carrier medium for chemical reactions. On the other hand, synthesis of AgNWs in water solution can be implemented in the presence of surfactants as capping agents. In some cases, additional chemical acts as both a reduction and a capping agent. For example, aromatic molecules, vitamin C or plant extract demonstrate such properties in water solution [14-16].

Employment of clove oil as medium for chemical reduction is another rather exotic was to AgNW synthesis [17]. Clove oil consists of many substances that provide reduction and capping properties. Synthesis of AgNWs in EG solution can be implemented at higher temperatures (about 180 °C) compared to aqueous synthesis, increasing the duration of synthesis process. However, there are methods that allow to bring down the reaction time, e.g. microwave-polyol method [19].

Choose of surfactant strongly influences the size and morphology during fabrication of AgNWs. Usually polyvinylpyrrolidone (PVP) is used as surfactant. The length of PVP molecule regulates the length of a silver nanowire. Molecular weight of PVP is 1300000 g/mol that determines the length of hydrocarbon skeleton of PVP molecule, which reaches 2 microns. PVP allows to synthesize AgNWs up to several microns length. Besides PVP other surfactants are used to make AgNWs, such as poly(diallyldimethylammonium)chloride (PDA) and dibutyl sebacate (DBS) [20, 21]. DBS allows to fabricate nanobelt structures, which demonstrate thickness about 20 nm, width about 60 nm and are several microns of length [21]. Silver nanorods fabricated in the presence of PDDS have length about 100 nm and diameter about 25 nm [20]. Variation of molar fraction Ag/PVP influences the AgNW morphology, too. Change of molar fraction Ag/PVP decreases yield of silver nanowires and aspect ratio [22, 23].

Synthesis of AgNWs in the presence of metal nanoparticles as the seeds allows to increase the yield of nanowires and the length of nanowires or fabricate the zigzag silver nanowires [24-26]. Increasing of seed size reduces number of silver nanowires. Zigzag silver nanowires are one dimensional nanoobjects, which consist of several straight-linear segments connected end-to-end [27]. Recently such silver nanoobjects have been accidentally observed, however the specific conditions for their synthesis have not been reported [28].

In the present work, we describe the synthesis of chain-like silver nanowires- silver nanochains (SNCs) in the presence of nickel nanoparticles as seeds and synthesis of silver nanowires in the presence of silver nanoparticles as seeds.

2. Experimental

2.1. Materials. We used Sigma Aldrich chemicals: silver nitrate (CAS # 7761-88-8), ethylene glycol (EG) (CAS # 107-21-1), polyvinylpyrrolidone (PVP) 10 000 and 360 000 (CAS # 9003-39-8), nickel acetate (CAS # 373-03-4), citric acid (CAS # 77-92-9), hydrazine-hydrate (CAS # 301-01-2) and distilled water.

2.2. Synthesis of silver nanoparticles (AgNPs). Fabrication of AgNPs was processed in two stages. At the first stage, the aqueous solution of silver nitrate and PVP were prepared. Silver nitrate (4.24 g) was dissolved in 25 ml of distilled water. PVP (2 g) 10 000 was dissolved in 200 ml of distilled water. At second stage, 1 ml of aqueous solution of silver nitrate and 0.03 ml of hydrazine-hydrate were dissolved in 200 ml of PVP aqueous solution at room temperature. Prepared solution was stirred during 20 minutes.

2.3. Synthesis of nickel nanoparticles (NiNPs). Fabrication of the NiNPs was processed in two stages, too. At the first stage, nickel acetate (0.62 g) was dissolved in 25 ml of distilled water. Then 0.07 g of citric acid was dissolved in 25 ml of ethylene glycol. At the second stage, 0.5 ml of aqueous solution of nickel acetate was dissolved in ethylene glycol contained citric acid. Resulting solution was heated up to 160 °C and was stirred for 2 hours.

2.4. Synthesis of silver nanowires (AgNWs). Silver nanowires were made in two different routes: in the presence of silver (i) and nickel (ii) nanoparticles as seeds. Each case was processed in 5 ml ethylene glycol heated to 160 °C. In the first case, we dissolved 0.01 ml of silver nanoparticle solution, in the second case - 0.1 ml of nickel nanoparticles solution in a reaction flask. The next stages of synthesis were the same for both cases. We prepared two additional solutions: silver nitrate (0.42 g) in EG (25 ml) and PVP 360 000 (0.9 g) in EG (25 ml). Both additional solutions were added to reaction flask drop wise: 1 ml AgNO₃/EG and

1.6 ml PVP/EG.

2.5. Characterization. Resulting nanowires and nanopartilces were deposited onto the surface of silicon oxide plate. Then silicon oxide plates covered with nanoobjects were washed by the mixture of water and ethanol several times to remove excess PVP molecules and other products of chemical reactions. Nanowires and nanoparticles located on dried silicon oxide plates were studied in scanning electron microscopes (SEMs): FEI Novanano, USA and CarlZeiss Sigma, Germany. UV/Vis absorption spectrum of AgNP solution was recorded with Promecolab PE-5400 UV spectrophotometer, Russia. Structure studies of nanowires and nanoparticles were performed with a X-Ray diffraction (XRD), Shimadzu XRD 7000, Japan.

3. Results

3.1. Silver and nickel nanoparticles for silver nanowire seeding. AgNPs have size about 300 nm, but some nanoparticles reach 80 nm in diameter. UV/Vis adsorption spectrum shows plasmon peak 409 nm that corresponds to typical spectrum range of silver nanoparticle solution [29]. Size of NiNPs was about 80 nm. The shape of AgNPs and NiNPs was close to spherical. XRD spectrum of NiNPs shows crystal form of FCC nickel.

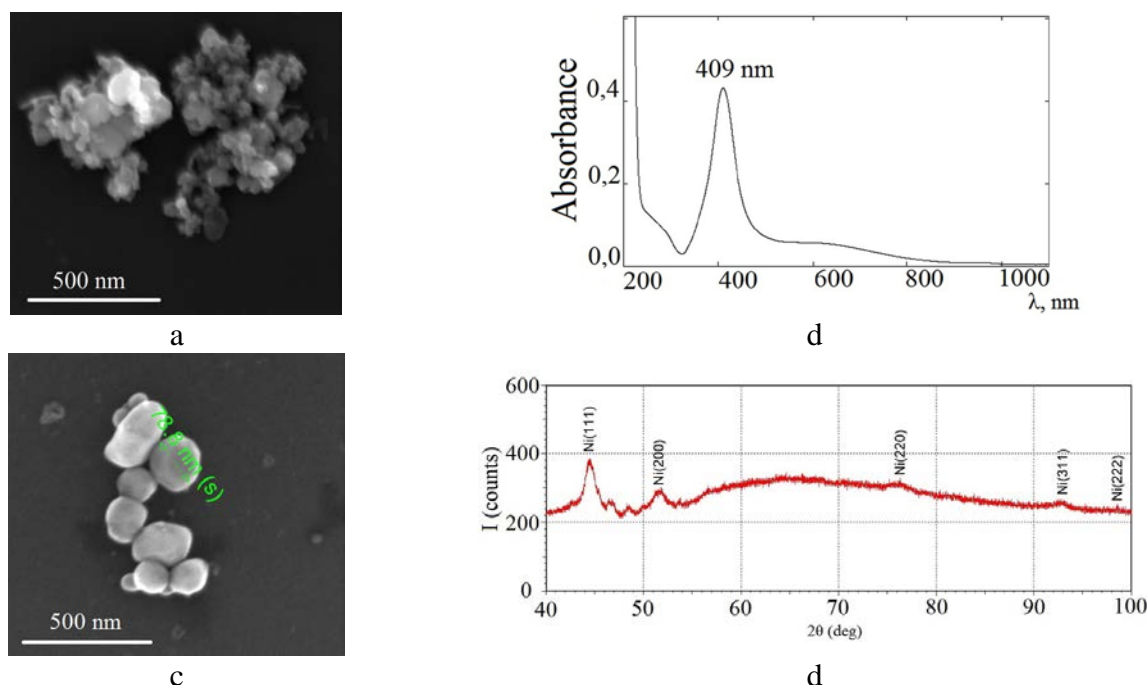


Fig. 1. Characteristics of resulting nanoparticles. (a) SEM images of AgNPs, (b) UV/Vis absorption spectrum of AgNP solution, (c) SEM images of NiNPs, (d) XRD spectrum of nickel nanoparticles.

We prepared two types of seeds: AgNPs and NiNPs, which were later used in the synthesis of silver nanochains. Figure 1 shows characteristics of the fabricated nanoparticles.

3.2. Synthesis of silver nanowires in the presence of silver nanopartilces

3.2.1. The role of temperature. Figure 2 shows the influence of synthesis temperature on the morphology of silver nanoparticles and nanowires. The synthesis temperature varied from 100 °C to 160 °C. Fabricated nanoobjects were characterized by SEM. At temperature below 120°C AgNPs were not observed. The size of AgNPs fabricated at 130 °C from 100 to 300 nm. Nanopartilces demonstrated close to spherical shape. Boost of temperature of synthesis allowed to increase the yield of silver nanowires was about 10 μm, diameter was about 120 nm, aspect ratio $P \approx 100$.

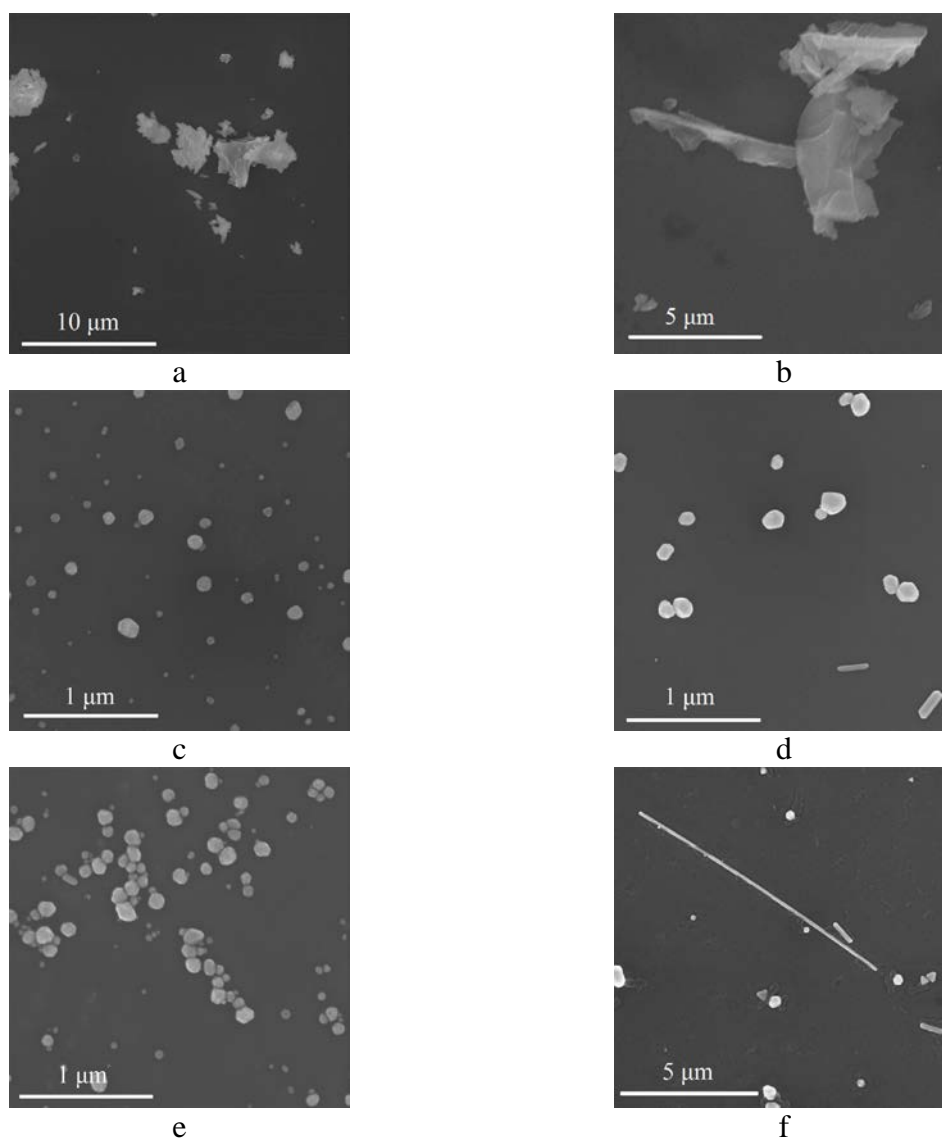


Fig. 2. Influence of synthesis temperature on the nanoobject morphology, SEM images: (a) 100 °C - absence of nanoobjects, (b) 110 °C - absence of nanoobjects, (c) 120 °C - spherical AgNPs, (d) 130 °C - spherical AgNPs, (e) 140 °C - spherical AgNPs, (f) 160 °C AgNWs, aspect ratio $P \approx 100$. Reaction time for all experiments was 10 minutes.

3.2.2. The role of reaction time. Figures 3 and 4 show the morphology evolution of reaction time that changed from 20 to 80 minutes. At 130 °C the size of AgNPs increased from 50 to 150 nm. After 80 minutes of synthesis some nanorods were observed. The length of nanorods was about 170 nm, diameter was about 50 nm and aspect ratio $P \approx 3$, respectively.

Silver nanowires were fabricated at 160 °C. Figure 4 shows increasing the length and aspect ratio of AgNWs. After 20 minutes of synthesis only AgNP were found, then after 40 minutes AgNWs were observed. The length of AgNWs was about 10 μm, diameter was about 100 nm, aspect ratio $P \approx 100$.

3.2.3. Synthesis of silver nanowires in the presence of nickel nanopartilces. NiNPs serve as seeds for synthesis silver nanochains. Synthesis was processed in hot EG with constant stirring during 80 minutes. Ethylene glycol solution of silver nitrate and PVP/EG solution were added in the reaction flask drop wise. Nanoobjects were fabricated at two different temperatures: 130 °C and 160 °C. Figures 5 and 6 show silver nanoobjects prepared at 130 °C and 160°C, respectively.

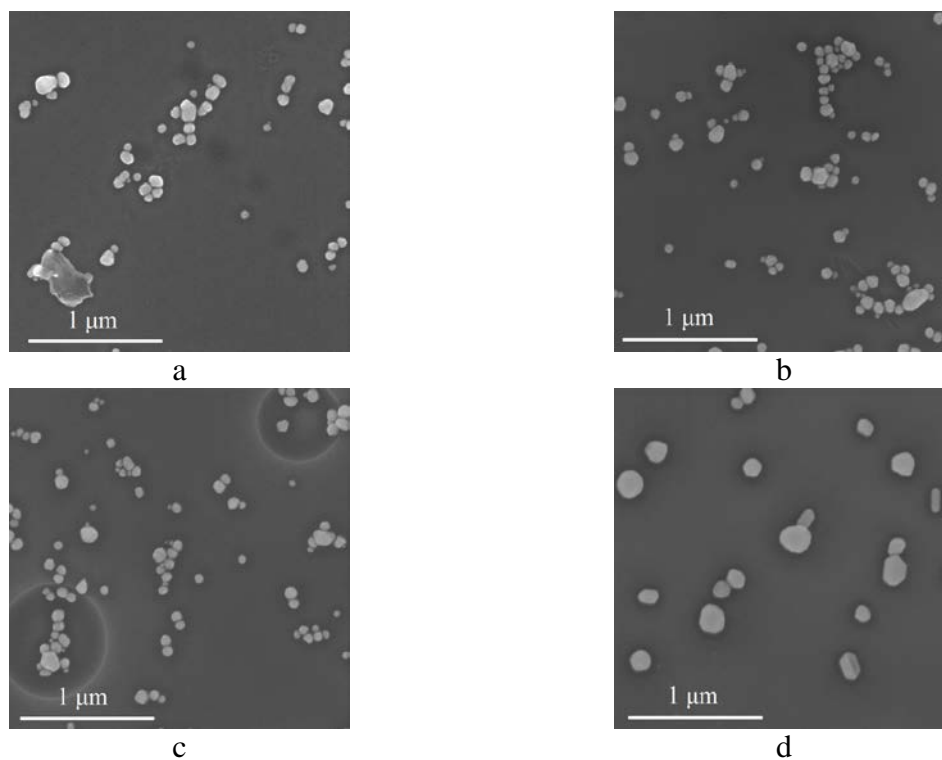


Fig. 3. Influence of reaction time on the morphology of nanoobjects at 130 °C, SEM images show spherical AgNPs with size depending on the synthesis duration: (a) 20 min, (b) 40 min, (c) 60 min, (d) 80 min.

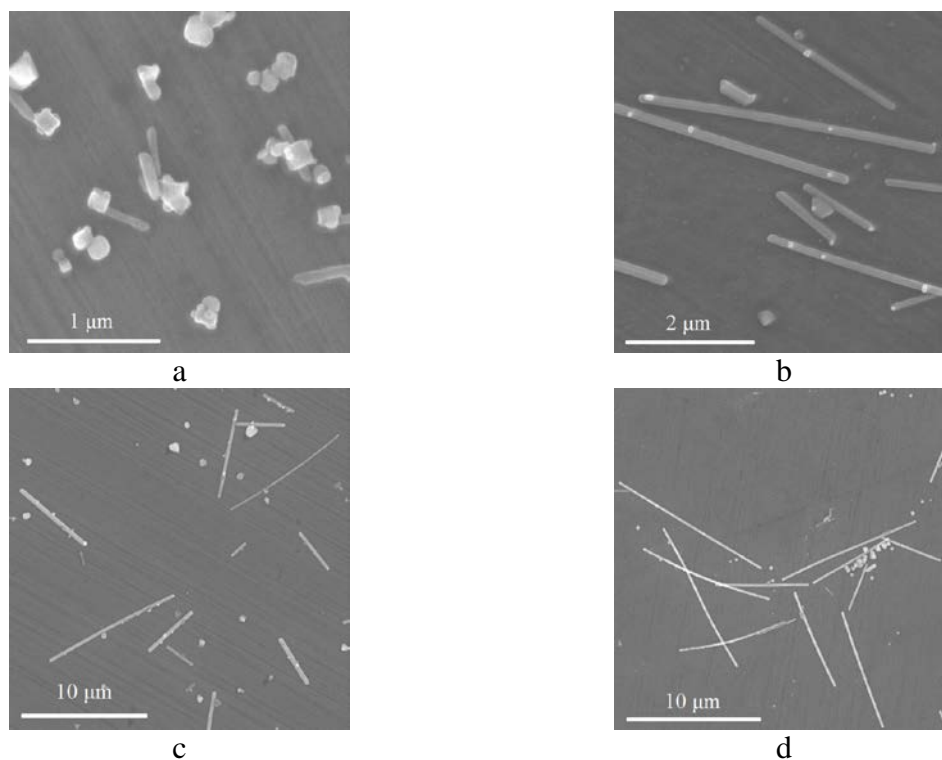


Fig. 4. Influence of reaction time on the AgNW morphology. Synthesis was processed at 160 °C; SEM images. Change of the aspect ratio (P) of AgNW: (a) 20 min only AgNP; (b) 40 min, $P = 15$; (c) 60 min, $P = 30$; (d) 80 min, $P = 100$.

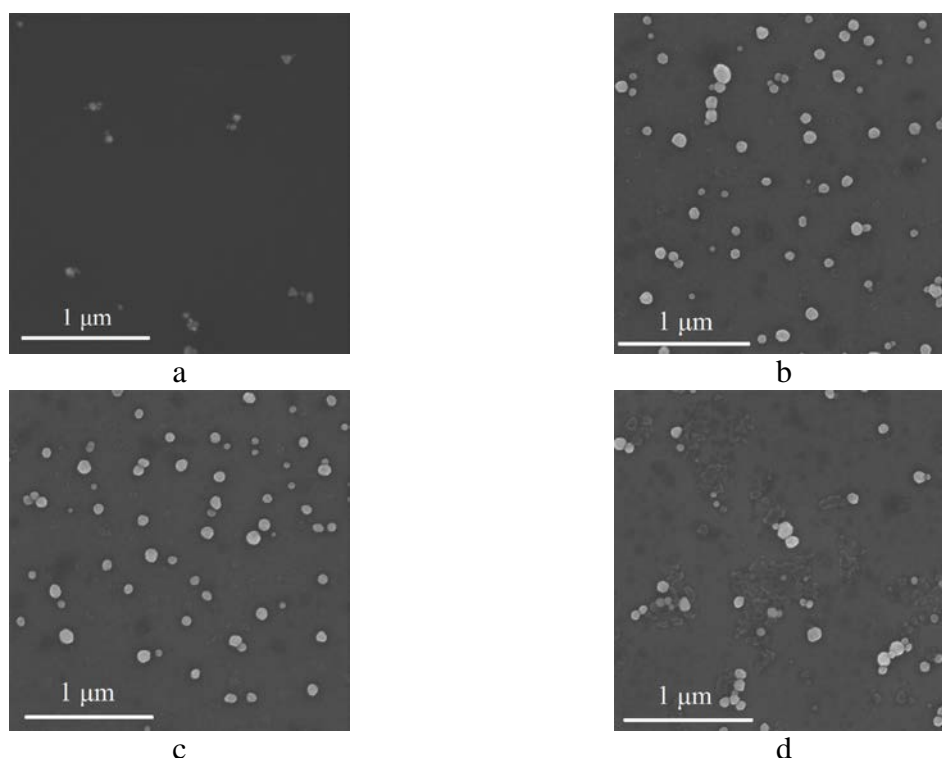


Fig. 5. AgNPs fabricated in the presence of nickel nanoparticles at 130 °C. Process duration was: (a) 20 min (b) 40 min, (c) 60 min, (d) 80 min.

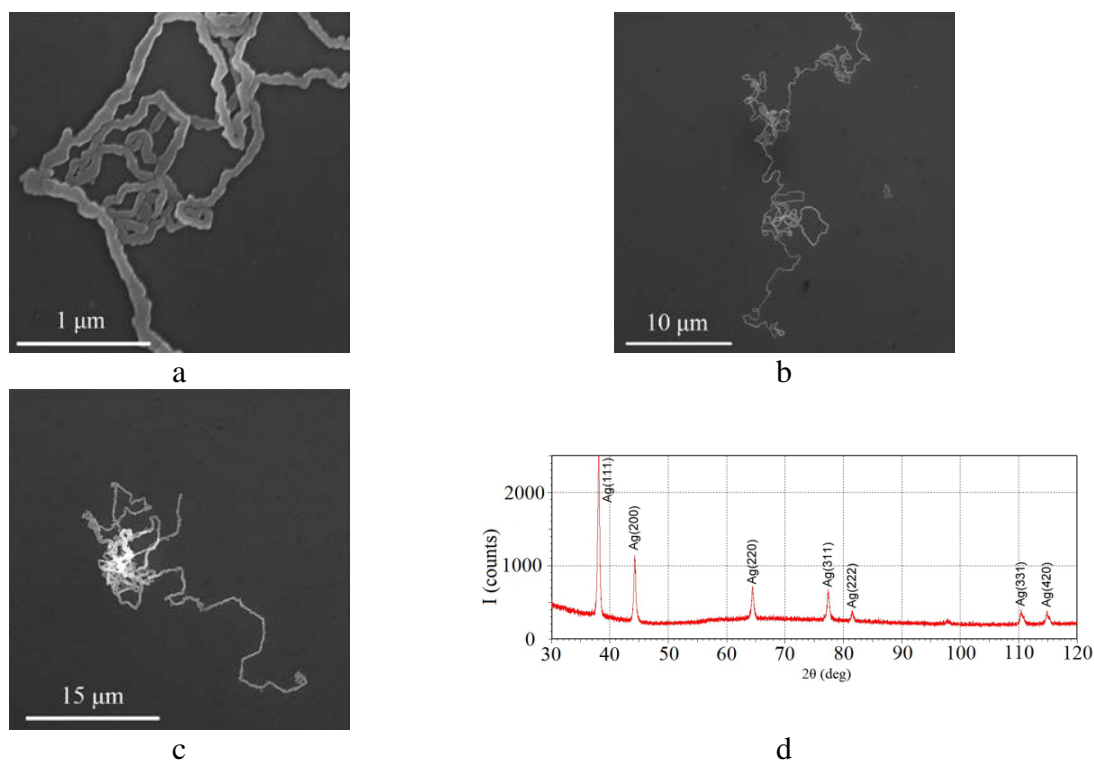


Fig. 6. Silver nanochains in the presence of NiNPs: (a)-(c) SEM image of produced silver nanochains, P = 1000, (d) XRD spectrum of SNCs.

Nanoparticles processed at 130 °C had a spherical form. The size of AgNWs was about 50 nm. The yield of AgNPs increased during synthesis. AgNWs were not observed at 130 °C. Silver nanochains (SNCs) were found at 160 °C after 20 minutes of synthesis. SEM analysis

Table 1. Influence of synthesis conditions on the morphology of Ag nanoobjects.

Reaction time, min	AgNPs			NiNPs	
	Below 130 °C	130 °C	160 °C	130 °C	160 °C
20	Absence of nanoobjects	AgNP 300-500 nm	AgNP 100-200 nm	Spherical AgNP 20-30 nm	SNCs, the length - 100 microns,
40	Absence of nanoobjects	AgNP 300-500 nm	AgNP 300-500 nm and AgNW 120 nm, length	Spherical AgNP 20-30 nm	Synthesis was stopped
60	Absence of nanoobjects	AgNP 300-500 nm	AgNP 300-500 nm and AgNW 120	AgNP 40-60 nm	
80	Absence of nanoobjects	Synthesis was stopped	Synthesis was stopped	AgNP 80 nm	
Number of nanoobjects	Nanoobjects were not observed	Is not changed	Is not changed	Increases	Is not changed

Acknowledgements.

This work was supported by the Ministry of Education and Science of the Russian Federation, State Task 16.2314.2017/4.6 and by European Social Fund's Doctoral Studies and Internationalisation Programme DoRa.

References

- [1] S.V.N.T. Kuchibhatla, A.S. Karakoti, D. Bera, S. Seal // *Progress in Materials Science* **52** (2007) 699.
- [2] E.-J. Lee, Y.-H. Kim, D.K. Hwang, W.K. Choi, J.-Y. Kim // *RSC Advances* **6** (2016) 11702.
- [3] A.B.V.K. Kumar, J. Jiang, C.W. Bae, D.M. Seo, L. Piao, S. Kim // *Materials Research Bulletin* **57** (2014) 52.
- [4] H. Liang, H. Wei, D. Pan, H. Xu // *Nanotechnology Reviews* **4(3)** (2015) 289.
- [5] N. Chou, Y. Kim, S. Kim // *ACS Applied Materials and Interfaces* **8(9)** (2016) 6269.
- [6] S. Vlassov, B. Polyakov, L.M. Dorogin, M. Vahtrus, M. Mets, M. Antsov, R. Saar, A.E. Romanov, A. Lohmus, R. Lohmus // *Nano Letters* **14(9)** (2014) 5201.
- [7] S.P. Stagon, H. Huang // *Nanotechnology Reviews* **2(3)** (2013) 259.
- [8] Y. Liu, Y. Chu, L. Yang, D. Han, Z. Lu // *Materials Research Bulletin* **40** (2005) 1796.
- [9] N. Duraisamy, S. Hong, K. Choi // *Chemical Engineering Journal* **225** (2013) 887.
- [10] J.M. Koehler, V. Nikunj Kumar, A. Knauer // *Nanotechnology Review* **396** (2014) 553.
- [11] Y. Gao, P. Jiang, L. Song, L. Liu, X. Yan, Zh. Zhou, D. Liu, J. Wang, H. Yuan, Z. Zhang, X. Zhao, X. Dou, W. Zhou, G. Wang, S. Xie // *Journal of Physics D: Applied Physics* **38(7)** (2005) 1061.
- [12] X. He, X. Zhao, Y. Chen, J. Feng, Zh. Sun // *Journal of Solid State Chemistry* **180** (2007) 2262.
- [13] C.J. Murphy, T.K. Sau, A.M. Gole, C.J. Orendorff, J. Gao, L. Gou, S.E. Hunyadi, T. Li. // *The Journal of Physical Chemistry B* **109** (2005) 13857.
- [14] R. Becker, F. Söderlind, B. Liedberg, P. Käll // *Materials Letters* **64** (2010) 956.
- [15] Y. Liu, Y. Chu, L. Yang, D. Han, Zh. Lu // *Materials Research Bulletin* **40** (2005) 1796.
- [16] T. Thunugunta, A.C. Reddy, Lakshmana Reddy D.C. // *Nanotechnology Reviews* **4(4)** (2015) 303.
- [17] A. Jeevika, Dh. R. Shankaran // *Journal of Colloid and Interface Science* **458** (2015) 155.

- [18] R.S. Boethling, D. Mackay, *Handbook of property Estimation Methods for Chemicals*. Environmental and Health Science (New York, Taylor and Francis Group 2000).
- [19] M. Tsuji, Y. Nishizawa, K. Matsumoto, N. Miyamae, T. Tsuji, X. Zhang // *Colloids and Surfaces A: Physicochemical and Engineering Aspects* **293** (2007) 185.
- [20] M. Luo, H. Huang, S. Choi, C. Zhang, R.R. Silva, H. Peng, Z. Li, J. Liu, Zh. He, Y. Xia // *ACS Nano* **9**(10) (2015) 10523.
- [21] B. Liu, W. Luo, X. Zhao // *Materials Research Bulletin* **44** (2009) 682.
- [22] M. Tsuji, K. Matsumoto, N. Miyamae, T. Tsuji, X. Zhang // *Crystal Growth & Design* **7**(2) (2007) 311.
- [23] C. Chen, L. Wang, G. Jiang, Q. Yang, J. Wang, H. Yu, T. Chen, C. Wang, X. Chen // *Nanotechnology* **17** (2006) 466.
- [24] C. Chen, L. Wang, H. Yu, G. Jiang, Q. Yang, J. Zhou, W. Xiang, J. Zhang // *Materials Chemistry and Physics* **107** (2008) 13.
- [25] C. Chen, L. Wang, H. Yu, J. Wang, J. Zhou, Q. Tan, L. Deng // *Nanotechnology* **18** (2007) 115612.
- [26] Y. Zhang, J. Wang, P. Yang // *Materials Research Bulletin* **48** (2013) 461.
- [27] D. Chen, L. Gao // *Journal of Crystal Growth* **264** (2004) 216.
- [28] H. Chen, Y. Gao, H. Yu, H. Zhang, L. Liu, Y. Shi, H. Tian, S. Xie, J. Li // *Micron* **35** (2004) 469.
- [29] R. Jin, Y.C. Cao, E. Hao, G.S. Metraux, G.C. Schatz, C.A. Mirkin // *Nature* **425** (2003) 487.

RELAXATION IN RESINS WITH LOW-FREQUENCY MECHANICAL CYCLING

V.I. Ivlev*, A.F. Sigachyov, N.E. Fomin, V.A. Yudin

Mordovia State University N.P. Ogareva, Bolshevistskaya, 68, Saransk, 430005, Russia

*e-mail: ivlevvi2010@mail.ru

Abstract. Hardened polyester and epoxy resins were tested for the relaxation of mechanical stresses, depending on the initial stress (2.6 ÷ 24 MPa), time and temperature (15 ÷ 45 °C). The dependence of stress on time in the relaxation of resins in the investigated ranges of mechanical stresses is described by the logarithmic function characteristic for stress relaxation in crystalline solids (metals).

Keywords: epoxy resin; polyester resin; relaxation; mechanical stress.

1. Introduction

Relaxation phenomena form a significant part of the properties of materials, including polymers, which may include cured resin. Naturally, the study of this group of properties of new materials is usually started immediately after the receipt of these materials in sufficient quantities.

Polyester and epoxy resins are a universal family of resins, on the basis of which receive composite materials, widely used in various fields of modern technology for more than a hundred years. Relaxation processes in these materials is also studied quite a long time and actively. However, due to the wide variety of composition and grades of these resins, the complexity of the atomic-molecular processes in them, especially when using them for the production of composite materials, there always remain questions requiring further investigation.

One of the manifestations of relaxation is mechanical hysteresis. As a rule, in dynamic experiments is often determined the energy losses of oscillations. In our previous experiments, the dependence of the effective (or conditional) modulus on deformation was studied for low-frequency mechanical cycling [1]. The effective modulus was defined as the tangent of the slope of the strain curve $E = d\sigma/d\varepsilon$ (σ is the mechanical stress, ε is the relative deformation).

In Fig. 1 shows the relationship between the stress and deformation $\sigma(\varepsilon)$ obtained during cycling. A characteristic feature of the obtained dependences $\sigma(\varepsilon)$ is the presence of a hysteresis, especially strong in the first cycle. The dependence of the effective modulus E on the magnitude of the mechanical stress upon loading and unloading the sample is shown in Fig. 2.

The curve $\sigma(\varepsilon)$ obtained during unloading after the first loading is very different from the curve obtained under loading, it is practically monotonic, with the exception of a small section at the lowest loads. At maximum loads, the unloading curve is steeper than the loading curve for low loads, on the contrary, so that the $E(\sigma)$ curves obtained during loading and unloading, when plotted on the same graph, overlap (Fig. 2). This feature is retained in subsequent cycles. From this we can conclude that the stress relaxation processes prevail at the initial stages of unloading (high stresses), and the deformation relaxation processes prevail at the final (small stresses).

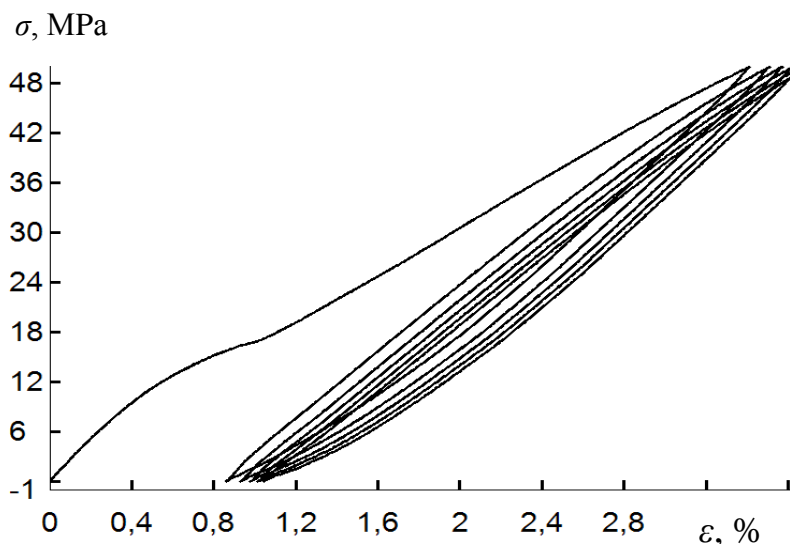


Fig. 1. Hysteresis in epoxy resin during deformation at a rate of $3 \cdot 10^{-4} \text{ c}^{-1}$.

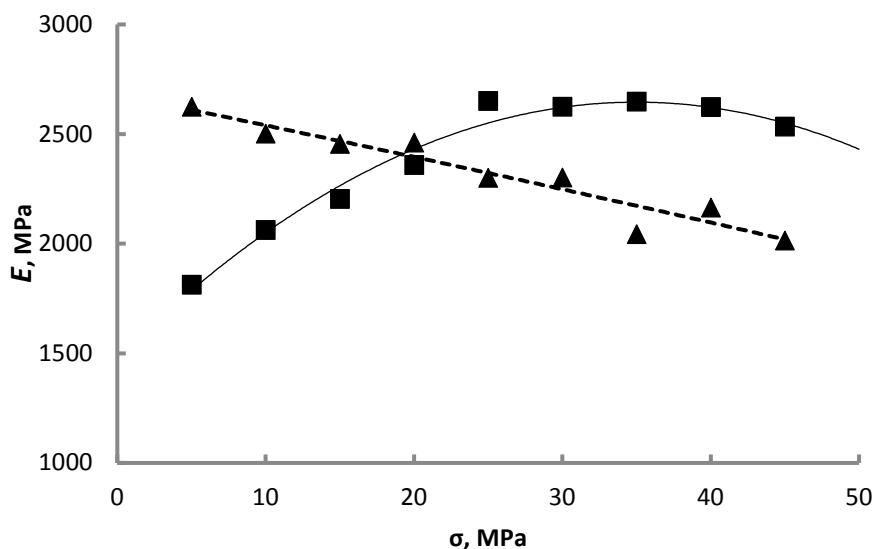


Fig. 2. The dependence of the effective modulus on the magnitude of voltage during cycling (epoxy resin).

The processes of strain relaxation (creep) of resins were investigated by us earlier [2, 3]. The aim of this work is more detailed study of stress relaxation in these materials.

2. Materials and methods of research

Polyester resin PN-1 produced by the enterprise "Combine" Kamensky "(GOST 27952-88). Resin PN-1 is a solution of unsaturated polyester based on diethylene glycol, maleic anhydride and phthalic anhydride in styrene. For curing resin was used hardener Butanox M-60 and the accelerator is OK (1.5 % active). Cure was carried out at 20 °C. The time interval between the preparation of samples and their rupture test and creep was not less than a week.

Epoxy resin ED-20 produced by the company "Karbohim". Samples for the study were prepared by a technique close to the technology for the preparation of building composites

based on epoxy resin: mixing the resin with the hardener Ethal-45M in a 2: 1 ratio, pouring into a mold, holding for 24 hours at room temperature, then 6 hours at 80 °C.

Investigation of the mechanical properties of PN-1 resin was carried out on a universal testing machine Shimadzu Autograph AG-X Series [4]. The samples of rectangular section with the sizes of the working part (between the grippers of the machine) 4 * 10 * 100 mm are used. The control of the test process and preliminary processing of the data obtained on this machine are carried out using the software TRAPEZIUM X * 1 [5].

The stress relaxation in the resin samples was examined at room temperature. The sample was loaded stepwise to a predetermined stress level, then the grippers of the machine were fixed, and the deformation was remained for from half an hour to two hours. Then the load increased to the next level and the record of the relaxation curve continued.

3. Test results and discussion

An example of the obtained in our experiments relaxation curves shown in Fig. 3.

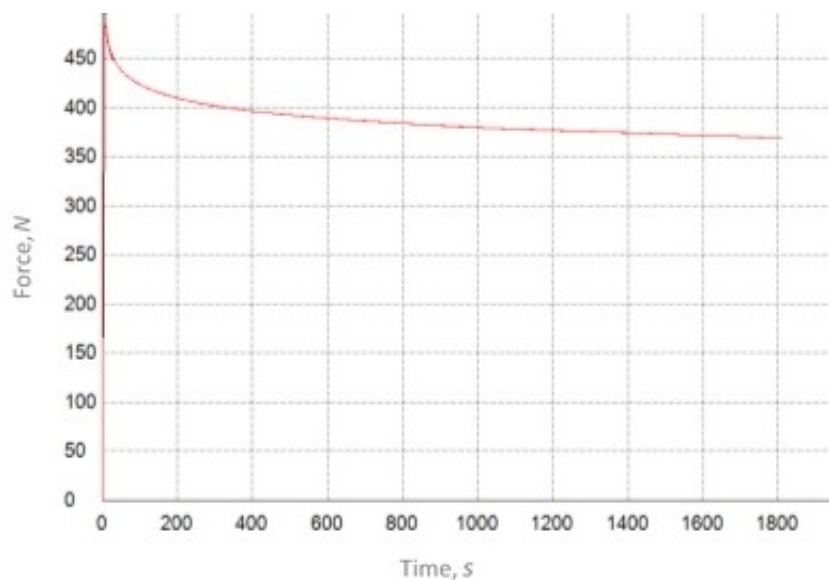


Fig. 3. The relaxation curves for the polyester resin at 12.5 MPa.

As is known, if the relaxation process proceeds through a single simple mechanism, its time dependence can be interpolated by an exponential

$$x = x_0 e^{-t/\tau}, \quad (1)$$

with the constants x_0 and τ . Then in semilogarithmic coordinates $\ln x(t)$ this dependence has the form of a straight line.

In Fig. 4 shows the dependence of $\ln \sigma(t)$ obtained for sample polyester resin (σ – mechanical stress). As can be seen, this dependence is clearly nonlinear. The analysis showed that the curve in Fig. 2 for any practical purpose can be interpolated by a polynomial of the third degree.

Garofalo notes that in 1904 it was found that the experimental data on relaxation of stresses in metals and alloys are well described by equation of the form

$$\sigma = \sigma_0 - \alpha_p \ln(1 + \tau_p t), \quad (2)$$

where σ_0 is the initial stress, α_p and τ_p are time-independent constants. [6]

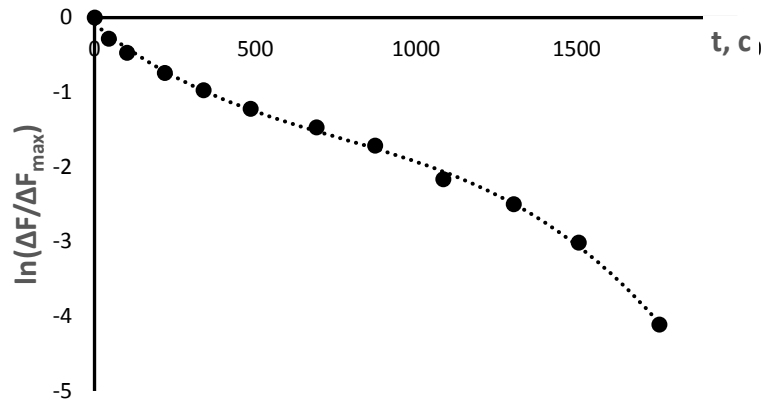


Fig. 4. Relaxation of stress in the resin PN-1 at a voltage of 12.5 MPa.

However, neither [6] nor in later works was not proposed physical mechanisms for this dependence.

In Fig. 5 shows the dependence of the stress on the value of $\ln(1 + bt)$ obtained for the polyester resin at different initial stresses. It turned out that all the experimental points fit near the common straight line with the criterion of reliability of the approximation $R^2 > 0.996$. This means that the time dependence of the voltage can be described by a function of the form:

$$y = a \ln(1 + bt), \quad (3)$$

where $y = (\sigma - \sigma_\infty)/(\sigma_0 - \sigma_\infty)$; σ is the stress at time t , σ_∞ , σ_0 is the relaxed and initial stress, respectively. The constants a and b are practically independent of the stress and are equal to $a \approx 0.15$ and $b \approx 0.7$. Note that the results are weakly sensitive to the value of the parameter b .

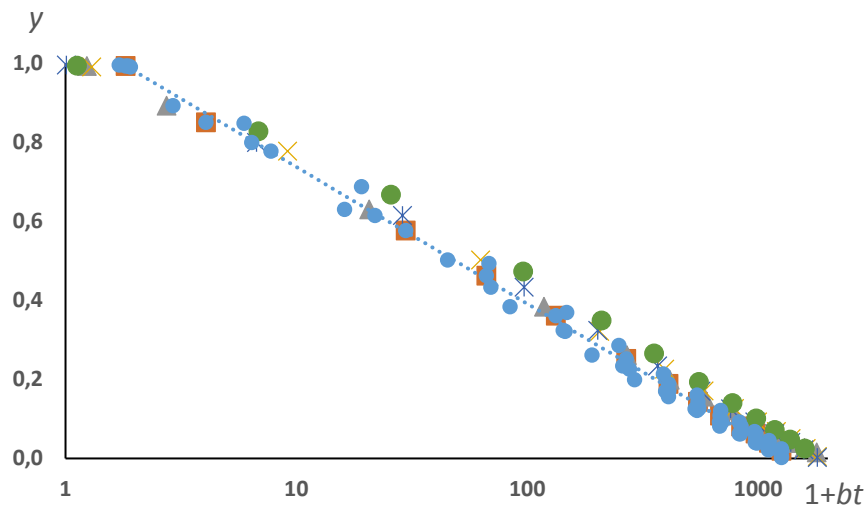


Fig. 5. Results of testing polyester resin for tension at different initial stress values (different markers correspond to different values of the initial stress).

The change in temperature in the interval from 15 to 35 °C did not reveal a noticeable effect on the value of the constants.

In the bending test, data qualitatively similar to those obtained with stretching were obtained, but with slightly different constants (Fig. 6): $a \approx 0.2$ and $b \approx 0.05$.

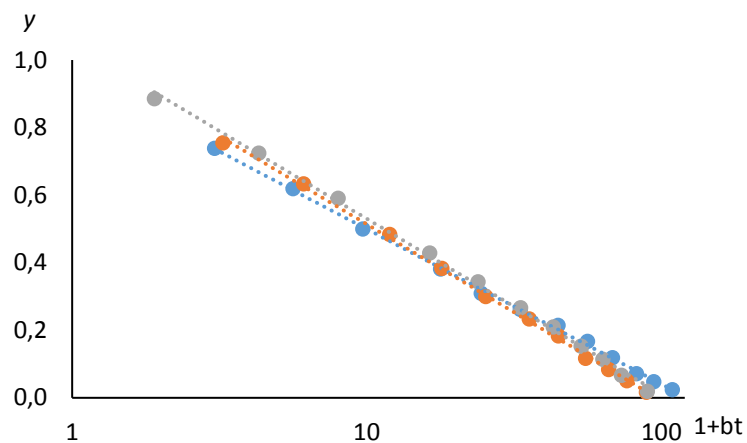


Fig. 6. Results of testing polyester resin for bending at different initial stress values (different markers correspond to different values of the initial stress).

Stress relaxation in epoxy resin occurs similar to the relaxation in polyester resin (Fig .7). Constants for this resin was equal to: $a \approx 0.16$ and $b \approx 0.3$.

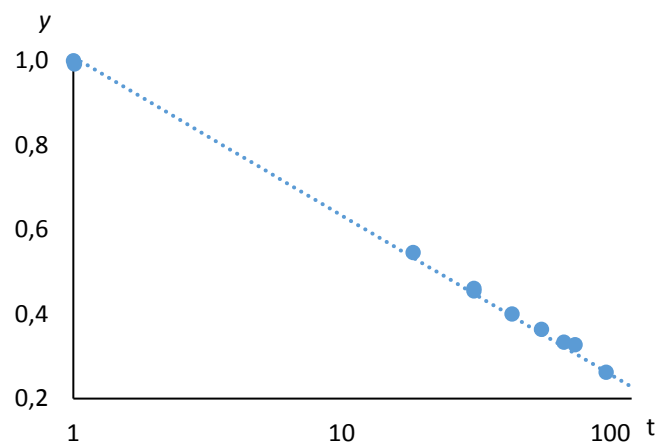


Fig. 7. The test results of the epoxy resin.

Functions (2) and (3) are actually the same. Therefore, stress relaxation in the glassy resin is at least qualitatively (mathematically) can be described in the same way as in crystalline metallic materials.

Our studies of creep in resins [2, 3] showed that it is well described by a logarithmic function of the form

$$\varepsilon = \varepsilon_e + \varepsilon_p + \varepsilon_0 \ln(1 + vt), \quad (4)$$

which is mathematically identical to the formula (2). From this we can draw the natural conclusion that the molecular mechanisms of stress relaxation and creep have the same nature.

The derivation of relation (3) for crystals was based on the notion that the material can be divided into elementary volumes with a characteristic size L [7]. It was assumed that this volume can undergo continuous deformation regardless of the deformation of the neighboring elementary volume. If the deformation in a given elementary volume has occurred, then the stresses in the neighboring elementary volumes cannot reduce this deformation.

In principle, there are no contraindications to the use of this model and to non-crystalline materials, especially as, at low temperatures, polymers are mechanically indistinguishable from simple elastic solids [8].

When analyzing the results of the creep study in resins, we made the assumption that some forms of local mobility, which are related to the movement of side groups or small fragments of the main chains [8], which play the same role as dislocations in crystals. Taking into account the similarities in the laws of creep and stress relaxation, it can be assumed that the motion of the same groups or fragments determines the relaxation of stresses.

4. Conclusions

1. Relaxation of mechanical stresses is described by a logarithmic function, which has the same form for both crystalline metals and amorphous cured resins.

2. Quantitative characteristics of stress relaxation in both of the studied resins under tensile test and bending are close, that can be interpreted in favor of the assumption about the similarity of the structural elements responsible for relaxation in these compounds.

3. Identical form of the function, describing the two types of relaxation processes (relaxation of mechanical stresses and creep) for substances of different nature (metals and polymers) and various structures (crystalline and amorphous) leads to the assumption of a deeper unity of the nature of these processes.

References

- [1] N.E. Fomin, V.I. Ivlev, A.F. Sigachyov, V.A. Yudin // *Physics and chemistry of material processing* **5** (2015) 66.
- [2] N.E. Fomin, V.I. Ivlev, V.A. Yudin, A.F. Sigachyov // *Materials Physics and Mechanics* **22** (2015) 78.
- [3] V.I. Ivlev, A.F. Sigachyov, N.E. Fomin, V.A. Yudin // *Materials Physics and Mechanics* **30** (2017) 61.
- [4] <http://www.ssi.shimadzu.com/products/literature/Testing/C224-E045.pdf>
- [5] <http://www.ssi.shimadzu.com/products/product.cfm?product=trapeziumx>
- [6] F. Garofalo. *Fundamentals of Creep and Creep-Rupture in Metals* (Metallurgy, Moscow, 1968). (In Russian).
- [7] R. Kahn (Ed.), *Physical Metallurgy* Vol. 3. (Mir, Moscow, 1968). (In Russian).
- [8] G.M. Bartenev, S.J. Frenkel. *Polymer physics* (Chemistry, Leningrad, 1990). (In Russian).

ON CALCULATION OF EFFECTIVE ELASTIC PROPERTIES OF MATERIALS WITH CRACKS

Ruslan L. Lapin¹, Vitaly A. Kuzkin^{1,2}

¹Peter the Great Saint Petersburg Polytechnic University, Saint Petersburg 195251, Russia

²Institute for Problems of Mechanical Engineering RAS, Saint Petersburg 199178, Russia,

* e-mail: lapruslan@mail.ru, kuzkinva@gmail.com

Abstract. A simple approach for calculation of anisotropic effective elastic properties of cracked materials is presented. Square computational domain containing randomly distributed cracks under plane strain conditions is considered. Effective elastic properties are expressed in terms of average displacement discontinuities on cracks in three test problems: uniaxial loading in two orthogonal directions and pure shear. These problems are solved using the displacement discontinuity method. Resulting effective compliances are averaged over realizations with different crack distributions. This approach is employed for calculation of effective elastic properties for two particular crack configurations: (i) one family of parallel cracks and (ii) two families of parallel cracks inclined at angle 30° . Crack densities up to 0.8 are considered. It is shown that for both configurations the effective elastic properties are orthotropic even at large crack densities. Dependencies of Young's moduli on crack density are obtained. At crack densities up to 0.1, the effective properties can be estimated analytically using the non-interaction approximation (NIA). At higher crack densities, the NIA strongly overestimates effective stiffnesses. Quantitative agreement with results obtained in the literature using more sophisticated methods is demonstrated.

Keywords: effective elastic properties; cracked materials; crack interactions; orthotropy; non-interaction approximation; boundary element method; displacement discontinuity method.

1. Introduction

Calculation of effective elastic properties of materials with cracks is a long standing problem in mechanics of materials. Changes in effective elastic properties due to cracks can be very significant [1]. Therefore accurate prediction of these properties is crucial in many fields, including mechanical engineering [2, 3], geomechanics [4, 5], material science [6] etc.

In literature, the effective elastic properties are computed both analytically and numerically. In the framework of analytical methods, effective elastic properties are represented as a function of crack density [1] (or crack density tensor [3]). At relatively low crack densities, the effective properties can be estimated using the non-interaction approximation (NIA) [3]. In the NIA, it is assumed that the effect of many cracks is equal to a sum of independent effects from individual cracks. The calculation of effective properties is reduced to calculation of average displacement discontinuity for a single crack subjected to a given loading at infinity. With increasing crack density, the effect of mutual influence of cracks become significant. Then more accurate approximate methods, such as differential scheme [7], self-consistent scheme [2], Mori-Tanaka scheme [8] should be used. However, these schemes yield different dependencies of effective properties on crack density and the choice of a proper scheme is not always straightforward. Moreover, approximate schemes [9], except for the NIA, are usually

limited to the case of uniform distribution of crack orientations (isotropic effective properties). Therefore, at high crack densities, anisotropic effective elastic properties are usually calculated numerically.

Numerical calculation of effective properties of cracked materials is also a challenge. To calculate the effective properties, deformation of the computational domain containing large number of cracks under the given loads should be considered. In the two-dimensional case, reasonable accuracy can be reached either if the number of cracks in the computational domain is of order of 10^4 or if averaging over realizations with different crack distributions is used. In the latter case, number of cracks in the computational domain can be of order of 10^2 . Periodic boundary conditions also allow to minimize finite size effects [1]. Deformation of the computational domain can be described using, for example, the finite element method (FEM) or the boundary element method (BEM). Finite element solution requires very fine mesh, especially at high crack densities. In BEM, only the boundaries are discretized. This allows to decrease the number of degrees of freedom, compared to FEM. At the same time, the matrix corresponding to a system of linear equations of BEM is dense. Therefore, the choice between two methods is not straightforward.

In the present paper, we present a simple approach for calculation of effective elastic properties in the two-dimensional case (plane strain). The square computational domain containing randomly distributed cracks is considered. For each crack distribution, deformation of the computational domain under three different loads is simulated using the displacement discontinuity method [10] (the simplest version of the BEM). Then effective compliances are calculated using average displacement discontinuities on cracks [3]. Additionally, the compliances are averaged over realizations in order to reduce finite size effects. This simple approach is employed for calculation of anisotropic effective elastic properties for two crack configurations: (i) one family of parallel cracks and (ii) two families of parallel cracks inclined at angle 30° . Numerical results allow to estimate the range of applicability of the NIA and to study anisotropic elastic properties of the cracked material. Comparison with results obtained in the literature using more sophisticated methods [1] is carried out.

2. Calculation of effective elastic properties of cracked materials

In the present section, we describe the approach for calculation of effective elastic properties of cracked materials. Two-dimensional statement (plane strain) is considered. The matrix material is isotropic, linearly elastic.

To calculate elastic properties, we consider deformation of a square computational domain containing cracks under three different loads: uniaxial load in two orthogonal directions and pure shear. In these cases, the mean strain, $\boldsymbol{\varepsilon}$, and applied stresses, $\boldsymbol{\sigma}^0$, are related to components of the effective compliance tensor M by Hooke's law as follows.

- Uniaxial load in the "horizontal" direction ($\boldsymbol{\sigma}^0 = \sigma^0 e_1 e_1$):

$$\begin{pmatrix} M_{1111} \\ M_{2211} \\ M_{1211} \end{pmatrix} = \frac{1}{\sigma^0} \begin{pmatrix} \varepsilon_{11} \\ \varepsilon_{22} \\ \varepsilon_{12} \end{pmatrix}. \quad (1)$$

- Uniaxial load in the "vertical" direction ($\boldsymbol{\sigma}^0 = \sigma^0 e_2 e_2$):

$$\begin{pmatrix} M_{1122} \\ M_{2222} \\ M_{1222} \end{pmatrix} = \frac{1}{\sigma^0} \begin{pmatrix} \varepsilon_{11} \\ \varepsilon_{22} \\ \varepsilon_{12} \end{pmatrix}. \quad (2)$$

- Shear load $\boldsymbol{\sigma}^0 = \sigma^0 (e_1 e_2 + e_2 e_1)$:

$$\begin{pmatrix} M_{1112} \\ M_{2212} \\ M_{1212} \end{pmatrix} = \frac{1}{\sigma^0} \begin{pmatrix} \varepsilon_{11} \\ \varepsilon_{22} \\ \varepsilon_{12} \end{pmatrix}. \quad (3)$$

Tractions corresponding to loads (1)-(3) are applied at boundaries of the computational domain. The mean strain is calculated. Given known the mean strain, the effective properties are calculated using formulas (1)-(3).

The mean strain, ε , is calculated using the following decomposition [3]:

$$\varepsilon = \varepsilon_0 + \Delta\varepsilon, \tag{4}$$

where ε_0 is the strain in material without cracks (known), $\Delta\varepsilon$ is the unknown extra strain due to cracks. The extra strain due to cracks, $\Delta\varepsilon$, is expressed in terms of the average displacement discontinuities (jumps of displacement) on cracks as follows [3]:

$$\Delta\varepsilon = \frac{1}{2A} \sum_k (bn + nb)^{(k)}, \tag{5}$$

where $b^{(k)}$ is the average displacement discontinuity on the k -th crack; $n^{(k)}$ is unit normal to k -th crack, A is the area of the computational domain. Crack openings, $b^{(k)}$, under given loads (1)-(3) are calculated using the displacement discontinuity method [10], described in the next section.

Thus, the effective elastic constants are computed as follows. For each crack distribution, cracks and sides of the computational domain are divided into boundary elements. The system of linear algebraic equations for displacement discontinuities in all boundary elements is solved under loading conditions, corresponding to (1)-(3). The extra strains due to cracks are calculated using formula (5). Then components of the effective compliance tensor are computed using formulas (1)-(3). Since the distribution of cracks is random, the resulting compliances are averaged over realizations with different crack distributions.

In the following sections, this simple procedure is employed for calculation of effective properties for two particular crack configurations.

3. The displacement discontinuity method (DDM)

In the present section, we describe numerical method used for calculation of displacement discontinuities on cracks.

The displacement discontinuity method (DDM), introduced in the paper [10], is the simplest version of the boundary element method [11]. Boundaries of the computational domain and cracks are divided into elements, each having the normal and the shear displacement discontinuities, D_y and D_x (Fig. 1). The displacement discontinuity along a crack is a piecewise constant function (e.g. zero order approximation is used).

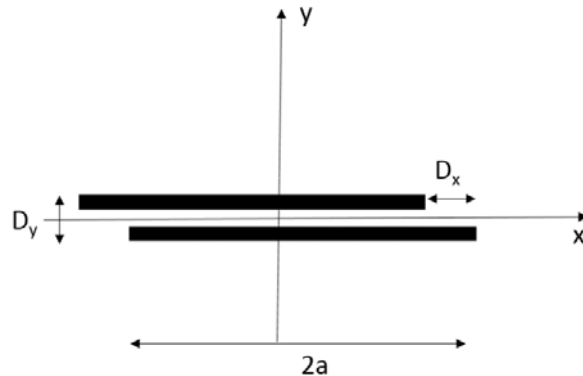


Fig. 1. Displacement discontinuities associated with one boundary element.

Each element can be subjected to the shear and normal tractions. The displacement discontinuities, D , and the tractions, T , at all elements form columns:

$$D = \begin{pmatrix} D_x^1 \\ D_y^1 \\ \dots \\ D_x^N \\ D_y^N \end{pmatrix}, T = \begin{pmatrix} T_x^1 \\ T_y^1 \\ \dots \\ T_x^N \\ T_y^N \end{pmatrix}, \quad (6)$$

where N is the total number of elements. Displacement discontinuities and tractions are interrelated by a system of linear equations:

$$\begin{aligned} T_x^i &= \sum_{j=1}^N A_{xx}^{ij} D_x^j + \sum_{j=1}^N A_{xy}^{ij} D_y^j, \quad i = 1, \dots, N, \\ T_y^i &= \sum_{j=1}^N A_{yx}^{ij} D_x^j + \sum_{j=1}^N A_{yy}^{ij} D_y^j, \quad i = 1, \dots, N. \end{aligned} \quad (7)$$

Here:

$$\begin{aligned} A_{xx}^{ij} &= -2G \left(-\sin(2\gamma) f_{xy} + \cos(2\gamma) f_{xx} + y(\sin(2\gamma) f_{xyy} - \cos(2\gamma) f_{yyy}) \right), \\ A_{xy}^{ij} &= -2Gy(\cos(2\gamma) f_{xyy} + \sin(2\gamma) f_{yyy}), \\ A_{yx}^{ij} &= 2G(2 \sin^2 \gamma f_{xy} + \sin(2\gamma) f_{xx} - y(\cos(2\gamma) f_{xyy} + \sin(2\gamma) f_{yyy})), \\ A_{yy}^{ij} &= -2G \left(f_{xx} - y(\sin(2\gamma) f_{xyy} - \cos(2\gamma) f_{yyy}) \right), \end{aligned} \quad (8)$$

$$f = -\frac{1}{4\pi(1-\nu)} \left(y \left(\arctg \frac{y}{x-a} - \arctg \frac{y}{x+a} \right) - (x-a) \ln \sqrt{(x-a)^2 + y^2} + (x+a) \ln \sqrt{(x+a)^2 + y^2} \right),$$

where γ is the angle between elements i and j ; G is the shear modulus; x, y are local coordinates of the j -th element in the coordinate system of the i -th element. Note that the matrix, corresponding to system (7), is dense.

Thus, displacement discontinuities on cracks, D , under given loads, are calculated using the system of linear equations (7). The resulting average discontinuities on cracks are used for calculation of effective compliances of the material as described in the previous section.

4. Test problem: opening of a single crack

To verify numerical implementation of the DDM, the problem of a single crack in a square domain under uniaxial tension is solved (see Fig. 2). This problem also allows to estimate the minimum number of elements required for discretization of cracks in calculations of effective properties.

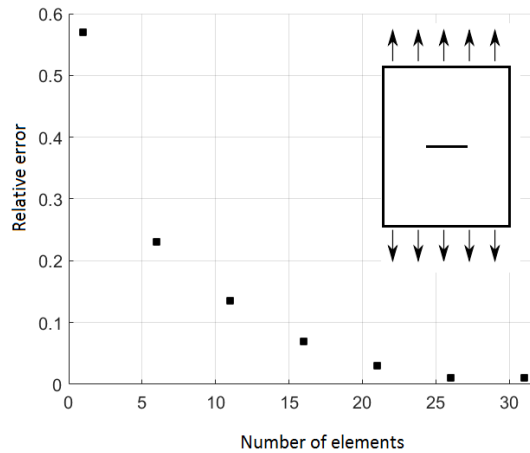


Fig. 2. Relative error in average crack opening as a function of number of elements per crack.

The crack and sides of the computational domain are divided into elements. The ratio of domain size to crack length is equal to 20. Trial and error approach shows that it is sufficient to

use 40 elements per side of the computational domain. Average opening of the crack is calculated. Results are compared with the exact analytical solution for a crack in an infinite domain [3]. The relative error (Δ) in average crack opening as a function of number of elements per crack is shown in Fig. 2.

Fig. 2 shows that the DDM overestimates the crack opening. Therefore, the compliance of cracked material is also overestimated. Acceptable accuracy (relative error about 3 %) is reached, when 20 elements per crack are used. Therefore, this number of elements is used in further calculations.

5. Calculation of anisotropic effective elastic properties

In the present section, we compute effective elastic properties for two crack configurations: (i) one family of parallel cracks and (ii) two families of parallel cracks inclined at 30° .

In our simulations, all cracks have the same length. To operate with dimensionless quantities, effective compliances are normalized by the shear modulus of the matrix. The 3D Poisson's ratio equal to $1/4$ is used, implying $1/3$ in the case of plane strain. Size of the computational domain is normalized by crack length.

The crack density ρ is calculated as [3]:

$$\rho = \frac{Nl^2}{4A}, \quad (9)$$

where N is the number of cracks in computation domain, l is a crack length, A is the area of the computation domain. Examples of crack arrays with different crack densities are shown in Fig. 3.

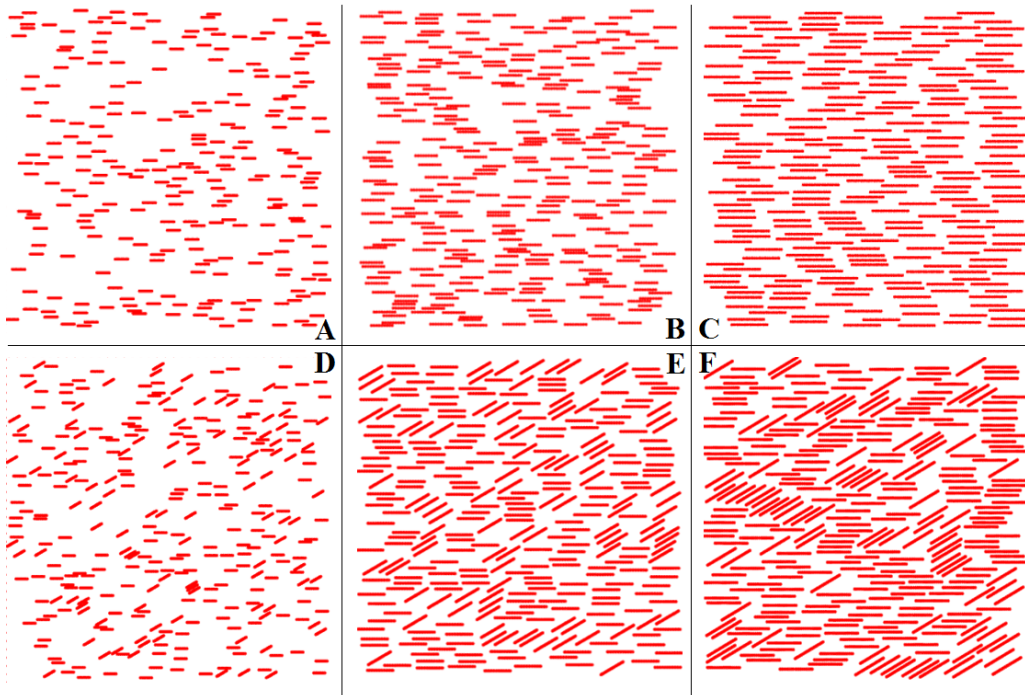


Fig. 3. Examples of crack arrays with different crack densities ($\rho = 0.1, \rho = 0.5, \rho = 0.8$). One family of parallel cracks (A)-(C) and two families of parallel cracks inclined at angle 30° (D)-(F).

In all simulations, crack densities were in the interval $0.01 \leq \rho \leq 0.8$. For each value of crack density, 450 to 650 crack arrays were generated, with locations of crack centers determined by random number generator and subject to the restriction of the minimal distance

between cracks being larger than 0.1 crack length. Details of numerical simulations are summarized in Table 1.

Table 1. Parameters of numerical simulations.

Parameter	Value
Number of cracks in one array	300-350
Number of boundary elements per one crack	20
Number of boundary elements per one side of the computational domain	40
Number of realizations for each value of crack density	450-650

5.1. One family of parallel cracks. Consider effective elastic properties of a material containing randomly distributed parallel cracks (see subfigures (A)-(C) in Fig. 3). The effective properties are calculated using the approach described in section 2.

It is shown that the effective elastic properties are orthotropic. One of the orthotropic axes is collinear with cracks. Non-zero components of the effective stiffness tensor (averaged over realizations) are shown in Fig. 4. Predictions of the non-interaction approximation and results obtained in the paper [3] are also shown in Fig. 4.

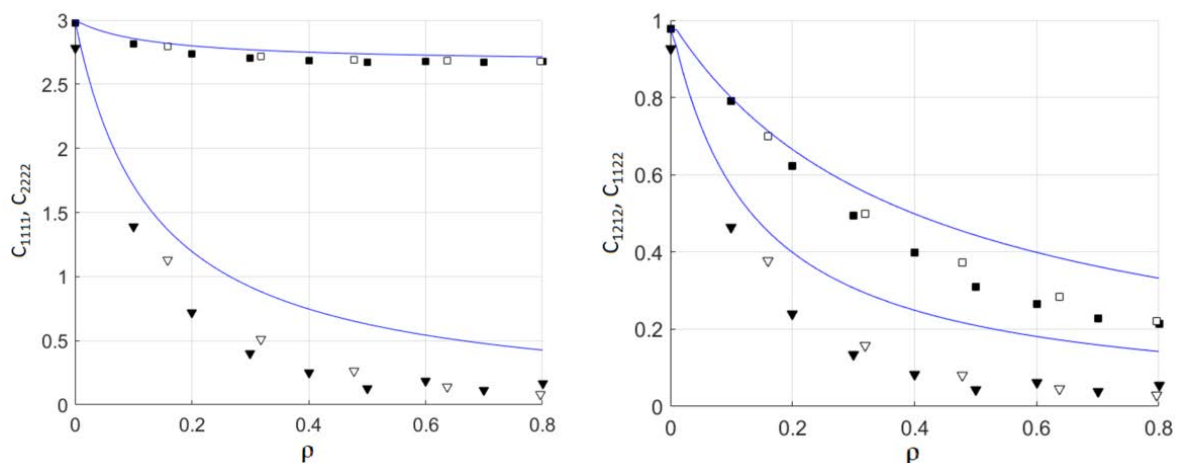


Fig. 4. Effective stiffnesses for a material with parallel cracks. Our results (filled squares and triangles) and results obtained in the paper [1] (empty squares and triangles). Solid lines show predictions of the non-interaction approximation.

It is seen from Fig. 4 that our results are in a good agreement with ones obtained in paper [1] by more accurate method. Stiffnesses, predicted by our method, are below the values obtained in the paper [1]. The reason for this difference is that the DDM slightly overestimates crack openings (see section 4). Therefore, compliances are also overestimated and stiffnesses are underestimated. At the same time, the approach described in the present paper is significantly simpler.

Note that the NIA has reasonable accuracy at crack densities up to 0.1. Therefore, in this case, the effective elastic properties can be estimated numerically.

From engineering point of view, it may be more informative to plot effective Young's moduli rather than stiffnesses. Young's moduli are related to components of the compliance tensor, M , as follows

$$E_x = \frac{1}{M_{1111}}, E_y = \frac{1}{M_{2222}}, \quad (10)$$

where the x -axis is directed along cracks. Effective Young's moduli of a material with parallel cracks are shown in Fig. 5.

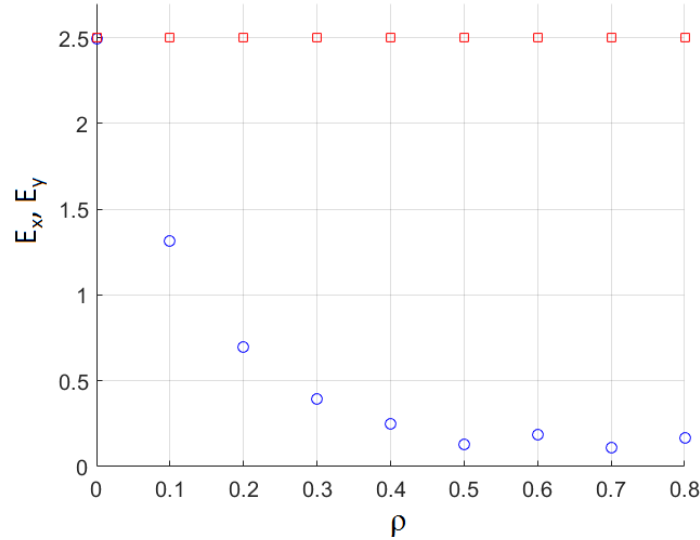


Fig. 5. Young's moduli of a material with parallel cracks, in the case of parallel family of cracks (squares – E_x , circles – E_y).

As expected, Young's modulus in the direction of cracks, E_x , does not depend on crack density. In contrast, Young's modulus E_y is significantly affected by cracks.

5.2. Two families of parallel cracks inclined at angle 30° . Consider effective elastic properties of a material containing two families of parallel cracks inclined at angle 30° (see subfigures (D)-(F) in Fig. 3). Partial crack densities of the two families differ by the factor of two: $\rho_1 = 2\rho_2$, $\rho_1 + \rho_2 \equiv \rho$. This problem was originally analyzed in the paper [3] using the non-interaction approximation. In the paper [3], it was shown that the effective elastic properties are orthotropic. The angle between one of the orthotropic axes and x -axis (horizontal in Fig. 3) is approximately equal to 9.8° (counter-clockwise rotation). In the present section, we show that at high crack densities the effective properties are still orthotropic.

The effective compliance tensor is computed as described in section 2. We assume that the effective properties are orthotropic. Principal axes of the compliance tensor are found as follows. Coordinate axes are rotated by angle α . Components of the compliance tensor in new (rotated axes) are calculated using formulas [12]:

$$M^{rot} = F^T M F, F(\alpha) = \begin{pmatrix} \cos^2 \alpha & \sin^2 \alpha & 2 \sin \alpha \cos \alpha \\ \sin^2 \alpha & \cos^2 \alpha & -2 \sin \alpha \cos \alpha \\ -\sin \alpha \cos \alpha & \sin \alpha \cos \alpha & \cos^2 \alpha - \sin^2 \alpha \end{pmatrix}, \quad (11)$$

where α is a rotation angle, F^T is transposed rotation matrix. Since the orthotropy of effective properties is approximate, we find the principal axes such that deviation from orthotropy, δ , has minimum. The deviation is measured by the Euclidean norm [13]:

$$\delta = \frac{\sqrt{M_{1112}^2 + M_{2212}^2 + M_{1222}^2 + M_{1211}^2}}{\|M\|} \quad (12)$$

Minimization of δ with respect to rotation angle α yields the orientation of principal axes. Dependencies of deviation from orthotropy, δ , on rotation angle, α , for several values of crack density are shown in Fig. 6. It is seen that for all crack densities δ has minimum at $\alpha \approx 9.5^\circ$. This value is in a good agreement with prediction of the non-interaction approximation ($\alpha_{NIA} \approx 9.8^\circ$). Therefore, the effective elastic properties are orthotropic even at high crack densities.

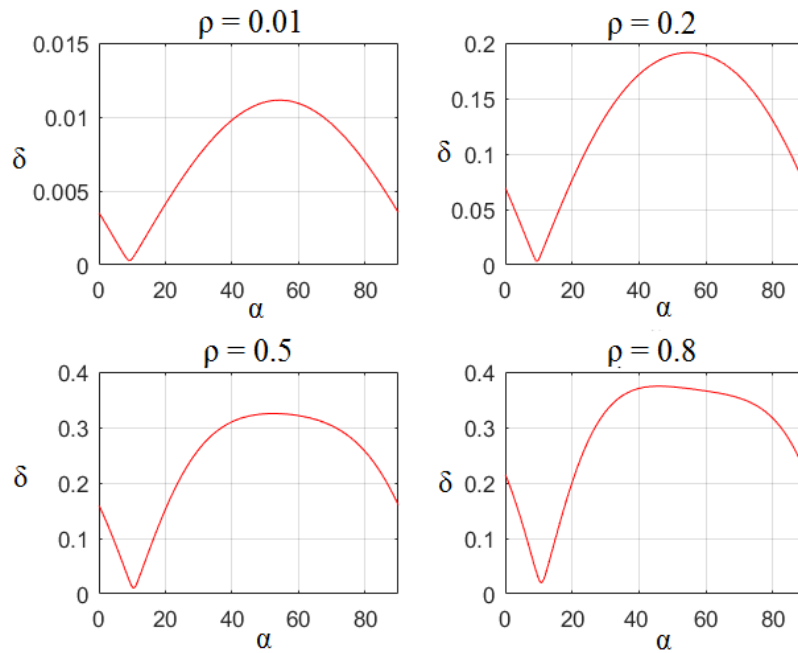


Fig. 6. Deviation from orthotropy, measured by norm (12), as a function of the rotation angle. Note that minimum value of deviation, δ , is less than several percent.

Effective Young's moduli in principal axes of the compliance tensor are calculated (see Fig. 7). In contrast to the previous problem, both moduli decrease with increasing crack density.

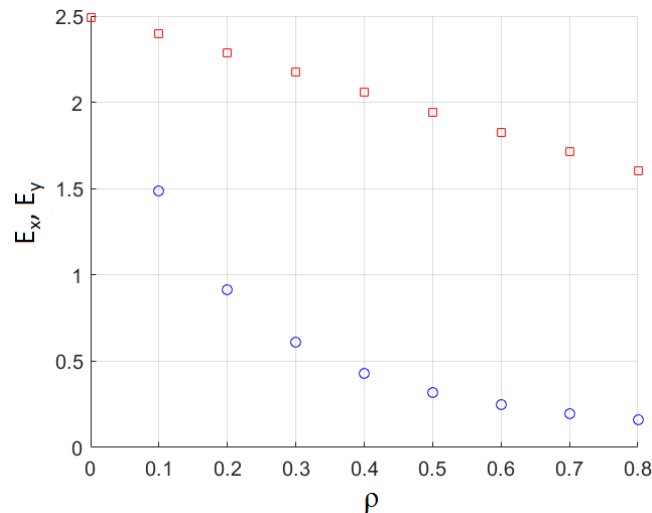


Fig. 7. Young's moduli for a material with two families of parallel cracks inclined at angle 30° (squares – E_x , circles – E_y). Here x and y are the principal axes of the compliance tensor.

6. Conclusions

A simple approach for calculation of effective elastic properties for cracked materials was presented. The approach has three main ingredients: (i) relation between extra strain due to cracks and average displacement discontinuities on cracks [3], (ii) the displacement discontinuity method [10] and (iii) averaging over realizations with different crack distributions. The approach was employed for calculation of effective elastic properties for two crack configurations: one family of parallel cracks and two families of parallel cracks inclined at angle 30° . Comparison with predictions of the non-interaction approximation was carried out. It was shown that the non-interaction approximation has acceptable accuracy for crack densities up to 0.1. Therefore, for these densities, the effective properties can be estimated

analytically. At higher crack densities, the non-interaction approximation strongly overestimates the effective stiffness. For both crack configurations, elastic properties are orthotropic even at large crack densities up to 0.8. Quantitative agreement with results reported in literature was demonstrated. The approach described above can be used in a variety of applications, including geomechanical problems, e.g. simulation of hydraulic fracturing in naturally fractured reservoirs [14].

Acknowledgement. *This research was financed by Ministry of Education and Science of the Russian Federation within the framework of the Federal Program "Research and development in priority areas for the development of the scientific and technological complex of Russia for 2014-2020", Activity 1.2., Agreement on Grant No. 14.575.21.0146 of 26 September, 2017, unique identifier: RFMEFI57517X0146.*

The authors are deeply grateful to M.L. Kachanov for statement of the problem and useful discussions. Numerical simulations have been carried out using facilities of the Supercomputer Center "Polytechnic" at Peter the Great Saint Petersburg Polytechnic University.

References

- [1] V.I. Kushch, I. Sevostianov, L. Mishnaevsky // *International Journal of Solids and Structures* **46** (2009) 1574.
- [2] B. Budiansky, R.J. O'Connell// *International Journal of Solids and Structures* **12** (1976) 81.
- [3] M. Kachanov // *Advances in Applied Mechanics* **30** (1993) 260.
- [4] V. Grechka, M. Kachanov // *Geophysics* **71** (2006) D85.
- [5] E. H. Saenger, O.S. Kruger, S. A. Shapiro // *Geophysical Prospecting* **52** (2004) 183.
- [6] Y.J. Liu, X.L. Chen // *Mechanics of Materials*, **35** (2003) 69.
- [7] Z. Hashin // *Journal of Mechanics and Physics of Solids* **36** (1988) 719.
- [8] Y. Benveniste // *Mechanics of Materials* **6** (1987) 147.
- [9] B. Orlovsky, E.H.Saenger, Y. Gueguen // *International Journal of Fracture* **124** (2003) L171.
- [10] S.L. Crouch, A.M. Starfield, *Boundary Element Methods in Solid Mechanics: with Applications in Rock Mechanics and Geological Engineering* (Allen & Unwin, London, Boston, 1983).
- [11] A.M. Linkov, *Boundary Integral Equations in Elasticity Theory* (Dordrecht-Boston-London, Kluwer Academic Publishers, 2002).
- [12] A. Bower, *Applied Mechanics of Solids* (CRC Press, 2009).
- [13] I. Sevostianov, M. Kachanov // *International Journal of Engineering Science*, **46** (2008) 211.
- [14] T. Bratton, D.V.Cahn, N.V. Que, N.V. Duc, P. Gillespie, D. Hunt, B. Li, R. Marcinew, S. Ray, B. Montaron, R. Nelson, D. Schoderbek. L. Sonneland // *Oilfield Review*, **18** (2006) 4.

IN-SITU MEASUREMENT AND FINITE ELEMENT SIMULATION OF THERMO-MECHANICAL PROPERTIES OF AA 6063 ALUMINUM ALLOY FOR MIG WELDMENT

S. Baharnezhad^{1*}, A. P. Golhin²

¹Department of mechanical engineering, École Polytechnique de Montréal, Canada

²Department of mechanical engineering, KN Toosi University of Technology, Iran

*e-mail: sadreddin.baharnezhad@polymtl.ca

Abstract. The *metal inert gas* (MIG) welding and the crucial parameters influenced on the thermal and mechanical behaviours, and microstructure of AA 6063 aluminum were investigated through the experiment and the FE simulation. A thermo-mechanical model was extended using the finite element software of ABAQUS. In this manner, the thermal distribution and time-temperature histories made during MIG welding were derived. To achieve more accuracy, a subroutine was developed by FORTRAN. The real-time temperature measurements and the effective parameters of the thermal distribution, including the welding speed and the arc voltage were studied by conducting MIG bead-on-plate welds and the residual stresses derived from the simulation were compared with the empirical observations. The results depicted that the simulation would estimate rigorously the temperature gradients and the fields of welding-induced stress. The microstructural and microhardness examinations were also conducted which allowed—alongside the TTT curve—the phases precipitated and the heat sink effects were studied and foreseen. Indeed, the microstructure images demonstrated that the overaged, agglomerated β -Mg₂Si phases, in the HAZ, and the modified β -AlFeSi pseudo-plate-like precipitates alongside the smaller and coarsened β -Mg₂Si phases, in the fusion zone, were precipitated.

Keywords: FE simulation, in-situ measurement, 6063 aluminum, welding residual stress, thermo-mechanical properties, TTT curve, microstructural examination.

1. Introduction

Welding of aluminium alloys has been always faced several challenges. Despite the high weldability properties of this metal, such limitations as high thermal conductivity, remarkable thermal expansion and contraction, low melting point, and many changes in the structure and properties shall be considered in in the welding processes [1,2]. Hence, in the aluminium joints, examination of welding processes, and consequently, the distribution of stress and heat on mechanical properties are of great importance. Distribution of residual thermal stress of welding depends upon several factors such as pieces size, specifications of materials, constraint conditions, heat input, type of joining, number of welding passes and their sequence, mixture of gases and metal transferring mode. Examination of all these factors during welding of different aluminum alloys is highly complicated and costly [3-7]. One of the interesting aluminum alloys for researchers and industry is AA6063 due to having a good weldability and its widespread applications in some of important industries such as defense, aerospace and automobile.

Simulation is widely used in the development of the research, production, and industrial processes today. Finite element method (FEM) is one of the most applied numerical techniques, which is employed in the various engineering sciences [8-11]. Accordingly, many models have been presented for simulation of the effect of various welding parameters on the base metal properties that can be analyzed by different numerical methods [12-14]. The results revealed that for a thin sheet, the temperature history of whole volumetric loading would comply with the empirical measurements. Goldak and his research team suggested a double ellipsoidal model, as a heat source, to raise accuracy of the results. They also introduced this model as a deep penetration welding model [15]. The main idea of this method is a Gaussian distribution of heat input on a double ellipsoidal as shown in Fig. 1. Guo *et al.* [16] studied on the formation of cold weld in Gas Metal Arc Welding (GMAW) of aluminum alloy 6005-T4 using experimental and numerical methods. They proposed three methods of heat inputting to enhance the weld penetration at the initial welding state. They also obtained the final weld profile and the maximum temperature in the HAZ. Their research was supported by some metallurgical characterizations and microhardness examinations. Anca *et al.* simulated an arc welding thermo-mechanically by FEM. They predicted the thermal histories and the residual stresses [14].

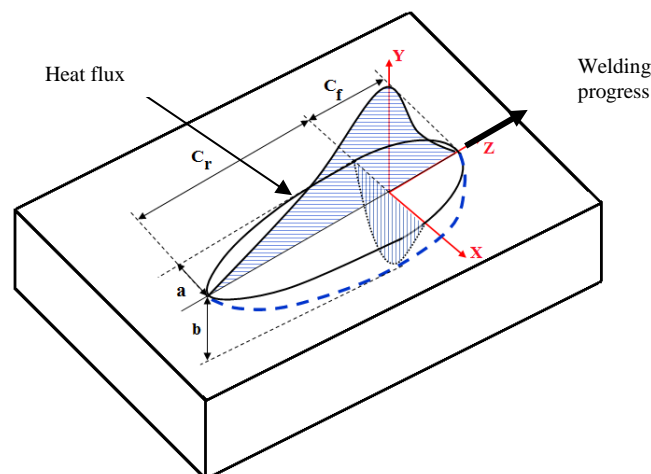


Fig. 1. Schematic of the double ellipsoid heat source configuration.

Chen *et al.* [17] investigated the thermal and mechanical behaviour of the weldments during arc welding using the experimental and numerical method. They developed a new technique for high temperature strain measurement in their experimental efforts so that they could measure the strain in a distance of 1 mm away from the fusion line. Meanwhile, they used the FEM to approve their claim.

Considering the effect of Metal Inert Gas (MIG) welding parameters on the mechanical properties of aluminum alloy 6063 joints, the finite element method was used as a high-precision approach in the present research. Also, in order to model the two-weld passes and import the molten elements into fusion zone, element birth and death technique was used. Simulation and analysis process was made by ABAQUS software in standard mode. To achieve a more accurate solution and use the moving heat source, a subroutine was developed in FORTRAN. The simulation output was compared with the experimental results. The results showed that the simulation would to forecast the thermal transient profile, the range of heat affected zone and the extension of residual stresses.

Based on the authors' knowledge, this is the first in the literature that reports the analysis of 6063 Al via both experimental GMAW and FEM by considering the time-dependent thermal and mechanical properties, real-time temperature measurements, including fusion zone, and

microstructure examinations. Previous studies focused mainly on the other Al grades and were more experimental, however, few studies on welding of Al 6063 for both empirical and numerical have been reported.

Nomenclature:

c	Thermal capacity, $J. kg^{-1}. K^{-1}$
C_{ijkl}	Elastic tensor
$d\varepsilon_{ije}$	Elastic strain
$d\varepsilon_{ijp}$	Plastic strain
$d\varepsilon_{ijth}$	Thermal strain
q	Thermal current density, $J. m^{-1}. K^{-1}$
q_s	Constant thermal flux at the surface, $J. m^{-1}. K^{-1}$
T_s	Surface temperature
T_{sur}	Surrounding environment temperature $^{\circ}K$
T_{∞}	Temperature of the fluid in contact with the work piece, K
σ_{sb}	Stefan-Boltzmann constant, $5.6704e-8 J. m^{-2}. s^{-1}. K^{-4}$
ε	Whole-body heat transfer coefficient
η	Surface normal axis
λ	Thermal conductivity coefficient, $J. m^{-1}. s^{-1}. K^{-1}$
ρ	Density, $kg^{-1}. m^{-3}$
Q	Energy generation rate, $W. m^{-3}$

2. Simulation

Finite element software of ABAQUS 6.10-1 was employed for modelling, mechanical and thermal analyses in this research. The schematic of the cross-section profile, with the welding sequence, and the 3-D finite element model of the thermal coupling of the joints is illustrated in Figs. 2 and 3, respectively.

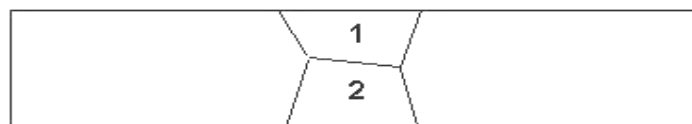


Fig. 2. Schematic of two-pass weld sequence used in the simulation.

Considering the symmetry, half of the shape geometry, has been modelled. Due to the high temperature gradient and stress in the heat-affected zone (HAZ), and to enhance the analysis precision, a higher element density was opted for these regions. In contrast, in order to increase the analytical convergence rate, and consequently, to reduce the solving time, the larger mesh sizes were provided for the farther regions. Also, the uncoupled thermo-mechanical analysis and the element birth-and-death technique were used to model the weld passes and filler metal deposition. In fact, three fields of heat, metallurgy, and mechanics are in contrast in the modelling of the welding process. The relationship of these three fields is cleared by choosing an analysis method for welding simulation. Since thermal and mechanical properties are correlated in FE modelling of weld and affect the metallurgical quality of weldment, hence both thermal and mechanical differential equations must be solved as correlated. Because of the low heat generated by the plastic strain while welding, the effect of surface strains on surface heat transfer coefficient can be ignored. Hence, the thermal and mechanical equations can be independently solved [15, 18-20]. Therefore, the present research used an uncoupled solution and the residual stress field was generated by elastic-plastic analysis.

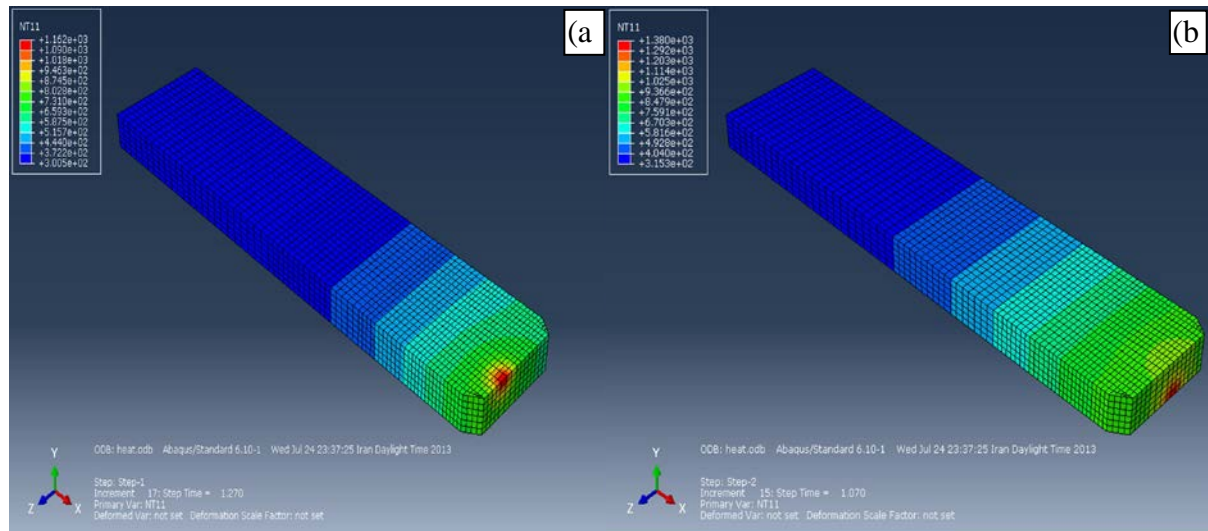


Fig. 3. Three-dimensional finite element model of the thermal coupling, (a) pass 1, (b) pass 2.

2.1. Thermal analysis. Heat transfer in welding is time-dependent and temperature distribution in an object is non-uniform and is a function of the spatial and temporal coordinates. Then, the time-dependent heat transfer equations are used to analyse this process. The principle of conservation of energy and Fourier’s law can be used to explain the differential equation of heat transfer independently from the strain generated as per Eq. 1:

$$\rho c \frac{\partial T}{\partial t} = \nabla \cdot (\lambda \nabla T) + Q \tag{1}$$

In this relation, c is the heat capacity, ρ is the density, λ is the thermal conductivity coefficient, and Q is the energy generation rate. Since the heat equation derivatives degrees are first order and quadratic regarding spatial and temporal coordinates, respectively, two boundary conditions and one initial condition are required for describing the system. The common boundary conditions often used in the thermal issues of welding are Dirichlet and Neumann boundary conditions proposed in the Eqs. 2 and 3, respectively [18]:

$$T = T_s, \tag{2}$$

where this is the surface temperature which is constant.

$$\{q\}^T \{\eta\} = -q_s \tag{3}$$

The Neumann condition refers to a given heat flux where η is the surface normal vector, q is the heat-flow density, and q_s is the constant heat flux at the surface. Insulated or adiabatic surface and the surface displacement are also according to Eqs. 4 and 5:

$$\{q\}^T \{\eta\} = 0 \tag{4}$$

$$\{q\}^T \{\eta\} = h_c (T_s - T_\infty), \tag{5}$$

where T_∞ is the fluid temperature in contact with the piece, T_s is the surface temperature, and h_c is the heat transfer coefficient of the object displacement (a function of temperature, surface position, and fluid velocity).

Radiation on the surface is calculated by Stefan Boltzmann law in Eq. 6:

$$\{q\}^T \{\eta\} = \varepsilon \sigma_{sb} (T_s^4 - T_{sur}^4), \tag{6}$$

where T_{sur} is the ambient temperature, ε is the object export coefficient, and σ_{sb} is constant of Stefan Boltzmann.

Heat flux was applied in mobile welding as a mobile thermal-volume source with an elliptical distribution of type of Goldak model [21]. To this end, a subroutine was written in FORTRAN language for applying heat flux in a 3-D model. In addition, for being close to the real conditions, all the mechanical and thermal properties were considered, based upon the data sources of Al6063 alloy spread by the references such as JMatPro software and ALLUSELECT,

temperature-dependent [22-24]. The heat flux equation in the front and back of the heat source was obtained by Eqs. 7 and 8.

$$q_f(x, y, z, t) = \frac{6\sqrt{3}f_f Q}{abc_f \pi \sqrt{\pi}} e^{-3x^2/a^2} e^{-3y^2/b^2} e^{-3z^2/c_f^2} \quad (7)$$

$$q_r(x, y, z, t) = \frac{6\sqrt{3}f_r Q}{abc_r \pi \sqrt{\pi}} e^{-3x^2/a^2} e^{-3y^2/b^2} e^{-3z^2/c_r^2} \quad (8)$$

In the above equations, the spatial coordinates of x and y are functions of time. Also, $f_r = 1.4$, $f_f = 0.6$ so that $f_r + f_f = 2$ [15], and parameters of C_f , C_r , b , and a are experimentally measured by cross-section properties of the weld pool and of the heat affected zone.

2.2. Stress analysis. For mechanical analysis of the temperature record, the thermal analysis was used as an input. Thermal stress and strain were also calculated in each temporal phase and the final state of the residual stress was obtained by the accumulation of thermal stresses and strains in the end-stage cooling. In welding process in which elastic-plastic deformation is made, the balance equations for the stress-strain rate are obtained by the following equation [25]:

$$d\sigma_{ij} = C_{ijkl} d\varepsilon_{kl} = C_{ijkl} (d\varepsilon_{kl} - d\varepsilon_{kl}^p - d\varepsilon_{kl}^{th}), \quad (9)$$

where C_{ijkl} is the elasticity tensor which includes Young's modulus and Poisson's ratio, $d\varepsilon_{ij}^e$ is elastic strain, $d\varepsilon_{ij}^p$ is plastic strain, and $d\varepsilon_{ij}^{th}$ is thermal strain.

Flow rules such as Prandtl-Reuss relations are used in the plastic zone. Given the associative flow rule, plastic flow direction is perpendicular to the surrender. In this rule, it is assumed that small plastic strain $d\varepsilon_{ij}^p$ is proportional to perverted tensions in every moment of loading. Therefore, the small plastic strain is obtained as Eq. 10,

$$d\varepsilon_{ij}^p = \frac{3}{2} \frac{d\varepsilon_p^{eq}}{\sigma^{eq}} S_{ij}, \quad (10)$$

in which:

$$d\varepsilon_p^{eq} = \sqrt{\frac{2}{3} d\varepsilon_{ij}^p d\varepsilon_{ij}^p} \quad (11)$$

$$\sigma^{eq} = \sqrt{\frac{3}{2} S_{ij} S_{ij}}, \quad (12)$$

where $\delta^{eq} = \delta_{yp}$ indicates the onset of plastic change in a moment and δ_{yp} value changes with temperature.

Yield stress of metals also increases by growing plastic strain [15,18-20]. Owing to imposing alternate tensile and compressive stresses to the object during welding, it should use the kinematic work hardening model [15,18,19]. Thus, a kinematic work hardening curve was considered based on the plastic strain at different temperatures. In the mechanical analysis, a linear eight-node cube element was employed, and the thermal history of the thermal analysis is imposed to the model as a thermal load. Then, the resulting stresses and strains are calculated by an elastic-plastic analysis of the object in every time interval. This operation is continued until the intended model gets cold at the ambient temperature. The calculated values in the final phase indicate welding residual stresses and strains [15,18-20].

3. Experimental procedures

3.1. Preparation of the coupons and temperature measurement. To prepare the coupons, among the sheets provided by the bus manufacturer, Oghab Afshan Co, some aluminum sheets of 6063 alloys in the size of $45 \times 11 \times 3$ mm³ were cut.

Upon surface preparing, the coupons underwent MIG welding by considering the input parameters such as flow rate, voltage, wire feeding speed, welding speed, etc. The final schematic of the coupons made for stress test is the same as depicted in Fig. 4.

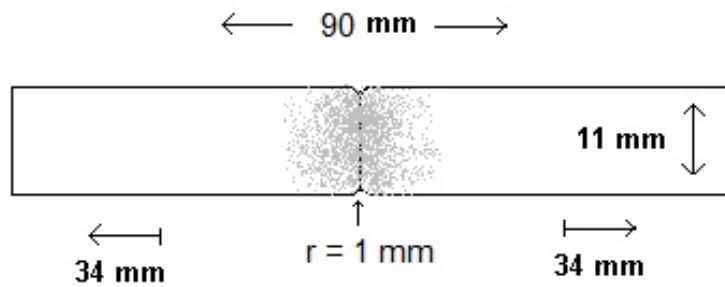


Fig. 4. Schematic of the tensile specimen welded by MIG.

To make the required welding connections, MIG machine MegaMax-SP500 with a rectifier was used. Welding gas source contained 100% argon with the shielding gas blowing rate of 15 Lit/min and recommended filler wire of ER5356 with a diameter of 1/2 mm and wire feeding speed of 10 m/min [26]. Table 1 shows the results of the chemical analysis of the parent metal and the filler wire used. The current source for all coupons was three-phase DC with output current of 110 ampere. Some suitable fixtures were used to stabilize the coupons and prevent from distortion during welding. The coupons were also cleaned up before welding by diluting phosphoric acid 5% and alcohol.

Table 1. Chemical compositions of the parent material and filler wire used [wt%].

Composition	Mg	Si	Fe	Mn	Zn	Cu	Cr	Ti	Al
Al 6063	0.75	0.45	0.26	0.08	0.07	0.03	0.02	0.01	Bal.
ER5356	5.1	0.27	0.43	0.11	0.10	0.10	0.90	0.80	Bal.

The manually welding was performed by a qualified welder in the butt joint. To determine the welding speed, trial and error were performed by a chronometer to make a suitable weld. The examined welding parameters were as per table 2.

Table 2. Welding operation parameters.

Coupons No.	Voltage [V]	Welding speed [mm/s]
1	5	1.66
2	5	2.50
3	5	5.00
4	3	2.50
5	6	2.50
6	9	2.50

The temperature at the different position the coupon was measured using the calibrated infrared thermometer (RayTek-RAY3IPLUS2M) with a spectral response of 1.6 microns, and with ±1% accuracy [27]. The IR thermometer was stabilized on the back side of the specimen and adjusted to record the temperatures-times at the 3 positions, parent metal, HAZ, and fusion line with the distance of 2, 6 and 15 mm from the weld centerline, respectively. These positions have been depicted in Fig 5-a.

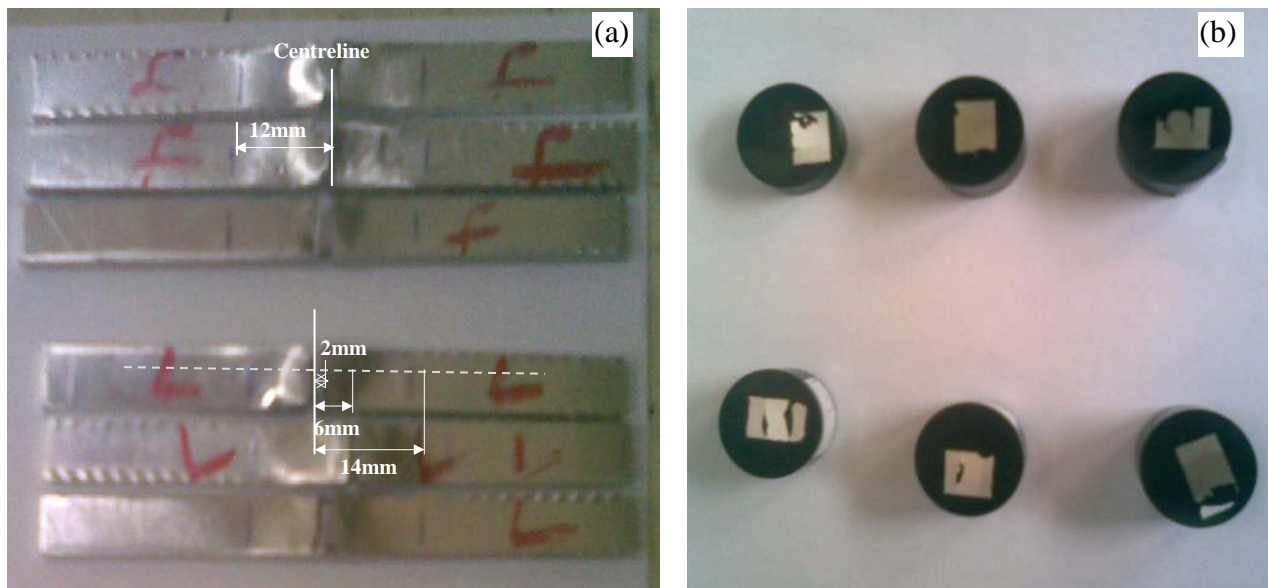


Fig. 5. The coupons of the 6063 Al sheets welded using MIG (a) distorted zones in the tensile test coupons, and (b) cross-section of the weld profile and the hardness test coupons.

3.2. Tensile test. To examine the tensile behaviour of the welded joints, the universal testing machine (Dartec model) was used. Flat jaw has been used in this research and the lower jaw was fixed and the upper one was mobile during the test. The tensile force ranges from 0 to 100 KN was imposed to the test coupons by the fixed velocity of 0.025 KN/s. In fact, six test coupons were prepared to conduct the tensile tests with the three various welding speeds and three operating voltages. The result contains the graphs of the engineering stress versus the engineering strain value.

3.3. Microhardness testing. A microhardness testing machine (InnovaTest 422A) was employed to measure the hardness at the 3 desired regions, fusion line, HAZ and parent metal. The Vickers hardness was conducted under a test force of 200 gr. To raise accuracy of the results, each hardness test was repeated three times and their averages were reported versus the specified distance from the fusion line.

3.4. Microstructural examination. To prepare the coupons of metallography, the welded zone in each sheet was separated by cutting and was, then, polished. To etch the coupons, the mixture solution of HCL 15%, HNO₃ 25%, HF 1% was used within 2 minutes in environmental conditions. For image capturing and measuring, the optical microscope (Leica DM1750 M) was employed by the Clemex software.

4. Results and discussion

4.1. Simulation output and comparison with the experimental results. The output from simulation analysis of the residual stresses can be seen in Figs. 6 and 7. According to the obtained results, the distorted zone is in approximately 10 mm of the weld line (Fig. 6) that is in good agreement with the observations (12 mm in Fig. 5 (a)).

As seen in Fig. 6, the residual stresses of the model simulated are compressive in the interval of 4-11 mm, and are tensile before the interval. The related 3D picture of the FEM model can be seen in Fig. 7.

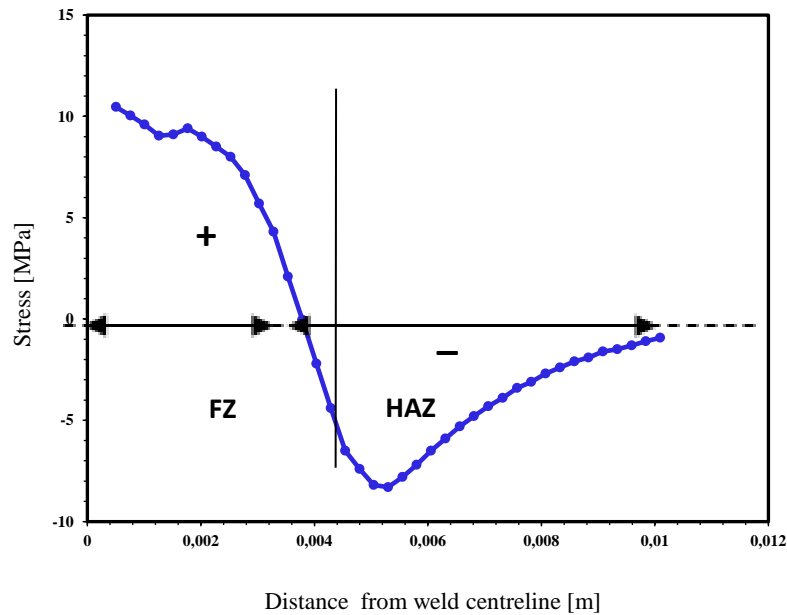


Fig. 6. The residual stress distribution in the HAZ and the fusion zone, at $t=250s$, perpendicular to the weld line, derived by the simulation.

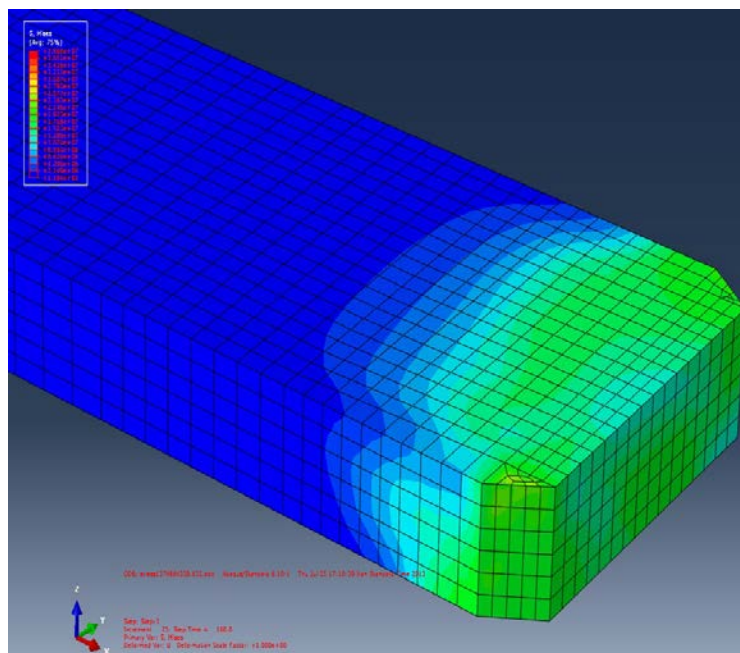


Fig. 7. Von Mises residual stress of the welded model.

4.2. Transient temperature analysis. Both the in-situ transient temperature measurements at 3 positions of the fusion line (FL) and HAZ, and the parent metal (PL) and those were calculated aiding the finite element method described above are compared in Fig. 8 (a) to (c), respectively. The diagrams demonstrate that the FEM values are in good conformity with the measured ones in terms of both trends and magnitude. The diagrams of a and b also depict how they follow a similar pattern so that they all reach a peak abruptly, and then, drop dramatically due to the strong heat sink, and eventually, decline steadily over the period. But Fig. 8 (c) depicted that how this rate has been much moderate, in contrast with the steel alloys which have an abrupt decrease, owing to the high rate of heat arrived from the previous transferred paths.

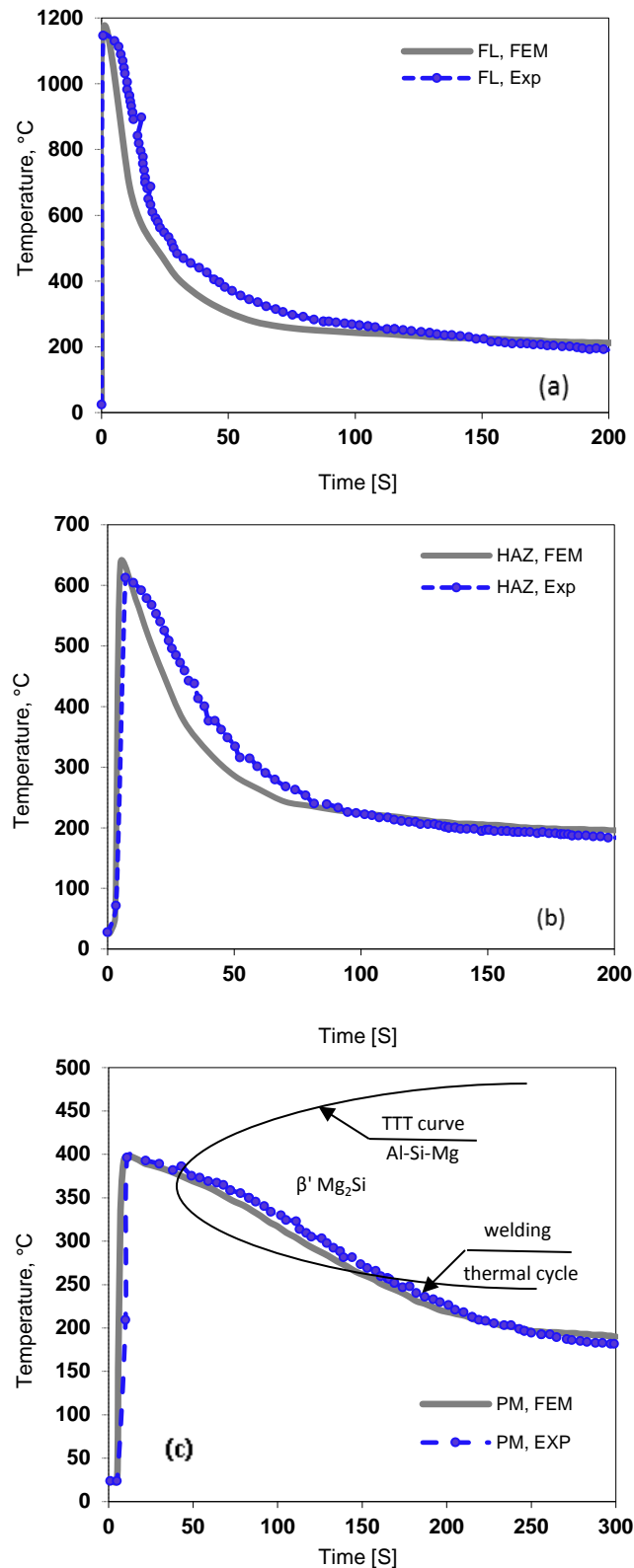


Fig. 8. Comparison between diagrams of the FEM and the in-situ temperature measurements for MIG welding of the 6063 Al sheets at the three regions, (a) the fusion line (FL), (b) the HAZ (FL+4), and (c) the parent metal (FL+12) alongside the TTT curve.

Since the temperature of the molten pool in GMAW of aluminum alloys is higher than 1227 °C, [28] compared to the melting range of the alloy that is between 616 to 654 °C, it is possible to increase the wire feeding speed that in return increases the deposition rate, which is

an economically considerable effect, especially when this also can be led to reach a soundness weld without increasing the risk of imperfections like as lack of fusion. Fig. 9 depicts a good agreement between the maximum temperatures forecasted and those were measured in the real-life experiment so that these values in the FZ were 1161°C and 1149°C, respectively. Fig. 8 (a) particularly depicted that because of the large heat sink phenomenon, the parent metals have not been fused at the very start-up of the welding so that there were been the thresholds in this regard.

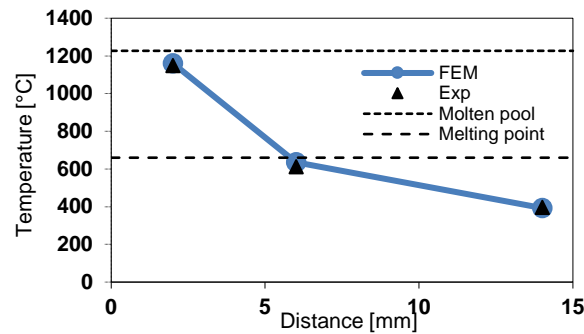


Fig. 9. Comparison between the experimental peak temperature measurements with the ones derived from the FEM vs. the distance from the fusion line. The average molten pool [28] and melting point temperatures were drawn as indicators.

4.3. Mechanical properties. As depicted in Fig. 10 (a), the more the welding speed, the more stress-strain values such that for the coupon (1), with the lowest welding speed, the conventional yield stress is 4.84 MPa, for the coupon (2), with the average speed, is 9.68 MPa, and for the coupon (3), with the highest welding speed, is 16.13 MPa. The ultimate tensile strength (UTS) for the coupons of (1), (2) and (3) were also 12.9, 26.45, and 45.16 MPa, respectively. Both of the above data were ascending and revealed that the UTSs were improved by increasing the welding speed and due to decrease the heat input.

The contrary is true for the arc voltage (Fig. 10 (b)). It means that by increasing the arc voltage, the tensile properties are decreased. Therefore, the conventional yield stress is 16.13 MPa with the low arc voltage in the coupon (4), 6.45 MPa with the average arc voltage in the coupon (5), and 6.05 MPa with the high arc voltage in the coupon (6). The ultimate strengths for the coupons 4, 5, 6 were also 41.29, 24.19, and 15.48 MPa, respectively, which has a descending trend.

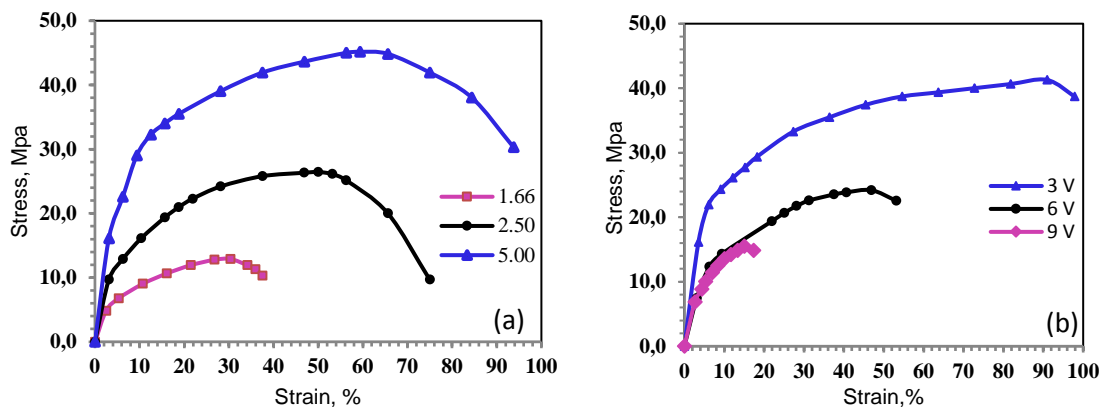


Fig. 10. The tensile test diagrams of the 6063 Al coupons welded by MIG in variant (a) welding speed [mm/s], and (b) voltage [v].

Fig. 11 (a) depicts that the hardness goes up by increasing the welding speed while the hardness curves move towards the smaller numbers by voltage increasing as depicted in Fig. 11 (b). The results are well-adapted to the data obtained from the simulation and the stress-strain curves. The dramatic drop in the sides of each curve is related to the HAZ which depicts much less hardness in comparison with the fusion zone (middle of the curves).

Considering the hardness values obtained and the average of 83 Vickers for the primary aluminum 6063 coupons, heat-affected zones have less hardness of approximately 20 units in Vickers scale. This observed feebleness in the HAZ was owing to the overaging, the partial dissolution, and the formation of undesired precipitations during the welding heat input cycle. To eliminate this deficiency and increase hardness of the weld surrounding zones, rolling down the weldment and explosive tapping are performed after thermal processing followed by welding. Recently, modern methods such as hardening by the pulsed laser beam and/or high-energy electron beams have been suggested. In both of the above tapping methods, hardness increases by work hardening mechanism. According to the information provided by the supplier, the primary parent metal of Al 6063 alloy contained 4.23% of fine phase of Mg_2Si .

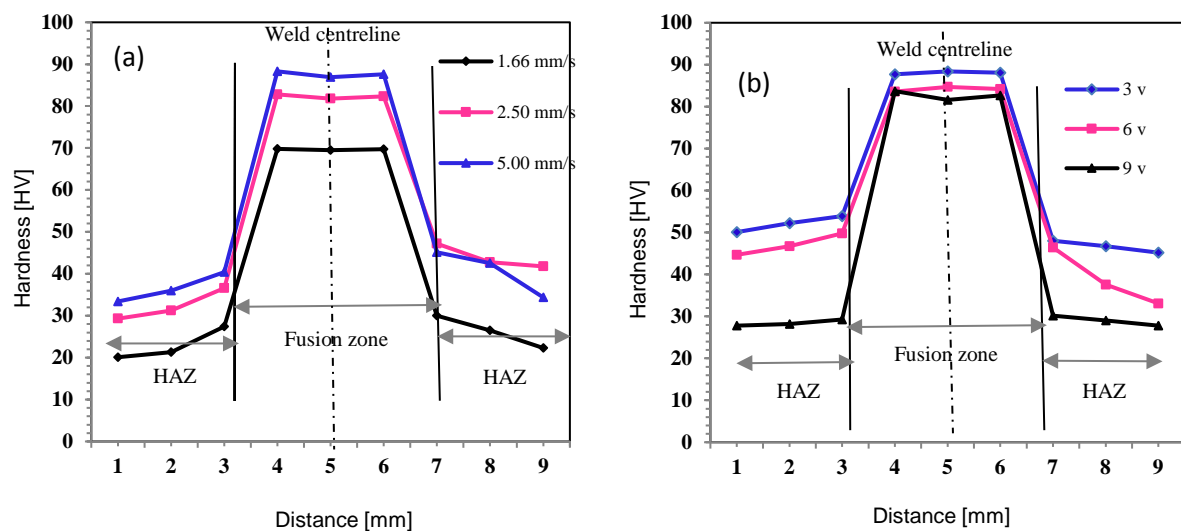


Fig. 11. The diagrams of hardness vs. mirror distance of the 6063 Al coupons welded by MIG with 2 specified regions: the fusion zone (FZ) and the HAZ, in the variant of (a) welding speed, and (b) voltage.

After welding, the computer analysis of the coupon images by Clemex software depicted that the mean percentage of the finer and darker phase of Mg_2Si is 2.27% (Fig. 12 (a)). This indicated a decrease in precipitation percentage after welding probably due to dissolution of precipitates exposed to welding heat. Reduction of precipitate percentage and grading structure shall be the result of the partial anneal in the HAZ accompanied by the dissolution and/or decomposition of the precipitates. If the diffusion circumstances are provided in the surrounding weld line, the hardness raises by increasing the precipitates percentage and their uniform dispersion in the matrix. Moreover, welding of 6063 Al alloy not only causes to eliminate the primary aging, but also brings to lose the dislocation density, their alignment and order which had been made from the previous cold work [1,29]. The dilution of the Mg_2Si percentage of the parent material is indeed crucial by using an appropriate filler metal to reduce the weld metal crack susceptibility.

As a modal comparison between the studied alloy and 6061 alloy, as the most analogous grade for that, since the 6063 alloy is more diluted than 6061 one (has the lower contents of Si

and Fe), the amount of $Al_xFe_ySi_z$ spreads (i.e $FeAl_3$, $FeAl_6$, Fe_3SiAl_{12} , Mg_2Si in a wrought form) [26] is not so sufficient, consequently, their mechanical properties are not greatly affected by its low cooling rate [30]. Besides, pursuant to the time-temperature transformation (TTT) curves reported in some literatures [31,32], whereas in the TTT curves of the alloy studied, the critical temperature range (the hardness falls down rapidly with the extension of isothermal time) is 300 to 410 °C and the nose temperature is 360 °C, however, compared with those values of 6061 Al which are 220 to 440 °C and 360 °C, respectively, it can be perceived that there is a lower percentage of the precipitates in 6063 alloy which that our observations demonstrated the same.

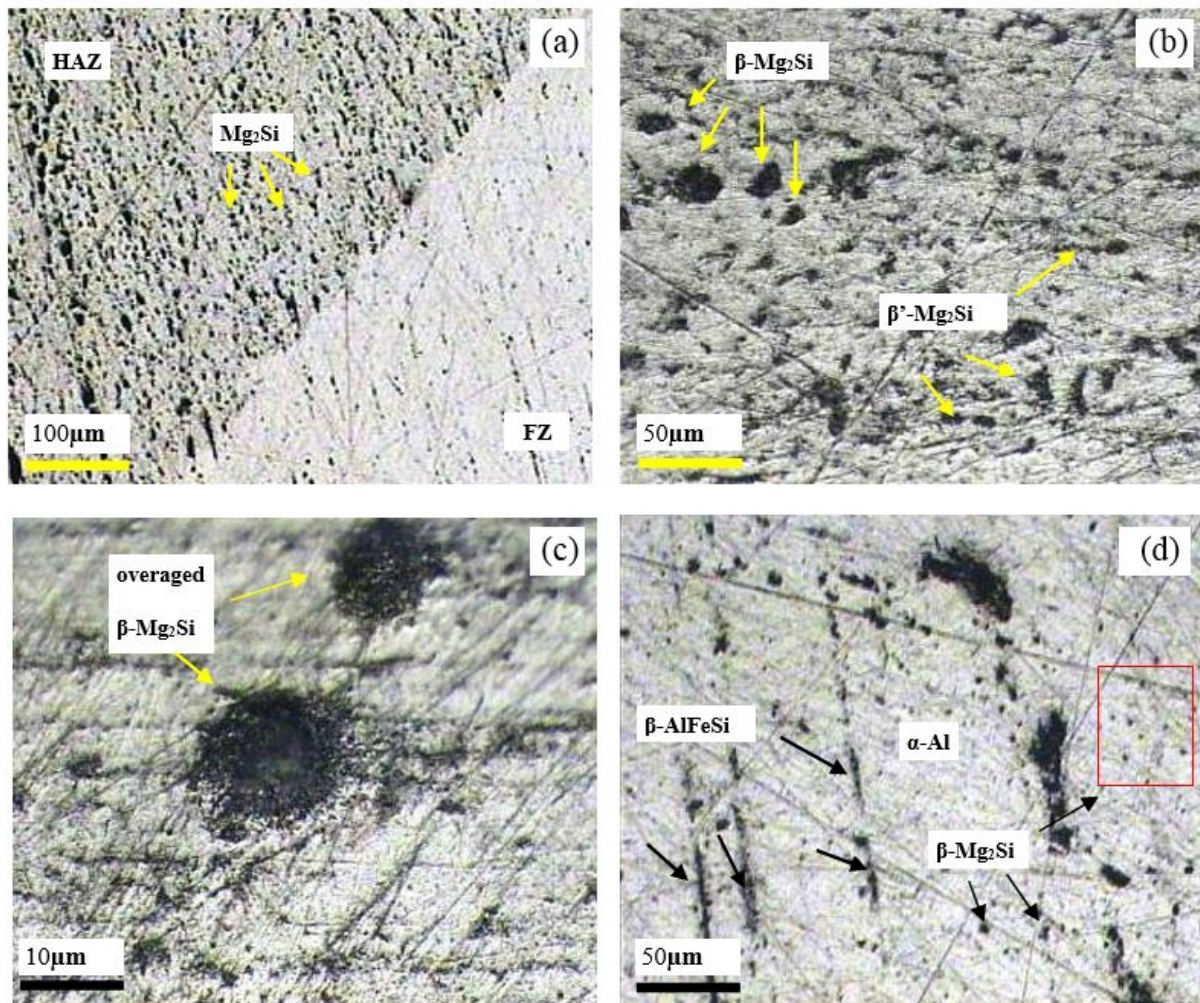


Fig.12. The microstructure images of the welded 6063 Al alloy, (a) the boundary between HAZ and FZ with the phases precipitated, (b) HAZ, (c) the overaged, agglomerated β - Mg_2Si in HAZ, and (d) Modified β - $AlFeSi$ pseudo-plate-like with the smaller and coarsened β - Mg_2Si precipitates in the FZ.

As depicted in Fig 12. b and c, HAZ has a microstructure with the overaged and rounded black precipitates containing β - Mg_2Si precipitates, equilibrium phase with a FCC crystal structure, were dispersed in the matrix. This region also may contain a little amount of the coarsened β' - Mg_2Si precipitates, developed rod-like with a hexagonal crystal structure, as the TTT curve forecasted it. The FZ is distinguished by its pseudo-plate-like dendrites, which contains the dark inter-dendritic network called β - $AlFeSi$ as shown in Fig.12 (d). In fact, these kind of precipitates are not exactly a plate-like, similar to what might see in the cast ingot, their shapes are partially modified from plate to sub-plate, owing to a rapid cooling rate of welding.

This region also contains, the finer Mg_2Si precipitates. These results are consistent with the findings of other researchers [16, 33-38].

Indeed, the TTT curve in Fig. 8 (c) depicts that the probability of formation of β' - Mg_2Si precipitates is not high, but by and large its trend is to increase by moving from FZ towards HAZ.

5. Conclusions

In this research, the welding simulation package of MIG welding of Al 6063 alloy was developed and the influences of the microstructure, thermal history and heat input, and some other crucial welding parameters, including velocity and voltage, on the mechanical and physical features of the welded alloy were examined. The main results of the empirical examinations and the simulation are as follows:

–The results of tensile and micro-hardness measurements indicated that the increase in the welding speed results in increasing hardness, tensile strength, and yield stress in 6063 aluminum alloy. While increasing in arc voltage results in decreasing in the above values.

–The results of the temperature gradients and the fields of welding-induced stress depicted that there is a good agreement between the simulation and the real-life measurements for the alloy. Actually, based on the FEM results, the distorted zones were extended along the weld centreline up to 10 mm. This almost had a compliment with the empirical observation, which was 12 mm. Indeed, the compressive thermal stresses were developed in the vicinity of the fusion line. Furthermore, the simulation results depicted that the residual stress on the intended model are compressive in the interval of 4 to 11 mm, from the weld centreline, and is tensile out of that which are in good accord with the experimental findings in terms of the appearance of the weldment.

–Based on both results of the FEM and the real-life temperature measurements, it has been found that owing to the large heat sink phenomenon, the parent metals have not been fused at the very start-up of the welding so that there were been the thresholds in this regard.

–The microstructural and microhardness examinations also illustrated that the parent metals have been heated up—partially annealed—moderately during the welding. The microstructure images depicted that the overaged, agglomerated β - Mg_2Si phases, in the HAZ, and the β - $AlFeSi$ pseudo-plate-like precipitates alongside the smaller and coarsened β - Mg_2Si , in the fusion zone, were precipitated. Moreover, a lower amount of β - Mg_2Si participates for the 6063 Al sheets in comparison to the 6061 one were found which was in accord with the predictions (considering the TTT curve) and those reported in the some literatures.

–The in-situ temperature measurements in the fusion zone and the HAZ made ability to foresee and analyze the phases participated and the related mechanical behaviour in the weldment. For instance, the TTT curves depicted that how by moving from the fusion line towards the HAZ, and beyond, the various cooling rates may lead up to the precipitation of β' - Mg_2Si .

Acknowledgment. *The authors express their gratitude to Prof. A. H. Raeouf for his advice, the department of metallurgy and materials, faculty of engineering of Semanan University and the automobile company, Oghab Afshan Co., for the lab facilities and materials supports.*

References

- [1] M. Mathers, *The welding of aluminum and its alloys* (Woodhead Publishing Ltd., Cambridge, England, 2002).
- [2] M. Olabode, P. Kah, J. Martikainen // *Proceedings of the Institution of Mechanical Engineers Part B Journal of Engineering Manufacture* **227** (2013) 1129.

- [3] M.A. Wahab, MJ Painter, M.H. Davies // *Journal of Materials Processing Technology* **77** (1998) 233.
- [4] C. S. Chen, J. G. Yang, A. H. Tan // *Materials Science and Technology* **25** (2009) 896.
- [5] J. Chen, C. Schwenk, C.S. Wu, M. Rethmeier // *International Journal of Heat and Mass Transfer* **55** (2012) 102.
- [6] Y. Tsujimura, S. Nakanishi, A.B. Murphy, M. Tanaka // *Quarterly journal of the japan welding society* **21** (2013) 5s-8s.
- [7] R. P. Verma, K.N. Pandey, Y. Sharma // *Proceedings of the Institution of Mechanical Engineers Part B Journal of Engineering Manufacture* **229** (2015) 1021.
- [8] J. A. Goldak, M. Akhlaghi, *Computational welding mechanics* (Springer, New York, USA, 2005).
- [9] W. Bleck, U. Reisgen, O. Mokrov, E. Rossiter, T. Rieger // *Advanced Engineering Materials* **12** (2010) 147.
- [10] J. Hu, H. L. Tsai // *Journal of Physics D: Applied Physics* **41** (2008) 065202.
- [11] S. Baharnezhad, H. Farhangi, A. A. Allahyari // *Journal of Mechanics in Medicine and Biology* **13** (2013) 1.
- [12] P.H. Chang, T.L. Teng // *Computational Materials Science* **29** (2003) 511.
- [13] C.K. Takemori, T.D. Müller, M.A. De Oliveira, *Numerical simulation of transient heat transfer during welding process*, In: *Int. Compress Eng. Conf.* (Purdue, USA 2010).
- [14] A. Anca, A. Cardona, J. Risso, V.D Fachinotti // *Applied Mathematical Modelling* **35** (2011) 688.
- [15] J.A. Goldak, A.A. Chakravarti // *Metal. Trans.* **15** (1984) 200.
- [16] H. Guo, J. Hu, H.L. Tsai // *Numerical Heat Transfer, Part A: Applications* **57** (2010) 392.
- [17] J. Chen J, X. Yu, R.G. Miller, Z. Feng // *Science and Technology of Welding & Joining* **20** (2015)181.
- [18] A. Kermanpur, M. Shamanian, V. Esfahani Yeganeh // *Journal of Materials Processing Technology* **199** (2008) 1.
- [19] D. Stamenkovic, I. Vasovic // *Scientific Technical. Rev.* **12** (2009) 57.
- [20] Z. Barsoum, *Residual stress analysis and fatigue assessment of welded steel structures* (Ph.D. Thesis, Kungliga Tekniska Hogskolan Stockholm, Sweden 2008).
- [21] S.A. Tsirkas, P. Papanikos, T.H. Kermanidis // *Journal of Materials Processing Technology* **134** (2003) 59.
- [22] *JMatPro 7.0 User's Guide* (Sente Software Ltd., Surrey, UK, 2013).
- [23] ALUSELECT, European aluminum association, Brussels. Databank for aluminum alloys, properties, applications and standards, 1990.
- [24] X.K. Zhu, Y.J. Chao // *Computers & Structures* **80** (2002) 967.
- [25] *ABAQUS/standard user's manual, v. 6.10.* (Hibbitt, Karlsson and Sorensen, Inc., Pawtucket, RhodeIsland, USA, 2010).
- [26] J.R. Davis, *Aluminum and aluminum alloys, ASM specially handbook* (ASM International, Materials Park, Ohio, USA, 1994).
- [27] R.N. Peter Childs, *Practical temperature measurements* (Butterworth-Heinemann, Oxford, UK, 2001) 238-288.
- [28] K. Ando, K. Nishiguchi, *Average temperature of the molten pool in TIG and MIG arc welding of steel and aluminum*, IIW Doc. 212-161-68, 1969.
- [29] G.E. Dieter, In: *Mechanical metallurgy* (McGraw-Hill, USA 1976), p. 232-291.
- [30] *ASM Metals Handbook, Heat treating* (ASM International, Materials Park, Ohio, USA, 1991) ch.8.
- [31] H. Li, C. Zeng, M. Han, J. Liu, X. Lu // *Transactions of Nonferrous Metals Society of China* **23** (2013) 38.

- [32] G.P. Dolan, J.R. Robinson // *Journal of Materials Processing Technology* 153-**154** (2004) 346.
- [33] S. Claves, M. Watanabe // *Microscopy and Microanalysis* **12** (2006) 1410.
- [34] C.E. Cross, D.L. Olson // *Welding Journal* **61** (1982) 381s-387s.
- [35] G.F. Vander Voort, In: *Metallography and Microstructures* (ASM International, Materials Park, Ohio, USA, 1985), ch.10.
- [36] P.M.G.P. Moriera, F.M.F de Oliveira, P.M.S.T. de Castro // *Journal of Materials Processing Technology* **207** (2008) 283.
- [37] R.R. Ambriz, G. Barrera, R. García and V.H. López // *Welding International* **24** (2010) 42.
- [38] J. Asensio-Lozano, B. Suárez-Peña, G.F. Vander Voort // *Materials* **7** (2014) 4224.

Submission of papers:

Manuscript should be submitted (**both MS Word and PDF**) by e-mail to: mpmjournal@spbstu.ru

After a confirmation of the paper acceptance, the authors should send the signed hard copy of the "Transfer of Copyright Agreement" form (available at <http://www.mpm.spbstu.ru> section "Authors") by regular post to "Materials Physics and Mechanics" editorial office:

Periodicals Editorial Office, Institute of Advanced Manufacturing Technologies, Peter the Great St.Petersburg Polytechnic University, Polytechnicheskaya, 29, St.Petersburg 195251, Russia.

The scanned copy of the signed "Transfer of Copyright Agreement" should be send by e-mail to: mpmjournal@spbstu.ru.

Filetype:

Authors are invited to send their manuscripts **as MS Word file with PDF format copy.**

MS Word file should be prepared according to the general instructions bellow; we are kindly asking the authors to look through the detail instruction at: <http://www.mpm.spbstu.ru>.

Length:

Papers should be limited to 30 typewritten pages (including Tables and Figures placed in the proper positions in the text).

Structure of the manuscript:

PAPER TITLE: CENTERED,

TIMES NEW ROMAN 14 BOLD, CAPITAL LETTERS

A.B. Firstauthor¹, C.D. Secondauthor^{2*} -Times New Roman 12, bold, centered

¹Affiliation, address, country - Times New Roman 10, centered

*e-mail: e-mail of the corresponding author - Times New Roman 10, centered

Abstract. Times New Roman 12 font, single line spacing. Abstract should not exceed 12 lines.

Paper organization. Use Times New Roman 12 font with single line spacing. Use *Italic* font in order to stress something; if possible, please, use **bold** for headlines only.

Page numbering. Please, do not use page numbering.

Tables, Figures, Equations. Please, see the sample file at <http://www.mpm.spbstu.ru> for more details.

References

References should be subsequently numbered by Arabic numerals in square brackets, e.g. [1,3,5-9], following the sample style below:

[1] A.K. Mukherjee // *Materials Science and Engineering A* **322** (2002) 1.

[2] L. D. Landau, A. M. Kosevich, E. M. Lifshitz, L. P. Pitaevskii, *Theory of elasticity*, Third Edition (Butterworth-Heinemann, 1995).

[3] C.C. Koch, I.A. Ovid'ko, S.Seal, S. Veprek, *Structural Nanocrystalline Materials: Fundamentals and Applications* (Cambridge University Press, Cambridge, 2007).

[4] A.E. Romanov, V.I. Vladimirov, In: *Dislocations in Solids*, ed. by F.R.N. Nabarro (North Holland, Amsterdam, 1992), Vol. 9, p.191.

[5] W. Pollak, M. Blecha, G. Specht // *US Patent 4572848*.

[6] <http://www.mpm.spbstu.ru>

Правила подготовки статей:

Рукопись (**английский язык, MS Word и копия PDF**) должна быть направлена в редакцию журнала по электронной почте: **mpmjournal@spbstu.ru**.

После подтверждения принятия статьи в печать, авторы должны отправить подписанные:

1. Соглашение о передаче авторских прав (форма размещена на сайте журнала: <http://www.mpm.spbstu.ru> в разделе «Авторам»); 2. Экспертные заключения о том, что материалы статьи не содержат сведений, составляющих государственную тайну, и информацию, подлежащую экспортному контролю; по адресу:

Россия, 195251, Санкт-Петербург, Политехническая, д. 29, Санкт-Петербургский политехнический университет Петра Великого, Институт передовых производственных технологий, Редакция периодических изданий.

Скан-копии подписанных документов просим направить по электронной почте: **mpmjournal@spbstu.ru**

Тип файла:

Редакция принимает **файлы MS Word с копией в формате PDF**. Статья должна быть подготовлена в соответствии с настоящей инструкцией, мы просим авторов также следовать более подробным инструкциям на сайте журнала <http://www.mpm.spbstu.ru> в разделе «Авторам».

Длина статьи:

Статья не должна превышать 30 страниц формата А4, включая Таблицы и Рисунки, размещенные непосредственно в соответствующих местах.

Общие правила оформления статьи:

НАЗВАНИЕ СТАТЬИ: ВЫРОВНЯТЬ ПО ЦЕНТРУ, ШРИФТ, TIMES NEW ROMAN 14 BOLD, ЗАГЛАВНЫЕ БУКВЫ

Автор(ы): **А.Б. Первыйавтор¹, В.Г. Автор^{2*}** - шрифт Times New Roman 12, bold, по центру

¹Наименование организации, адрес, страна - шрифт Times New Roman 10, по центру

* e-mail автора, представившего статью - шрифт Times New Roman 10, по центру

Аннотация. Аннотация статьи составляет не более 12 строк. Используйте шрифт Times New Roman 12, одинарный межстрочный интервал

Как организовать текст статьи. Используйте шрифт Times New Roman 12, одинарный межстрочный интервал. При необходимости выделить какую-либо информацию используйте *курсив*. По возможности, избегайте использования в тексте статьи **полужирного** шрифта, используйте его только для заголовков и подзаголовков.

Номера страниц. Пожалуйста, не используйте нумерацию страниц

Таблицы, Рисунки, Уравнения. Подробные правила оформления данных элементов статьи приведены в инструкции на сайте журнала <http://www.mpm.spbstu.ru>

Литература

Ссылки приводятся в тексте в квадратных скобках [1,3,5-9]. Стиль оформления ссылок:

[1] В. Ф. Бакиров, Р. В. Гольдштейн // *Прикл. Мат. Мех.* **68** (2004) 170.

[2] А.К. Mukherjee // *Mater. Sci. Eng. A* **322** (2002) 1.

[3] Л.Д. Ландау, Е.М. Лифшиц, *Теория упругости* (Наука, М., 1988).

[4] С.С. Koch, I.A. Ovid'ko, S.Seal, S. Veprek, *Structural Nanocrystalline Materials: Fundamentals and Applications* (Cambridge University Press, Cambridge, 2007).

[5] А.Е. Romanov, V.I. Vladimirov, In: *Dislocations in Solids*, ed. by F.R.N. Nabarro (North Holland, Amsterdam, 1992), Vol. 9, p.191.

[6] W. Pollak, M. Blecha, G. Specht // *US Patent 4572848*.

[7] <http://www.mpm.spbstu.ru>

МЕХАНИКА И ФИЗИКА МАТЕРИАЛОВ

32 (2) 2017

Учредители: Санкт-Петербургский политехнический университет Петра Великого,

Институт проблем Машиноведения Российской академии наук

Издание зарегистрировано федеральной службой по надзору в сфере связи,
информационных технологий и массовых коммуникаций (РОСКОМНАДЗОР),

свидетельство ПИ №ФС77-69287 от 06.04.2017 г.

Редакция журнала

Профессор, д.т.н., академик РАН, А.И. Рудской – главный редактор

Профессор, д.ф.-м.н., член-корр. РАН, Д.А. Индейцев – главный редактор

Профессор, д.ф.-м.н. И.А. Овидько (1961 - 2017) – основатель и почетный редактор

Профессор, д.ф.-м.н. А.Л. Колесникова – ответственный редактор

Доцент, к.т.н. А.С. Немов – ответственный редактор

Е.О. Касяненко – выпускающий редактор

А.И. Хайрутдинова – редактор, корректор

Телефон редакции

+7 (812) 591-65-28

E-mail: mpmjournal@spbstu.ru

Компьютерная верстка А.В. Шимченко

Подписано в печать 21.11.2017 г. Формат 60x84/8. Печать цифровая
Усл. печ. л. 9,0. Тираж 100. Заказ ____.

Отпечатано с готового оригинал-макета, предоставленного автором
в Издательско-полиграфическом центре Политехнического университета Петра
Великого. 195251, Санкт-Петербург, Политехническая ул., 29.
Тел.: (812) 552-77-17; 550-40-14.

The simulation of carbon nanotubes as macromolecular coils: interfacial adhesion G.V. Kozlov, I.V. Dolbin	103-107
Carbon-based nanostructure created by Ba and Cs atomic layer deposition on the vicinal 3C-SiC(111) surfaces G.V. Benemanskaya, P.A. Dementev, S.A. Kukushkin, M.N. Lapushkin, A.V. Osipov, S.N. Timoshnev	108-116
The study of the interaction of hydrogen impurity with point and linear defects in palladium and nickel G.M. Poletaev, I.V. Zorya, E.S. Medvedeva, D.V. Novoselova, M.D. Starostenkov	117-122
Generalized thermoelastic axi-symmetric deformation problem in a thick circular plate with dual phase lags and two temperatures R. Kumar, V.R. Manthena, N.K. Lamba, G.D. Kedar	123-132
An effective method to find Green's functions for layered media N.S. Markov, A.M. Linkov	133-143
Copper crystals with fragmented structure and developed surface in temperature fields N.N. Gryzunova, A.A. Vikarchuk, A.M. Gryzunov, A.E. Romanov	144-151
Shock-induced structural instabilities and spall-strength of maraging steels Yu.I. Mescheryakov, N.I. Zhigacheva, A.K. Divakov, Yu.A. Petrov	152-164
Effect of titanium carbide addition on the workability behavior of powder metallurgy aluminum preforms during hot deformation S. Narayan, A. Rajeshkannan	165-177
Defects in thin epitaxial layers of $(Al_xGa_{1-x})_2O_3$ grown on Al_2O_3 substrates A.V. Kremleva, D.A. Kirilenko, V.I. Nikolaev, A.I. Pechnikov, S.L. Stepanov, M.A. Odnoblyudov, V.E. Bougrov, A.E. Romanov	178-185
Mathematical model of ultrasound transmission in gradient materials synthesized in arc surfacing under contact loading V.D. Sarychev, A.Y. Granovskiy, S.A. Nevskii, S.V. Konovalov, V.E. Gromov, M.V. Temlyantsev	186-193
Study of antireflection coatings for high speed 1.3 -1.55 μm InGaAs/InP PIN photodetector E.S. Kolodeznyi, I.I. Novikov, A.G. Gladyshev, S.S. Rochas, K.D. Sharipo, L.Ya. Karachinsky, A.Yu. Egorov, V.E. Bougrov	194-197
Synthesis of silver nanochains with a chemical method I.M. Sosnin, M.N. Turkov, M.R. Shafeev, E.V. Shulga, I. Kink, A.A. Vikarchuk, A.E. Romanov	198-206
Relaxation in resins with low-frequency mechanical cycling V.I. Ivlev, A.F. Sigachyov, N.E. Fomin, V.A. Yudin	207-212
On calculation of effective elastic properties of materials with cracks Ruslan L. Lapin, Vitaly A. Kuzkin	213-221
In-situ measurement and finite element simulation of thermo-mechanical properties of AA 6063 aluminum alloy for MIG weldment S. Baharnejhad, A.P. Golhin	222-236